UNIVERSIDAD POLITÉCNICA DE MADRID
Escuela Técnica Superior de Ingenieros de Telecomunicación

Scleral biomechanics and myopia development and control

DOCTORAL THESIS

Submitted for the degree of Doctor by:

Lupe Ivette Villegas Lopez
Master Sciences, Technologies and Santé

Madrid, 2024

UNIVERSIDAD POLITÉCNICA DE MADRID
Escuela Técnica Superior de Ingenieros de
Telecomunicación

Doctoral Degree in Biomedical Engineering

Scleral biomechanics and myopia development and control

DOCTORAL THESIS

Submitted for the degree of Doctor by:

Lupe Ivette Villegas Lopez
Master Sciences, Technologies and Santé

Under the supervision of:
Dra. Susana Marcos Celestino

Madrid, 2024

Title: Scleral biomechanics and myopia development and control

Author: Lupe Ivette Villegas Lopez

Doctoral Programme: Biomedical Engineering

Thesis Supervision:

Dra. Susana Marcos Celestino, Profesora de Investigación, Instituto de Óptica-CSIC & Professor, Institute of Optics - University of Rochester (Supervisor)

External Reviewers:

Thesis Defense Committee:

Thesis Defense Date:

This thesis has been partially supported by Spanish Government Grant (PRE2018-086169)

To my parents, my sister, my husband, and myself

ACKNOWLEDGEMENT

I would like to thank my thesis supervisor, Prof. Susana Marcos, for giving me the opportunity to be part of the Visual Optics and Biophotonics Lab, and Dr. Francisco Rojo for giving me the opportunity to obtain a Ph.D. degree at UPM.

I would like to thank the Spanish government for the grant that allowed me to do this thesis.

Thanks to Judith Birkenfeld and James German for their mentoring, fruitful discussions, guidance and support during all the experiments. Thanks to Daniel Pascual for helping me turn my crazy ideas into something that works, moves, or can be used as a support for tissues and animals. Thanks to Pilar Urizar, Alberto de Castro and Fernando Zvietcovich for teaching me OCT techniques.

Thanks to Prof. Luis Revuelta Rueda for his guidance and support in handling the animals. Also, to Juanan for his help with all the technical paperwork. Special thanks to Javier Fernandez and the staff of the Veterinary Clinic *Animales Exóticos* for teaching me and helping me with the handling of the guinea pigs. Special thanks to Luis San Frutos and Pablo Casar.

Thank you, Pilar and Alejandra, for your time, your craziness, your food, your teas, for leaving me out of the office, for helping me in the lab, for rescuing me when I needed it, for being part of this daily life.

Thank you to the members of the Viobio lab, because in one way or another you are part of this thesis. Thanks to Mar, Paula, Edu, Sara, Andrés, Elena, Paulina, Rocío, Álvaro, Alberto, Lucie, Eduardo, Carmen, Víctor, Ana and Nohelia.

Thanks to all the rabbits and guinea pigs (cuyes) who literally gave their lives in this thesis.

Gracias por creer siempre en mi Herminia, Marco y Vero, even if there are kilometers of distance in between. Moitas grazas Carmiña, German, María, Antoine, Inés and Alex. Merci d'avoir fait partie de mon soutien moral au fil des ans.

Pablo, thank you for your support, your persistence, your patience, your love and your craziness. If I have not thrown in the towel, it is because of you.

ABSTRACT

The sclera is the main supporting tissue of the internal structures of the eye. Biomechanical changes in the scleral tissue can be related to ocular diseases such as myopia. Myopia is a global public health problem that is currently considered a new pandemic due to its enormous magnitude. At present, the role of scleral remodeling as a modulator of myopia and potential moderator of myopia progression is not fully understood. The main objective of the work described in this thesis is to develop new methods to determine the role of the sclera and its modulation in the development and control of myopia.

The biomechanical responses of porcine and rabbit scleral tissues were studied using deformation imaging and elastography. Air-puff Optical Coherence Deformation Imaging revealed that scleral deformation changed across species (porcine or rabbit) and geographically at different locations on the same eye globe. In porcine eyes, maximum scleral deformation occurred in the superior and inferior sclera, and in rabbit eyes in the equatorial nasal and inferior sclera, for the same air-pulse configuration. Multi-directional Optical Coherence Elastography allowed radial mapping of mechanical properties at different locations and orientations of the eye globes and showed that the sclera was stiffer circumferentially and anteriorly than meridionally and posteriorly. The highest shear modulus values were found in the superior circumferential sclera. These results demonstrate that the tissue response depends on the internal structure (biochemical composition and collagen fibers organization), which varies between animal models and scleral regions.

Cross-linking has been proposed as a potential treatment for myopia, by stiffening the scleral tissue and halting axial elongation. The effects of Rose Bengal-green light and Riboflavin-ultraviolet light cross-linking on the biomechanical and swelling properties of rabbit sclera were investigated. Rose Bengal-green light cross-linking induced scleral stiffness to the same extent as riboflavin-ultraviolet light cross-linking. In addition, non-crosslinked tissue swelled more rapidly than crosslinked scleral tissue, and an inverse relationship between swelling and scleral stiffness was observed. Changes in the scleral collagen organization were examined by Second Harmonic Generation microscopy. The results suggest that Rose Bengal-green light cross-linking has potential for future *in vivo* studies as a method for the treatment of myopia, if the challenge of the photoinitiator and light irradiation reaching the posterior sclera is overcome.

Several pharmacological treatments have been proposed for myopia control. In particular, we tested *in vivo* latanoprost (an ocular hypotensive agent) and atropine (a dopamine-releasing agent) in monocular form-deprived myopia-induced guinea pigs. Myopic eyes were instilled daily with saline, latanoprost, or atropine for nine weeks. Ocular biometry, scleral biomechanics and collagen fiber organization were measured. The results suggest that latanoprost was as effective as atropine in inhibiting myopia progression by reducing axial length and refractive error. Both treatments attenuated the decrease in Young's modulus in myopic eyes, but only atropine increased the shear modulus. Consistent with these biomechanical differences, scleral collagen organization appeared to be at least partially restored in pharmacologically treated eyes.

In summary, this thesis used custom-developed technologies to characterize mechanically and structurally the sclera of common animal models. The scleral changes observed in myopia suggest that the sclera is a target tissue to prevent myopia progression.

RESUMEN

La esclerótica es el principal tejido de soporte de las estructuras internas del ojo. Las alteraciones biomecánicas de la esclerótica pueden deberse a enfermedades oculares como la miopía. La miopía es un problema de salud pública mundial considerada como una nueva pandemia. Actualmente, no se conoce del todo el papel de la remodelación de la esclerótica como modulador y potencial moderador de la progresión de la miopía. Lo que deja de manifiesto el objetivo principal de esta tesis, que es desarrollar nuevos métodos para determinar el papel de la esclerótica y su modulación en el desarrollo y control de la miopía.

Se ha estudiado la respuesta biomecánica de la esclerótica de porcino y conejo utilizando imágenes de deformación y elastografía. Las imágenes de deformación por pulso de aire revelaron que la deformación de la esclerótica fue diferente entre especies y entre las localizaciones en el globo ocular. En los ojos porcinos, la máxima deformación de la esclerótica se encontró en la región superior e inferior, y en los ojos de conejo en la región nasal ecuatorial e inferior. La elastografía multidireccional de coherencia óptica permitió cartografiar radialmente las propiedades mecánicas en diferentes localizaciones y orientaciones de los globos oculares y mostró que la esclerótica era más rígida circunferencialmente y en la región anterior, que meridionalmente y en la región posterior. Estos resultados demostraron que la respuesta tisular depende de la estructura interna (composición bioquímica y organización de las fibras de colágeno), que varía entre modelos animales y regiones de la esclerótica.

El entrecruzamiento de la esclerótica se ha propuesto como posible tratamiento de la miopía, ya que rigidiza la esclerótica y detiene la elongación axial. Se investigaron los efectos sobre las propiedades biomecánicas y de hinchamiento la de la esclerótica de conejo después de la reticulación mediante Rosa de Bengala con luz verde y Riboflavina con luz ultravioleta. La reticulación con Rosa de Bengala y luz verde indujo el mismo incremento de rigidez en la esclerótica que con Riboflavina y luz ultravioleta. Además, el tejido no reticulado se hinchó con mayor rapidez que el reticulado, y se observó una correlación inversa entre la hinchazón y la rigidez de la esclerótica. La reticulación también generó cambios en la organización del colágeno de la esclerótica. Los resultados sugieren que la reticulación con Rosa de Bengala y luz verde es un potencial método para tratar la miopía en futuros estudios *in vivo*.

Se han propuesto varios tratamientos farmacológicos para el control de la miopía. En particular, probamos *in vivo* latanoprost (un agente hipotensor ocular) y atropina (un agente liberador de dopamina) en cobayas con miopía inducida por privación monocular. A los ojos miopes se les instiló diariamente solución salina, latanoprost o atropina durante nueve semanas. La refracción, la biometría ocular, la biomecánica de la esclerótica y la organización de las fibras de colágeno fueron medidas. Los resultados sugirieron que el latanoprost fue tan eficaz como la atropina para inhibir la progresión de la miopía reduciendo la longitud axial y el error refractivo. Ambos tratamientos atenuaron la disminución del módulo de Young, pero sólo la atropina aumentó el módulo de cizallamiento. En consonancia con estas diferencias biomecánicas, la organización del colágeno de la esclerótica pareció restablecerse, al menos parcialmente, en los ojos tratados farmacológicamente.

En resumen, esta tesis utilizó tecnologías desarrolladas a medida para caracterizar mecánica y estructuralmente la esclerótica de modelos animales comunes. Los cambios escleróticos observados en la miopía sugieren que la esclerótica es un tejido diana para prevenir la progresión de la miopía.

TABLE OF CONTENT

LIST OF FIGURES

LIST OF TABLES

ABBREVIATIONS AND ACRONYMS

ACUS	Air-Coupled Ultrasonic
ACUS-OCE	Air-Coupled Ultrasonic Optical Coherence Elastography
AP	Air-puff Pressure
AXL	Axial Length
BSS	Balanced Salt Solution
C	Cornea
DA	Degree of Anisotropy
EN	Equatorial Nasal
ET	Equatorial Temporal
FEM	Finite Element Model
FD	Form-Deprived
FDM	Form-Deprivation Myopia
GAG	Glycosaminoglycan
I	Inferior
IN	Inferior Nasal
IT	Inferior Temporal
IOP	Intraocular Pressure
MAA	Major-Axis Angle
maxMPAC	Maximum value of Modified Planar Anisotropy Coefficient
mRLFE	Modified Rayleigh-Lamb Frequency Equation
N	Nasal
NFA	Normalized Fractional Anisotropy
OCE	Optical Coherence Elastography
OCT	Optical Coherence Tomography
OC	Order Coefficient
SS-PhS-OCT	Swept-Source Phase-Sensitive Optical Coherence Tomography

PBS	Phosphate-Buffered Saline
PN	Posterior Nasal
PT	Posterior Temporal
PG	Proteoglycan
UVX	riboflavin with Ultraviolet light Crosslinking
RB	Rose Bengal
RGX	Rose Bengal with Green light Crosslinking
SXL	Scleral Crosslinking
SHG	Second-Harmonic Generation
SE	Spherical Equivalent
S	Superior
SN	Superior Nasal
ST	Superior Temporal
T	Temporal
UVA	Ultraviolet A
WHO	World Health Organization

1. INTRODUCTION

1.1. Motivation

The sclera is the major connective tissue of the eye, the main contributor to the shape of the eye and the mechanical support of the eyeball. Mechanical scleral remodeling may be associated with certain ocular conditions such as myopia. Myopia is a public health problem affecting millions of people which prevalence rate is increasing worldwide according to the World Health Organization (WHO) (World Health Organization and Brien Holden Vision Institute, 2016). Therefore, there is a need to evaluate the mechanical properties of the sclera not only to understand the role of the sclera in the pathogenesis of myopia, but also to evaluate and guide the development of effective treatment of myopia.

Traditional measurements to assess the scleral biomechanical properties are typically destructive, such as tensile tests in which strips of tissue are cut from the ocular globe. In recent years, alternative optical techniques have been developed, initially for the mechanical characterization of the cornea in intact eyes and in many cases on corneas *in vivo*. These techniques include air-puff deformation imaging and optical coherence elastography, which allow quantification of tissue mechanical properties based on the response of the tissue to an external stimulus. Finally, the mechanical properties of the tissue result from the microscopic ultrastructure of the tissue, including the extracellular matrix and in particular the collagen organization and interweaving, which can be quantified using second harmonic generation microscopy imaging. The application of these imaging modalities allows a multi-level approach to understand the mechanical response of the sclera, to investigate factors that affect scleral remodeling in pathology and treatment, and to identify biomarkers that can monitor disease development and treatment. For the purpose of the current thesis, we will investigate the scleral properties in animal models of myopia and in different alternatives for myopia control.

Today, there are several proposed approaches to control myopia progression, some of which have recently been introduced into clinical practice (optical alternatives such as multifocal contact lenses or spectacle lenses with designs that modulate the peripheral image degradation, or pharmacological agents such as atropine).

These interventions can alter the quality of vision and have side effects, so their safety and efficacy need to be proven. Some other proposed interventions, such as latanoprost, an agent used in the treatment of glaucoma, will benefit from a better understanding of the mechanisms by which they may alter the myopia pathway. Given the critical role of the sclera in myopia, as the "last stop" of the retinal signaling cascade that leads to axial elongation, the investigation of the associations between myopia and scleral mechanical properties and structure appears to be of paramount importance. In addition, cross-linking, a surgical technique, has been used in recent years to stiffen the cornea in keratoconus, a disease that compromises the mechanical integrity of the cornea and impairs vision. Similarly, cross-linking has been proposed as a potential technique to halt the myopia progression by stiffening the sclera. In the cornea, several cross-linking modalities have been investigated, including different photoinitiators, irradiation wavelengths, initiator vehicles, dosages, and irradiation times. Investigating the efficacy of different scleral cross-linking modalities (e.g., ultraviolet light with Riboflavin or green light with Rose Bengal) will shed light on the appropriateness of these techniques for scleral stiffening. Furthermore, unlike the cornea, which is fully accessible for cross-linking intervention, irradiation of the posterior sclera is challenging. Coupled with the fact that the scleral properties change radically in different regions, understanding the differential effects of cross-linking in these different scleral regions is critical to selecting the optimal scleral zone for intervention. Finally, mechanical models of the eye that incorporate scleral modeling based on detailed experimental measurements of the scleral properties will undoubtedly allow for better treatment guidance.

1.2. Objectives of this thesis

To develop new methods to determine the role of the sclera and its modulation in the development and control of myopia.

In particular:

1. To characterize the biomechanical properties of the sclera across the ocular globe using mechanical techniques such as tensile testing and optical techniques such as air-puff deformation and optical coherence elastography.
2. To compare and correlate the properties of the sclera obtained by mechanical and optical techniques.

3. To determine the collagen organization in the sclera using Second Harmonic Generation microscopy.
4. To implement and validate a new method of scleral crosslinking using Rose Bengal and green light in animal models.
5. To compare two crosslinking methods: the new method (Rose Bengal with green light) with a method used in the standard practice for corneal keratoconus treatment (Riboflavin with ultraviolet light).
6. To study the effect on the biomechanical and swelling properties of scleral tissue after induction of scleral crosslinking.
7. To evaluate changes in biomechanical properties and collagen organization after scleral crosslinking.
8. To quantify anatomical dimensions and refractive errors of the eye in a myopia-induced animal model.
9. To quantify changes in the biomechanical properties of the sclera of eyes in a myopia-induced animal model.
10. To evaluate the influence of pharmacological treatments (atropine and latanoprost) on anatomical dimensions and refractive errors of the eye in a myopia-induced animal model.
11. To investigate the influence of pharmacological treatments (atropine and latanoprost) on the biomechanical properties of the sclera and the scleral collagen organization in myopia-induced animal model (guinea pig) with monocular form-deprivation.

1.3. Hypothesis

First

Biomechanical properties of the scleral tissue can be estimated using air-puff deformation imaging and optical coherence elastography. We will characterize the scleral biomechanic of intact eyes using air-puff deformation imaging and optical coherence elastography. The elastic properties of the scleral tissue will be determined using finite element modeling and elastic models. We will compare the results from optical techniques with those obtained by mechanical techniques such as tensile testing.

Second

Rose Bengal with green light irradiation, previously tested in the cornea as a collagen cross-linking treatment, can be translated to the sclera. We will apply Rose Bengal in scleral tissue of porcine and rabbit eyes and then irradiate with green light.

Third

Cross-linking causes an increase in stiffness in the corneal tissue, so scleral cross-linking is a potential treatment to stop the progression of myopia. We will quantify the stiffness variation, using tensile test, and the collagen organization, using second harmonic generation microscopy, in the posterior sclera before and after treated with crosslinking techniques (Rose Bengal with green light irradiation and Riboflavin with ultraviolet light irradiation).

Fourth

Pharmacological treatments not only affect the biometry and refractive error of the eye, but also the biomechanical properties of the sclera in a myopia model. We will induce myopia in guinea pig eyes using the monocular form-deprivation technique, treat the eyes with pharmacological agents (atropine and latanoprost), and determine the scleral biomechanics of treated and untreated eyes using tensile testing and optical coherence elastography. In addition, the collagen organization of the scleral tissue will be examined by second harmonic generation.

1.4. Structure of this thesis

This thesis addresses the measurement of the scleral biomechanical properties using two optical techniques (air-puff deformation imaging and optical coherence elastography) and a mechanical technique (uniaxial tensile test) and prove the influence of two crosslinking methods (Rose Bengal with green light and Riboflavin with ultraviolet light) and two pharmacological therapies (atropine and latanoprost) in scleral tissue. Besides, scleral tissue was visualized by second harmonic generation microscopy. Methodologies were developed to measure *ex vivo* the scleral stiffness in order to study the scleral behavior as a function of different factors such as scleral region (nasal, temporal, superior, inferior), type of animal model used (porcine, rabbit and guinea pig), treated method (crosslinking or pharmacological), and after myopia-induced and treatment (pharmacological and crosslinking) during *in vivo* studies.

This thesis is structured as follows:

Chapter 2: This chapter provides an overview of important biological, medical, and mechanical aspects of the sclera related to myopia development and its control. The chapter includes the anatomy of the eye, the role of scleral remodeling in myopia, proposed methods for controlling myopia progression (some tested in animal models and others emerging as clinical interventions in children), and techniques for quantifying the biomechanics of scleral tissue.

Chapter 3: This chapter describes all the methods and materials used in this thesis, including ocular tissue preparation, animal preparation for *in vivo* studies, measurement devices implemented and used in this thesis, optical imaging technologies used for sclera characterization, air-puff deformation imaging, optical coherence elastography, mechanical testing, second harmonic generation, animal models used for *in vivo* studies, and cross-linking and pharmacological methods used for myopia treatment.

Chapter 4: This chapter presents the protocols and results of *ex vivo* experiments in porcine and rabbit eyes using an air-puff excitation device coupled to a custom-built high-speed OCT system (air-puff deformation imaging). The biomechanical behavior of one corneal and six scleral locations was quantified by measuring maximum deformation, temporal displacement, temporal velocity, and arc length of scleral tissue deformation.

Chapter 5: This chapter presents the protocols and results of *ex vivo* experiments in rabbit eyes using optical coherence elastography. The biomechanical behavior of one corneal and four scleral locations was estimated by subjecting the eyes to air-coupled ultrasound deformation and detecting the propagating waves. Mechanical properties were compared with those obtained from tensile testing in the same eyes. Finally, the shear modulus, Young's modulus, and anisotropy parameters (normalized fractional anisotropy, modified planar anisotropy coefficient, major axis angle) of the scleral tissue were quantified.

Chapter 6: This chapter presents the protocols and results of *ex vivo* experiments in rabbit eyes using two photo-crosslinking methods: Rose Bengal with green light and Riboflavin with ultraviolet light. The effectiveness of the crosslinking method was assessed by uniaxial tensile testing of crosslinked and uncrosslinked scleral strips in a controlled hydration process. The collagen fibers of the scleral tissue were visualized using Second Harmonic Generation. Young's modulus, swelling ratio and swelling rate, and order coefficient (collagen organization parameter) were quantified.

Chapter 7: This chapter presents the protocols and results of the *in vivo* and *ex vivo* experiments performed on guinea pigs. For the *in vivo* experiments, each guinea pig had one form-deprived myopic eye and one control eye. All myopic eyes were treated by instillation of saline, latanoprost, or atropine. Axial lengths and refractive errors of each eye were measured during myopia induction. In *ex vivo* experiments, changes in scleral biomechanics of enucleated eyes were determined by optical coherence elastography and tensile tests. Shear modulus and Young's modulus were quantified. Finally, the organization of collagen fibers in the scleral tissue was assessed by second harmonic generation microscopy.

Chapter 8: This chapter summarizes the achievements of this thesis.

Chapter 9: This chapter summarizes the conclusions of the studies included in this thesis.

Chapter 10: This chapter lists the publications and conference contributions resulting from the work on this thesis.

2. STATE OF THE ART

In this chapter, we review the physiological background of the scleral tissue in the eye and the status of animal models of myopia, proposed methods for myopia control, and current techniques for determining scleral biomechanics. In summary, the sclera is a connective tissue composed mainly of collagen fibers. Scleral remodeling in myopic eyes is induced by hyperopic defocus; these changes in the sclera due to myopia have been studied in animal models. These models have provided information on ocular growth, refraction, scleral variation, and treatment-induced changes. Characterization of the biomechanical properties of the sclera is crucial for understanding the mechanisms underlying the prevention of myopia progression, where differences in scleral tissue have been identified in myopic eyes compared to non-myopic eyes. Mechanical tests (e.g. uniaxial/biaxial tensile tests) are most commonly used to estimate the material properties of scleral tissue, but recently, optical-based techniques have shown advantages in characterizing ocular tissues, despite the difficulties due to the high scattering of the sclera.

2.1. The Eye

The eye is a complex organ of the visual system that plays an essential role in the reception of visual information. The mammalian eye is composed primarily of the cornea, lens, sclera, and retina (see Figure 2.1). The cornea refracts light entering the eye, while the lens focuses light on the back of the eye (retina). Between the cornea and the lens is the aqueous humor, a low-viscosity transparent fluid. When the eye focuses, the ciliary muscle, in the ciliary body, changes the shape of the lens. The sclera is a hard, opaque tissue (white part of the eye) that covers and protects the internal structures of the eye. The retina is a nerve layer that converts light into chemical and electrical signals that are transmitted to the brain through the optic nerve. The shape of the ocular layer is maintained by the pressure of a transparent, viscous fluid, mainly water, called the vitreous humor. The fluid pressure inside the eye is called intraocular pressure (IOP).

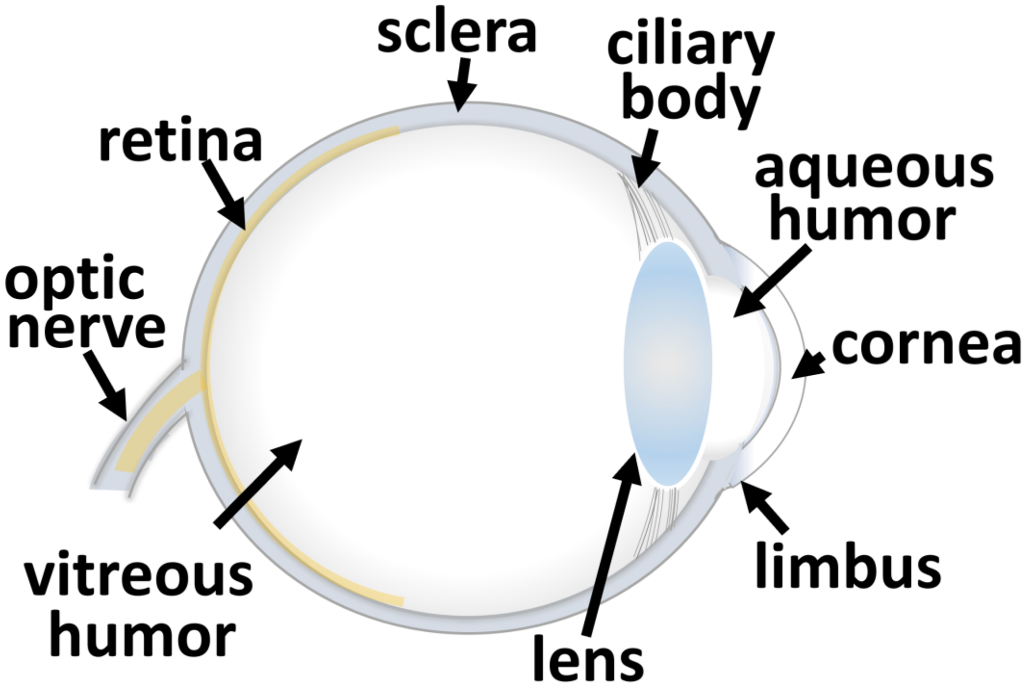

Figure 2.1: Schematic drawing of the sagittal section of the eye. After light passes through the cornea, the lens focuses it on the retina. The retina detects the incoming light and generates electrical impulses. These impulses are sent to the brain through the optic nerve.

In terms of shape and structure, human and animal eyes differ mainly in their dimensions. The approximate size of human eyes is 24.3 mm x 23.7 mm x 22.0-24.8 mm (horizontal x vertical x axial globe diameter), with no significant difference between sex and age groups in adults with non-ophthalmic diseases (Bekerman et al., 2014). On the other hand, the approximate dimensions (horizontal x vertical x axial globe diameter) of the animals most commonly used in ophthalmic research are 25.5 mm x 24.5 mm x 21.6 mm in porcine eyes (Bartholomew et al., 1997), 6.1 mm x 16.1 mm x 15.1-16.2 mm in rabbit eyes (Barathi et al., 2002; Bozkir et al., 1997), and 9.1 mm x 9.0 mm x 8.8 mm in guinea pigs (Dong et al., 2019). Recent reports of the axial length of the human eyes compared to those of the species used in this thesis indicate that the human eye is longer than the adult German Landrace pig (by 1.5 times) (Runge et al., 2024), the adult New Zealand White rabbit (by 1.7 times) (Runge et al., 2024), the 7-weeks-old *Cavia porcellus* guinea pig (by 2.8 times) (Dong et al., 2019). In addition, human, rabbit and guinea pig eyes were found to have a more spherical shape than porcine eyes, which have an ellipsoidal shape. In fact, the vertical globe diameter (superior-inferior axis) is at least 3 mm longer than the axial length in a porcine eye (Bartholomew et al., 1997;

Runge et al., 2024). It is evident that variations in eye size are determined by the age and breed of the animal, with the eye growing to a standard size in adulthood.

2.1.1. The sclera

The sclera is a connective tissue that not only protects the intraocular tissues but also provides stable support for changes in IOP and ocular movements (Watson and Young, 2004). The strength of this opaque layer is based on the organization of the collagen within it, which is related to the macroscopic elastic properties of the scleral tissue. The sclera has some microscopic layers, from outer to inner: Tenon's capsule, episclera, sclera proper (stroma), and *lamina fusca* (Boote et al., 2020; Watson and Young, 2004), see Figure 2.2. Tenon's capsule is a layer that covers the ocular globe from the optic nerve to the corneal limbus. The episclera, composed of bundles of collagen and elastic fibers, is attached to Tenon's capsule. The *lamina fusca* fuses with the underlying choroid. The sclera proper is composed of collagen fibrils (consisting mainly of type I and type III collagen) of various diameters and lengths (25-230 nm in diameter) that assemble into intertwined fiber bundles or defined lamellae (0.5-6 μm in thick) (Boote et al., 2020; Komai and Ushiki, 1991; Watson and Young, 2004). The interfibrillar matrix is occupied by proteoglycans and glycosaminoglycans. Proteoglycans are firmly linked to collagen fibrils at specific binding sites. The approximate composition of human sclera is 68% water, 28% collagens, <3 other proteins, <1 proteoglycans and 0.6 elastin (Boote et al., 2020).

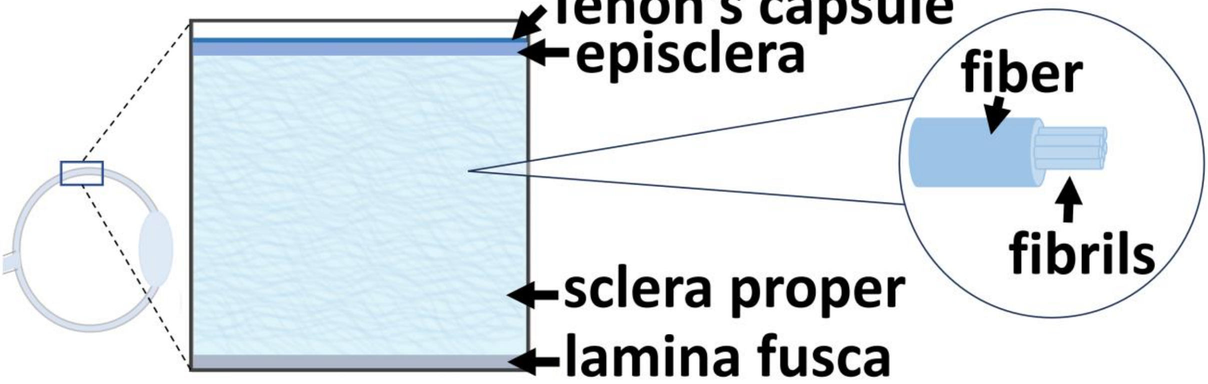

Figure 2.2: Schematic drawing of the interior of the scleral tissue. The sclera is composed of: Tenon's capsule, episclera, sclera proper (stroma), and *lamina fusca*. The sclera proper is composed mainly of collagen fibers.

2.1.2. Collagen

Collagen is an abundant protein in connective tissues as the sclera and cornea. Collagen molecules have an elongated rod-like structure with a length of 300 nm and a diameter of approximately 1.5 nm, depending on the type of collagen (Ottani et al., 2002). The collagen molecules are hierarchically arranged to form a nanometer diameter fibril, and the fibrils are further assembled into irregular bundles that form the scleral lamellae, see Figure 2.2. Since human scleral tissue contains approximately 90% collagen by weight (Norton and Rada, 1995), it is reasonable to assume that alterations in collagen fibrils will affect scleral biomechanics as a whole.

The organization of collagen fibers, as well as the diameter of collagen fibrils, can determine the physiological and optical properties of tissues. The overall biomechanical behavior of the tissue is influenced by mechanical properties of substructures such as collagen fibrils (Gachon and Mesquida, 2022; Harper and Summers, 2015). For example, although type I collagen predominates in both corneal and scleral tissues, the cornea appears transparent and the sclera opaque. This is because the collagen fibril diameter in the human cornea is in the range of 30-32 nm (Daxer et al., 1998; Komai and Ushiki, 1991) and the fibrils have a highly uniform packing that produces large-scale order in the extracellular matrix, a critical parameter for corneal transparency (Chakravarti et al., 2000; Raspanti et al., 2000). In contrast, the sclera has fibrils 25-300 nm in diameter (Han et al., 2005; Watson and Young, 2004; Yamamoto et al., 2000) that form inhomogeneous tubular structures with high stiffness thin shells that are responsible for scleral opacity.

2.1.3. Proteoglycans and glycosaminoglycans

Bundles of collagen fibrils are organized in the extracellular matrix of the sclera, where collagen fibrils interact with adjacent fibrils of the same bundle through various other non-collagenous proteins such as proteoglycans (PGs) (Atta et al., 2022; Borcherding et al., 1975; Hocking et al., 1998). Proteoglycans are negatively charged hydrophilic molecules consisting of a small protein core and a few glycosaminoglycan (GAG) chains. Proteoglycans are normally attached to collagen fibril by their protein core and interact with each other through their side chains (Hocking et al., 1998). PGs and GAGs play an important functional role in tissue hydration and solute diffusion (Koob and Vogel, 1987), as the water-binding capacity (swelling effect) of these molecules alters the organization and alignment of collagenous extracellular matrix (Murienne et al., 2016; Yang and O'Connell, 2018). This reorganization is mediated by collagen-proteoglycan interaction, which is directly related to mechanical coupling of the fibrils and ultimately generates a mechanical stress distribution throughout the tissue (Murienne et al., 2016; Pachenari and Hatami-Marbini, 2021; Raspanti et al., 2000) that determines the biomechanical properties of the sclera.

2.2. Myopia

Myopia is a common cause of distance refractive error, and its prevalence is increasing every year. The "myopia boom" has affected populations worldwide, especially in Asian countries, where 90% (in 2015) of Chinese adolescents and young adults are myopic (Dolgin, 2015). The problem has been exacerbated in recent years by the Covid-19 restrictions. A recent study in Hong Kong children (6 to 8 years old) found that myopia increased by 4% in 2020 and 11% in 2021 compared to the stable prevalence between 2015-2019 (pre-COVID-19) (Zhang et al., 2023). According to estimates for 2030, the expected percentage of the population with myopia will be higher in Asia (Asia-Pacific: 58%, East Asia: 57%), but will still be considered high in Europe (Western Europe: 45%, Central Europe: 42%, and Eastern Europe: 39% in 2030) (Holden et al., 2016). In Spain, one in five children (aged 5 to 7) is myopic, which reflects an alarming increase in childhood myopia from 16.8% to 19.7% (2016-2021), with an estimated increase of up to 30.2% by 2030 (Sánchez-Tena et al., 2024). By 2050, it is estimated that there will be 4758 million myopic people in the world (50% of the world's population) (Holden et al., 2016; World Health Organization and Brien Holden Vision Institute, 2016). Myopia is now considered a new pandemic.

2.2.1. Myopia and sclera

Myopia (nearsightedness) is an ophthalmic disease characterized by excessive axial elongation of the eye (Vera-Diaz, 2010), see Figure 2.3a. The exact mechanism of action is still unknow, but it appears that myopia is probably induced by hyperopic defocus, which leads to mechanical remodeling of the scleral tissue. Scleral remodeling in myopic eyes may induce a biochemical imbalance in the extracellular matrix, leading to an increase in the activity of metalloproteinases (enzymes involved in the degradation of connective tissue)

(Guggenheim and McBrien, 1996; Summers Rada et al., 2006; Yu and Zhou, 2022) and a decrease in GAG synthesis (Avetisov et al., 1983; Rada et al., 2000; Troilo et al., 2006), affecting the structural integrity of the tissue. The overall effect is that myopia weakens sclera, especially at posterior pole. Scleral weakness is characterized by thinning of the sclera (McBrien et al., 2009, 2001, 2000), thinning and loss of the collagen fiber bundles (Summers Rada et al., 2006; Watson and Young, 2004), reduction in the collagen fibril diameter (less than 60-70 nm) (Curtin et al., 1979; Harper and Summers, 2015) and disorganization of fibril assembly (Curtin et al., 1979; Curtin and Jampol, 1986), see Figures 2.3b and 2.3c. Therefore, structural changes in the sclera of myopic eyes may indicate changes in the elastic properties of the sclera.

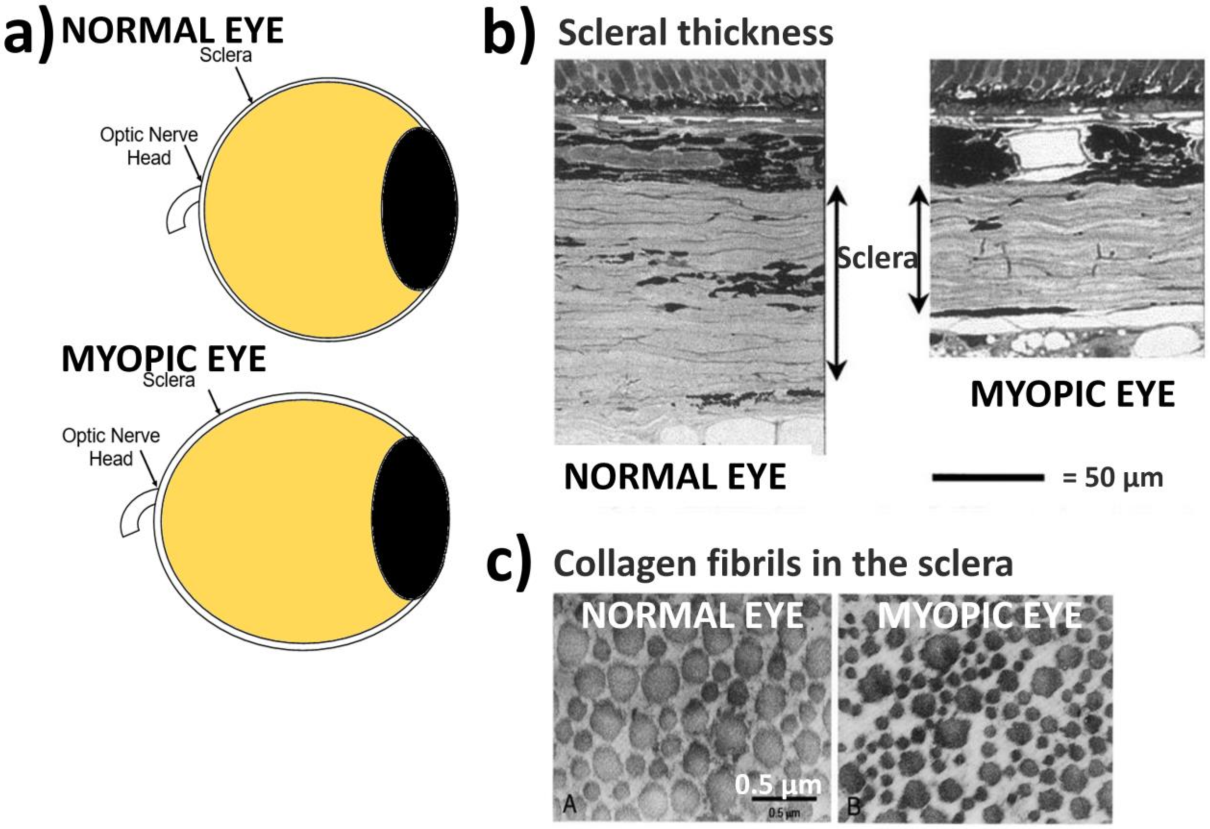

Figure 2.3: Structural changes in scleral tissue due to myopia. a) Schematic representation of the change in axial length produced in myopic eye compared to non-myopic eye (normal eye). b) Micrographs of the transverse section of posterior scleral showing the difference in thickness between normal and myopic eye of a tree shrew. Figure adapted from McBrien N. et al. (2001) *Invest. Ophthalmol. Vis. Sci.* (McBrien et al., 2001)c) Microscopic images of collagen fibrils in the sclera of normal and myopic human eyes. Figure adapted from: Curtin BJ. (1986). *Retina* (Curtin and Jampol, 1986) and Harper A. and Summers J. (2015) *Exp Eye Res* (Harper and Summers, 2015).

Microstructural changes result in altered biomechanical response of the scleral tissue. Several studies have reported change in the elastic properties of sclera, such as reduced scleral tensile strength in human eyes with high myopia (Avetisov et al., 1983), more than ~25% greater posterior scleral elongation in myopic eyes than in control eyes in the tree shrew (Phillips and McBrien, 1995), increased rate of scleral creep in human sclera of eyes developing myopia (McBrien et al., 2009), lower scleral Young's modulus (difference of at least 2 MPa) of myopic eyes compared to normal eyes in guinea pigs (Chu et al., 2016; Guo et al., 2022; Wang and Corpuz, 2015). These studies have shown that changes in microscopic structures induce macroscopic changes in the elastic properties of the sclera.

2.2.2. Diopter

The diopter is a measure of the curvature of the wavefront of a light source formed and is represented by the letter "D" (Corboy, 2003). The curvature of the wavefront varies inversely with distance from the source (i.e., the shorter the distance, the greater the curvature). Diopters can be described as positive (convergence) or negative (divergence) depending on how the light rays propagate.

A lens can bend (refract) the vergence (convergence or divergence) of light rays due to the curvature of its surface. Therefore, diopters are also a measure of lens power. A lens can converge (positive power) or diverge the light rays (negative power). For example, a +1.5 D lens converges parallel rays to a point at 0.67 (1/1.5) meters away and a -1D lens diverges by 0.67 meters.

2.2.3. Refractive error

The eye is responsible for focusing light rays on the retina, but if the rays are not focused on the retina, refractive errors occur. Thus, emmetropia (no refractive error) occurs when the rays hit the retina, and ametropia (refractive error) occurs when the rays hit somewhere else (see Figure 2.4a). Ametropia can be caused by variations in the axial length of the eye, variations in the refractive indices, errors in the curvature of the refractive surfaces, shifts in the position of the crystalline lens, or a combination of these factors (Corboy, 2003; Schwiegerling, 2004). Ametropia requires a corrective lens whose sign and power define and measure the refractive error.

Spherical ametropia occurs when the refractive surfaces of the eye are equally curved in all meridians (like the surface of a sphere). In this case, parallel rays of light arriving in all meridians (directions) are refracted equally and arrive at a single focal point (on the retina in the case of the eye). Spherical ametropias are hyperopia and myopia (Schwiegerling, 2004). In a hyperopic eye, rays are focused behind the eye (see Figure 2.4b), so hyperopic eye needs positive lenses to bring the rays together on the retina. In a myopic eye, the rays are focused in front of the retina, see Figure 2.4c. Therefore, myopic eyes must use a negative lens to redirect the rays to the retina.

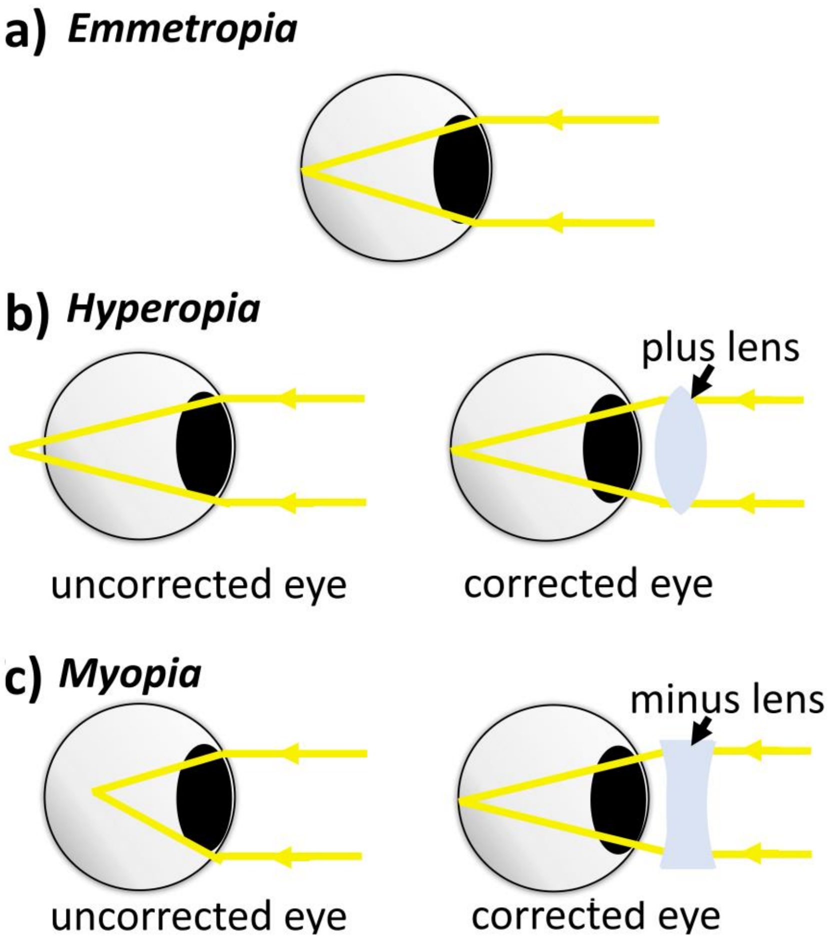

Figure 2.4: Illustration of the emmetropia, hyperopia and myopia in a schematic eye. a) In an emmetropic eye, parallel rays of light are focused on the retina. b) In a hyperopic eye, parallel rays of light are focused behind the retina. The hyperopic eye is corrected by a positive lens. c) In a myopic eye, parallel rays of light are focused in front of the retina. The myopic eye is corrected by a negative lens. Figure adapted from: Corboy (2003). *The retinoscopy book*. (Corboy, 2003)

Aspheric ametropias occur when the refractive surfaces of the eye (especially the anterior cornea) do not have the same radius of curvature in all directions (i.e. they are not spherical) (Corboy, 2003). Since refraction depends on the curvature of the surface (it increases as the curvature increases), the principal meridians would refract rays differently, defining astigmatism. Specifically, the corneal surface has two principal meridians (focal points) in the eye. In astigmatism, the principal meridians can be myopic, hyperopic or a combination of the two. Refractive errors (ametropias) can be evaluated using retinoscopy, autorefractometers and wavefront sensors (Cooper et al., 2011; Yakar et al., 2023).

2.2.4. Animal models of myopia

Animal models of myopia have provided information about eye growth, refraction, eye size in the development of myopia, and scleral variation at the high myopia obtained. As well as have been widely used to test treatments. The most commonly studied myopia-inducing species are chicken (*Gallus gallus domesticus*), tree shrew (*Tupaia glis belangeri*), marmoset (*Callithrix jacchus*), guinea pig (*Cavia porcellus*), and macaque monkey (*Macaca mulatta*) (Summers Rada et al., 2006). The first reports of myopia induced in animals date back to the 1970s. Myopia was induced in chicks (Wallman et al., 1978), monkeys (Wiesel and Raviola, 1977) and tree shrews (Sherman et al., 1977) by depriving the retina of form vision using a translucent diffuser and lid sutures. In 1988, myopia was induced in chicks by using negative lenses of specific refractive powers that impose hyperopic defocus on the retina (Schaeffel et al., 1988). Human myopia development has been studied for decades in experimental animals, resulting in the discovery of several mechanisms controlling axial length.

Myopia can be induced in animals by negative power lenses or by form-deprivation (Boote et al., 2020; Summers Rada et al., 2006). These common myopization mechanisms are based on the failure of the emmetropization process in young animals in the presence of degraded images by diffusion (form-deprivation, open-loop), where the eye elongates to project the image in focus on the retina in the presence of a negative power lens or slows axial elongation in the presence of a positive power lens. In general, emmetropization is the process of adapting refractive power to the axial length of the eye during postnatal development (most infants are hyperopic (Vera-Diaz, 2010) to induce emmetropia (no refractive error), see Section 2.2.3. Since emmetropization can be controlled mainly by a visual feedback loop mechanism (Boote et al., 2020; Schaeffel and Feldkaemper, 2015), myopia can result from an abnormal visual stimulus on the retina (defocus) that alters emmetropization, causing the retinal signal to induce scleral remodeling and axial elongation, modulating the visual stimulus that completes the loop.

In the schematic eye model (Figure 2.4.c), negative lenses are placed in front of the eye to perturb the feedback system. Negative lenses can shift the focal plane away from the cornea, creating a new focal point for the retina, resulting in an increase in axial length. Lens induction has been demonstrated in guinea pigs (Dong et al., 2019; Howlett and McFadden, 2009; Xiao et al., 2014).

The form-deprivation myopia (FDM) model involves suturing the eyelid, wearing a translucent diffuser or diffusing lens over the eye, or wearing a face mask to open the feedback loop that results in axial elongation of the eye. FDM has been shown to be effective in guinea pigs (Dong et al., 2011; El-Nimri and Wildsoet, 2018; Howlett and McFadden, 2006; Jiang et al., 2011; Lu et al., 2006; Pan et al., 2021; Wu et al., 2007).

One of the aims of this thesis is to investigate the relationship between myopia and scleral tissue using the guinea pig as an animal model. Myopia was induced in guinea pigs by form deprivation and changes in axial length and refractive error were measured. The possible influence of myopia on the elastic properties of the scleral tissue was then investigated.

2.3. Proposed methods for controlling myopia progression

Several clinical interventions are currently available to control myopia, including spectacles with peripheral scattering or microlenses, multifocal contact lenses and pharmacological agents. In this thesis, we focus on two pharmaceutical interventions and photo-crosslinking.

Some proposed pharmaceutical interventions to control myopia are atropine, pirenzepine, and 7-methylxanthine (W. Wang et al., 2021). Atropine is a mydriatic (cycloplegic and pupil dilating) agent that is widely used in clinical practice. Several clinical trials have evaluated the safety and efficacy of daily use of low doses of atropine (0.01%, 0.025% and 0.05%) with few or no side effects (Chia et al., 2012; Clark and Clark, 2015; Yam et al., 2019). Atropine has been shown to be effective in reducing myopia progression in children (aged 6-12 years) at doses of 0.01% atropine after 2 years of use in the overall 5-year study (Chia et al., 2016). Pirenzepine is an antimuscarinic drug (blocks acetylcholine receptors) with a moderate response in stopping myopia progression (Huang et al., 2016; Ostrin et al., 2004), and reported side effects such as excessive mydriasis (dilated pupils), abdominal cramps preceded by a flu (Tan et al., 2005), and conjunctival allergic reaction (Siatkowski et al., 2004), so clinical trials or clinical use were mostly discontinued. 7-Methylxanthine is an adenosine antagonist that has been reported to strengthen the sclera in rabbits (Trier et al., 1999) and guinea pigs (Cui et al., 2011). In clinical studies, 7-methylxanthine appears to be effective in reducing myopia progression (Lai et al., 2023; Trier et al., 2023), although longer-term clinical studies are needed to analyze and verify these results. Looking forward, atropine seems the most promising pharmacologic treatment for its effectiveness, mild side effects, and apparent long-term effect on myopia progression.

IOP-lowering agents have also been considered as potential myopia treatments (P. Wang et al., 2021). Increased IOP has been associated with increased axial elongation in children (Quinn et al., 1995). The two IOP lowering agents used in preclinical studies for the treatment of myopia are brimonidine and latanoprost. Brimonidine has been shown to prevent axial elongation in lens-induced myopic guinea pigs (Y. Liu et al., 2017) and form-deprived myopic guinea pigs (Yang et al., 2021). Latanoprost has been reported to affect axial elongation in form-deprived myopic chicks (Jin and Stjernschantz, 2000; Uddin et al., 2022), monkeys (Beach et al., 2019) and guinea pigs (El-Nimri and Wildsoet, 2018), with no reported side effects. However, there are no studies in humans to ensure its benefit in myopia progression.

Current experimental therapies to prevent myopia progression involve molecular signaling. Recent studies in animal models of myopia have suggested the use of specific molecules that induce changes in signaling pathways during myopia progression. It appears that up/down regulation of these molecules mediating the retina-sclera pathway also affects scleral remodeling and alters ocular growth (W. Wang et al., 2021). For example, dopamine, a neurotransmitter responsible for mediating interactions in the retina, may be involved in the axial elongation process. Some studies have shown that the intraocular injections of dopamine in lid-sutured rabbits (Gao et al., 2006) and apomorphine (dopamine receptor agonist) in form-deprived guinea pigs (Jiang et al., 2014) prevented myopic progression. Although several studies have shown inhibitory effects of dopamine agonists, the mechanism of inhibition requires further investigation (Feldkaemper and Schaeffel, 2013; Jain et al., 2023; Zhou et al., 2017). Another example is retinoic acid. Retinal retinoic acid can increase axial length and refractive error in myopia-induced guinea pigs (Jiang et al., 2011; McFadden et al., 2004; Wu et al., 2023) and produce a 30% reduction in scleral stiffness in mice (Brown et al., 2023). Despite the promising response, most of these studies are still in the preclinical phase.

Strengthening the sclera by crosslinking to prevent myopia progression has also been proposed as a potential treatment for myopia (Zhang and Lai, 2021). Collagen crosslinking agents have been widely used in ophthalmic clinical practice in corneal tissue to halt the progression of keratoconus (Raiskup et al., 2023). Collagen cross-linkers can be divided into chemical crosslinkers and photo-crosslinkers. The most common chemical crosslinking agents used in the treatment of myopia include: genipin, which has been tested in rabbit, tree shrew, and guinea pig sclera (El Hamdaoui et al., 2021; Guo et al., 2022; Levy et al., 2018; Liu and Wang, 2017; Wang and Corpuz, 2015); and glyceraldehyde, which has been tested in guinea pig, rabbit, and porcine sclera (Chu et al., 2016; Wollensak and Iomdina, 2008; Wollensak and Spoerl, 2004). On the other hand, photo-crosslinkers use an agent that is activated by light irradiation. The most commonly used techniques include the combination of riboflavin with ultraviolet light, which has been tested in rabbit, guinea pig, and human sclera, (Dotan et al., 2014; Li et al., 2017; Liu et al., 2016; Wang et al., 2015; Wollensak et al., 2005; Wollensak and Iomdina, 2009; Zhang et al., 2013); riboflavin with blue light tested in rabbit, rhesus monkey and guinea pig sclera (Iseli et al., 2015, 2008; Li et al., 2021; Wang et al., 2023); Rose Bengal with green light tested in porcine and rabbit sclera (Villegas et al., 2024a, 2021; Villegas Lopez et al., 2020); methylene blue with red light tested on rats (Gerberich et al., 2021). Thus, ophthalmic crosslinking represents a new generation of procedures for myopia progression, although improved strategies are needed to take advantage of the procedure.

After exploring alternative and complementary treatments for retarding myopia progression, we have proposed in this thesis the use of two pharmacological agents: atropine and latanoprost, and two scleral cross-linking techniques: riboflavin with ultraviolet A light and Rose Bengal with green light.

2.3.1. Pharmacological agents: atropine and latanoprost

In the current thesis, we chose to investigate two agents (Atropine and Latanoprost) among the differently proposed pharmacological interventions. While there is literature on the potential mechanisms of these agents mediating myopia inhibition, their effects on the scleral modulation are not well known.

Atropine is a naturally occurring alkaloid in plants and is primarily extracted from *Atropa belladonna* (National Center for Biotechnology Information, 2023). The exact mechanism of action of atropine in myopia control is not fully understood, but it is thought to work through accommodation-related mechanisms. One possible pathway is modulation of dopamine release, which appears to be associated with a reduction in axial growth of the eye (Dhillon et al., 2008; Iuvone et al., 1989; Nickla et al., 2010; Schwahn et al., 2000). Side effects associated with high doses (>0.1%) (Shih et al., 1999) have led to proposals to use much lower concentrations (0.01%-0.05%); in fact, the American Academy of Ophthalmology recommends the use of 0.01% atropine for myopia control in children (Pineles et al., 2017).

Latanoprost is a prostaglandin analog approved for the treatment of elevated IOP, such as in patients with glaucoma (Alm, 2014). Latanoprost increases aqueous humor outflow and lowers IOP. Specifically, the ciliary body contains several prostaglandin receptors whose activation by latanoprost appears to stimulate the activity of metalloproteinases (Lindsey et al., 1997; Ocklind, 1998). Metalloproteinases are enzymes (see section 2.2.1) involved in extracellular matrix remodeling (Russo et al., 2008), and upregulation of metalloproteinases is associated with scleral remodeling (Summers Rada et al., 2006). Thus, latanoprost appears to affect aqueous production rate (Russo et al., 2008). In clinical trials, latanoprost has been shown to be a safe treatment for pediatric glaucoma with mild and infrequent side effects (Black et al., 2009) and with efficacy dependent on age and glaucoma diagnosis (Maeda-Chubachi et al., 2013).

2.3.2. Scleral crosslinking (SXL)

Collagen crosslinking using riboflavin instillation with ultraviolet A (UVA) light irradiation has been used to strengthen the scleral collagen being, effectively increasing the tensile strength of the tissue. Riboflavin (also known as vitamin B2) is a vitamin found naturally in some foods (Blackburn et al., 2021). Riboflavin can be activated by exposure to UVA light. Activated riboflavin generates oxygen radicals that can react with collagen molecules inducing new covalent bonds (Raiskup and Spoerl, 2013; Wollensak, 2006), thereby stiffening the sclera. Whether the covalent bonds are between collagen fibrils, within fibrils, or between other molecules is still under investigation (Hayes et al., 2013). To our knowledge, Riboflavin with UVA light crosslinking (UVX) has been tested in at least one human trial. Li et al. (Li et al., 2023) applied SXL by riboflavin with UVA irradiation (surgical procedure) to one eye of patients with pathologic myopia blindness, resulting in a favorable response in controlling myopia progression at one year, with no significant effect on posterior pole blood flow.

Rose Bengal with green light crosslinking (RGX) has previously been used in *ex vivo* studies to stiffen corneal tissue (Bekesi et al., 2017, 2016b; Cherfan et al., 2013; Wang et al., 2018; Zhu et al., 2016). Rose Bengal (RB) is an organic compound (xanthene) used as a dye that is activated by visible light. Green light-activated RB generates singlet oxygen, which mediates the formation of covalent bonds between collagen fibrils and thus increases stiffness (Cherfan et al., 2013; Kochevar and Redmond, 2000; Redmond and Kochevar, 2019). Clinical studies have evaluated the efficacy and safety of RGX in the cornea, showing no evidence of damage in the deep central cornea, retina, or iris in rabbit eyes (Gallego-Muñoz et al., 2017; Lorenzo-Martín et al., 2018; Soeken et al., 2018; Zhu et al., 2016). In the cornea, advantages of RGX include shallower penetration (protecting the endothelium), no dehydration and tissue thinning, and much shorter application times. In preclinical studies, Wollensak et al. (Wollensak and Spoerl, 2004) evaluated the scleral cross-linking by RGX in human and porcine eyes *ex vivo* and reported a non-significant increase in Young's modulus (23.1 MPa in Rose Bengal/light-treated vs. 22.82 MPa in untreated human sclera) after 10 minutes of RB with 60 minutes of white light irradiation.

2.4. Biomechanics of scleral tissue

The characterization of the biomechanical properties of the sclera is crucial for understanding the mechanisms underlying the prevention of myopia progression (Wang and Cao, 2022). Several studies have shown that the scleral tissue of myopic eyes has less stiffness than emmetropic eyes, suggesting that the sclera of myopic eyes may be more extensible compared to that of a non-myopic eye under the same loading profiles (McBrien et al., 2009).

The sclera is considered to be a nonlinear material with viscoelasticity and anisotropy (Wang and Cao, 2022). The biomechanical properties of the mammalian sclera are regionally dependent, with different elastic properties between the anterior, equatorial and posterior sclera (Curtin, 1969; Ndlovu et al., 2022; Phillips and McBrien, 1995). Generally, the posterior sclera stretches less (is stiffer) than the equatorial sclera under uniaxial tension (Phillips and McBrien, 1995), the equatorial sclera deforms more than the posterior sclera under the same air pulse (Bronte-Ciriza et al., 2021), the anterior sclera has more internal tension (is more difficult to stretch) than the posterior sclera, and the sclera of the posterior regions of the eye has a lower Young's modulus (is less stiff) than the equatorial or anterior regions (Elsheikh et al., 2010).

The sclera also exhibited anisotropic behavior, making stiffness measurements dependent on the direction of the sclera (Coudrillier et al., 2012; Elsheikh et al., 2010; Pijanka et al., 2012). Previous studies have shown a preferential directionality in that the sclera has higher strain in the circumferential direction than in the meridional direction in porcine sclera (Cruz Perez et al., 2014; Ndlovu et al., 2022). Characterization of scleral anisotropy is important for predicting its response to different mechanical stimuli, as well as an indicator of changes in collagen organization, for example in the context of myopia (Hoerig et al., 2022; Markov et al., 2018).

2.4.1. Mechanical techniques

Several techniques have been used to estimate the biomechanical properties of the sclera. The most commonly used because of their ease of application are uniaxial/biaxial tensile tests, compression tests, and inflation tests. Uniaxial mechanical tests have been used on monkey, human, and rabbit sclera (Downs et al., 2005; Elsheikh et al., 2010; Girard et al., 2007); biaxial tensile tests have been used on human and porcine sclera (Cruz Perez et al., 2014; Eilaghi et al., 2010; Ndlovu et al., 2022); and compression tests have been used on bovine, porcine, and human sclera (Battaglioli and Kamm, 1984; Mortazavi et al., 2009) to characterize scleral specimens. These tests provided a first valid estimate of the material properties of the sclera in one or two directions.

To determine the tissue elasticity over the entire ocular surface, mechanical techniques have been combined with inverse analysis methods to estimate parameters of the constitutive models. For example, ultrasound speckle tracking during mechanical testing (Cruz Perez et al., 2014) allows measurement of deformation through the thickness of the sclera under equal biaxial loads. Using a constitutive model, it is possible to obtain the strain distribution through a section of the sclera. In addition, inflation assays allow the testing of intact eyeballs (no destruction of the eye, no scleral strips or specimens are used), mimicking scleral behavior closer to *in vivo* conditions. The mechanical properties of the tissue are quantified by an inverse analysis process using finite element models based on specific ocular geometry and experimental data. Inflation tests have been applied to analyze the biomechanics of human posterior sclera (Coudrillier et al., 2012; Grytz et al., 2014; Whitford et al., 2016) and porcine sclera (Girard et al., 2009) to determine regional variations in mechanical behavior across the ocular surface.

2.4.2. Optical techniques

Recently, optical-based techniques have shown advantages in characterizing scleral tissue over mechanical techniques. Brillouin microscopy is a novel technique that uses low-power near-infrared laser light to determine the local Young's modulus (mechanical compressibility) of tissue. Brillouin has been successfully applied to corneal biomechanics (Eltony et al., 2022; Scarcelli and Yun, 2012; Webb et al., 2020), but scleral measurements are more challenging due to the high scattering properties of the sclera. Only one study has been published using Brillouin data from porcine sclera (Shao et al., 2016). The major advantage of this technique is the lack of external excitation, although the relationship between Brillouin modulus and mechanical moduli, which is relevant for predicting mechanical response, is still under investigation.

Several dynamic techniques, generally first developed to study the cornea, have been proposed to characterize scleral tissue. In these techniques, the tissue is subjected to external excitation (e.g., air pulse, ultrasound, or contact probe) while an Optical Coherence Tomography system acquires images. Biomechanics are determined from the image analysis of the tissue response. In *ex vivo* studies, air pulse-induced deformation combined with finite element modeling has been applied to obtain the dynamic response of scleral tissue from human donors (Nguyen et al., 2019) and porcine eyes (Bronte-Ciriza et al., 2021). In addition, Air-Coupled Ultrasonic Optical Coherence Elastography (ACUS-OCE) has been applied to *ex vivo* porcine anterior sclera to account for tissue shear modulus (Zvietcovich et al., 2020b). In *in vivo* studies, OCE has been used to measure scleral biomechanics in healthy human subjects (Ramier et al., 2020). In this technique, the sclera was excited by a vibrating contact probe placed on the ocular surface to generate surface waves whose propagation is related to the shear modulus of the tissue. These techniques offer numerous advantages over traditional tensile testing, including non-contact, high-resolution biomechanical imaging of scleral tissues. and the ability to visualize and quantify elasticity in three dimensions.

Modulation of scleral biomechanics may play a fundamental role in the treatment of myopia, and the macroscopic mechanical properties are influenced by the scleral ultrastructure. During this thesis, tensile testing, air-puff deformation imaging, optical coherence elastography were used as biomechanical techniques, and second harmonic generation microscopy as a method to measure scleral collagen organization were used to characterize the response of the sclera to variations in anatomical location, cross-linking, and pharmacological methods to control myopia progression.

2.5. Integrated Techniques in Scleral Biomechanics: Imaging, Crosslinking, and Myopia

2.5.1. Air-Puff Deformation Imaging Techniques in Biomechanical Analysis

Myopia is an ocular condition that affects the structure of all tissues of the globe and alters their biomechanical response. Since the sclera constitutes most of the connective tissue of the globe, quantification of scleral biomechanics is closely related to the development of myopia. Thus, non-invasive quantification of ocular mechanical properties is important to avoid tissue compromise and to quantify changes in ocular response caused by surgery or ocular disease. Maintaining the integrity of the ocular globe during e*x vivo* measurements, as in air-puff deformation experiments, has avoided compromising the eye. In this thesis, the biomechanical response of porcine and rabbit sclera was investigated in the eyeball using air-puff deformation imaging technique.

Air-puff deformation imaging techniques have been widely used for cornea biomechanics (Mlyniuk et al., 2021). In recent years, the air-puff technique has introduced not only accurate tonometers (Curatolo et al., 2020a, 2020b; Jiménez-villar et al., 2019; Roberts et al., 2017), but also methods to obtain information on the normal and pathological response of the cornea through rapid and non-contact mechanical stimulation (De Stefano et al., 2018; Nan-Ji et al., 2022). Currently, parameters such as corneal thickness or stiffness indices can be obtained using the same system (Eliasy et al., 2018; Roberts et al., 2017; Vinciguerra et al., 2016) and with a single measurement. In fact, air-puff deformation imaging has been used in clinical practice to determine further influence of the corneal surface shape on the deformation event (Yousefi et al., 2022) and to detected deformation asymmetries in keratoconus patients (Curatolo et al., 2020b; Salvetat et al., 2015).

Air-puff excitation devices have been coupled to customized OCT systems to measure corneal deformation in different directions (Curatolo et al., 2020b; Dorronsoro et al., 2012) and to study corneal apex deformation (Jiménez-villar et al., 2019; Maczynska et al., 2019b). By coupling to an OCT, these systems can measure the spatiotemporal deformation of the cornea, from which deformation parameters such as temporal symmetry or maximum apex indentation can be obtained (Kling and Marcos, 2013; Salvetat et al., 2015). However, it is not possible to obtain a direct measure of the elastic properties of the tissue. To obtain Young's modulus or shear modulus values, inverse optimization techniques of FEMs has been used. This type of technique has allowed to isolate the elastic properties of the tissue from other factors (Bekesi et al., 2016a; Bronte-Ciriza et al., 2021; Elsheikh and Wang, 2007).

In this thesis, an air-puff excitation device coupled with a custom-built high-speed SS-OCT system was used to monitor the deformation of eye globe tissue in *ex vivo* porcine and rabbit eyes. Spatio-temporal deformation profiles were estimated for six scleral locations and one corneal location and compared between the two animal models. FEM-based inverse algorithms were used to reconstruct elastic properties using acquired air-puff deformation data from porcine eyes.

2.5.2. Optical Coherence Elastography in Biomechanical Analysis

Characterization of the mechanical properties of sclera plays an important role in vision. Sclera is the main supporting tissue of the eye that protects the intraocular system, whose structure consists mainly of collagen fibers arranged in lamellar units (Komai and Ushiki, 1991; Watson and Young, 2004). Myopia is associated with an increase in the longitudinal size of the eye and its consequent increase in mechanical stress on the tissues, in addition to a thinning of the collagen fiber bundles (David et al., 1997; Watson and Young, 2004). These alterations are related to changes in the structure of the sclera (Girard et al., 2009; McBrien et al., 2009; McBrien and Gentle, 2003; Phillips et al., 2000) that may affect its biomechanics. In human and animal sclera, variations in elastic properties that depend on the region of the sclera (Elsheikh et al., 2010; Girard et al., 2011) and the direction of collagen fibers (Coudrillier et al., 2012; Cruz Perez et al., 2014; Grytz et al., 2014) have been previously described. Despite previous work on animal models and human sclera, non-contact, non-invasive, and non-destructive measurement of the biomechanical properties of the sclera remains a challenge. In this thesis, the mechanical anisotropy of rabbit sclera was investigated in the eyeball using a wave-based OCE technique.

The biomechanical properties of the sclera have been studied using a variety of techniques (Boote et al., 2020), but little has been done to quantify these data across the entire eyeball. Recent studies have applied inflation testing (Coudrillier et al., 2012; Elsheikh and Anderson, 2005; Grytz et al., 2014; Whitford et al., 2016) and air-puff induced deformation combined with finite element modeling (Bronte-Ciriza et al., 2021; Nguyen et al., 2019) to quantify the dynamic response of the sclera in *ex vivo* studies. In recent *in vivo* studies, anterior scleral thickness has been measured in human by ultrasound (Ebneter et al., 2015), collagen fiber orientation in peripapillary sclera using polarization-sensitive OCT in rats (Baumann et al., 2014) and human (Willemse et al., 2020). Ramier et al. (Ramier et al., 2020) applied OCE to measure scleral biomechanics in healthy human subjects. In this technique the sclera was excited by a vibrating contact probe to produce surface waves which propagation is related to the tissue shear modulus. It was the first *in vivo* measurements of the shear modulus in the human eye. The mechanical anisotropy of scleral tissue was not investigated in this study, perhaps because the experimental configuration with lateral excitation is not optimal to capture anisotropy.

There is considerable evidence that the scleral properties are highly anisotropic due to the fiber distribution (Coudrillier et al., 2012; Elsheikh et al., 2010; Pijanka et al., 2012; Voorhees et al., 2018). Previous studies have demonstrated the preferential orientation of collagen fibrils in scleral tissue using inflation testing (Grytz et al., 2014; Schwaner et al., 2020) and wide-angle X-ray scattering (Pijanka et al., 2014, 2012). Regional stiffness values have been extracted from uniaxial testing (Elsheikh et al., 2010; Girard et al., 2011) and bi-axial testing (Cruz Perez et al., 2014; Ndlovu et al., 2022). This is important to predict the response of the sclera to different mechanical stimuli, and is also indicative of changes in collagen organization, e.g. in myopia (Hoerig et al., 2022; Markov et al., 2018). However, it has been challenging to experimentally assess scleral anisotropy of intact tissues (whole globe) noninvasively. Recently, emerging optical techniques, such as Brillouin microscopy (Eltony et al., 2022; Scarcelli et al., 2015), Magnetic resonance Elastography (Litwiller et al., 2010) and Optical Coherence Elastography (Larin and Sampson, 2017), have been applied to quantify corneal biomechanics. OCE is a versatile technique that can be combined with different stimuli (Kirby et al., 2017) such as micro-air-puff stimulation (Singh et al., 2016b; Wang and Larin, 2014), piezoelectric excitation (Villegas et al., 2022; Zvietcovich et al., 2020b), acoustic micro-tapping (Kirby et al., 2021; Pitre et al., 2020), air-coupled ultrasonic (Villegas et al., 2023b; Zvietcovich et al., 2020a) to detect mechanical waves propagating in the cornea and sclera. Thus, wave-based OCE has demonstrated its feasibility for estimating the deformation response of ocular tissues and could be a great tool for use in mapping sclera stiffness.

In this thesis, a non-contact excitation ACUS-OCE system was applied to investigate the biomechanical properties at different locations in the rabbit sclera. The effect of orientation-dependent wave propagation was evaluated by estimating the wave speed and shear modulus. In addition, Young's modulus was obtained from tensile tests. The results provided new insights into the mechanical performance of the location on healthy sclera and demonstrated that ACUS-OCE is a valuable tool for assessing sclera anisotropy.

2.5.3. Scleral crosslinking in Biomechanics Analysis

Scleral crosslinking has been proposed as a potential treatment to halt the progression of myopia. Several *ex vivo* and *in vivo* studies in rabbits have demonstrated scleral stiffening by photo-crosslinking (Blackburn et al., 2021). This crosslinking technique uses a combination of a photosensitizing solution, as riboflavin, and light. It has been shown that riboflavin with UVA light increases Young's modulus in rabbit scleral tissue by 320% (Wollensak and Iomdina, 2009), 35% (Zhang et al., 2013), 179% (Wang et al., 2015), and 113% (Zhang et al., 2014). In addition, riboflavin with blue light has also shown an increase shear modulus in rabbit scleral tissue by 76% (Schuldt et al., 2015) and 235% (Iseli et al., 2015). Although there are differences in the reported magnitude of effect related to different measurement techniques and specificities of UVX treatment, all reports indicate an increase in stiffness with the procedure. However, these studies showed a moderate to severe inflammatory response in the treated area after UVA irradiation (Zhang et al., 2013) and blue light irradiation (Iseli et al., 2015), as well as changes in collagen structure and cellular reactivity in scleral tissue treated with high-intensity blue light irradiation (Iseli et al., 2015). However, despite the promise of scleral stiffening, translating these methods to human trials remains challenging. Some post-treatment complications have been reported, including moderate to severe inflammatory response in the treated area (Gerberich et al., 2021; Iseli et al., 2015; Zhang et al., 2013), changes in collagen structure in scleral tissue treated with high-intensity light irradiation ($480-780\,J/cm^2$) around $450\,nm$ (Iseli et al., 2015), and retinal degradation near the optic nerve head in the peripapillary sclera treated with methylene blue/red light (Gerberich et al., 2021). In this thesis, Rose Bengal in combination with green light is presented as a new method for SXL, alternative to UVX, with potentially lower risks.

Rose Bengal is a photoactivated collagen cross-linking agent in clinical use (Redmond and Kochevar, 2019; Singh et al., 2004) that is activated by low-toxicity light in the visible spectrum. RGX (Rose Bengal with 532-nm light) has been shown to increase corneal stiffness, measured by uniaxial tensile tests (Cherfan et al., 2013; Wang et al., 2018; Zhu et al., 2016) and air-puff corneal deformation imaging (Bekesi et al., 2017, 2016b) and to increase collagen fiber organization, measured by SHG microscopy (Germann et al., 2020). In addition, the efficacy and safety of RGX have been evaluated in corneal cross-linking studies which showed that there was no evidence of damage to the cornea, retina and iris of rabbit eyes after treatment with RB and exposure to green light ($68\,J/cm^2$ energy (Soeken et al., 2018) and $150\,J/cm^2$ energy (Zhu et al., 2016)). This suggests that Rose Bengal, together with green light, may function properly as a cross-linker in collagen-rich tissues, so it could be used to stiffen the sclera.

Previous studies have compared the corneal cross-linking efficacy of RGX and UVX. Rose Bengal alone in RGX showed no decrease in corneal thickness compared to the photosensitizer riboflavin in dextran solution in UVX. Moreover, the photosensitizer installation and light exposure times were significantly shorter with RGX (around 10 min) than with UVX (around 60 min). Interestingly, the shallower penetration of RB into the cornea (protecting corneal endothelium) resulted in lower volumetric stiffness and yet a higher magnitude of tensile stiffness as estimated by air-puff deformation imaging (Bekesi et al., 2017, 2016b). Specifically in rabbit corneas, Bekesi et al. (Bekesi et al., 2016b) observed an 11% decrease in corneal deformation after RGX and 33% after UVX, which translated into 11-fold and 6.2-fold increase in stiffness of the treated tissue, respectively. Singh et al. (Singh et al., 2016a) reported a 3% decrease in rabbit corneal thickness after RGX and 30% after UVX, along with a 1.0-fold and 1.5-fold increase in stiffness (integrating the entire corneal depth), estimated by optical coherence elastography. Lorenzo-Martin et al. (Lorenzo-Martín et al., 2018) conducted in vivo studies in rabbits to compare the corneal healing process after RGX and UVX methods. They found that the stromal cell damage caused by UVX was localized in the anterior and medial zone, whereas the damage caused by RGX was only localized in the anterior zone. In scleral tissue, the efficacy of RGX/UVX in human and porcine eyes was evaluated only by Wollensak et al. (Wollensak and Spoerl, 2004), along with other chemical cross-linking methods. They reported a 2.5-fold (porcine) and 1.3-fold (human) increase in stiffness after UVX and a non-significant increase (1.0-fold in porcine and 1.0-fold in human) after 10 minutes of

RB with 60 minutes of white light irradiation. In addition to differences due to cross-linking method specificities, potential confounding factors associated to the swelling properties of the tissue have also been recognized (Doughty, 2000; Huang and Meek, 1999; Yang and O'Connell, 2018).

Tissue swelling is important for understanding the role of stress distributions between collagen fibers and the extrafibrillar matrix in the overall mechanical behavior of the sclera. Differences in the rate of swelling of bovine ocular tissues have been reported as a function of the type of saline used to hydrate (Doughty, 2000) and the type of tissue being hydrated, with the sclera being the tissue to swell more (1/3 more) than the bovine cornea (Huang and Meek, 1999). In addition, computational modeling has identified an influence on tissue hydration due to collagen fiber angle and lamellar structure (Yang and O'Connell, 2018). Furthermore, the potential effect of swelling with cross-linking has been previously investigated by observing a decrease in stiffness with increasing hydration (thickness measurements) in cross-linked bovine corneas (Hatami-Marbini and Jayaram, 2018; Hatami-Marbini and Rahimi, 2016). These changes in tissue stiffness due to hydration appear to be related to the internal structure of the tissue, specifically the GAG chains (Koob and Vogel, 1987), which cause swelling by attracting water molecules to the extrafibrillar matrix. In addition, some studies have reported that removal of GAGs increases stiffness in human sclera by 1.1-fold (Murienne et al., 2016), increases stress in porcine sclera by 2-fold (Hatami-Marbini and Pachenari, 2021) and decreases stress in porcine cornea by 1.7-fold (Hatami-Marbini, 2023). These potential effects on the biomechanical properties of the tissue have made it important to measure the swelling properties of the sclera.

In this thesis, the effects on the biomechanical and swelling properties of scleral tissues after induction of cross-linking by RGX and UVX methods in the nasal and temporal regions of rabbit eyes were investigated. Biomechanical properties were evaluated by uniaxial tensile tests. Swelling was evaluated by a combination of hydration process and tensile behavior in crosslinked and uncrosslinked scleral tissues.

2.5.4. Myopia induction and it role in scleral biomechanics

The development of myopia has been studied in experimental animal models for decades (Schaeffel and Feldkaemper, 2015). Myopia was first found to be induced in animals by eyelid suturing (Wiesel and Raviola, 1977), and more recently, myopia induction has been reported using form-deprivation models (Guggenheim and McBrien, 1996; Howlett and McFadden, 2006; McBrien et al., 2001) or by lens-induced models (Howlett and McFadden, 2002, 2009; Liu et al., 2016). In these animal models of myopia, the vision of one eye of young animals is manipulated for a period of time by eyelid suture, form deprivation or lens wear, while the contralateral eye is allowed to grow normally. The retinal signaling cascade induced by blur has been reported to upregulate metalloproteinase activity, which may lead to scleral remodeling (Harper and Summers, 2015; Troilo et al., 2006) making the posterior sclera more susceptible to axial elongation (Girard et al., 2009; McBrien et al., 2009; Phillips and McBrien, 1995) and consequently to myopia.

Structural changes associated with induced myopia in animal models have reported scleral extracellular matrix remodeling caused by the increase in metalloproteinase activity in posterior sclera of myopic eyes (Guggenheim and McBrien, 1996; Zhao et al., 2018), increase in the rate of retinoic acid synthesis and reduction in rate of scleral glycosaminoglycans synthesis in longer marmoset eyes (Summers et al., 2021; Troilo et al., 2006). Effects that may precede scleral thinning and tissue loss found in the posterior pole of myopic-deprived tree shrews (McBrien et al., 2001) and guinea pigs (Jiang et al., 2011). These alterations in the sclera have been associated with ocular enlargement accompanied by myopia led to biomechanical changes in particular mechanical weakening of the posterior sclera (McBrien et al., 2009, 2001; Phillips et al., 2000).

The guinea pig is considered a rapid model of myopia in mammals (Zheng et al., 2024). The guinea pig eye was first introduced as a myopia model by McFadden and Wallman (McFadden and Wallman, 1995). Recently, the guinea pig model has been shown to have several advantages, such as the development of deprivation myopia in a short period of time (5-10 days (Howlett and McFadden, 2002, 2009)), the guinea pig has large pupils (facilitates back reflection from the retina, which helps in ocular biometry measurements), the guinea pig has a high reproductive capacity and is an inexpensive and easy to handle animal. In addition, the guinea pig model has responded to lens-induced defocus similarly to tree shrews and chickens (Howlett and McFadden, 2009).

Studies in guinea pigs have elucidated the role of light wavelength and light intensity in the development of refractive errors. Researchers have reported that low temporal frequency green light (0-0.5 Hz) induces myopia in guinea pigs (Tian et al., 2019), and guinea pigs exposed to high-intensity illumination showed a greater hypermetropic shift than those exposed to low-intensity illumination (Li et al., 2014). The effects of retinoic acid and dopamine on myopia have also been investigated in guinea pigs. These studies have reported that retinoic acid can increase refractive error (Jiang et al., 2011; McFadden et al., 2004; Wu et al., 2023) and have shown a complex effect on dopamine signaling in induced myopia (Jiang et al., 2014).

In recent years, the sclera has been identified as a potential target for myopia treatment, by stiffening the scleral tissue using either pharmacological (Wang et al., 2021) or crosslinking (Backhouse and Gentle, 2018) approaches. Pharmacologic agents such as atropine and latanoprost have previously been used for myopia control in clinical practice and research. Atropine has already been shown to be effective in slowing myopia progression in children with a treatment duration of at least one year (Huang et al., 2016; Kaiti et al., 2022; Shih et al., 1999). Atropine administered to children has produced changes in refraction of $0.53\,D$ and axial elongation of $-0.15\,mm$ at low doses (0.01% w/v atropine), $0.59\,D$ and $-0.21\,mm$ at moderate doses (0.1% w/v atropine), $0.70D$ and $-0.21\,mm$ at higher doses (0.5%-1% w/v atropine) (Huang et al., 2016). However, ocular adverse effects associated mainly with high doses of atropine, including dilated pupil (mydriasis) and/or accommodative paralysis (cycloplegia) (Kaiti et al., 2022), have led to the recommendation to use lower concentrations (Pineles et al., 2017).

Atropine (1% w/v) has also been previously tested in guinea pig models of myopia and shown to be effective in slowing myopia progression in lens-induced myopia with daily instillation (Zhu et al., 2022) and in deprivation-induced myopia with peribulbar injections (Zhou et al., 2020). Of note, choroidal thickening (1-2% at 6 weeks of induction) with atropine instillation (Zhu et al., 2022) contrasted with choroidal thinning (5% at 2 weeks of induction) with peribulbar atropine injection (Zhou et al., 2020), presumably due to choroidal perfusion. Atropine also attenuated the reduction in scleral hypoxia and choroidal blood flow in form-deprived eyes (Zhou et al., 2020). Because the hypoxic scleral response plays a role in scleral extracellular matrix remodeling (Wu et al., 2018), atropine may control the myopia development. In addition, atropine has been shown to stimulate collagen I and fibronectin production in scleral fibroblasts and inhibit their production in choroidal fibroblasts (Cristaldi et al., 2020). This suggests that atropine may strengthen the scleral extracellular matrix while increasing permeability in the choroid. Nevertheless, the mechanism by which atropine affects scleral development in the myopic context remains unclear.

Another proposed pharmacological therapy for myopia control is latanoprost. Latanoprost is a prostaglandin analog that lowers IOP by increasing aqueous humor outflow. Briefly, latanoprost activates prostaglandin receptors in the ciliary body (see Section 2.1), which may stimulate metalloproteinase activity associated with scleral extracellular matrix remodeling (Lindsey et al., 1997; Ocklind, 1998; Russo et al., 2008). In clinical practice, latanoprost (0.005%) has shown to lower IOP in pediatric glaucoma without adverse side effects (Black et al., 2009; Raber et al., 2011), for example, showing an IOP reduction of $7.2\ mmHg$ after 12 weeks of treatment (Maeda-Chubachi et al., 2011).

In animal research, latanoprost has previously been tested in a form-deprivation myopia model in guinea pigs. Guinea pigs with deprivation-induced myopia were treated with daily application of latanoprost (0.005%), which not only slowed myopia progression by reducing IOP ($-5.2\ mmHg$ vs. $1.8\ mmHg$), but also produced smaller changes in refraction ($-2.3\ D$ vs. $-8.2\ D$) and axial elongation ($0.06\ mm$ vs. $0.29\ mm$) compared to untreated myopic eyes after 10 weeks (El-Nimri et al., 2019; El-Nimri and Wildsoet, 2018). In addition, scleral collagen fibers in latanoprost-treated myopic eyes were more evenly spaced, with a lower percentage of small fibers (38%) and more similar to fellow eyes, compared to a higher percentage of smallest fibers (52%) in the sclera of untreated deprived eyes (El-Nimri et al., 2019). Furthermore, although latanoprost (administered daily to guinea pigs for 2 weeks) did not affect refractive error, axial length, retinal thickness or choroidal thickness, the choroidal vessels appeared to be dilated (El-Nimri et al., 2022). This enlargement of the choroidal vessels in latanoprost-treated guinea pig eyes could hypothetically be explained by the choroidal vasculature being constricted by the extracellular matrix (choroidal extracellular matrix is reduced by increased metalloproteinase activity as an effect of latanoprost) (El-Nimri et al., 2022; Wang et al., 2001).

Despite the reported changes in ocular shape, to our knowledge, the effect of latanoprost and atropine on the mechanical properties of the sclera has not been investigated. In this thesis, we evaluated changes in refractive error and axial length in a form-deprived guinea pig model (the contralateral eye remained as a control). We examined the effects of atropine and latanoprost treatments on the control of axial elongation and refractive error. In addition, the techniques implemented and used in previous chapters (OCE, uniaxial tensile test, SHG microscopy) were used to study the mechanical and structural properties of the sclera in myopic eyes, myopic-treated eyes, and untreated nonmyopic eyes.

3. METHODS AND MATERIALS

This chapter describes the experimental and theoretical techniques used in this thesis. The systems used in this work were custom-developed instruments (Air-puff Optical Coherence Deformation Imaging, Multi-directional Ultrasound Optical Coherence Elastography, Second Harmonic Generation Microscopy) and a commercial device (UStretch Mechanical Test System) available at the Visual Optics and Biophotonics Lab, Instituto de Óptica "Daza de Valdés", CSIC, Madrid. The animals were handled in the Faculty of Veterinary at the Complutense University, Madrid.

The author of this paper has used and applied the optical and mechanical systems to determine the biomechanics of scleral tissue from porcine, rabbit, and guinea pig eyes. The optical imaging systems were customized by Andrea Curatolo, James Germann, Judith Birkenfeld, Alberto de Castro, Fernando Zvietcovich and Pilar Urizar.

The author of this thesis modified all the algorithms, adapting them from cornea to sclera and adding all the new functionalities in the MATLAB interfaces to quantify from scleral images all the biomechanical parameters explained in this chapter. The finite element model was developed by Andres de la Hoz. The air-puff deformation image processing algorithm was developed by Eduardo Martínez-Enríquez. The elastography image processing algorithm was developed by Fernando Zvietcovich. The second harmonic generation processing algorithm was developed by James Germann.

The author of this thesis positioned and restrained the animals during the procedures, administered treatments, and monitored the response of the animals during all the experiments. The animals were monitored with the assistance of Javier Fernández Martínez (veterinarian) and Luis Revuelta Rueda (animal project supervisor). Due to the requirements of this work, the author of this thesis has obtained a certificate to handle animals used, bred or supplied for experimental and other scientific purposes, including teaching, issued by the Comunidad de Madrid (Certificate No.: CAP-00453.2-24 15).

The author of this thesis, under the supervision of Prof. Susana Marcos: (1) designed and implemented the experiments, (2) handled and tested the animals and their tissues, (3) developed all the analysis routines for image processing and for data processing, and (4) evaluated and interpreted all the data presented.

3.1. Ocular tissue preparation

This thesis used porcine eyes (n=20), rabbit eyes (n=60), and guinea pig eyes (n=12) in experiments aiming at characterizing the mechanical properties of the sclera as well as its corneal organization. This section describes specific eye globe handling protocols used in the experiments throughout the thesis.

3.1.1. Porcine tissue

Eyes form adult pigs (6–8-month-old) were obtained 2h after enucleation from a slaughterhouse ("Justino Gutiérrez" S.L, Valladolid, Spain) and were kept refrigerated at temperatures around 4 ^{0}C. The ocular fat was removed before the measurement. The scleral regions in each eye were identified as temporal (T) and nasal (N) as shown in Figure 3.1a and 3.1b. The strips were stored in a custom humidity chamber (less than 30 min) humidified with balanced salt solution (BSS, sterile, Bausch-Lomb, Australia).

3.1.2. Rabbit tissue

Ocular globes were obtained from adult New Zealand White rabbits (14–16-week-old, 2-3 kg, female) from a farm affiliated with the Faculty of Veterinary of the Complutense University (Madrid, Spain). Rabbits were euthanized and their eyes were enucleated (see Figure 3.1a top panel). Eyes were kept refrigerated at temperatures around $4^{0}C$. Conjunctival tissue and muscles were removed from all eyes. The scleral regions in each eye were identified as temporal (T) and nasal (N) as shown in Figure 3.1a. The eyeballs were divided into quadrants according to the equatorial circumferential line (red line, Figure 3.1b) and the central meridional line (green line, Figure 3.1b) following the rectus muscles. The equatorial line divided the sclera into anterior and posterior, and the meridional line into superior and inferior. The equatorial circumferential line divided the sclera into anterior and posterior and the meridional line divided into superior and inferior. Rabbit eyes were cut into strips, according to the specific protocols for each experiment. The retina and choroid were carefully scraped off. The strips were stored in a custom humidity chamber (less than 30 min) humidified with phosphate-buffered saline (PBS) solution (Sigma-Aldrich, Milwaukee, WI, USA).

All rabbits were euthanized by cervical dislocation in the context of veterinary activities (such as birth control, reproductive control, teaching) for which the Faculty of Veterinary of the Complutense University of Madrid is responsible. These activities have been approved for an Animal Experimentation Committee with the number: (CEA)-UCM-5414122021-2021.

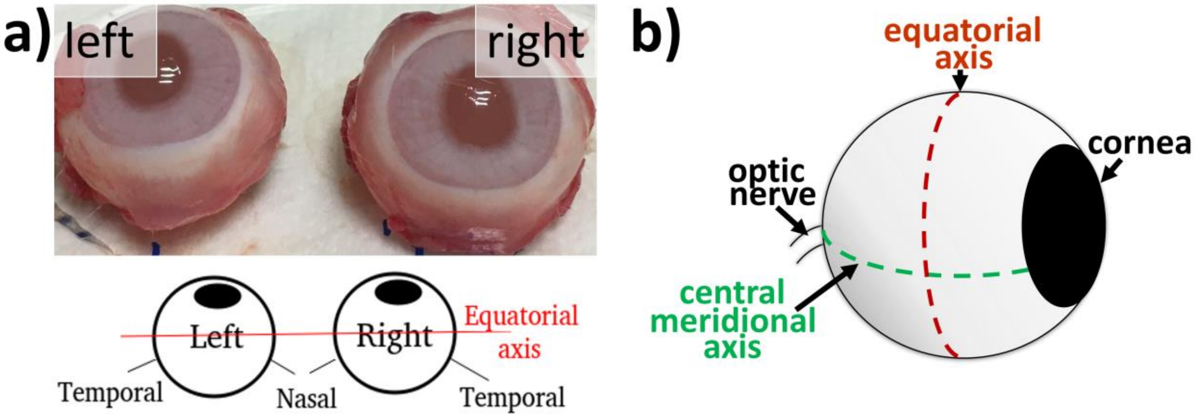

Figure 3.1: Ocular zones marked and identified in illustrations and photographs of animal eyes. a) A photograph of rabbit eyes is shown with the nasal and temporal regions identified. b) The equatorial circumferential axis (red line) defined the separation of the anterior and posterior zones. One of the meridional axes, the central axis (green line), separated the superior sclera from the inferior sclera.

3.2. Guinea pig animal model

Tricolor guinea pigs (*Cavia porcellus*, 0–12-week-old) were housed in the veterinary facilities of the Departamento de Fisiología Animal (Faculty of Veterinary of the Complutense University of Madrid, Madrid). The pups were kept with their mothers in their natural litters (animals of less than 4 weeks old) and then as single-sex groups of maximum 3 animal per cage (animals more than 4 weeks old). Guinea pigs were reared in situ on a 12-hours-light/12-hours-dark cycle (on at 9:00 and off at 21:00). Animals were housed in transparent plastic cages (65 *x* 45 *x* 20 cm^3) with a wire roof. Cage floors were lined with compressed paper product (chemical-free, biodegradable and dust-free). Luminescence (550±50 lux) in the center of each cage was measured using a digital illuminance meter (ILM 1332A, RS PRO, 0.01-200000 lux, 0.1 lux) and room temperature was maintained at 22°C. Animals had free access to water and vitamin C-supplemented food. All animals were euthanized by an overdose of anesthesia (pentobarbital, 50 mg/kg). To avoid suffering, the animal was previously relaxed with inhalational anesthesia (isoflurane, 1.5-2% oxygen, 2 min).

Guinea pigs were treated according to European (Directive 2010/63/EU of the European Parliament and of the Council) and Spanish (Real Decreto 53/2013) regulations. This study was approved by the Animal Care and Ethics Committee at Faculty of Veterinary of the Complutense University (Madrid, Spain). The treatment and care of animals were conducted according to the ARVO Statement for the Use of Animals in Ophthalmic and Vision Research. This animal experiment project has been registered and authorized by the Dirección General de Agricultura, Ganadería y Alimentación (Comunidad de Madrid, Madrid, Spain) with the number: PROEX 046.6/22 with the title (in Spanish): "Caracterización de los cambios debido a diferentes tratamientos en la esclerótica de cobayas durante el uso de difusores".

3.3. Myopia and refractive error

Myopia is associated with a refractive error (see Sections 2.2.2 and 2.2.3) that affects a person's ability to see distant objects clearly (Vera-Diaz, 2010). To determine the refraction of an eye, the spherical equivalent should be estimated from the measured refractive errors (see section 3.10.3). Currently, two quantitative categories are defined to describe the degree of myopia in humans: *myopia* and *high myopia* (Flitcroft et al., 2019; World Health Organization and Brien Holden Vision Institute, 2016). *Myopia* has been defined as: "a condition in which the spherical equivalent objective refractive error is $\leq -0.50\ D$ in either eye". *High myopia* has been defined as: "a condition in which the spherical equivalent objective refractive error is $\leq -5.00\ D$ in either eye".

3.4. Measurement devices

3.4.1. UStretch Mechanical Test System

UStretch CellScale (Figure 3.2.) is a uniaxial stretcher for measuring the mechanical properties of biomaterials (Cellscale, 2017). The stretching parameters can be set by means of a software interface that is provided for the manufacturer. A test sequence can be defined by specifying the displacements in either percent strain or millimeters, the test duration in seconds, the force in millinewtons, the preload magnitude in millinewtons during the first or during each repetition, and the strain control function. For example, the ramp function applies displacement at a constant nominal rate, which is equivalent to engineering strain or constant velocity. During the test, three graphs are displayed on the right-hand side of the screen: force versus time, displacement versus time and force versus displacement (proportional to nominal engineering strain). The results are provided in a folder containing the output images taken at a defined frequency and an Excel file containing the force, displacement, and time data of the tests.

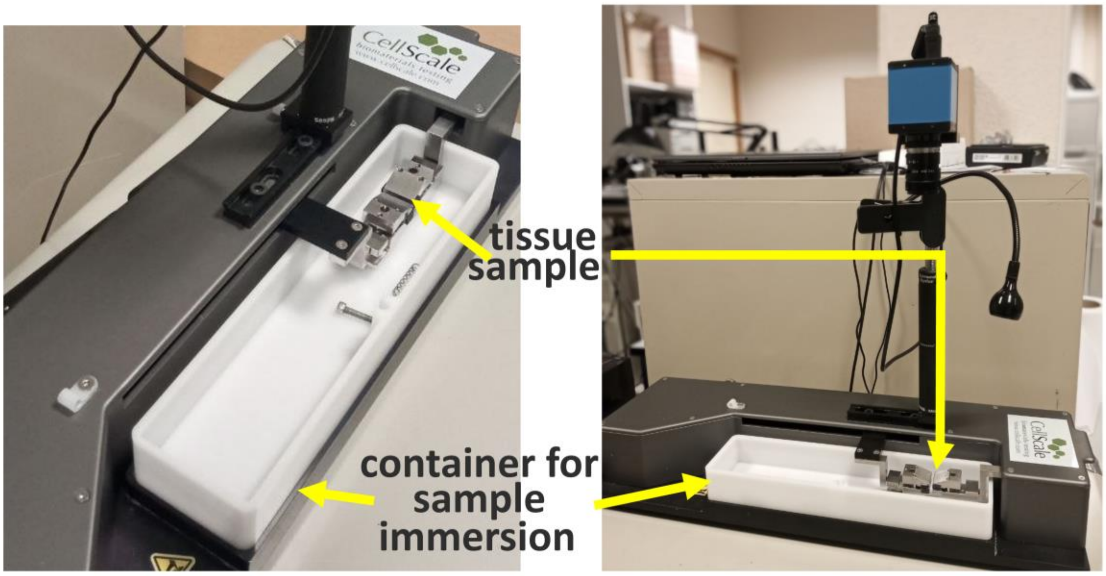

Figure 3.2: Photograph of the uniaxial stretcher. The stretcher (UStretch CellScale) was used for all tensile measurements. The tissue strips were placed between the forceps and samples were stretched 5 to 7 times until a predetermined elongation was reached. The samples were immersed in saline during all stretching procedures.

3.4.2. Streak retinoscope

A streak retinoscope (Corboy, 2003) is a self-illuminating instrument with a projection system that illuminates the retina with rays that project a line/streak of light and an observation system to see the retinal reflex, see Figure 3.3a. The projected streak of light is rotated by turning the sleeve of the instrument. The sleeve also is moved up/down to select diverging rays (plane mirror effect) or converging rays (concave mirror effect). The light reflected from the illuminated retina enters the retinoscope through an aperture and exits through the peephole. Refractive errors associated with myopia, hyperopia and astigmatism can be detected by observing the characteristics of the moving retinal reflex.

When the correcting lenses (Figure 3.3b) neutralize the movement of the reflex (see Figure 3.4), the power of these lenses gives the measure of the refractive error (see Section 2.2.2). To neutralize, one hand is used to hold the retinoscope and rotate the sleeve, and the other hand is used to place the lenses in front of the eye, see section 3.10.3 for further explanation.

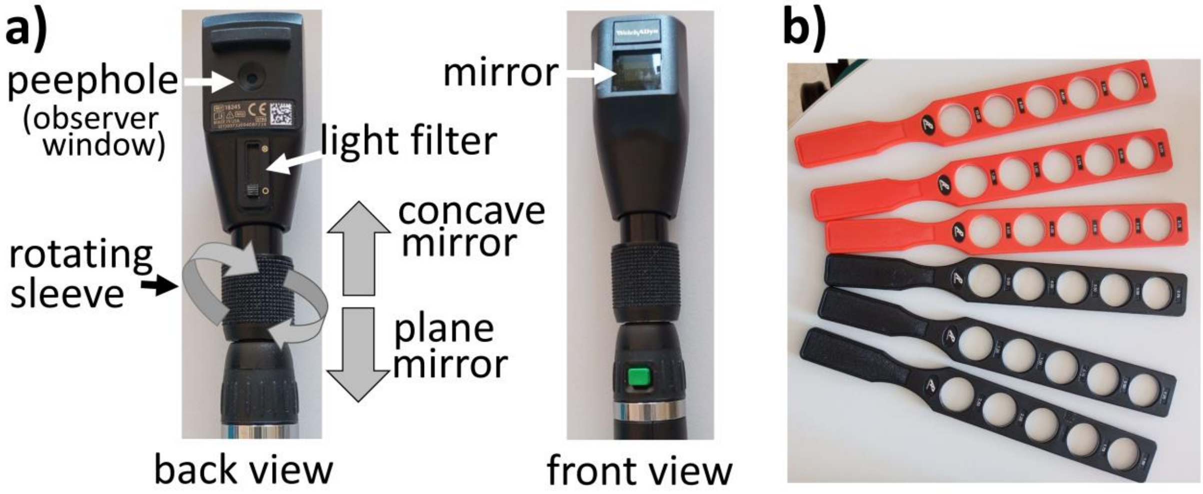

Figure 3.3: Streak retinoscope and lens. a) Photographs of the retinoscope (Welch-Allyn 18200 Retinoscope) used for refraction measurements. b) Retinoscopy lens rack set with positive (from 0.25 D to 5 D) and negative lenses (from -0.25D to -5D).

The plane mirror technique has been used for measurements on guinea pigs using the Welch-Allyn streak retinoscope model 18200 (The Welch Allyn, NY, USA) with a lens rack. The movement of the streak projected onto the retina can be observed by shaking the retinoscope while looking through the peephole (Welch Allyn, 2020). The emerging rays can be seen as a reflex in the subject's pupils. If the emerging rays have not converged to a point, the retinal reflex moves in the same direction as the streak moves; this is the WITH motion reflex. If the rays have diverged, the reflex moves in the opposite direction to the motion of the streak; this is the AGAINST motion reflex, see Figure 3.4.

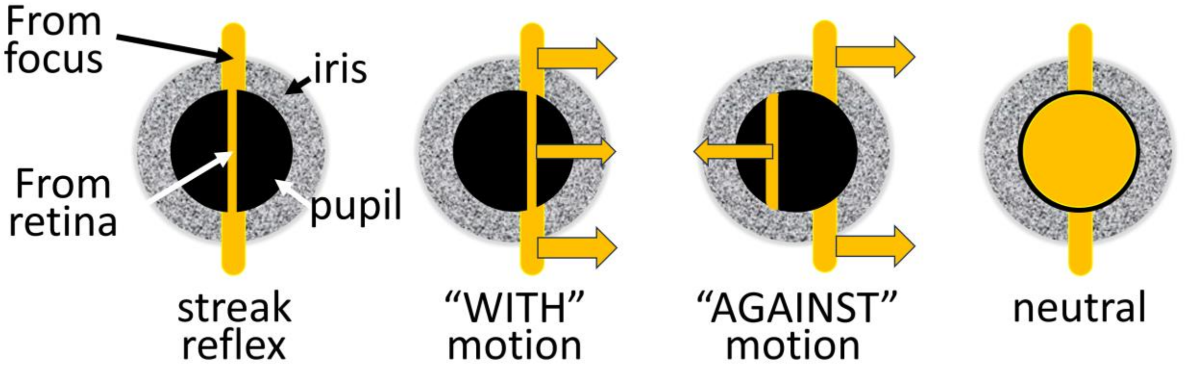

Figure 3.4: Movement of retinal reflex and neutralized effect. Illustration of "WITH", "AGAINST", and neutral states of movement of the retinal reflex when the retinoscope's streak light is shone on the subject's retina.

3.5. Optical Imaging technologies

Optical Coherence Tomography (OCT) is a conventional technique available to view inside of the eye. In short, the scanning beam of light passes through the ocular structures along the visual axis, and the ocular structures can be imaged with high resolution. Anterior Segment OCT systems are commercially available for morphologic observations of the cornea and crystalline lens of the eye, and generally for 1-D axial measurements. The 3D quantitative Anterior Segment OCT systems used in the current thesis are custom developed in our group and previously reported (Urizar et al., 2023). These systems are further provided with tools (ranging from automatic segmentation to scan and optical distortion correction methods) for full 3-D quantification. This system was used in the current thesis as an optical Biometer in guinea pigs, allowing visualization of the entire axial structure of the eye in a single scan, identifying structures such as the anterior and posterior boundaries of the cornea, the anterior and posterior boundaries of the lens, and the posterior boundary of the retina. Furthermore, the OCT was coupled and synchronized with air-puff (Curatolo et al., 2020b) and with an ultrasound transducer (Villegas et al., 2023b) to excite the cornea and measure air-puff corneal deformations, and multi-directional shear wave propagation. On the other hand, Second Harmonic Generation Microscopy (Germann et al., 2018) was used to image collagen in corneal and scleral tissues.

3.5.1. OCT air-puff deformation imaging

OCT air-puff measurements were performed using a custom-developed swept-source OCT (SS-OCT) combined with air-puff excitation unit (Birkenfeld et al., 2023; Bronte-Ciriza et al., 2021). The SS-OCT system, described in (Curatolo et al., 2020b), was used to characterize the anterior segment of the eye (cornea, crystalline lens) in subjects and scleral tissue in animal models. The swept source (SL132120, Thorlabs, Newton, NJ, USA) has a light source centered at 1300 nm. The system uses a Mach-Zender interferometer configuration with a dual balanced photodetector (PDB480C-AC, Thorlabs, USA). To allow the air-puff unit (Figure 3.5) to be inserted between the lens and the eye, the sample arm of the system was designed with a 2" aperture f-theta telecentric scanning lens (LSM05, Thorlabs, USA). For ultrafast transverse scanning (deformation events of tens of milliseconds), the system uses galvanometric scanning mirrors (Saturn 1B, ScannerMAX, Pangolin, USA). These characteristics resulted in an axial rate of $200\ kHz$, an axial resolution of $16\ \mu m$, a depth of field of $5.15\ mm$, a large transverse field of view of $15\,mm$ on both orthogonal axes, and an ultra-fast transverse scanning pattern repetition frequency of $1\ kHz$.

Scleral and corneal deformation was induced using an industry-standard tonometer air-puff unit (Nidek Co., Japan). The unit has a piston-based air-puff module that is coupled to the SS-OCT system. It has an optical window at the rear, allowing it to be mounted in front of the objective lens and aligned coaxially with the OCT scanning beam. To reduce shadowing of the nozzle wall in the OCT image, the optical window at the front of the air-puff unit was made of transparent methacrylate (with a $2.4\,mm$ wide hole in the middle), see Figure 3.5. For *ex vivo* measurements in porcine eyes, the voltage controlling the piston speed was set to $48\,V$, being $15.4\,kPa$ the maximum apical air-pulse pressure. For *ex vivo* measurement in rabbit eyes the maximum air-puff pressure (AP) was switched between two configurations AP1: $7.28\ kPa$ $(23.3\ V)$ and AP2:$15.4\ kPa$ $(48\ V)$.

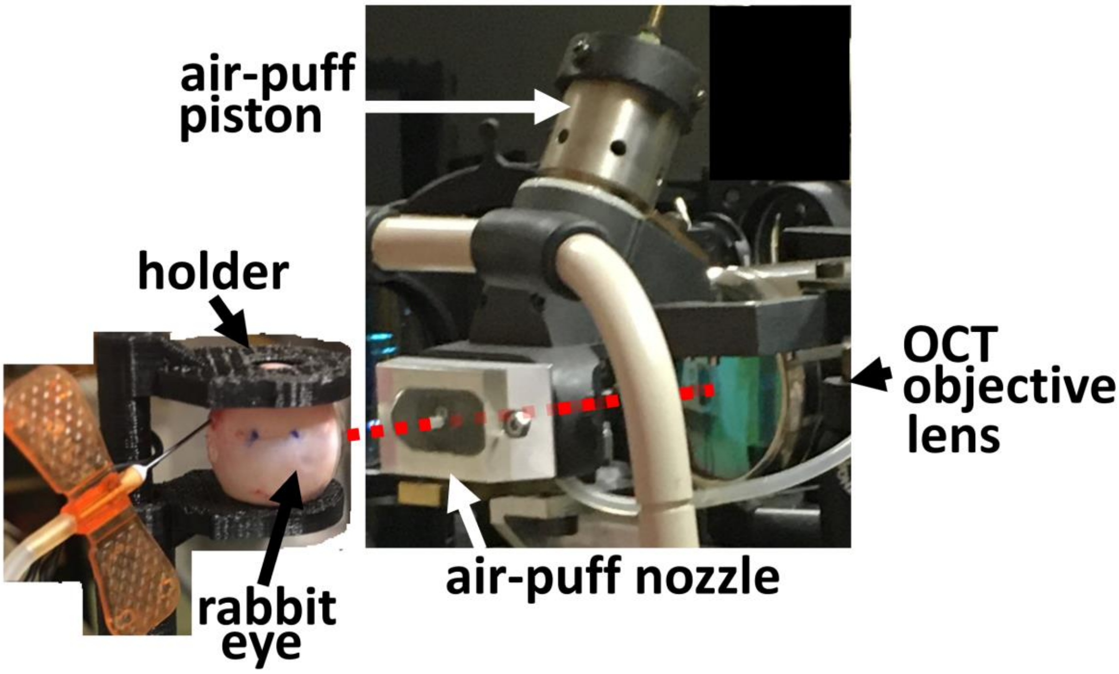

Figure 3.5: Photographs of OCT air-puff imaging system. Shown is an e*x vivo* eye placed in the eye-holder and mounted in front of the air-puff nozzle and the SS-OCT system. The laser had a light source centered at 1300 nm (shown as the red dotted line). OCT images were collected at each location during the air-puff deformation. The nozzle was aligned with the OCT sample arm to acquire multiple scans while the air-puff excitation source induced a deformation of the tissue at specific locations. The intraocular pressure of the eye was kept constant during the procedure.

3.5.2. Optical Coherence Elastography system

OCE measurements were performed using a swept-source phase-sensitive optical coherence tomography system (SS-PhS-OCT), combined with a transducer excitation, see Figure 3.6 (Villegas et al., 2023b; Zvietcovich et al., 2022). The SS-PhS-OCT is a custom-built system reported in previous publications (Curatolo et al., 2020b; McAuley et al., 2022). The swept source (SL132120, Thorlabs, Newton, NJ, USA) has a light source centered at 1300 nm (VCSEL) with a spectral 3dB-bandwidth (50 nm) and an axial scan rate of 200 kHz. The OCT axial resolution in air is 16 μm. The sample arm was designed using a scan lens (LSM05, Thorlabs, USA) to produce a transverse resolution in air of 40 μm at the focal plane, and a depth of field of 5.15 mm. System provides a multi-directional scanning for corneal and scleral topography and elastography using galvanometric scanning mirrors (Saturn 1B, Scanner MAX, Pangolin, USA). For *ex vivo* measurements in rabbit eyes, multi-directional functionality was used to acquire 8 directions (16 semi-axes) over a transverse range of 15 mm length at pattern repetition frequency of 1 kHz.

The Air-Coupled Ultrasonic transducer was co-focused and coaxially aligned with the sample arm of the SS-PhS-OCT (Zvietcovich et al., 2022) to acquire multiple scans of wave propagation while the transducer induces elastic waves at the central cornea and on the scleral surface (Figure 3.12a). The acoustic transducer has an aperture diameter of 15 mm to allow for OCT imaging, while the tissue is being excited by the acoustic beam with a lateral spot size of approx. $0.6\,mm$. The transducer was excited with a 3-cycle 2kHz train of square pulses modulating at $0.5\,MHz$ signal which was amplified with a radiofrequency amplifier (100A250A, Amplifier Research, USA).

The multidirectional M-B scanning protocol (Wang and Larin, 2014; Zvietcovich et al., 2017b) was used during the acoustic stimulation to capture the tissue excitation along all the 8 radial directions. In our protocol, the OCT system captured 450 A-scans with temporal resolution of $\Delta t = 5\ \mu s$ after at each spatial point. Each direction consisted of 100 spatial positions along each B-scan covering transversal range of $15\,mm$ (spatial sampling resolution of $0.15\,mm$). The data were reorganized in 2D + time format. The total acquisition time was 1.8 s, including the 8 radial scans centered at each measurement location.

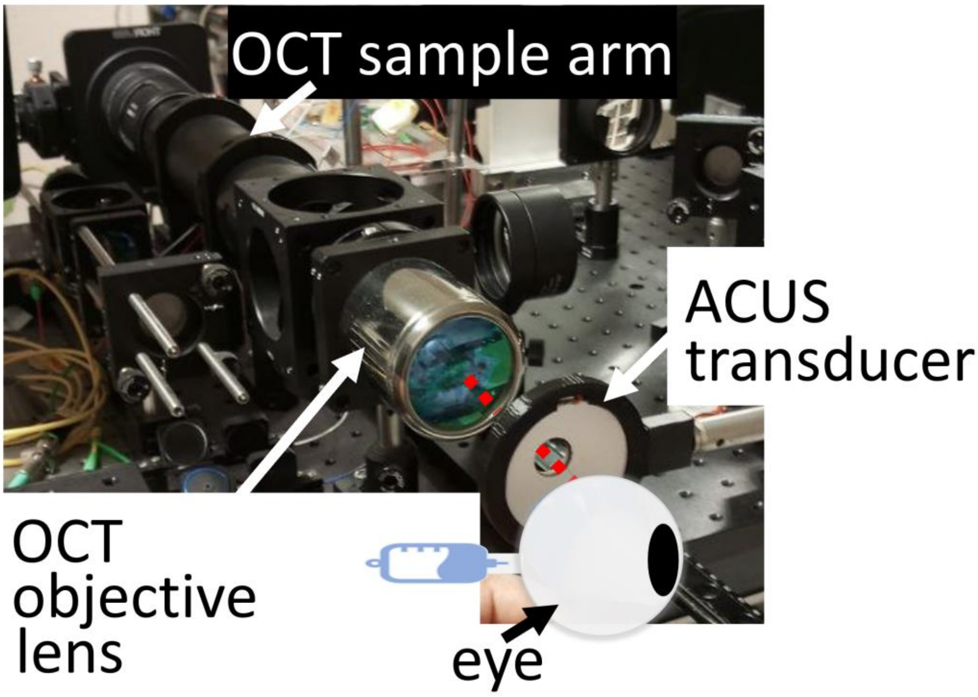

Figure 3.6: Photograph of the Optical Coherence Elastography system. Shown is an illustration of an eye placed in front of the air-coupled ultrasonic (ACUS) transducer and the SS-PhS-OCT system. The laser had a light source centered at 1300 nm (shown as the red dotted line). The ACUS transducer was aligned with the OCT sample arm to acquire multiple scans while the transducer induced elastic waves at specific locations.

3.5.3. SS-OCT 3D Biometer

Ocular axial dimensions were measured using a custom-developed Swept Source Optical Coherence Tomography (SS-OCT 3D Biometer) imaging system (Figure 3.7). The SS-OCT 3D Biometer was already used in previous publications for axial length measurements (Urizar et al., 2023) in a model eye to image the entire ocular axial structure. A similar method (but based on spectral OCT with a spectrometer and a line C-MOS camera) has been used previously in our group before for 3-D biometry in guinea pigs (Pérez-Merino et al., 2017). In the SS-OCT 3D Biometer, the swept source LASER (SL100060, Thorlabs, Newton, NJ, USA) had a light source centered at 1060 nm (VCSEL) with a spectral 10-dB-bandwidth of 100 nm and a A-scan rate of 60 kHz. These characteristics resulted in a full width at half maximum (FWHM) axial resolution of 11 μm in air. The signal was acquired with a balanced photodetector (PDB481C-AC, Thorlabs, USA) to allow an axial scan range of 33 mm in air. The sample arm was combined galvanometric scanners to deflect light with a 2” aperture f-theta telecentric objective lens (LSM05, Thorlabs, USA) to produce a transverse resolution range of $23 - 31\ \mu m$ at retinal focal plane, and a depth of field of 5.15 mm. The system provided different scanning patterns (such as meridional, raster) for measuring axial dimensions using galvanometric scanning mirrors (Saturn 1B, Scanner MAX, Pangolin, USA). For *in vivo* measurements in guinea pigs, the raster scanning functionality was used to acquire two orthogonal scans over a transverse range of 8 mm length at pattern repetition frequency of 60 kHz.

The M-B mode protocol was used for the acquisition of structural sectional frames along all raster scans. The OCT system captured 300 A-scan repetitions (M-mode acquisition during 1.5 s) in each measurement position with a spatial sampling resolution of 27 um. Each scan consisted in 100 repetitions covering 8 mm every 17 μs. The total acquisition time was 3 seconds.

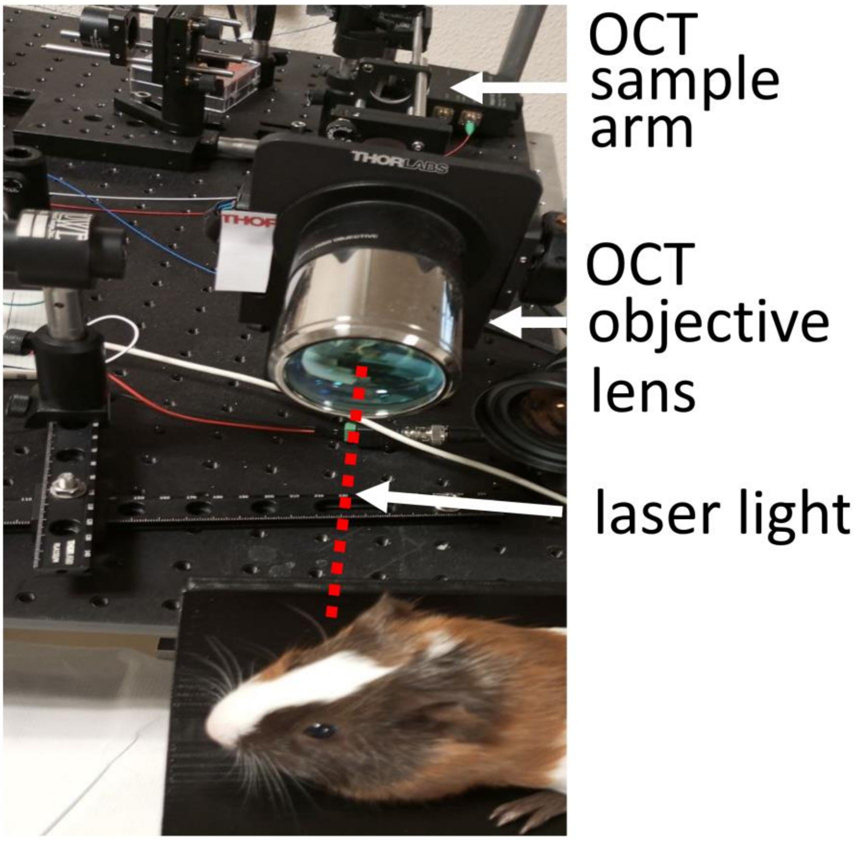

Figure 3.7: Photograph of the 3D Biometer System. Shown is a guinea pig placed in front of the OCT objective of the SS-OCT 3D Biometer. The laser had a light source centered at 1060 nm (shown as the red dotted line). The OCT sample arm acquires multiple scans of the guinea pig eye using a raster scanning functionality.

3.5.4. Second-Harmonic generation microscopy

A second harmonic generation (SHG) microscope obtains images by collecting the frequency-doubled light produced by focusing intense coherent light on a material with a non-centrosymmetric molecular structure, such as collagen (Freund and Deutsch, 1986; Roth and Freund, 1979). Since the difference between the light source and the frequency-doubled light is quite large, it is possible to separate the two different types of light. Interestingly, this technique does not require any treatment of the tissue, as the process depends solely on the intrinsic properties of the material.

Collagen fibers in the ocular tissues were imaged using a custom-developed two-photon microscope with SHG capability, see Figure 3.8. The system was previously used to quantify collagen fibers in porcine cornea (Germann et al., 2018) and rabbit cornea (Germann et al., 2020). An infrared laser source (MaiTai Ti-Sapphire, 80 fs pulses, 80 MHz) was tuned to 800 nm center wavelength. A 0.9NA water immersion objective (Olympus LUMPLANFL60XM) was used to focus the excitation beam, and a second objective (Olympus LUMPLANFL40XM, 0.8NA) was used to collect the SHG signal. The signal was reflected through a long-pass filter ($665\ nm$) after being collected through a band-pass filter ($395 - 415\ nm$). The filtered SHG signal was collected with a photomultiplier tube (Hamamatsu H10682-210-PMT). The excitation beam was swept across the sample using scanning galvanometric mirrors (Cambridge Tech model 6215H) while the sample was moved along the optical axis using a motor (Thorlabs Z825B).

Collagen images ($150x150\ \mu m^2$) were acquired at a resolution of $400x400\ pixels^2$ with a step size of $4\ \mu m$ through the depth of the tissue. Multiple sequential image stacks (z-stacks) were acquired for a depth range of $300 - 500\ \mu m$ (depending on the thickness of the corneal and scleral tissue). The SHG images were acquired in approximately 2.6 seconds/image (dwell time at each pixel was $16\ \mu s$) and each pixel had a corresponding scale of $0.375\ \mu m/pixel$.

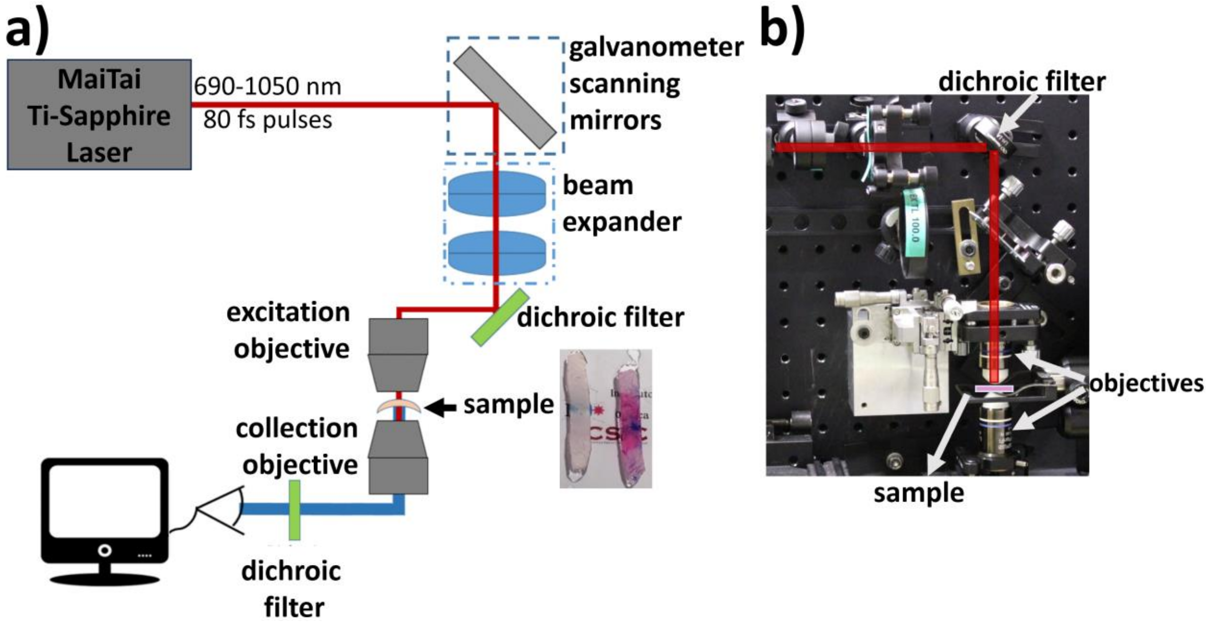

Figure 3.8: Schematic of SHG microscope. a) SHG images were obtained from corneal and scleral samples. The excitation source emitted 80-fs pulses with a center wavelength of 800 nm. The beam was scanned across the sample and doubled light was collected in the forward and backward directions using the objectives. b) The photograph shows one filter, both objectives and the sample position. Image modified from an image kindly provided by Dr. James Andrew Germann.

3.6. Air-puff deformation imaging methods

3.6.1. Air-puff deformation measurement protocols

The eyes are mounted in the customized holder and connected to a liquid column system to control the IOP, see Figure 3.9. The column is filled with BSS (salt solution). The needle is not removed until all measurements are completed to ensure that the IOP remained constant. The IOP is set to a fixed value of 15 $mmHg$. The eyes are then positioned in each one of the predetermined locations to face the OCT scanning beam/air-puff nozzle (see Section 3.5.1). The apex of the selected ocular location is centered with the OCT's optical axis, using real time OCT image preview on cross-axes scans. For convenience, the most anterior point of each scleral location is defined as "scleral apex".

OCT air-puff measurements are collected along two scans (orthogonal axes), each of which was 15 mm long. A complete measurement consist of a total of 100 cross-axes scans, with each axis sampled by 64 A-scans. The total acquisition time of a complete data set is 100 ms (one cross-axes scan per ms). After a set of three measurements for each location, the eye position is changed carefully to the next location and the eye globe is moisturized with BSS.

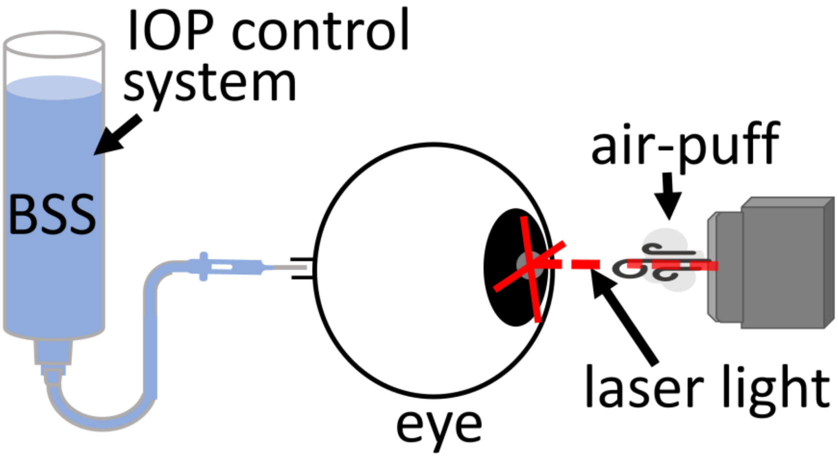

Figure 3.9: Schematic of the air-puff OCT measurement. The eye is placed in front of the air-puff nozzle that is connected to the OCT system. The air-puff excitation source deformed the ocular tissues while the OCT system collected images over two directions (orthogonal axes, represented as red lines over the eye) at a specific location on the eye. IOP was held constant at 15 mmHg by a monitoring system connecting a saline-filled syringe to the eyeball (through the optic nerve head) and a water column (see left side of the figure). BSS indicates balanced salt solution.

3.6.2. Hyperelasticity model and finite element analysis

Biological tissues are heterogeneous composite materials composed of different media. Constitutive theories have been developed to describe and reproduce the behavior of biological tissues. Based on the theory of nonlinear continuum mechanics, mechanical properties can be derived from the strain-energy density function W expressed as a function of Green-Lagrange strain tensors (Chagnon et al., 2017). A two-parameter Yeoh hyperelastic material model, defined by Equation 3.1, has been used to model the nonlinear elastic behavior of the cornea and sclera (Elsheikh, 2010; Grytz et al., 2014; Woo et al., 1972).

$$W = C_{10}(I_1 - 3) + C_{20}(I_1 - 3)^2 \tag{3.1}$$

In the studies presented in this thesis, the density function is expressed in terms of the first invariant of the Cauchy-Green deformation tensor I_1, and two material parameters (C_{10} and C_{20}). The second power in the last term of the equation affects the C_{20} parameter at higher strains and the C_{10} parameter at lower strains. Thus, the relative values (C_{20}/C_{10}) can be used as an indication of the non-linearity of the material.

Finite element model (FEM) of the globe is constructed using ANSYS Workbench (ANSYS Inc, U.S.A.). The globe is modeled as a three-dimensional, rotationally symmetric solid to reduce the computational burden, see Figure 3.10a. The dimensions used were taken from the literature (Asejczyk-Widlicka et al., 2008; Olsen et al., 2002) to model a porcine eye globe and from measurements of *ex vivo* eyes in our laboratory to model a rabbit eye globe. The thickness profile of the sclera is considered not uniform, with the sclera being thickest near the limbus and the area closest to the optic nerve head ($\sim 1\,mm$), but thinnest near the equatorial plane. The thickness variation is shown in the proposed geometry in Figure 3.10b. The model includes two solids (cornea and sclera), each with a uniform material definition as defined in Equation 3.1, and a boundary region representing the experimental conditions (the custom holder around the sclera), see Figure 3.10. The interior of the globe is meshed with hydrostatic fluid elements (De La Hoz et al., 2024), and a pressure of $15\,mmHg$ (the same IOP as in the experiments, see Section 3.6.1) is applied to the central node of the fluid element mesh. The air-puff load is applied as a spatially and temporally varying pressure. The spatial and temporal profiles obtained from the air-puff measurement over time are used (Curatolo et al., 2020a).

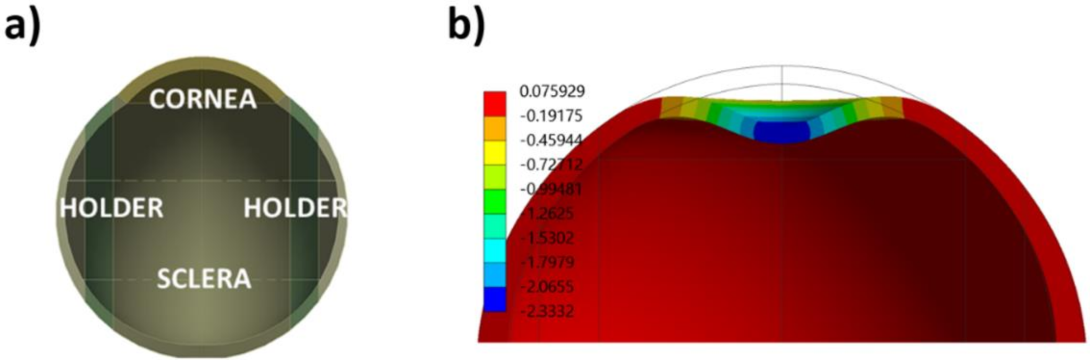

Figure 3.10: Representation of the geometry used in the finite element simulations and a spatial deformation resulting from a simulation. a) Cornea, sclera, and the eye-holder were considered as materials of the eye globe into the model. b) Example of the spatial deformation of the inferior sclera (location I). The image shows the deformation at the central point (apex). This point was used to estimate the apex displacement in the optimization process. This image was published in (Bronte-Ciriza et al., 2021), and is used with the permission of the authors.

To obtain scleral and corneal material properties from air-puff results, an optimization process was created in a script using MATLAB 2018a (MathWorks, USA). The optimization process consists of (Bronte-Ciriza et al., 2021) (1) creating a function to run ANSYS, (2) evaluating the FEM for a set of material parameters, (3) retrieving the temporal profile (center point displacement over time), and (4) comparing the obtained results with corresponding experimental measurements of apex displacement. For the 2-parameter Yeoh model (Equation 3.1), the Nelder-Mead simplex method (Lagarias et al., 1998) is used as an optimization algorithm to minimize the difference between the experimental and simulated apex displacements from t=0 to the time of maximum deformation. Once the two parameters (C_{10} and C_{20}) are obtained, the secant Young's modulus corresponding to 10% strain is calculated from the simulated stress-strain curves.

3.6.3. Estimation of air-puff resulting parameters

OCT images (Figure 3.11a) are obtained from resampled spectral data files using routines (Curatolo et al., 2020a; Gora et al., 2009) written in MATLAB 2018a (MathWorks, USA), after correction for the refractive index difference of the methacrylate window (5 mm thick) in the center of the image (see the center of the Figure 3.11a). Subsequently, the corneal and scleral surfaces are detected from the deformation images using a nearest-neighbor pixel algorithm (Bronte-Ciriza et al., 2021; De La Hoz et al., 2024). Surface detection consists of selecting/determining the central point of the surface (maximum deformation) and sequentially scanning the image in ±x-direction. In this second step, pixels close to the previously detected surface points are identified (at least three consecutive pixels with an intensity threshold). The segmented points are then fitted to a ninth-order polynomial to obtain a continuous interpolation of the data. The semi-automated segmentation process is applied to all images, allowing correction of specific images.

From the segmentation results, four deformation parameters are estimated: the maximum apex deformation, the temporal deformation, the deformation speed, and the arc length for all seven locations (corneal and scleral tissue). The parameters are estimated using a smaller size ($5.6\,mm$ in length centered at the apex) defined on the image (see dashed yellow rectangle in Figure 3.11b) instead of the total size calculated on the image. The maximum apex deformation is defined as the distance between the segmented line of the initial state and the highest concavity line at the apex (Figure 3.11c). The temporal deformation (temporal profile) of the apex displacement is defined as the relative distance (deformation state with respect to the initial state) of the apex point as a function of time. The deformation speed is the derivative value of the temporal deformation (displacement-time) curve, and the arc length is defined as the segmentation length inside the defined transverse size (dashed yellow rectangle, see Figures 3.11b and 3.11d).

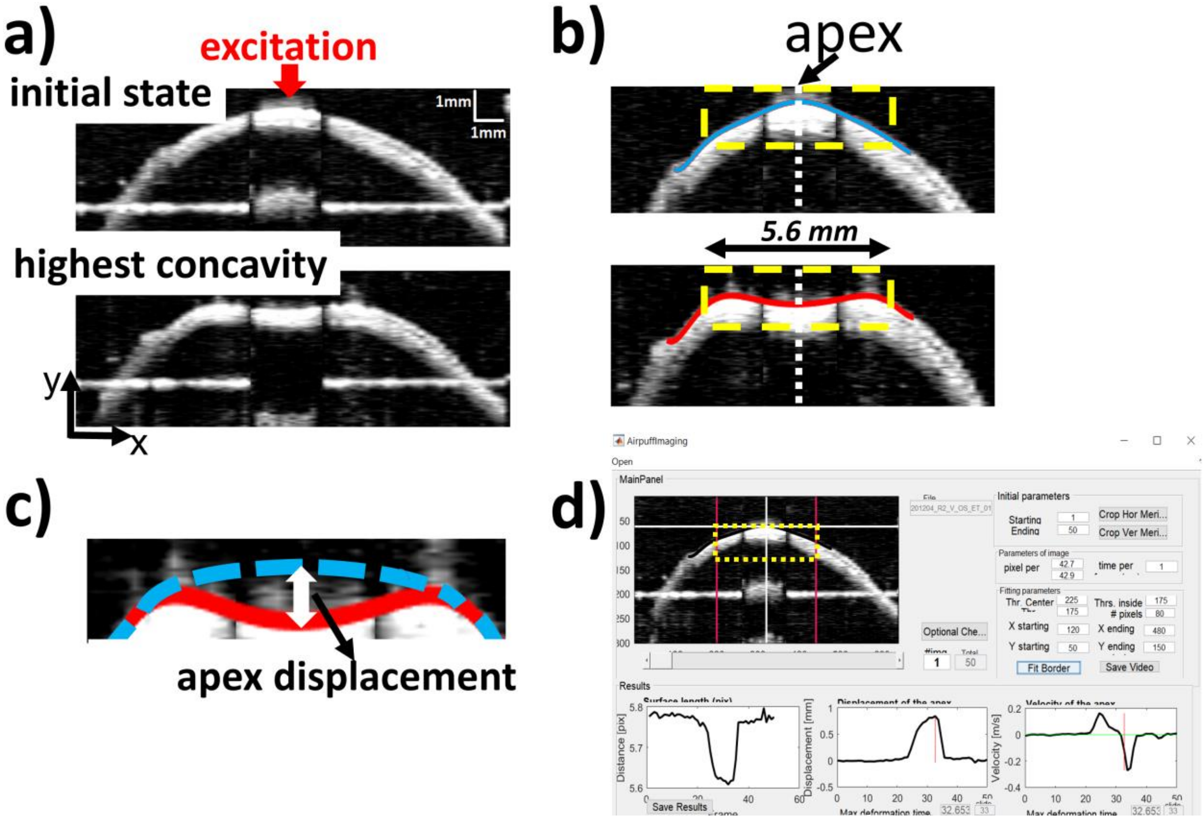

File 201204_R2_V_OS_ET_01

Initial parameters
Starting 1
Ending 50

Parameters of image
pixel per 42.7 42.9
time per 1

Fitting parameters
Thr. Center 225 175
Thrs. inside 175
pixels 80
X starting 120
X ending 480
Y starting 50
Y ending 150

#img 1
Total 50

Max deformation time 32.653 33

Figure 3.11: Figure. OCT air-puff deformation images and apex displacement estimation. a) Example of OCT images showing the resting and the maximum deformation positions of the scleral tissue during air-puff deformation measurements. The scale bar represents 1 mm in air. b) Detail of the segmented surfaces over the same OCT images are shown in the initial (blue line) and highest concavity (red line) states. The dashed yellow rectangle represents the defined transversal size (5.6 mm) in the image to calculate the deformation parameters. c) Displacement is defined as the distance between the resting curve (initial state) and the deformation curve during air-puff excitation. Displacement was measured along time. d) Screenshot of the MATLAB interface window, interface was used to read, segment all OCT images, as well as, to visualize the results. The figure shows the same segmented images and results used in the example in (a) and (b).

3.7. Optical Coherence Elastography methods

3.7.1. OCE measurement protocols

As with the air-puff protocols described above, the OCE measurements are performed by mounting the ocular globes in a custom-made holder and aligning the corneal/scleral locations with the sample arm of the OCT system (Figure 3.12a). A 25-gauge needle connected to a monitoring system is inserted through the optic nerve head to monitor IOP. The system measures the saline pressure at the tip of the needle and is adjusted to maintain IOP at 15 $mmHg$ during all experiments.

Samples are excited with the ACUS-OCE technique (see Section 3.5.2) to generate elastic waves on the sample surface (Figures 3.12b and 3.13b). OCE measurements were performed at five locations in each eye using multi-directional scan pattern (8 directions), see Figure 3.12c. Three repeated measurements are made at each site, 30 seconds apart to avoid wave coupling. The average of the measurements is used for calculation. The eyeball is kept hydrated with drops of BSS (saline solution) between measurements. Wave speed and thickness values are obtained from the images acquired (Figure 3.13a) by the ACUS-OCE system for each location and each of the 16 angles ($0° - 337.5°$ in steps of $22.5°$). Since the data are obtained from both left and right eyes, all measure speeds are inverted with respect to the vertical axis to consider them all as left eyes. In addition, corneal and scleral thicknesses are determined by automatic segmentation of OCT images at each tested location. The shear modulus (see Section 3.7.3) is estimated from mean phase speed and thickness data obtained from ACUS-OCE measurements at each tested location and on each of the 16 semi-axis (8 directions).

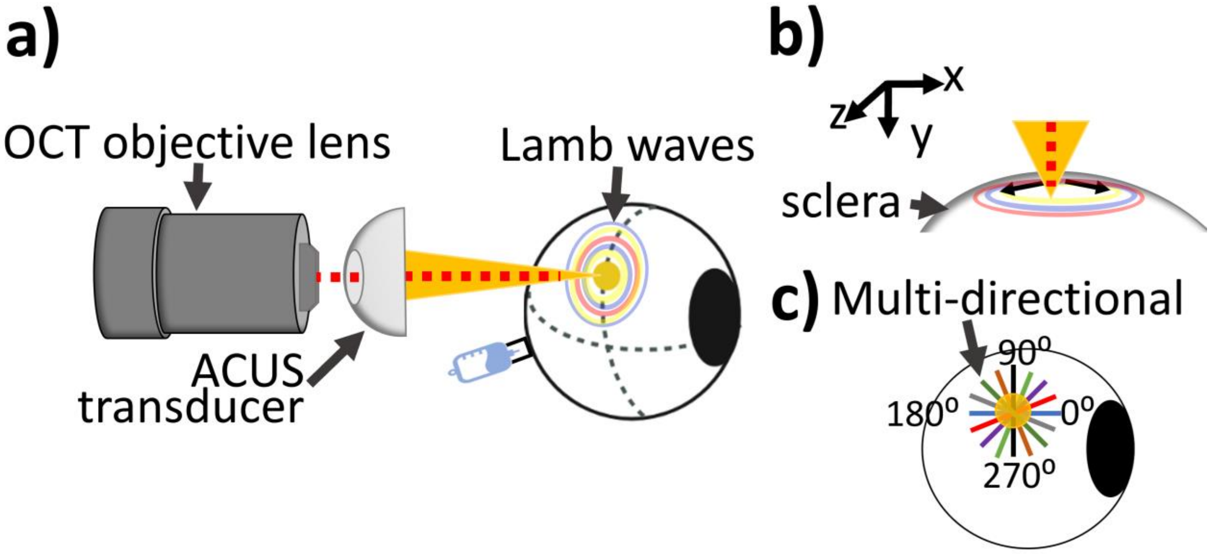

Figure 3.12: Schematic of the Optical Coherence Elastography measurements. a) Illustration of the placement of an experimental eye and the generation of waves over the scleral tissue. The Lamb waves propagate over the tissue surface at the same time as the tissue is scanned by the OCT system. b) Another perspective of the wave propagation (shown in multicolor) over the ocular tissue is shown. c) The colored lines indicate the 8 acquisition axes (directions) of the OCT system in a schematic eye. This image was published in (Villegas et al., 2024b), and is used with the permission of the authors

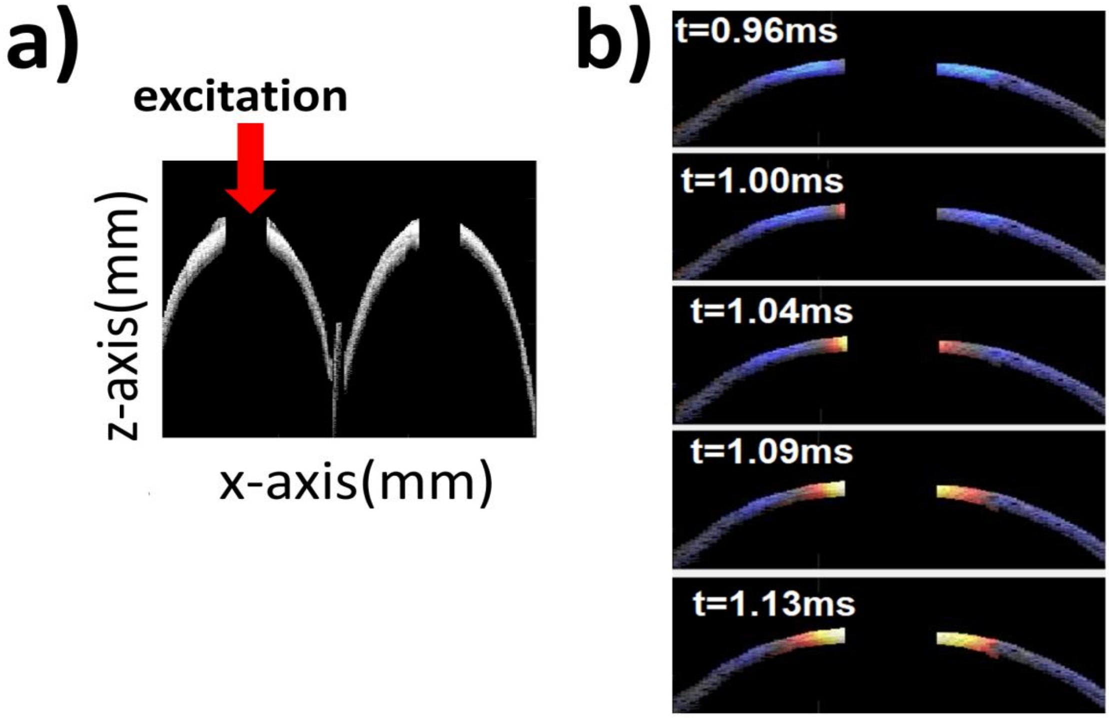

Figure 3.13: Images from the OCE system. a) Example of a OCT B-mode image of rabbit scleral tissue from two acquisition half-axes (two directions). The ultrasound excitation point is indicated by the red arrow. b) Images show the lamb wave propagation (colored pattern) on the scleral tissue surface over time.

3.7.2. Estimation of phase speed

The wave propagations (see Figure 3.13b) are collected in a three-dimensional dataset (x, z, t) (see Section 3.7.1) and the axial particle speed V_{xz} is obtained from the optical phase difference $\Delta\varphi_{xz}(x, z, t)$ between two consecutive A-scans at a given position using the equation (Zvietcovich et al., 2017a):

$$V_{xz}(x, z, t) = \frac{\Delta\varphi_z \lambda}{4\pi n \Delta t} \tag{3.2}$$

λ is the central wavelength of the light source (1300 nm), n is the refractive index of the sample for cornea n_{cornea}~1.376 and n_{sclera}~1.42 for sclera (Meek and Knupp, 2015; Nemati et al., 1996), and Δt is the temporal resolution ($\Delta t = 5\ \mu s$).

Mechanical waves are considered to propagate as in thin membranes, where the excitation wavelength is of the same order of magnitude as the membrane thickness. Then the perturbation generated in these membranes can be described as Lamb waves (Lamb, 1881) of the cornea and sclera, these membranes are subjected to a solid-fluid interface on the inner surface and to a free boundary condition on the outer surface.

Thus, the phase speed of these Lamb waves can be quantified using the previously reported Fourier estimators (Wang and Larin, 2014; Zvietcovich et al., 2022). In summary, the wave speed calculation performed in the space-time domain (Equation 3.2 and Figure 3.14a) is converted to the spectral domain by applying the 2D Fourier transform (Figure 3.14b). Lamb wave speed v_L can then be obtained using (Zvietcovich et al., 2020b):

$$v_L(x, z, \omega) = \frac{\omega}{\sqrt{\varphi_x^2 + \varphi_z^2}} \tag{3.3}$$

The transformed signal (Equation 3.3) is evaluated at the excitation frequency of $\omega = 2\pi f = 2\pi \cdot 2\,kHz$ to estimate the phase speed per each of the 16 semi-axes. Additionally, polar plots are used to present the phase speed (in m/s) as a function of the measured wave propagation, and to provide a visual assessment of tissue anisotropy (see Figure 3.14c).

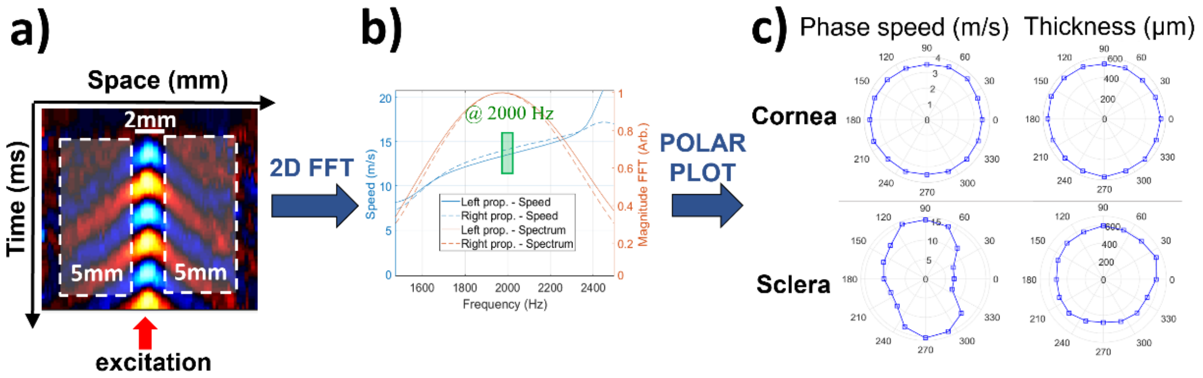

Figure 3.14: Corneal and scleral phase speed and thickness estimation. a) Example of a spatio-temporal map of wave propagation in the ocular tissue along one direction. The ultrasound excitation point is indicated by the red arrow. The dashed boxes (5 mm size along time) represent the boundaries used to calculate the phase speed. b) The calculated speed from the spatio-temporal map (show in blue), together with the Magnitude FFT (shown in orange) in function of the frequency, allows the phase speed estimation at a frequency of 2 kHz (shown as the green rectangle). c) Phase speed and thickness are presented in polar plots for each of the 16 measured semi-axes. This image was published in (Villegas et al., 2024b), and is used with the permission of the authors

3.7.3. Calculation of shear modulus

The phase speed v_{ph} of the Lamb waves at a given frequency is a parameter related to the elastic properties of the tissue (Rose, 1999; Viktorov, 1967). Lamb waves can be modeled using analytical approaches to find relationships between Lamb wave speed shear modulus, corneal thickness, and other parameters (Han et al., 2017; Kirby et al., 2017). In fact, Han *et al.* (Han et al., 2017) demonstrated the use of modified Rayleigh-Lamb frequency equation (mRLFE) together with phase speed to quantify the viscoelastic properties of the cornea.

The shear modulus is estimated from the mRLFE (see Equation E.4 in Annexes, Section E). This approach has been applied to phase speed data assuming, as first approximation, that corneal and scleral tissue are isotropic, homogenous, and viscoelastic material (Zvietcovich et al., 2020b). Although this model does not fully account for the anisotropy of the data since it will require a priori information of scleral biomechanics, it has been assumed tissue isotropy in a constrained region of interest and propagation direction as a first approximation to quantify direction-dependent elastic moduli for interrogating scleral anisotropy.

The shear modulus was calculated from phase speed and thickness data obtained from OCE measurements at each tested location and on each of the 16 semi-axis (8 directions) by solving the mRLFE at each radial direction. The Newton-Raphson optimization method (Scipy-Pyton v3, (Virtanen et al., 2020)) was used to find the roots of the mRLFE. The method is constrained to finding roots around $10\ kPa$ (values found in experimental studies (Schuldt et al., 2015; Sloan et al., 2014)).

The mRLFE (for more information, see the Annexes, Section E) is solved using excitation frequency of $2\ kHz$, tissue density of $988\ kg/m^3$, Poisson's ratio of 0.498, shear viscosity of $0.55\ Pa\ s$, vitreous fluid density of $1000\ kg/m^3$(water), wave speed in the vitreous fluid of $1500\ m/s$. Thickness is also included in the model. Both corneal and scleral thickness are determined by automatic segmentation of B-mode OCT images (Figure 3.13a) using an edge detection algorithm (Zvietcovich et al., 2022) at each eye location. The algorithm detects the external and internal surface of the tissue and measures the thickness averaged within a 5-mm lateral window located at each semi-axis. The measured thickness is corrected by the corresponding refractive indices (cornea n_{cornea}~1.376 and sclera n_{sclera}~1.42 (Meek and Knupp, 2015; Nemati et al., 1996)).

3.7.4. Mechanical tissue anisotropy quantification

Both corneal and scleral tissues are fibrous, which makes them mechanically responsive. Therefore, quantifying the mechanical anisotropy of these tissues is essential to understand their biomechanical response. The anisotropy of wave speed obtained from OCE in ocular tissues is assessed by calculating four parameters, (1) the degree of anisotropy (DA), (2) the normalized fractional anisotropy (NFA) (Couade et al., 2011; Singh et al., 2016b), (3) the maximum Modified Planar anisotropy coefficient (maxMPAC) (Lankford et al., 1950; Singh et al., 2016b), and (4) the major-axis angle (MAA) of the speed polar plots.

The degree of anisotropy DA is a parameter based on wavefront propagation in an anisotropic homogeneous elastic medium as defined by Thomsen (Thomsen, 1986). This fractional parameter was adapted as the difference between vertical $v_{L_{90°}}$ and horizontal $v_{L_{0°}}$ phase speed at each location, see Equation 3.4. For $DA < 0.2$ show weak-to-moderate anisotropy. The parameter is calculated by the following equation:

$$DA_{locatopm} = \frac{v_{L_{90°}} - v_{L_{0°}}}{v_{L_{0°}}} \tag{3.4}$$

The fractional anisotropy NFA is a single estimation of the anisotropy degree using average ($v_{L_{mean}}$), maximum ($v_{L_{max}}$), and minimum ($v_{L_{min}}$) phase speed values at each location, see Equation 3.5. NFA values close to zero show smaller speed differences and low anisotropy, while values close to 1 are associated with greater differences and high anisotropy.

$$NFA_{location} = \sqrt{\frac{(v_{L_{max}} - v_{L_{mean}})^2 + (v_{L_{min}} - v_{L_{mean}})^2}{{v_{L_{max}}}^2 - {v_{L_{min}}}^2}} \tag{3.5}$$

The spatial anisotropy is determined after calculating the modified planar anisotropy coefficient $MPAC_{\theta}$ which uses phase speed as a measure of the planar-transverse strain ratio, at each semi-axis θ_i:

$$MPAC_{\theta_i} = \frac{1}{2}(v_{L_{\theta_i}} - 2\, v_{L_{\theta_i+45°}} + v_{L_{\theta_i+90°}}) \tag{3.6}$$

In this case, values greater than 1 (high anisotropy) correspond to an "earing" behavior (the ripple at the edge of the polar graph that represents the effects of speed in planar anisotropy (Wright, 1965). The $maxMPAC$ (Equation 3.6) was determined for all locations in each eye.

Finally, the major-axis angle MAA in the phase speed polar plots is obtained using principal component analysis at all scleral locations. The phase speed data was processed using MATLAB R2021a (The MathWorks Inc., 2021) to return the principal components coefficients. The MAA corresponds to the direction of the first principal axis measured from the corneal limbus to the optic nerve head.

3.8. Mechanical testing and hydration methods

3.8.1. Tensile test protocols

Samples (from corneal or scleral tissue) are subjected to uniaxial tensile test to measure Young's modulus. Uniaxial tensile tests are performed using a UStretch (CellScale, Waterloo, Canada, see Section 3.4.1). Strips of rabbit and guinea pig eyes are stretched by applying axial elongation with a defined stretch magnitude. The stretch variation is the distance between clamps. The stretch magnitude is defined according to the type of material. For rabbit tissue, initial free length between the clamps is set to $6\,mm$ and stretch magnitude is set to $0.7\,mm$ (11.7% strain). For guinea pig tissue, initial free length between the clamps is set to $4\,mm$ and stretch magnitude is set to $0.6\,mm$ (15.0% strain). Strips are subjected to loading/unloading cycles test at a rate of $1.0\,mm/min$ with a preload force of $0.05\,N$ (rabbit tissue) and $0.02\,N$ (guinea pig tissue) during the first cycle only (see schematic Figure 3.15a). Preconditioning allows higher measurement repeatability and also simulates tissue normally exposed to IOP (Cheng et al., 2009; McKee et al., 2011; Shadwick, 1990). The force-displacement curves are stabilized by the final cycle, as previously reported (Elsheikh et al., 2010; Park et al., 2021). During the stretching, the strips are kept immersed in saline solutions (PBS or BSS), see Figure 3.15b. Force-displacement measurements at last cycle are used for calculation of stress-strain curves for all strips. A schematic protocol and a photograph of testing apparatus are included in Figure 3.15.

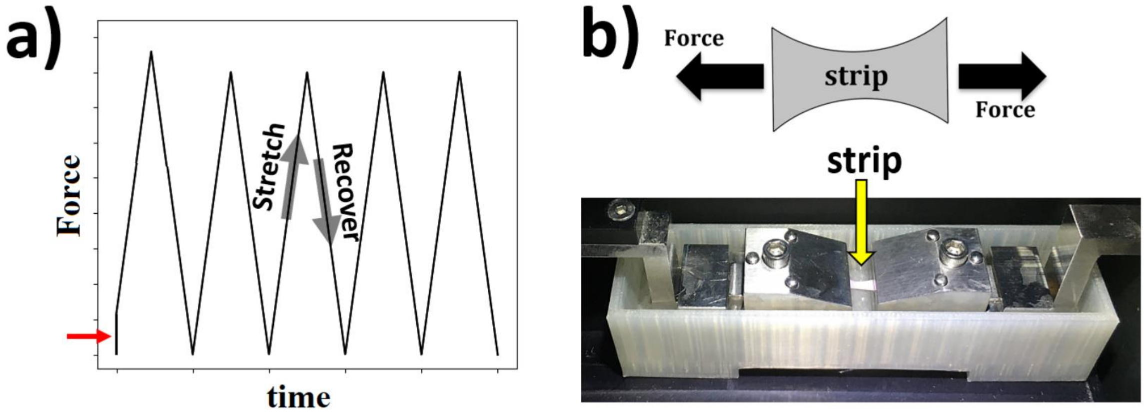

Figure 3.15: Stress-recovery protocol for tissue strips. a) Schematic of the experimental protocol for the stress-relaxation test. The tissue samples were subjected to the stretch-recovery test with an initial preload time indicated by a red arrow. b) The photograph shows the scleral strip held in place by clamps at the ends and in a container with saline solution.

3.8.2. Calculation of Young's modulus from stress-strain curves

The results of the mechanical tests (Section 3.8.1) are reported as variations of the applied force during the stretching phase of each cycle. Figure 3.16 shows an example of data obtained after scleral strip extensiometry. Force-time (Figure 3.16a) and force-displacement (Figure 3.16b) data are recorded during each axial test, and stress-strain (σ - ε) (Figure 3.16c) data are calculated. In each cycle, the displacement speed of the clamps is kept constant ($1.0\ mm/min$). The peak load values decreased progressively with each subsequent cycle until they converged after 5 cycles of preconditioning.

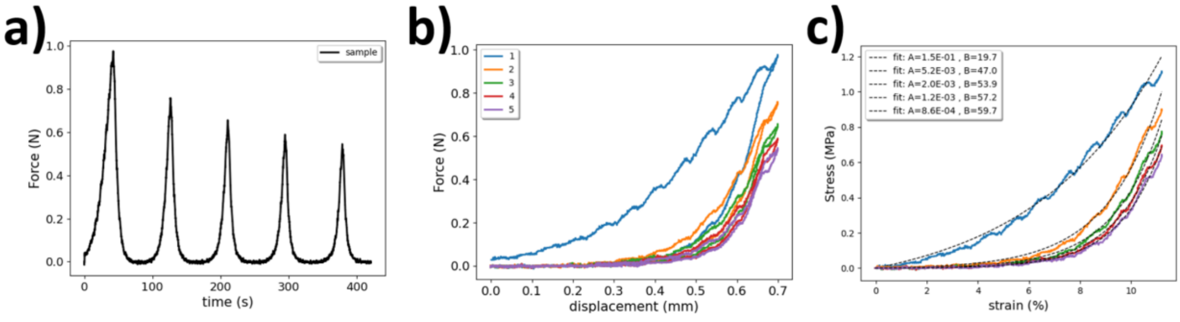

Figure 3.16: An illustrative example of the measured load-displacement cycles during uniaxial indentation of a scleral strip. a) Force-time curves are measured for each cycle, in the example 5 cycles. The duration of hold-ups in the load peaks and valleys are kept constant. b) Force-displacement curves show load/unload cycles (one color for each cycle). The displacement speed is kept constant. c) Stress-strain curves are obtained from force-displacement data. Only the load curves are adjusted to obtain the Young's modulus. The fitted constants for each cycle are shown in the upper left rectangle.

Tensile stress σ is calculated as the force applied F to the cross-sectional area ($t \cdot w$, thickness × width of the strip center), and the strain ε is determined as the ratio of strip elongation ΔL to the initial length Lo (Equation 3.7). Sample length and thickness (see Section 3.8.6) are measured using a caliper (analogue, Alca, 0.05 mm, 1-150 mm) and a micrometer (digital, Mitutoyo, model 293-240-30). The initial length is measured as a function of the clamp-to-clamp distance on the load cell. Thus, stress-strain curve provides a direct indication of specimen response by eliminating the effect of specimen size.

$$\frac{\sigma}{\varepsilon} = \frac{\frac{F}{t \cdot w}}{\frac{\Delta L}{Lo}} \tag{3.7}$$

The resulting stress-strain curves of the scleral tissue showed nonlinear behavior, so the data are fitted with the exponential function (Elsheikh et al., 2010; Fung, 1993, 1967):

$$\sigma = A(e^{B\varepsilon} - 1) \tag{3.8}$$

A and B in Equation 3.8 are the fit constants obtained by the Levenberg-Marquardt algorithm (SciPy, Python v3) (Virtanen et al., 2020) constrained to a region $A, B > 0$. This nonlinear least-squares algorithm finds the local minimum of a function, in this case Equation 3.8, by minimizing the sum of squares. In these experiments, only data from the load cycles of the stress-strain curves (see Figure 3c) are fitted.

The elastic modulus can be defined as instantaneous scleral stiffness as a function of a specific strain. Thus, the Young's modulus E is expressed as a derivative result of Equation 3.8 as:

$$E = \frac{d\sigma}{d\varepsilon} = AB(e^{B\varepsilon}) \tag{3.9}$$

3.8.3. Estimation of strain from IOP in rabbit eyes

To compare the Young's modulus obtained from rabbit scleral strips with intact eyes at a specific IOP (fluid pressure inside the eye), and stress-strain relationships are determined by approximations. The sclera of rabbit eyes is considered as a spherical shell of radius r and thickness t filled with vitreous humor (viscous liquid inside the eye, see Section 2.1). The fluid pressure difference ΔP inside the eye (the external pressure minus the internal pressure), just below the inner layer of the sclera, can be estimated by the Young-Laplace equation (Landau L and Lifshitz E, 1987) as:

$$\Delta P = \frac{2\gamma}{r} \tag{3.10}$$

where γ is the surface tension pulling away a section of the scleral surface.

Considering that the tension γ over the entire scleral thickness is similar to the stress produced along the scleral strips $\gamma \cdot t \approx \sigma$, see Section 3.8.2. Joining the Equations 3.8 and 3.10, and using Taylor series approximation, we obtain:

$$\frac{\Delta P\, r}{2t} \approx AB\varepsilon_{IOP}(1 + B\varepsilon_{IOP}) \tag{3.11}$$

The parameters used to estimate the physiological strain ε_{IOP} from Equation 3.11 are the axial length of rabbit eyes transformed in eye radius as $r = 8.12mm$ (Barathi et al., 2002), the normal range of rabbit IOP $15 \leq \Delta P \leq 25\, mmHg$ (Vareilles et al., 1977), scleral thickness $t = 315 \pm 48\, \mu m$ (see Table C.4 in Annexes), and fit constants $A = 0.0016 \pm 0.0012\, MPa$, $B = 59.6 \pm 10.9$. Scleral thickness and fit constants are obtained from experimental data for naïve scleral tissue (see data in Annexes, section C). The estimated strain was around $6\% \leq \varepsilon \leq 8\%$.

3.8.4. Tensile testing in combination with hydration process for scleral strips

The aim of this method is to evaluate the effect of dehydration/rehydration on tissue stiffness that may occur due to the tensile method itself (Hatami-Marbini and Pachenari, 2020; Hatami-Marbini and Rahimi, 2014), and/or to photo-crosslinking techniques (Doughty, 2000; Huang and Meek, 1999). In this test (see Figure 3.17), scleral strips $(3\, mm \times 20\, mm)$ were divided into two groups according to rehydration time: $40\, min$ and $100\, min$. The samples are dehydrated (during 24h, room temperature), rehydrated at 21^0C by instillation of $10\mu L/10min$ PBS solution and mounted on a uniaxial stretcher (see Section 3.8.1). All samples are tested after rehydration period rather than after dissection. During the rehydration period, strips weights are measured with a precision balance (digital, OHAUS EX124/AD, 0.1mg) every ten minutes. Strips are processed in a controlled environment at 21±2^{0}C and 37±1% humidity (digital, CLEWARE humidity sensor, 0.01^{0}C/0.01% RH) during all procedures.

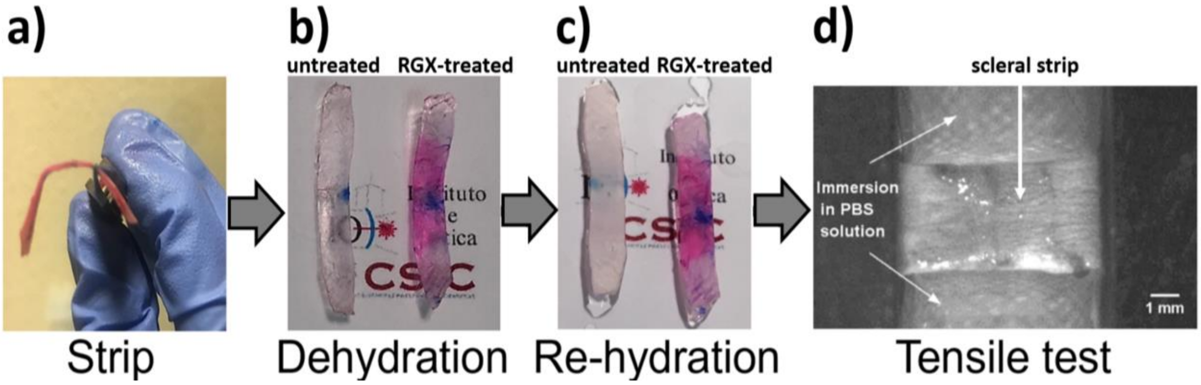

Figure 3.17: Schematic sequence of hydration-tensile test. a) Strips of untreated/treated scleral tissue were b) dehydrated (24 h), c) rehydrated during 40 min or 100 min, and d) mounted in a uniaxial stretcher.

3.8.5. Calculation of the swelling ratio and swelling rate

The effects of dehydration/rehydration are quantified by the swelling ratio, defined as the percentage of PBS uptake due to the increase in tissue weight. The swelling ratio is determined by the equation:

$$swelling\ ratio\ (\%) = \frac{W_{wet} - W_{dry}}{W_{dry}} x100 \tag{3.12}$$

In equation 3.12, the weights of scleral strips before W_{dry} (after 24h of dehydration) and after W_{wet} (during rehydration period) soaking in PBS solution are compared (see Section 3.8.4). Subsequently, the *swelling rate* $(\%/min)$ is estimated as the slope of the linear part of the swelling-time curves in units of percentage PBS uptake per minute (see Figure 3.18). The swelling rate quantified the speed of weight increase of the scleral strip.

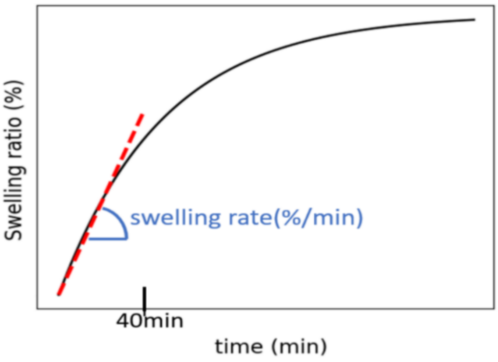

Figure 3.18: Representation of the shape of selling-time curve after a controlled PBS hydration of tissue strips. Swelling rate is calculated from the slope of the swelling-time curves. This image was adapted from (Villegas et al., 2024b), and is used with the permission of the authors.

3.8.6. Thickness, width and length data of strips

The thickness is measured at the center of each strip immediately before the tensile test (see Section 3.8.1). Thickness was carefully measured (three times, mean values were used) with a micrometer (digital, Mitutoyo, model 293-240-30). Mean values (coefficient of variation <3%) are used to quantify the cross-sectional area (thickness × width of the center of the scleral strip). During the hydration-tensile test (see Section 3.8.5), the weight of the strip is repeatedly checked twice between thickness measurements to be sure of the hydration value of the strip before it was mounted in the tensile test.

3.9. Second Harmonic Generation methods

Corneal and scleral tissues are placed on a glass slide, covered with BSS (saline solution) and protected with a coverslip placed over the specimen. The slides are placed between the objectives of a customized SHG microscope (see section 3.5.4). Briefly, the beam is scanned across the sample tissue and focused with a high numerical aperture objective. The focus is translated through the sample along the optical axis using a motor. Frequency-doubled light is collected in the forward and backward directions. Tissue collagen images ($150\,\mu m\, x 150\,\mu m$) are collected through the depth of the tissue (see Figure 3.19).

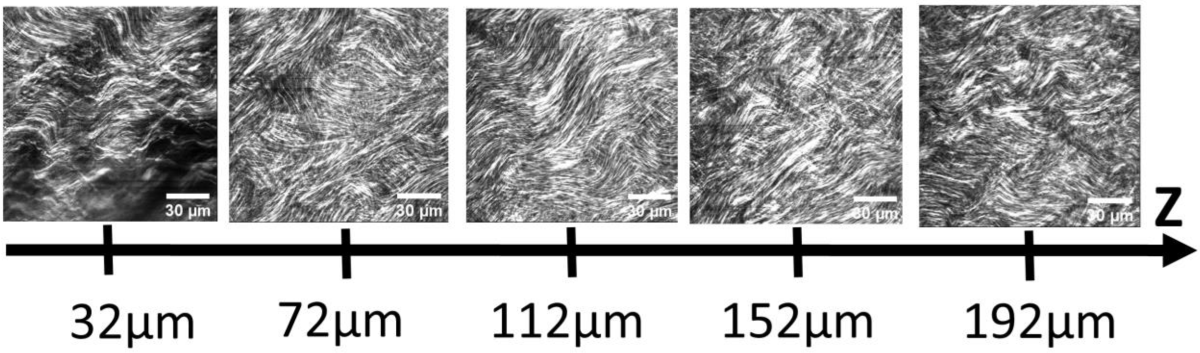

Figure 3.19: Example images of collagen fibers in the rabbit sclera. The images were taken from the inside of the scleral tissue at 40 microns steps through the depth of the tissue. Depths vary by region and animal model. For example, we found a mean scleral thickness of 1070 µm for porcine eyes and 340 µm for rabbit eyes in the same region (nasal posterior).

Changes in collagen organization along the tissue depth are determined by image processing. The SHG images are analyzed using MATLAB code (Germann et al., 2018). From each set of images, the order coefficient (OC) was quantified. The OC (Germann et al., 2020, 2018) allow the quantification of the uniformity of the collagen fiber orientation and the straightness of the fibers along the depth. In summary, after applying a Fourier transform to each image, the points with the highest Fourier coefficient in the transformed image are selected, counted and grouped into a set of angular windows (see Figure 3.20). If all the points are in two windows (due to the symmetry of the Fourier transform), the coefficient will be high. On the other hand, if the points are distributed over all angular windows, the coefficient will be low. The analysis windows are set with an angular width of 7.5° and an angular offset of 1.5° between adjacent windows. OC values are normalized with 0 representing a uniform distribution of collagen angles in all windows and 1 representing all collagen fibers being highly linear (oriented in one direction).

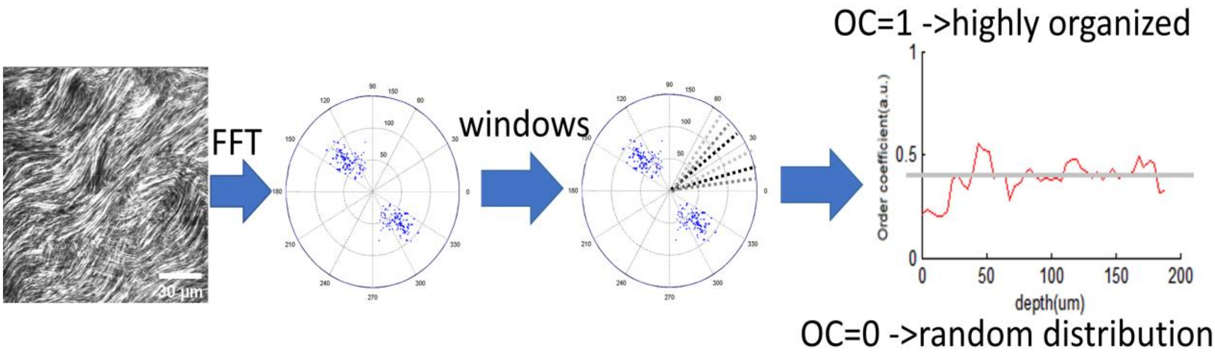

Figure 3.20: Quantification of the collagen fibers orientation. The order coefficient (OC) is a measure of fiber orientation and straightness. Fourier transform is applied to each image. Then points with the highest Fourier coefficient are grouped into angle windows. OC values close to 0 indicate a uniform distribution and values close to 1 indicate a preferential orientation of collagen fibers.

3.10. *In vivo* methods

3.10.1. Form-deprivation myopia in guinea pigs

FDM is induced in guinea pigs (see Section 3.2) by placing a diffuser in one eye for 10 weeks (starting on postnatal day 14). To facilitate diffuser placement, animals are anesthetized by inhalation (isoflurane, 1.5-2% oxygen) for 1-2 minutes. All diffusers are handmade translucent hemispheres molded in plastic sheets (0.3 *mm* in thickness) and characterized to have suitable dimensions and to transmit 53±5% of the light measure by digital illuminance meter (ILM 1332A, RS PRO, 0.01-

200000 lux, 0.1 lux). The diffusers are attached to one of the guinea pigs' eyes using glue and two rings of Velcro material. One Velcro ring is attached to the diffuser and the other is symmetrically attached to the fur surrounding the eye, as in previous experiments in guinea pigs (El-Nimri and Wildsoet, 2018; Howlett and McFadden, 2006). The Velcro allows the diffuser to be removed for cleaning or measurement of the eye. The claws are occasionally bandaged to ensure that the diffusers remain in place. Animals were monitored for the 12-hour light period. Ocular biometry (Section 3.10.2) and retinoscopy (Section 3.10.3) were measured in both eyes at 0, 2, 4, 6, 8, and 10 weeks during myopia induction.

3.10.2. Estimation of ocular axial lengths

Ocular axial lengths in guinea pig eyes are obtained *in vivo* from the OCT images captured with the custom-developed SS-OCT 3D Biometer (see Section 3.5.3). Awake animals are immobilized (wrapped in a towel) and held in the proper position to align with the optics of the instrument (see Figure 3.21). To align the animal's eye, a live visualization of the internal structures is used in combination with a homemade motion bed set to move up/down and forward/backward, and the animal's attention is occasionally drawn by hand clicks. To reduce accommodation, eyes are dilated with 1 drop of tropicamide (ophthalmic solution, 10 mg/ml, Alcon Healthcare S.A.) 20-30 minutes before measurement. Form-deprived (FD) and fellow eyes were measured during myopia induction period.

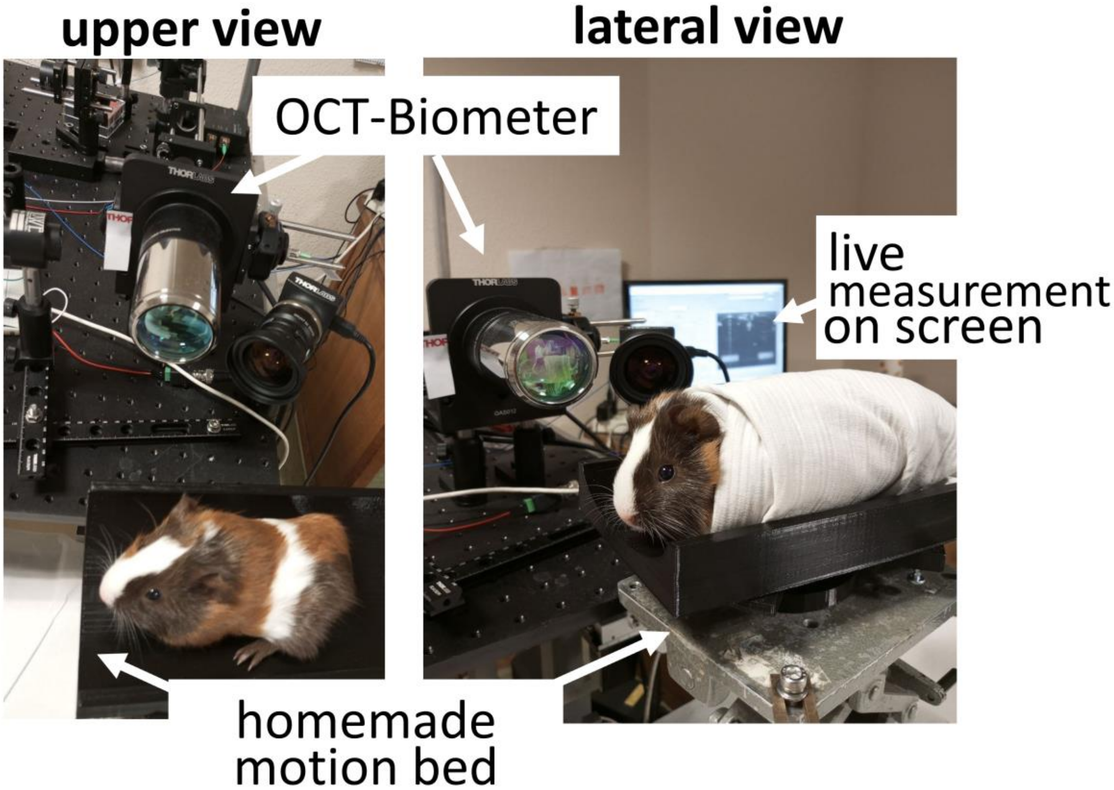

Figure 3.21: Photographs of guinea pigs during OCT 3D Biometer measurement. Animals were placed in a homemade bed and the eye was aligned coaxially with the OCT scanning beam.

The axial dimensions of the eye are obtained from the signal of several OCT image scans. Individual eye structures were determined from a series of 10 images around the central raster scan (see Section 3.5.3). MATLAB code (Curatolo et al., 2020b; Urizar et al., 2023) can be used to visualize the eye structures in the B-scans (Figure 3.22a) as well as the corresponding overlapped signal from the central pixels (Figure 3.22b). Manual border identification is performed using the peak positions of the mean signal of the central pixels (10 pixels). The signal peaks are associated with the surface of the inner eye structures. The axial length (AXL) is measured as the distance from the outer corneal surface to the retinal pigment epithelium (inner limiting membrane of the retina) (Hitzenberger, 1991; Schmid et al., 1996). The distance value is then corrected for the refractive indices (cornea: 1.376, vitreous humor: 1.3346 and lens: 1.401 (de Castro et al., 2020; Pérez-Merino et al., 2017) and the previously measured pixel resolution of $6.9\ \mu m/pix$ (Urizar et al., 2023; Villegas et al., 2023a). OCT measurement is repeated three times in each measurement session per eye.

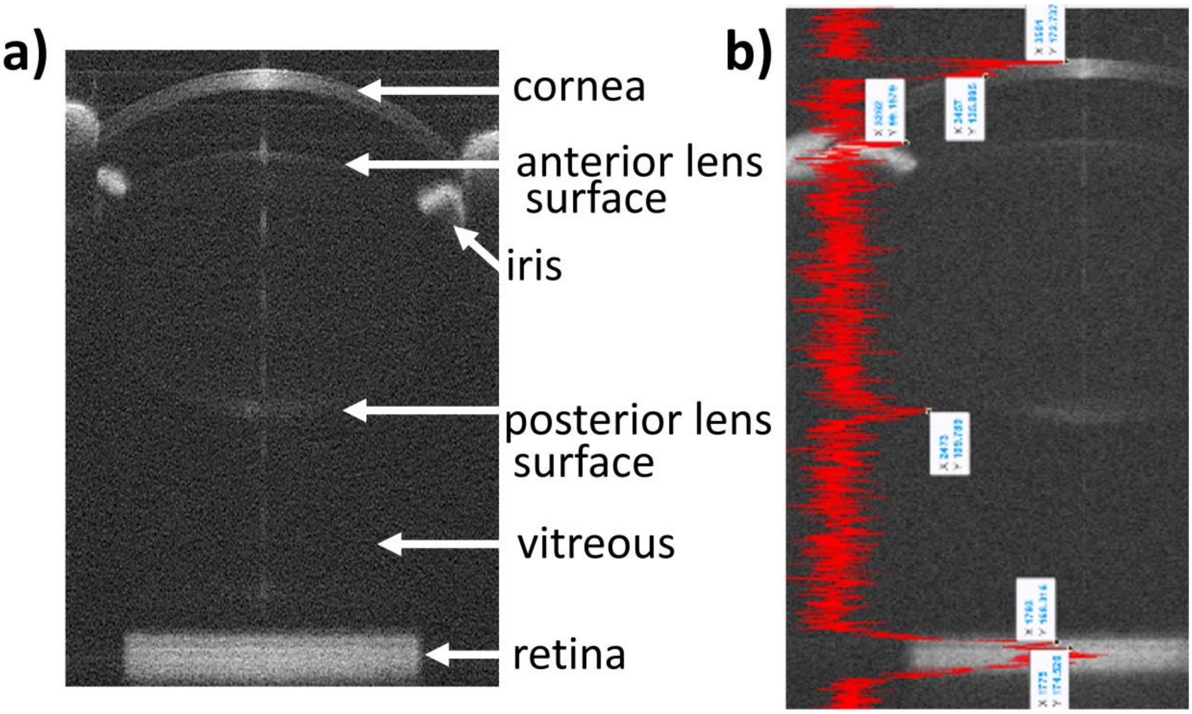

Figure 3.22: Image of a guinea pig eye obtained by SS-OCT 3D Biometer. a) Shown is the image of an eye where internal structures of the eye can be identified including corneal surfaces, lens surfaces and retina. b) Ocular axial dimensions of the eye were measured by superimposing the signal of central pixels on the image of the eye.

3.10.3. Retinoscopy and estimation of refractive error

Cycloplegic retinoscopy is a standard procedure to determine and quantify refractive error in patients with totally paralyzed accommodation (cycloplegic). In retinoscopy, a beam of light is directed to illuminate the retina, and the examiner observes the reflections in the pupil (see Section 3.4.2). A cycloplegic eye is under the influence of a pupil-dilating agent. Pupil dilation is controlled by retraction of Müller's muscle, trabecular meshwork and vascular smooth muscle. In this thesis, we have used a commercial streak retinoscope (model 18200, The Welch Allyn, NY, USA) to measure objective refraction of guinea pig eyes. For these measurements, eyes are dilated with 1 drop of tropicamide (ophthalmic solution, 10 mg/ml, Alcon Healthcare S.A.) 20-30 minutes before retinoscopy.

Guinea pigs are immobilized by wrapping them in a towel to facilitate alignment as in Figure 3.23. The examiner sits in front of the guinea pig holding the retinoscope and trial lenses. The guinea pig's eye is then aligned on the same axis as the retinoscope (optical axis), which is coaxial with the examiner's eye, see section 3.4.2. Looking through the peephole of the retinoscope, the examiner observes the reflexes in the guinea pig's pupil. A 360° sweep of the entire pupil (in all orientations/meridians) is made with the light streak, clockwise (by rotating the handle) and using a plane mirror effect (lowest position), see Figure 3.3a. At each orientation, a reflex is observed. A principal meridian is detected when the reflex was continuous (no "break").

For neutralization, the reflex is neutralized (see Figure 3.4) in the pupils of the guinea pigs using positive spherical lenses (in the case of WITH motion reflex) and using negative spherical lenses (in the case of AGAINST motion reflex). The spherical lenses are changed until the reflex filled the guinea pig' pupil and no longer moved (neutralized meridian). The dioptric equivalent of the working distance (distance between the patient's eye and the examiner's eye) is subtracted from the gross power measurement. The net measurement is reported as: lens power (in diopters) minus working distance (in diopters) at the neutralized meridian. This method is often used in children or to avoid holding more than one lens at a time, as in guinea pigs. In this work, these measurements have been conducted with the assistance of Paula Olalla Perez (technician).

To easily compare refractive measurements, the spherical equivalent (SE) is determined per eye. SE is a single number representation of an eye's refractive error. It was determined by the spherical component power (S) and cylinder component power (C), as (Enaholo et al., 2023): $SE = S + C/2$.

For example, supposes guinea pig's eye was neutralized with +3/+5 spherical lenses at 180/90 meridians (vertical/horizontal). A gross measurement is recorded per meridian as: $+3.0s \times 180$ $+5.0s \times 90$. The corrected net refraction (~ 0.67 meters correspond to $1.5\ D$, see Section 2.2.2) is: $+1.5s \times 180$ $+3.50s \times 90$. To indicate the approximate net ametropia of the eye, the measurement is then transformed to plus cylinder form: $1.5s\ + 2.0c \times 90$. Thus, the SE is $2.5\ D$. All measurements are given in diopters. The small letters (s: spherical and c: cylindrical) represent the type of lenses used for neutralizing.

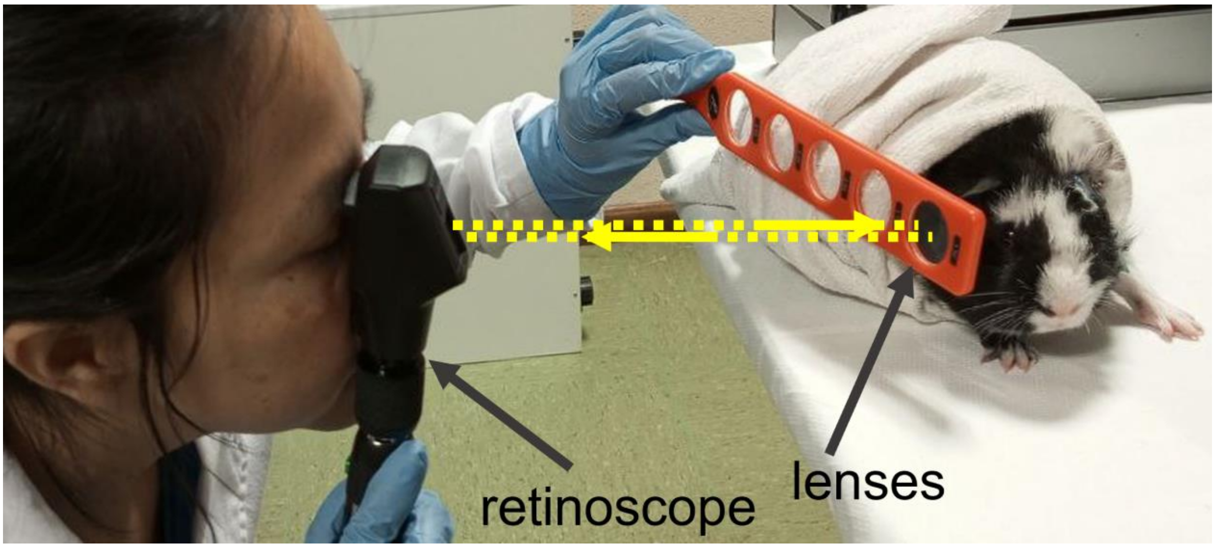

Figure 3.23: Photograph of a guinea pig undergoing retinoscopy. The guinea pig is restrained with a towel and placed in front of the examiner. The retinoscope projects a beam of light and the examiner observes the reflections in the guinea pig's pupil through a peephole. The lenses of a rack were changed until each principal meridian was neutralized (the reflection filled the guinea pig's pupil).

3.11. Proposed methods for myopia treatment

3.11.1. Photo-crosslinking method: Rose Bengal with green light

The Rose Bengal with green light crosslinking (RGX) method uses a solution of 0.1%(w/v) Rose Bengal (Sigma-Aldrich, 95 % pure, Milwaukee, WI) in PBS and a 532-nm green laser at $200\,mW/cm^2$ irradiance (FPYL-532-200T-FC105-LED, Frankfurt Laser Company, Friedrichsdorf, Germany). The marked scleral area is immersed in Rose Bengal solution for $120\,s$, irradiated for $200\,s$, immersed again in Rose Bengal solution for $30\,s$, and irradiated for another $200\,s$ (Cherfan et al., 2013), for a total treatment of $9\,min$ and $10\,s$ (see illustration in Figure 3.24). The total energy fluence rate was $80\,J/cm^2$.

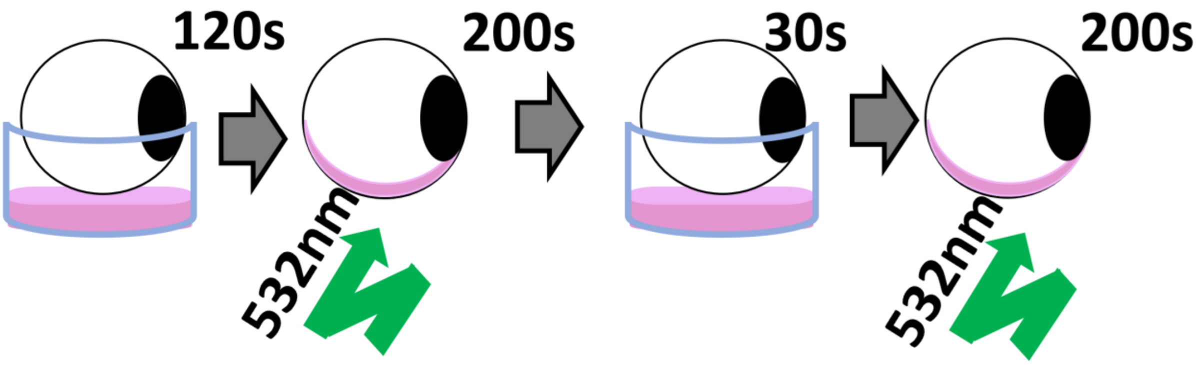

Figure 3.24: Illustration of RGX crosslinking method. The eyes were immersed in 0.1% RB for 120 s, irradiated with 523-nm green light for 200 s, immersed again in RB solution for 30 s, and irradiated for another 200 s.

The green laser was coupled to a fiber (105 μm) and light was collimated by a lens that provided a measured output irradiance of 200 mW/cm^2 measured by a power meter (PM100A, Thorlabs with power sensor of $200-1100\,nm$ wavelength, $50nW-500\,mW$ power range) on a 10-mm diameter surface. The profile of the laser is gaussian (FWHM=7.3mm, $1/e^2$= 11.4mm), i.e. 76.2% of the peak power at 10 mm radius.

3.11.2. Photo-crosslinking method: riboflavin with UVA light

The riboflavin with UVA light crosslinking (UVX) method uses a 0.1%(w/v) riboflavin solution (Ribocross TE, IROS Srl, Napoli, Italy) and a 365-nm UVA lamp at $3mW/cm^2$ (UV-X1000, IROC, Institute for Refractive and Ophthalmic Surgery, Zurich, Switzerland). The marked scleral area is instilled with riboflavin solution every 5 min for 30 min, and then riboflavin is instilled every 5 min with UVA irradiation for an additional 30 min (Wollensak et al., 2003), for a total treatment of 60 min (Figure 3.27). The total energy fluence rate was 5.4 J/cm^2.

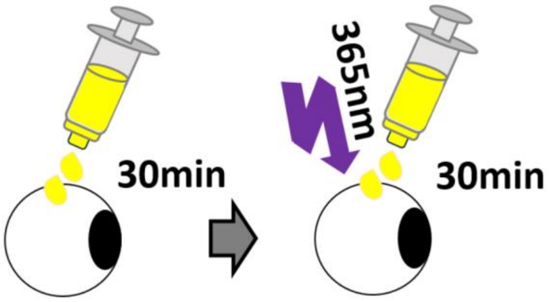

Figure 3.25: Illustration of UVX crosslinking method. The eyes were instilled with 0.1% riboflavin for 60 min and irradiated with 365-nm UVA light for 30 min.

The UVA lamp has a homogenous beam profile with a diameter of $9\,mm$. The output irradiance was measured by a power meter (YK-34UV, Lutron, $290-390\,nm$ wavelength range, $1.99\ -19.99\,mW/cm^2$ power range) to obtain $3\,mW/cm^2$ on the 10-mm diameter surface of the sample.

3.11.3. Pharmacological treatment: atropine

This treatment consists of daily instillation of one drop of atropine solution (ophthalmic, Colirofta, 10 mg/ml, Alcon Healthcare S.A.) into the eye for 10 weeks.

3.11.4. Pharmacological treatment: latanoprost

This treatment consists of daily instillation of one drop of latanoprost solution (ophthalmic, Xalatan, 50 μg/ml, Pfizer GEP S.L.) into the eye for 10 weeks.

4. RESULTS

This chapter presents the results of the thesis. For clarity, the results have been divided into four different subchapters. The first subchapter is about scleral biomechanics using Air-puff Deformation Imaging, the second subchapter is about scleral biomechanics using Optical Coherence Elastography, the third subchapter is about scleral biomechanics after scleral crosslinking, and the last subchapter is about scleral biomechanics and biometric measurements after myopia induction.

4.1. Scleral Biomechanics using Air-Puff Deformation Imaging

This subchapter presents protocols and results of *ex vivo* experiments on the entire globe of porcine and rabbit eyes using OCT air-puff deformation imaging technique. The biomechanics behavior of corneal and scleral tissue was quantified by measuring the maximum apex deformation, the deformation speed, and the arc-length.

This subchapter is based on the contributions of the author to two papers.

First, the paper entitled "Estimation of scleral mechanical properties from air-puff optical coherence tomography" published in Biomedical Optics Express (2021). The authors of the paper are David Bronte-Ciriza, Judith S. Birkenfeld, Andres de la Hoz, Andrea Curatolo, James Germann, Lupe Villegas, Alejandra Varea, Eduardo Martínez-Enríquez, Susana Marcos. The author of this thesis (1) performed part of the experimental measurements in this paper, (2) developed a MATLAB interface from previously written routines to easily handle the OCT images, (3) obtained the resulting parameters from half of the measurements.

Second, the paper entitled "A simple computational model for scleral stiffness assessments via air-puff deformation OCT" published in Frontiers in Bioengineering and Biotechnology (2024). The authors of the paper are Andres de la Hoz, Lupe Villegas, Susana Marcos and Judith S. Birkenfeld. The author of this thesis (1) performed the experimental measurements in this paper, (2) developed a MATLAB interface from previously written routines to easily handle the OCT images, (3) obtained the resulting parameters from all the experimental measurements, (4) analyzed the results from the experimental measurements.

In addition, the author of this thesis presented the following contributions using the same air-puff system: *oral presentation* at 17th Edition of the Scientific Seminars of the Optical Society on December 17, 2020 (Virtual) with the title "Comparison of scleral biomechanics in rabbit and porcine models using OCT air-puff deformation imaging", and *poster presentation* at Optics and Photonics for scientific progress 2021 of the University of Surrey Institute on April 13-14, 2021 (Virtual) with the title "Investigation on scleral biomechanics in rabbit model using OCT air-puff deformation imaging with two excitation configurations".

A summary of the above contributions is presented in this subchapter.

4.1.1. Protocols

4.1.1.1. Preparation of porcine and rabbit eyes

Five enucleated porcine eyes (see section 3.1.1) and four enucleated rabbit eyes (see section 3.1.2) were obtained and processed (less 48-hours postmortem). Seven locations (1 corneal, 6 scleral) were identified and marked: central cornea (C), equatorial nasal (EN), posterior nasal (PN), equatorial temporal (ET), posterior temporal (PT), superior (S) and inferior (I) sclera as displayed in Figure 4.1a. The EN, ET locations were placed at 10 mm (porcine eyes) and at 7 mm (rabbit eyes) from the limbus (along equatorial axis, red line in Figure 4.1a) and PT, PN locations were placed at 13 mm (porcine eyes) and 10 mm (rabbit eyes) from limbus along central meridional axis (green line in Figure 4.1a).

Animal model	Number of eyes	Method	Resulting parameter
porcine	5	OCT air-puff test (section 4.2.2) AP2 =15.4 kPa IOP= 15 $mmHg$	maximum apex displacement, temporal apex displacement, temporal apex speed, arc length.
		Finite element simulations (section 4.2.2)	Young's modulus
rabbit	4	OCT air-puff test using two air-puff configurations (section 4.2.2) AP1 = 7.8 kPa, AP2 = 15.4 kPa	maximum apex displacement, temporal apex displacement, temporal apex speed, arc length

		IOP = 15 $mmHg$	

Table 4.1: Overview of the different experiments and data collection. AP1: air-puff pressure 1. AP2: air-puff pressure 2.

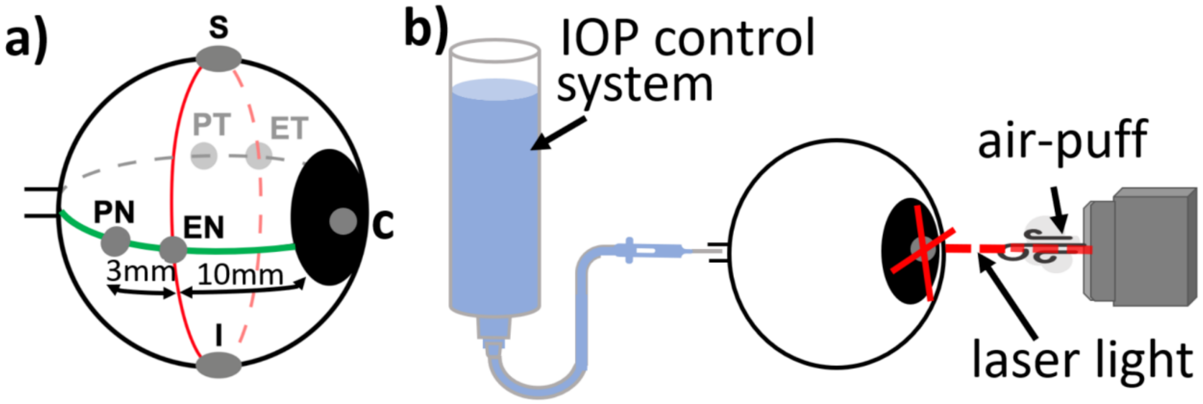

Figure 4.1: Schematic representation of an *ex vivo* ocular globe and OCT air-puff test. a) Seven locations were marked over each *ex vivo* porcine and rabbit eye for air-puff excitation. The gray dots represented the locations: central cornea (C), equatorial nasal (EN) and temporal (ET) sclera, posterior nasal (PN) and temporal (PT) sclera, superior (S) and inferior (I) sclera. b) Eye was mounted in front of the OCT air-puff system. The intraocular pressure (IOP) of the eye was held constant by a water column system with a needle through the optical nerve. Measurements were collected over two orthogonal directions (red lines over cornea).

4.1.1.2. Air-puff parameters after corneal and scleral measurements

Ocular globes were mounted in the customized holder and the corneal/scleral locations were aligned to the sample arm of the OCT air-puff system (see Figure 4.1b and Section 3.5.1). IOP was maintained at 15 mmHg during all experiments (see Table 4.1). Each location was deformed after air-puff excitation while OCT images were collected (see Section 3.6.1). The corneal and sclera apex deformation as function of time (temporal deformation), deformation speed, the maximum apex displacement, and the arch length values were obtained from the images acquired by the OCT system for each location (C, EN, PN, ET, PT, S, I) in horizontal and vertical meridians. Finally, the Young's modulus was estimated at 10% strain (see Section 3.6.2) after comparing the simulated apex displacement from the finite element modeling with the experimental data (from porcine eyes only).

4.1.1.3. Statistical analysis

Statistical analysis was performed using IBM SPSS (Version 25.0, , Armonk, NY: IBM Corp). Pairwise comparisons between the maximum deformations at different location were done using the non-parametric Friedman test and the repeated measures procedure ANOVA. Bonferroni adjustment was used for multiple comparisons. Significance was set at p-value of 0.05. All values in bar plots are indicated as mean± standard deviation.

4.1.2. Evaluating Biomechanics with Air-Puff Deformation Imaging

4.1.2.1. Comparison of maximum apex deformation in porcine and rabbit eyes

The maximum displacement of the apex was compared for porcine eyes (see Figure 4.2a) and rabbit eyes (see Figure 4.2b) at the same locations. The deformation depended not only on the location, but also on the animal model (e.g., rabbit and porcine have different tissue thicknesses) and the air-puff outflow force (AP1, AP2). In porcine eyes, the highest values were found for the cornea ($0.98 \pm 0.10\, mm$), inferior ($0.92 \pm 0.26\, mm$) and superior ($0.83 \pm 0.19\, mm$) sclera using AP2 configuration. Lower values were measured for the equatorial and posterior scleral locations (see Table 4.2). In rabbit eyes, the largest deformations after AP1 configuration occurred in the cornea ($0.86 \pm 0.02\, mm$) and the equatorial sclera (ET:$0.86 \pm 0.04\, mm$, EN:$0.82 \pm 0.02\, mm$). Lower values were measured in the remaining scleral locations (S, I, PN PT), ranging from $0.58\, mm$ to $0.76\, mm$ (see Table 4.2). Using the same AP2 configuration, the maximum deformation in rabbit eyes was different from that in porcine eyes at the same locations. The highest values were found for EN (0.98±0.02 mm), cornea ($0.90 \pm 0.04\, mm$) and inferior ($0.86 \pm 0.05\, mm$). The values were in the range of $0.63\, mm$ to $0.83\, mm$ for the remaining scleral locations (ET, PN, PT, S, see Table 4.2). In rabbit eyes, deformations amplitude increased by 25% after the high-pressure configuration (AP2) at all locations, except at ET location which instead significantly decreased ($p<0.01$) by 26% (yellow arrow in Figure 4.2b).

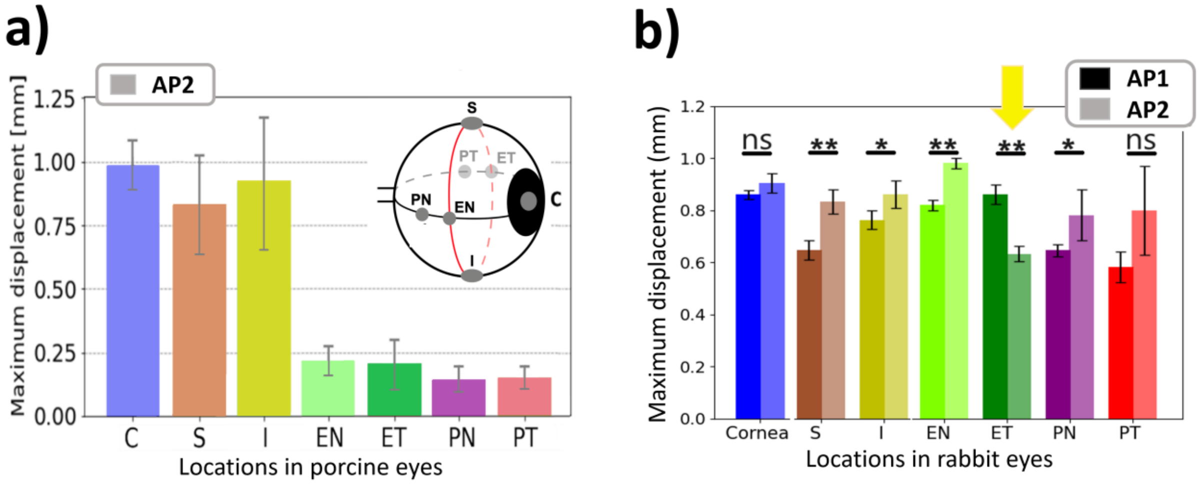

Figure 4.2: Maximum displacement of the apex at different locations in porcine and rabbit eyeballs. a) Bar chart of the maximum deformation measured in five porcine eyes. The air-puff configuration had a pressure of 15.4 kPa (AP2). b) Bar plot of the maximum deformation in four rabbit eyes. Two air-puff configurations of 7.8 kPa (AP1) and 15.4 kPa (AP2) were used. Higher values were measured after AP2 configuration except to ET location (see yellow arrow) The p-values are shown as asterisks, where *: $p<0.05$, **: $p<0.01$, *‘ns’*: non significance ($p>0.05$). Colors differentiate the 7 locations in the eye: C (cornea), S(superior), I (inferior), EN (equatorial nasal), ET (equatorial temporal, PN (posterior nasal), PT (posterior temporal). The IOP was maintained at 15 mmHg for all eyes. Figure (a) was adapted from: (Bronte-Ciriza et al., 2021), and is used with the permission of the authors.

	Location	Maximum displacement (mm)	
		Porcine tissue	**Rabbit tissue**
Cornea	**C**	0.980.10	0.90±0.04
Sclera	**S**	0.83±0.19	0.83±0.04
	I	0.92±0.26	0.86±0.05
	EN	0.21±0.06	0.98±0.02
	ET	0.20±0.10	0.63±0.03
	PN	0.14±0.05	0.78±0.10
	PT	0.15±0.04	0.80±0.17

Table 4.2: Mean values ± standard deviation of apex maximum displacement. The deformation measurement was performed using the AP2 configuration. Measurements were taken at seven marked points (C, S, I, EN, ET, PN, PT) on the surface of the porcine and rabbit eyeballs.

4.1.2.2. Comparison of displacement of the apex in porcine and rabbit eyes

Displacements were determined as a function of the time for all eyes at all locations. Maximum deformation was quantified from these displacement-time curves (see Section 4.2.2 and Section 3.6.3) at ~16 *ms* for porcine eyes and ~31 *ms* for rabbit eyes. By a visual inspection, higher deformations were observed at C, S, I locations in porcine eyes (see Figure 4.3a) and at ET, C, I in rabbit eyes (see Figure 4.3b).

Normalized displacement-time curves (Figures 4.3c and 4.3d) showed differences between corneal (blue line) and scleral (black line) tissues in both animal models. It was found a greater initial displacement in cornea than in sclera. A greater initial displacement was observed in the cornea than in the sclera. In addition, the return displacement after maximum was longer in the sclera than in the cornea in porcine eyes. In contrast, Figure 4.3d shows the same return displacement in rabbit eyes.

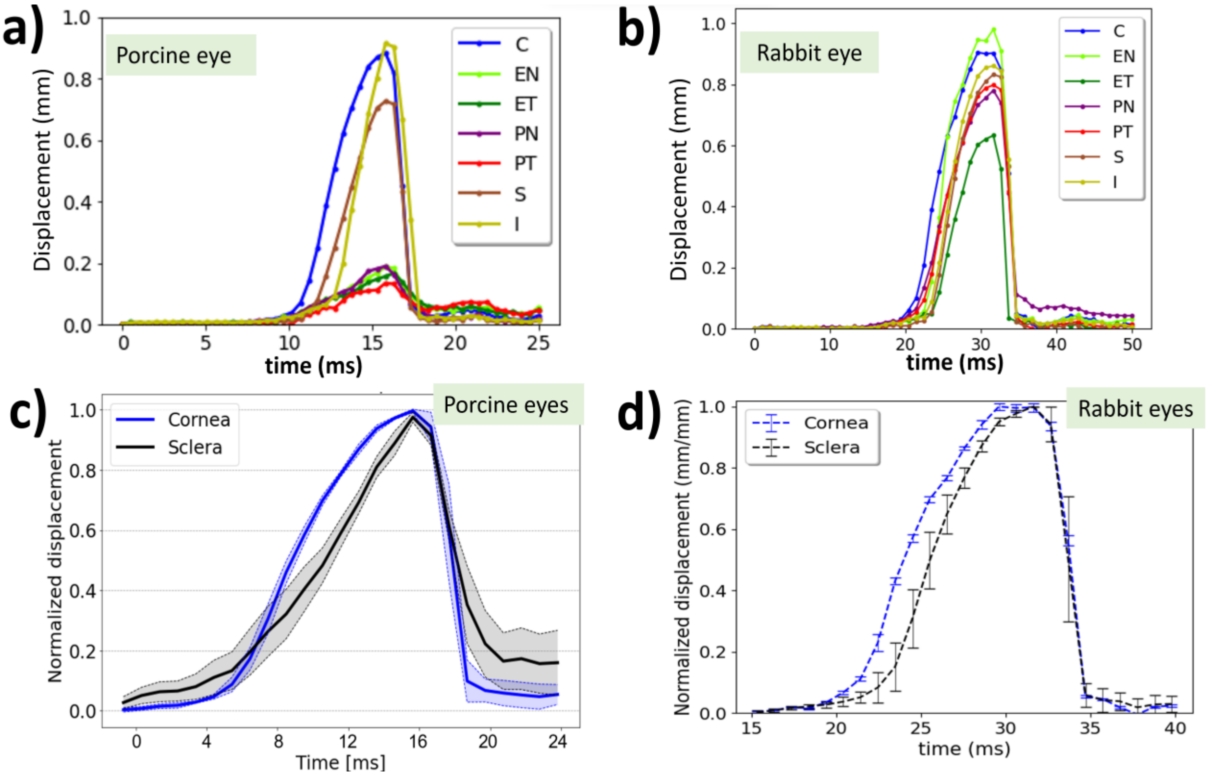

Figure 4.3: Apex displacement versus time curves in porcine and rabbit eyes. Displacement measurements as a function of time are shown for a sample porcine (a) and rabbit (b) eye at the seven locations using the AP2 as the air-puff configuration. Porcine data were used around the maximum deformation to reduce the time scale. The

normalized displacement as function of time is shown for the cornea and the sclera of porcine eyes (c) and rabbit eyes (d). Figure d has been rescaled for comparison between porcine and rabbit data. Shaded areas and error bars represent standard deviation values. Figures (a) and (b) were adapted from: (Bronte-Ciriza et al., 2021), and are used with the permission of the authors.

4.1.2.3. Comparison of speed deformation of the apex in porcine and rabbit eyes

Apex speed as the function of time was calculated from displacement-time curves (see Figure 4.4, upper panel) for corneal and scleral locations in porcine and rabbit eyes. Maximum speeds were quantified from speed-time curves (see Figure 4.4, lower panel). In porcine eyes, tissue reached higher speed values in the C, I and S before (C: $0.15 \pm 0.02\ m/s$, I: $0.13 \pm 0.06\ m/s$, S:$0.10 \pm 0.02\ m/s$) and after (C:$0.48 \pm 0.19\ m/s$, S:$0.37 \pm 0.18\ m/s$, I:$0.30 \pm 0.09\ m/s$) maximum displacement. In rabbit eyes, the highest speed values using AP2 occurred in the C and EN (C:$0.18 \pm 0.10\ m/s$, EN: $0.26 \pm 0.02\ m/s$) before maximum displacement. In contrast, the speed values after maximum displacement were higher in the S and I (S:$0.50 \pm 0.11\ m/s$, I: $0.50 \pm 0.13\ m/s$), see Table 4.3. The return speeds (after maximum displacement) to the initial position in porcine and rabbit were 3 to 4 times faster than the deformed speeds (before maximum displacement) during AP2 at all locations. The return speed was just twice as high in rabbit using AP1 configuration, for further information see in Annexes, Section A.

Location	**Maximum speed (m/s)**			
	Before maximum displacement	**After** maximum displacement	**Before** maximum displacement	**After** maximum displacement
	Porcine tissue		**Rabbit tissue**	
C	0.15±0.02	0.48±0.19	0.18±0.10	0.45±0.00
S	0.10±0.02	0.37±0.18	0.16±0.03	0.50±0.11
I	0.13±0.06	0.30±0.09	0.26±0.05	0.50±0.13
EN	0.03±0.02	0.07±0.05	0.26±0.02	0.48±0.04
ET	0.02±0.01	0.05±0.02	0.12±0.04	0.48±0.09
PN	0.02±0.01	0.04±0.02	0.12±0.04	0.33±0.08

PT	0.02±0.01	0.04±0.02	0.13±0.02	0.40±0.22

Table 4.3: Mean values ± standard deviation of apex maximum speed. The deformation measurement was performed using the AP2 configuration. Measurements were performed at seven marked points (C, S, I, EN, ET, PN, PT) on the surface of porcine and rabbit eyeballs.

In addition, the time interval between speed extremes (see Figure 4.4, lower panel) was estimated at all locations for porcine and rabbit eyes. The highest time intervals were in the C and PT sclera ($10.37 \pm 0.38\, ms$ by AP1, $9.8 \pm 0.50\, ms$ by AP2) for both air-puff configurations (see Annexes, Section A). Time intervals were longer in porcine cornea ($10.20 \pm 0.6\, ms$ by AP2) and rabbit cornea ($10.82 \pm 0.5\, ms$ by AP1, $11.30 \pm 0.70\, ms$ by AP2) than in porcine sclera ($5.80 \pm 1.40\, ms$ by AP2) and rabbit sclera ($9.12 \pm 0.96\, ms$ by AP1, $8.89 \pm 0.81\, ms$ by AP2).

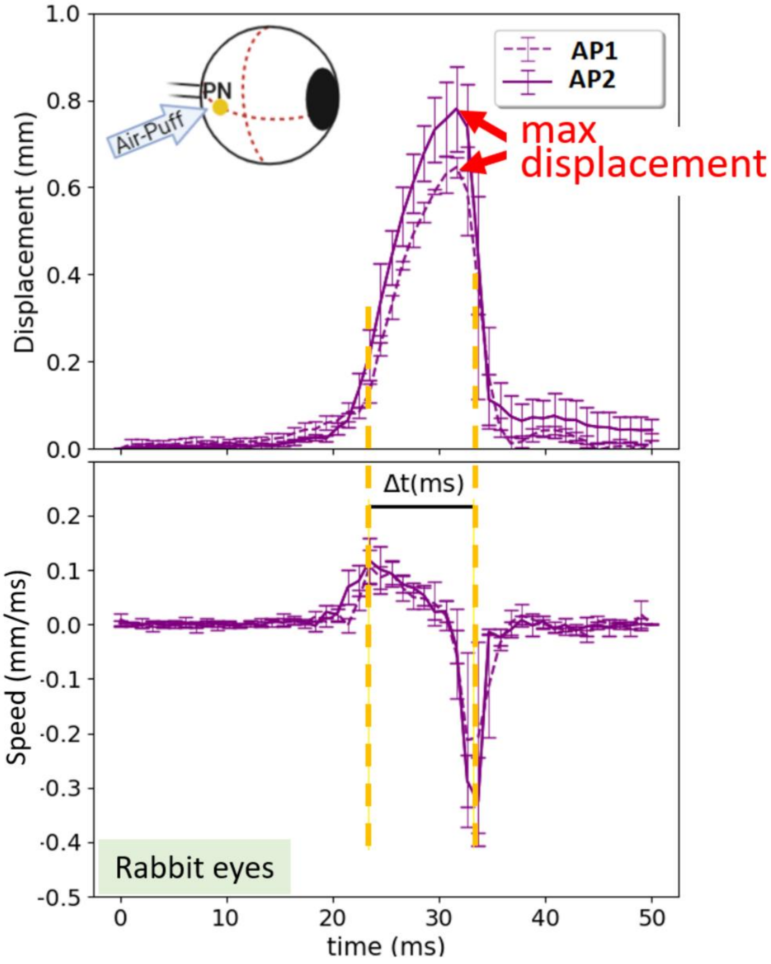

Figure 4.4: Apex displacement and speed versus time at a scleral location. Example of displacement-time and speed-time curves at the PN (posterior nasal) scleral location in

two rabbit eyes. One eye was measured with AP1 configuration and the other eye with AP2 configuration. The time interval (Δt) between speed extremes was measured as shown in the figure.

4.1.2.4. Comparison of arc length during the air-puff deformation in porcine and rabbit eyes

The change in arc length as a function of time was semi-automatically estimated for porcine and rabbit eyes at all locations (see Section 3.6.3) to study the compression/extension of the tissue during the air puff deformation event. There was a clear difference between the resting time ($0-4\,ms$, $24-25\,ms$ in porcine eyes and $0-20\,ms$ and $40-50\,ms$ in rabbit eyes) and the deformation event time ($4-20\,ms$ in porcine tissue and $20-40\,ms$ in rabbit tissue), see Figure 4.5. The time of the maximum deformation was indicated by the black dotted line at $15.6\,ms$ for porcine eyes (see Figure 4.5a) and $31\,ms$ for rabbit eyes (see Figure 4.5b).

In all cases, there was initial compression (decreased in arc length) except in the posterior temporal sclera in porcine tissue and in the superior sclera in rabbit tissue. In the case of porcine eyes, there was a marked difference in superior and inferior sclera, where initial compression was followed by a large extension (increased in arc length) at the time of maximum deformation (dashed black line in the Figure 4.5). Also, the cornea showed maximum compression with respect to the scleral tissue. In rabbit eyes, however, the cornea showed compression behavior similar to that of the other scleral tissues. In this case, the inferior sclera showed the greatest compression. Even when using the same air-puff configuration (AP2), compression values were higher in rabbit eyes than in porcine eyes.

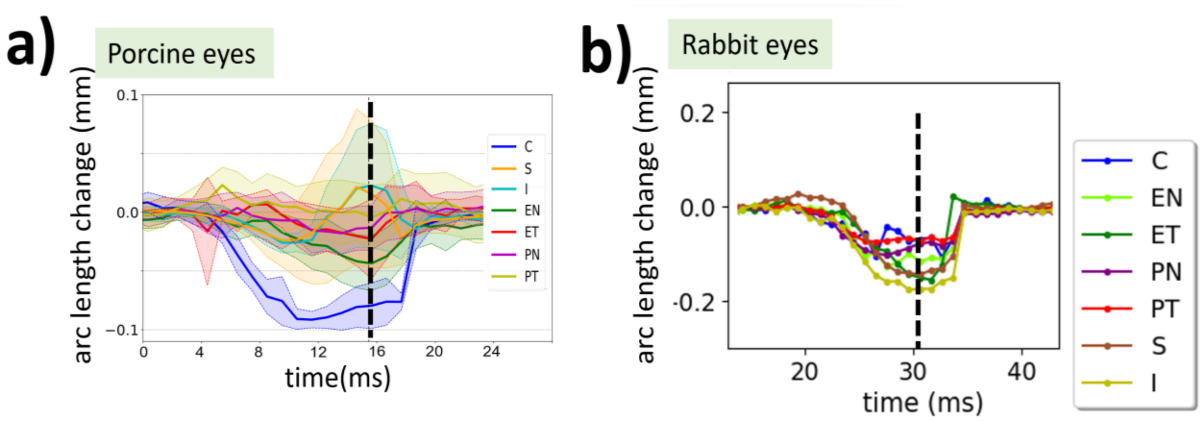

Figure 4.5: Mean values of change in arc length as a function of time during the deformation event. Values for each location in porcine (a) and rabbit (b) eyes. The black dashed vertical line indicates the time of maximum deformation. Note the difference in scale between the porcine and rabbit arc length versus time figures. Figure (a) was adapted from (Bronte-Ciriza et al., 2021), and is used with the permission of the authors.

4.1.2.5. Young's modulus from FE simulations using measurements in porcine eyes

Young's modulus at 10% strain for corneal and scleral locations (C, S, I, EN, ET, PN, PN) was obtained from porcine data only using FE inverse optimization method (see Section 3.6.2). The lowest Young's moduli were found at locations C, S and I (C:$0.69 \pm 0.14\,MPa$, S:$2.19 \pm 0.43\,MPa$, I:$1.84 \pm 0.30\,MPa$). The highest Young's modulus was estimated at scleral location ET ($6.04 \pm 2.11\,MPa$), see results in Figure 4.6. The sclera was 3 to 7 times stiffer than the cornea. In addition, the relative values of the C_{20}/C_{10} from the Yeoh material model were used as an indication of tissue non-linearity (see Annexes, Section A). The ratio of these parameters indicates a greater non-linear elastic response in the cornea than in the sclera.

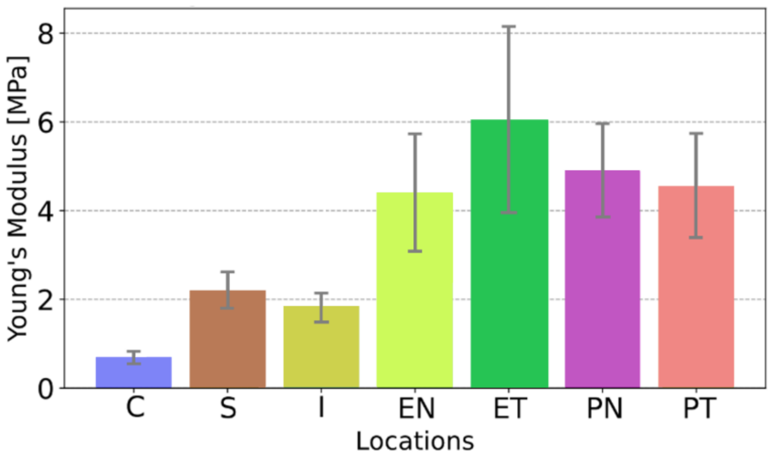

Figure 4.6: Young's modulus calculated from finite element simulations for porcine eyes. Young's modulus was estimated from simulated strain-stress curves at 10% strain for corneal and scleral locations (C, S, I, EN, ET, PN, PN). This image was adapted from (Bronte-Ciriza et al., 2021), and is used with the permission of the authors.

4.2. Scleral Biomechanics using Optical Coherence Elastography

This subchapter presents protocols and results of *ex vivo* experiments on the entire rabbit eyes using ACUS-OCE to compare biomechanics at four different scleral locations and in the cornea. The biomechanical behavior was quantified by subjecting the ocular tissue to air-coupled ultrasound deformation, detecting the propagating waves, and quantifying the shear modulus in the cornea and sclera.

This subchapter is based on the paper "Revealing regional variations in scleral shear modulus in a rabbit eye model using multi-directional ultrasound optical coherence elastography" published in Scientific Reports (2024). The authors of the paper are Lupe Villegas, Fernando Zvietcovich, Susana Marcos and Judith S. Birkenfeld. The author of this thesis (1) performed the experimental measurements in this paper, (2) developed a methodology for quantifying the shear modulus from propagation speed data, (3) obtained and analyzed the resulting parameters from all the measurements, (4) wrote the draft of the paper.

In addition, the author of this thesis presented the following contributions using the same OCE system: *poster presentation* at Association for Research in Vision and Ophthalmology (ARVO) Annual Meeting on May 1-4, 2022 in Denver-USA with the title "Spatial characterization of scleral biomechanics in *ex vivo* rabbit eyes using multi-meridian Optical Coherence Elastography"; *poster presentation* at Optica Fall Vision Meeting of the University of Rochester on October 21-23, 2022 in Rochester-USA with the title "Experimental assessment of scleral anisotropy using multi-meridian air-coupled ultrasonic optical coherence elastography"; and *oral presentation* at SPIE Photonics West Conference on January 25-30, 2024 in San Francisco-USA with the title "Scleral anisotropy in *ex vivo* rabbit eyes using ultrasonic optical coherence elastography"; (SPIE Digital Library, vol. 12844, pp. 32-34).

A summary of the above contributions is presented in this subchapter.

4.2.1. Protocols

4.2.1.1. Preparation of rabbit eyes

Seven freshly enucleated rabbit eyes were obtained and processed as described in Section 3.1.2. Five locations (1 corneal, 4 scleral) were identified and marked:

central cornea (C), superior nasal (SN), inferior nasal (IN), superior temporal (ST), and inferior temporal (IT), as displayed in Figure 4.7a. The locations were placed $3\,mm$ from the limbus (approximately on the equatorial plane) and $10\,mm$ from each other.

Group name	Number of eyes	Method	Resulting parameters
untreated	7	ACUS-OCE measurements (Section 4.2.1.2) and tensile test (Section 4.2.1.3)	Shear modulus, Young's modulus, thickness, and tissue anisotropy parameters (normalized fractional anisotropy, modified planar anisotropy coefficient, the major-axis angle).

Table 4.4: Overview of the different experiments and data collection. ACUS-OCE: air-coupled ultrasonic Optical Coherence Elastography.

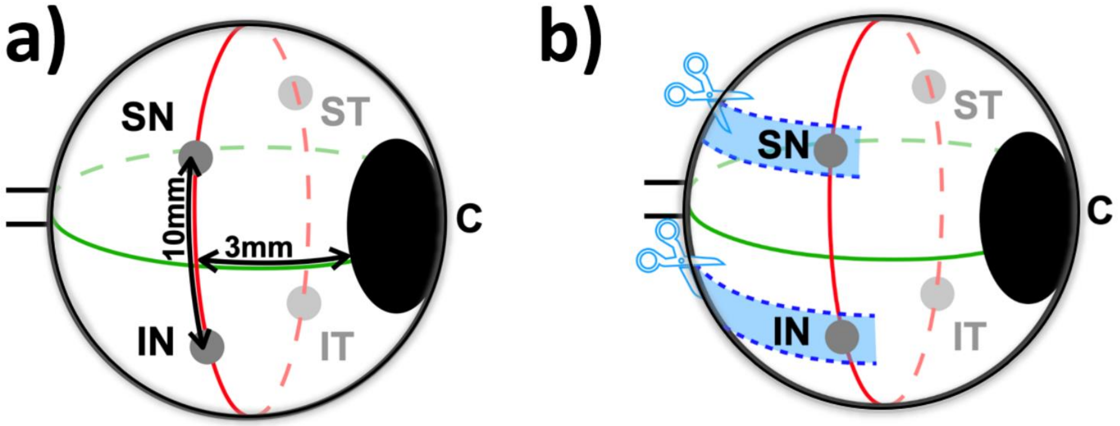

Figure 4.7: Schematic of the eye for OCE experiments. a) Diagram of the globe showing the central corneal (C) and scleral locations: superior nasal (SN), inferior nasal (IN), superior temporal (ST), and inferior temporal (IT). One of the circumferential axes (equatorial line) of the eye is shown in red and one of the meridional axes (nasal-temporal meridional line) in green. b) After OCE measurements, sclera strips were cutting along meridional direction as showed in representative blue dashed lines.

4.2.1.2. OCE measurements of cornea and sclera

Rabbit ocular globes were mounted in a custom-made holder and the corneal/scleral locations were aligned to the OCT system sample arm (see Section 3.7.1). IOP was maintained at 15 $mmHg$ during all experiments (see Table 4.4). Each location was excited with the ACUS-OCE technique to generate elastic waves on the ocular surface. Phase speed and thickness values (see Section 3.7.2) were obtained from the images acquired by the ACUS-OCE system for each location (C, ST, SN, IT, IN) and each of the 16 angles (in steps of 22.5°). Shear modulus was estimated using the Rayleigh-Lamb wave model (see Section 3.7.3).

4.2.1.3. Mechanical testing after OCE technique

After the OCE measurements, scleral and corneal strips were extracted from the globes within 24 hours and mechanically stretched. All measurements were completed on the same day. Eye tissue strips were mounted on a uniaxial testing machine (see Section 3.8.1). Briefly, tests were carried out by applying axial extension at a rate of 1.0 mm/min with a preload force. During the tests, the specimens were kept immersed in BSS (saline solution). All specimens were cut (see Figure 4.7b) and tested immediately after the OCE measurements (see Section 3.7.1.). Stress-strain curves were used after five preconditioning cycles. Young's modulus was estimated from the data of these curves at 7%. It was This value of the strain was estimated for IOP=15 $mmHg$ using A=.0008 MPa, B=80.0 (see Section 3.8.3).

4.2.1.4. Statistical analysis

Statistical analysis was performed using IBM SPSS Statistics (Version 27.0, Armonk, NY: IBM Corp). Data were label and compared between locations (C, SN, IN, ST, IT) and zones (anterior, posterior, meridional, circumferential). Shapiro-Wilk test was applied to prove normality in all variables. ANOVAs were conducted to assess differences between the means in the parametric variables: phase speed and major axis angle. Non-parametric Kruskal-Wallis H tests were used to compare differences between the average values in the following variables: shear modulus, thickness, Young's modulus, NFA and maxMPAC. Location and zone effects were evaluated using a post-hoc test with a Bonferroni correction for multiple comparison. Statistical significance was set at p-value of 0.05. Spearman correlation coefficient was used as an inferential statistic to test the relationship between elastic properties of the tissue. All values in bar plots are indicated as mean± standard deviation and the boxplots display the first quartile, median, and third quartile.

4.2.2. Evaluating biomechanics with Optical Coherence Elastography

4.2.2.1. Scleral speed mapping

Phase speed was calculated for each of the five locations and 16 directional angles using the protocols described in Section 4.2.1. The phase speed data were represented on polar plots (see Figure 4.8), which provide a global map of speed propagation in the corneal and scleral tissues. Visual inspection of Figure 4.8 shows that the mean phase speed values as a function of angle of propagation appear to have a circular symmetry for the cornea and non-circular symmetry for all scleral locations, suggesting that the rabbit sclera is anisotropic.

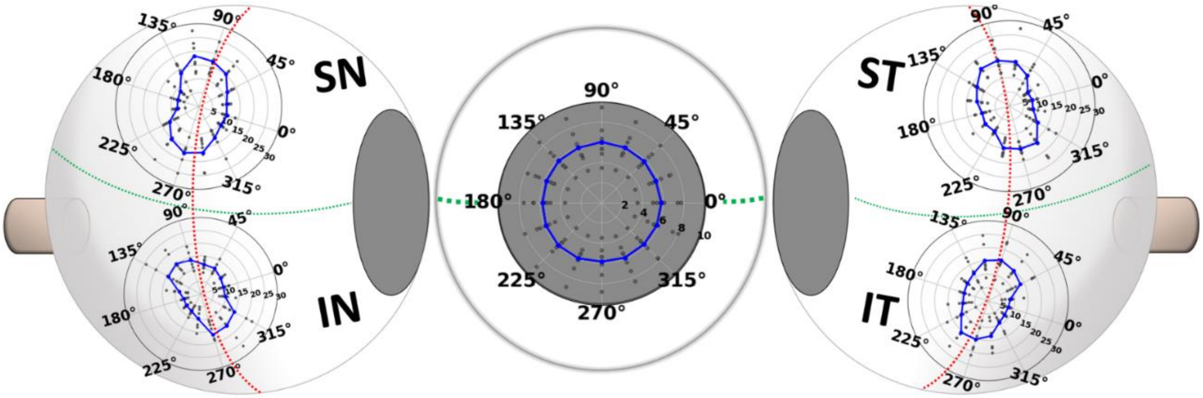

Figure 4.8: Mapping of ocular globe regions using wave propagation velocity. Polar plots of values of phase speed as function of propagation angle measured by the ACUS-OCE method in cornea (C), superior-nasal (SN), inferior-nasal (IN), superior-temporal (ST) and inferior-temporal (IT) locations of the rabbit. The dark blue line shows the mean value of the phase speed at each angle for all samples at constant IOP=15mmHg, the data points are shown as gray dots. Note that the scale of the central graph (cornea) is different from that of the adjacent graphs (sclera), the scale units are 2 m/s for the cornea and 10 m/s for the sclera. This image was adapted from (Villegas et al., 2024b), and is used with the permission of the authors.

An exploratory estimation of the symmetries of the sclera and cornea was made using only the vertical and horizontal axes of the polar plots in both the sclera and the cornea. Table 4.5 shows the phase speed results on these two specific axes for the five locations. The V-H ratio was defined as the mean vertical speed divided by the mean horizontal speed. For all samples, the calculated coefficients suggest a more circularly symmetric behavior of the cornea with a calculated V-H ratio of 1, in contrast to a more horizontally symmetric ("earing") behavior of the sclera with a V-H ratio close to 2.

	Location	**Wave propagation angle**				**V-H ratio**
		Horizontal Axis		**Vertical Axis**		
		0^{0}	**180^{0}**	**90^{0}**	**270^{0}**	
Phase speed in CORNEA (m/s)	C	5.80±1.42	5.75±1.32	6.04±1.91	5.83±1.73	1.0
Phase speed in SCLERA (m/s)	SN	10.64±1.58	7.89±1.63	17.15±4.41	17.59±4.23	1.9
	IN	9.27±1.66	6.86±1.16	13.90±3.45	16.73±7.03	1.9
	ST	8.30±1.64	9.83±1.95	16.52±4.50	15.53±2.33	1.8
	IT	7.91±0.99	9.48±1.17	16.04±5.15	15.21±4.80	1.8

Table 4.5: Mean phase speed (m/s) for cornea and sclera calculated for each location at specific angle. Values show mean ± standard deviation, and Vertical-Horizontal (V-H) ratio between vertical and horizontal axes. The values of the V-H ratio close to 1 indicate more circular symmetric behavior.

The effect of eye rotation on polar tracing was specifically investigated in one eye. The eye was rotated 90 degrees counterclockwise, and ACUS excitation was applied at the same location (SN in this case). The results of phase speed are shown in the polar plots of the same unrotated (Figure 4.9a) and rotated (Figure 4.9b) eye. It can be seen in Figure 4.9c that the speed values are almost superimposed.

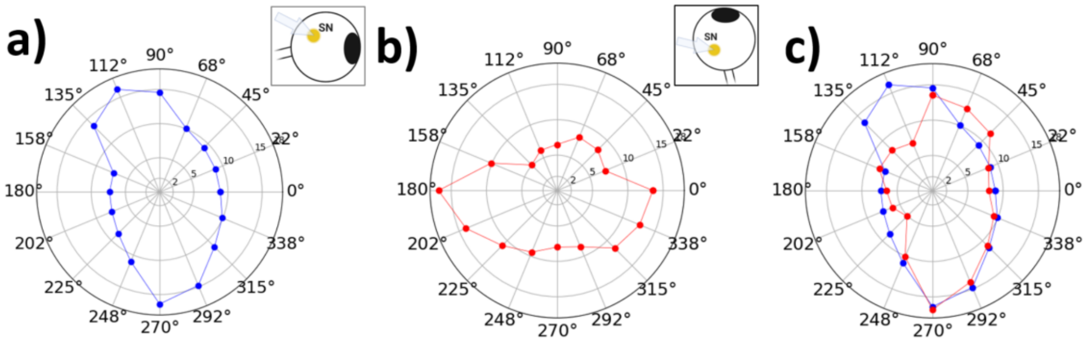

Figure 4.9: The anisotropic effect is not influenced by the technique. Mean values of phase speed as function of propagation angle measured by ACUS-OCE in the same eye at the same scleral point (SN) before (a) and after (b) 90 degrees rotation. c) Both plots are combined on the same axes.

4.2.2.2. Phase speed, thickness, and shear modulus: corneal and scleral comparisons

The phase speed, the shear modulus, and the thickness of the sclera and cornea were determined for each location and directional angle. The scleral phase speed from the four polar plots (SN, ST, IN, and IT) were pooled and the data were grouped into cornea, anterior and posterior zones, and meridional and circumferential orientations.

The anterior zone (orange, Figure 4.10) was defined as the semi-axes at angles 0°, 22.5°, and 337.5° (in SN and IN locations) and the semi-axes at angles 157.5°, 180°, and 202.5° (in ST and IT locations). The posterior zone (purple) was defined as the semi-axes at angles 157.5°, 180°, 202.5° (in SN and IN locations), and 0°, 22.5°, and 337.5° (in ST and IT locations).

The meridional zone (green, Figure 4.10) was defined with the semi-axes at angles 0°, 22.5°, 157.5°, 180°, 202.5°, and 337.5°, and the circumferential zone (red) at angles 67.5°, 90°, 112.5°, 247.5°, 270°, and 292.5°. Values labeled "cornea" (light blue color) were calculated as the average of the corneal data at all angles.

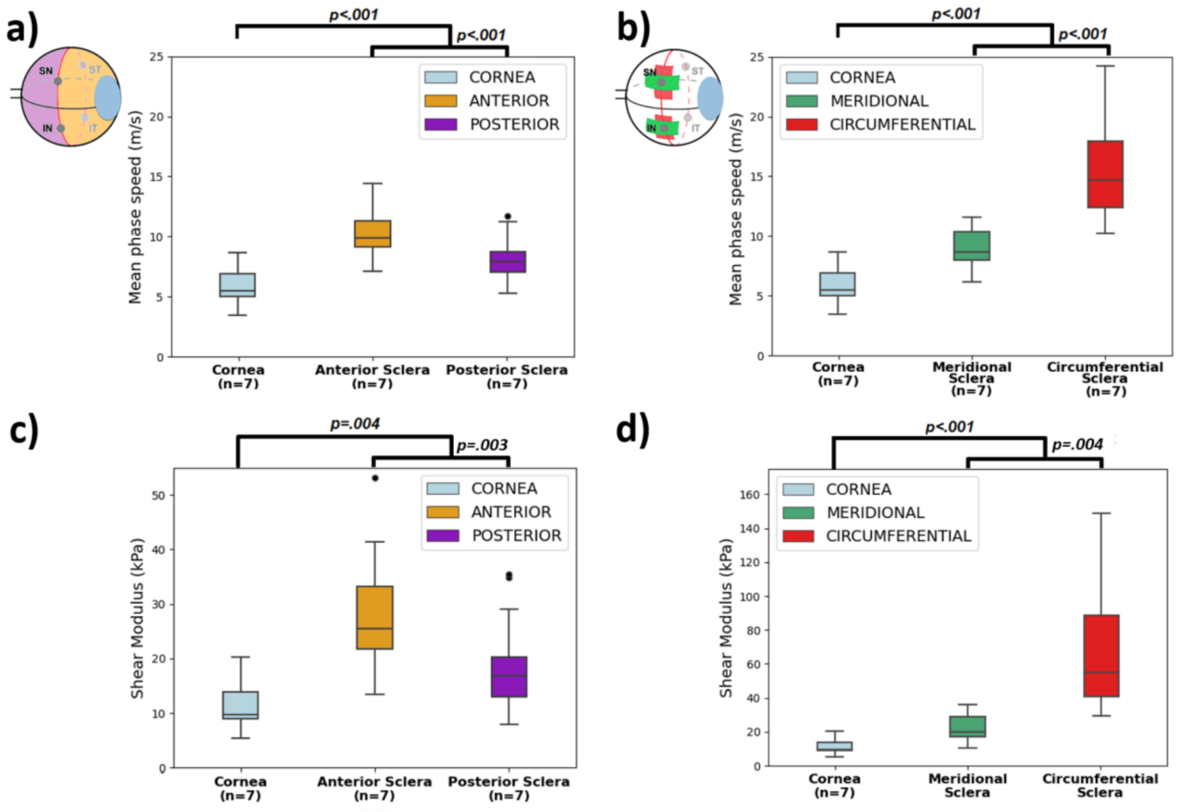

Figure 4.10: Phase speed and shear modulus depends on the scleral zone. The mean values of corneal and scleral phase speed and shear modulus per zone are shown. Data was divided according to eye regions as cornea (light blue), anterior sclera (orange), posterior sclera (purple), meridional sclera meridional (green) and circumferential sclera (red). The mean scleral values were calculated form data at the four investigated locations (SN, IN, ST, IT). Error bars in plots are the 95% confidence interval, the bottom and top of the box are the 25th and 75th percentiles. This image was adapted from (Villegas et al., 2024b), and is used with the permission of the authors.

The mean phase speed and the shear modulus distributed by zone are shown in Figure 4.10. Comparison of corneal and scleral data showed that the mean phase speed propagated significantly slower (p<.001) in corneal tissue ($5.9 \pm 1.4\, m/s$, light blue bars) than in scleral tissue ($12.1 \pm 3.2\, m/s$). In scleral tissue, the wave propagated significantly faster (p<.001) in the anterior globe than in the posterior globe ($10.1 \pm 1.8\, m/s$ vs. $8.0 \pm 1.7\, m/s$, Figure 4.10a), and in the circumferential direction than in the meridional direction ($15.4 \pm 3.7\, m/s$ vs. $9.1 \pm 1.5\, m/s$, Figure 4.10b). On the other hand, shear modulus is significantly (p=.004) lower in the corneal tissue ($11.2 \pm 4.1\, kPa$, light blue bars) than in the scleral tissue ($44.0 \pm 31.5\, kPa$, all locations). Shear modulus is significantly higher (p≤.004) in the anterior than the posterior globe ($27.3 \pm 1.8\, kPa$ vs. $17.8 \pm 1.4\, kPa$, Figure 4.10c), and in the circumferential than in meridional directions ($65.4 \pm 31.9\, kPa$ vs. $22.5 \pm$

7.2 kPa, Figure 4.10d). Phase speed and shear modulus values are given in Table 4.6 and Table 4.7.

Zone	Phase Speed (m/s)	Thickness (µm)	Shear Modulus (kPa)
Cornea	5.9 (5.7-7.0)	511.1(487.9-534.4)	11.2 (9.6-12.9)
Anterior sclera	10.1(9.4-10.8)	319.4(307.3-331.5)	27.3 (23.7-30.9)
Posterior sclera	8.0 (7.4-8.7)	314.1(295.6-332.7)	17.8 (15.0-20.7)

Table 4.6: Mean values (and 95% confidence intervals) of phase speed, thickness, and shear modulus for three zones: cornea, anterior sclera and posterior sclera. Further comparisons between locations are shown in Annexes, Section B.

Zone	Phase Speed (m/s)	Thickness (µm)	Shear Modulus (kPa)
Cornea	5.9 (5.7-7.0)	511.1(487.9-534.4)	11.2 (9.6-12.9)
Meridional sclera	9.1 (7.9-10.1)	316.8 (299.5-334.0)	22.5 (19.7-25.3)
Circumferential sclera	15.4 (14.3-16.5)	314.5 (297.3-331.8)	65.4 (53.0-77.8)

Table 4.7: Mean values (and 95% confidence intervals) of phase speed, thickness, and shear modulus for zones: cornea, meridional sclera and circumferential sclera. Further comparisons between locations are shown in Annexes, Section B.

4.2.2.3. Phase speed, thickness, and shear modulus: scleral comparisons

Differences in mean phase speed, mean thickness and mean shear modulus of the sclera were compared between each location (SN, IN, ST, IT, see Figure 4.7a) and each zone. Figure 4.11 shows the results of the phase speed (Figure 4.11a and 4.11d), sample thickness (Figure 4.11b and 4.11e), and shear modulus (Figure 4.11c and 4.11f) for the anterior (orange bars), posterior (purple bars), meridional (green bars) and the circumferential (red bars) zones of the sclera, and for all scleral locations individually. Figure 4.11a shows significantly ($p \leq .032$) higher phase speeds in the anterior zones compared with the posterior zones at the following locations: SN, IN and ST (see Annexes, Section B). In addition, phase speed measurements along the circumferential direction were significantly higher ($p = .001$) than in meridional direction at all locations (Figure 4.11d).

Scleral thickness was measured at each location as described in Section 4.2.1.2. Pairwise comparisons showed that scleral thickness ($316.8 \pm 39.8\,\mu m$) was significantly lower (p<.001) than corneal thickness ($511.1 \pm 58.9\,\mu m$), see Tables 4.6 and 4.7. In a further comparison, the highest scleral thickness values were located at the posterior/meridional scleral location in SN ($364.5 \pm 53.2\,\mu m$/ $348.1 \pm 39.9\,\mu m$) and the lowest thickness values were located at the posterior/meridional scleral location in IT ($276.2 \pm 27.7\,\mu m$/ $289.5 \pm 30.9\,\mu m$), see Figures 4.11b and 4.11e. There were no differences in scleral thickness for the remaining locations.

The shear modulus was estimated from the mRLFE model (see Section 3.7.3) using the measured phase speed and thickness data from each half-axis (see Section 4.2.1.2). When analysed by location, the mean shear modulus of the anterior sclera ($28.5 \pm 6.0\,kPa$ (SN) and $30.4 \pm 13.5\,kPa$ (ST)) was significantly higher (p≤.046) than those of the posterior sclera ($18.7 \pm 9.0\,kPa$ (SN) and $18.7 \pm 8.6\,kPa$ (ST)) only at the superior location (SN and ST in Figure 4.11c). The mean shear modulus in the circumferential direction was also significantly higher (p≤.004) than in the meridional direction at all scleral locations (see Figure 4.11c). Shear modulus values for all locations are given in Annexes, Section B.

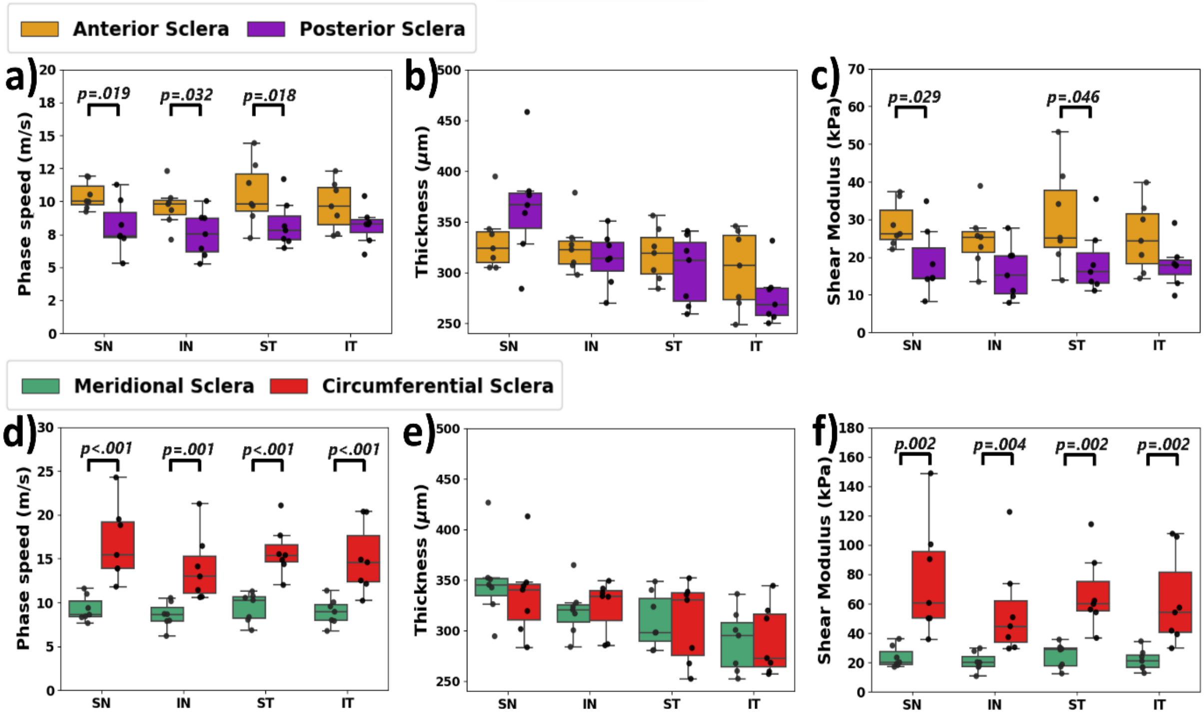

Figure 4.11: Comparison between measurements at each scleral location. Comparison between measurements in anterior region (orange), posterior region (purple), along meridional axis (green) and circumferential axis (red) at the corresponding scleral

locations. (a, d) Phase speed, (b, e) shear modulus and (c, f) thickness evaluated for all seven rabbit eyes at 15mmHg. The line inside the box is the median, and data points are shown as black circles. *p* values have been shown on the graph only for significant variations. Data is given in Annexes, Section B. This image was published in (Villegas et al., 2024b), and is used with the permission of the authors.

4.2.2.4. Speed anisotropy of cornea and scleral tissue

Mechanical anisotropies of ocular tissues were determined using phase speed values. Speed anisotropies were quantified by the following parameters: degree of anisotropy (Figure 4.12a), normalized fractional anisotropy (Figure 4.12b), the maximum value of the modified planar anisotropy coefficient (Figures 4.12c and 4.13), and the major-axis angle (Figure 4.14a). Degree of anisotropy (Equation 3.4) and NFA (Equation 3.5) were simple metrics comparing vertical/horizontal and maximum/minimum phase speeds, respectively (see Section 3.7.4). On the other hand, maxMPAC (MPAC was quantified by Equation 3.6) attempts to estimate the directional angle variations and MAA shows the direction of the first principal axis on the polar plots. DA, NFA and maxMPAC showed a significant difference in anisotropy between the cornea and sclera ($p \leq .040$), with the sclera being more anisotropic (25 times in DA, 3 times in NFA, and 11 times in maxMPAC). There was no significant difference between scleral locations ($p = .94$). In addition, the angle-dependent MPAC was plotted as a function of each directional angle to show differences in corneal and scleral locations (see Figure 4.13). The MPAC values show a circular pattern for the cornea and an earring pattern for the sclera.

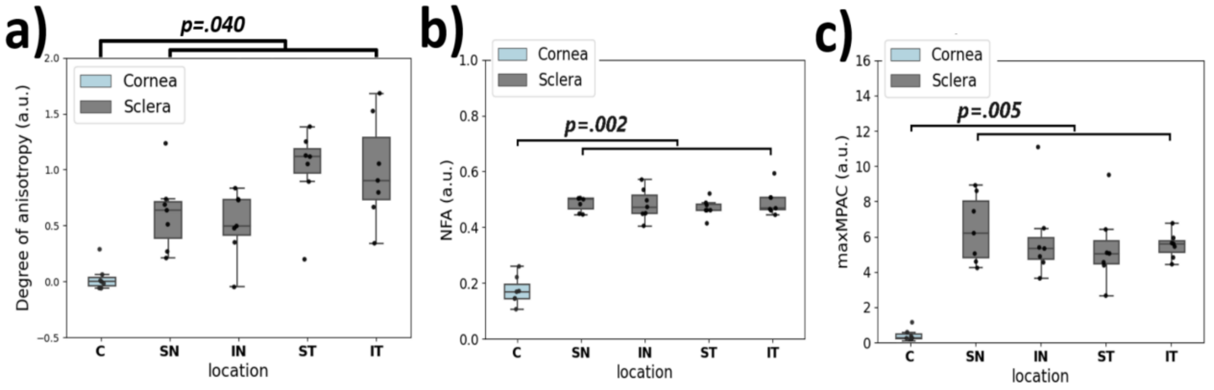

Figure 4.12: Phase speed anisotropy of corneal and scleral locations. Shown here is (a) the degree of anisotropy, (b) the normalized fractional anisotropy (NFA) and (c) the maximum value of the modified planar anisotropy coefficient (maxMPAC) for the cornea and the sclera. The line inside the box is the median, and data points per eye are shown as black

circles. p-values are shown only for significant variations. This image was adapted from (Villegas et al., 2024b) and is used with the permission of the authors.

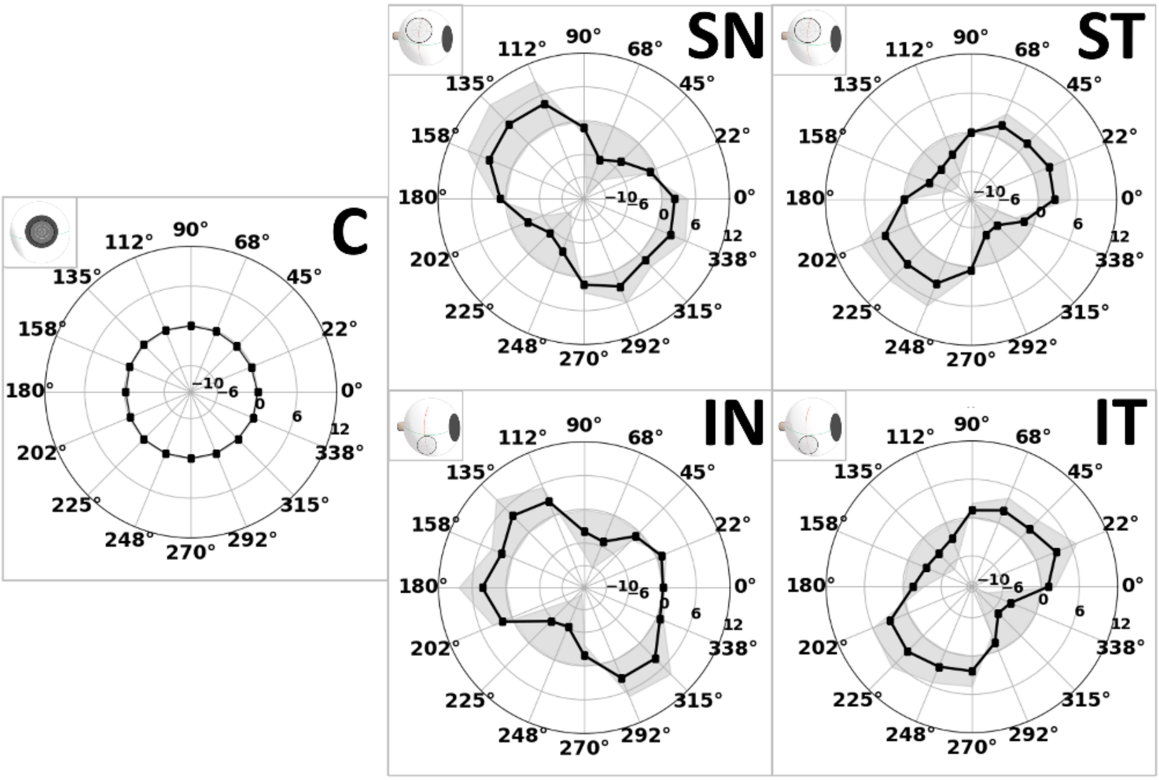

Figure 4.13: Modified planar anisotropy coefficient for corneal and scleral locations. Polar plots of calculated values of MPAC using Equation 3.6 for each radial direction (16 semi-axes in total) for cornea (C) and sclera (above: superior-nasal (SN) and superior-temporal (ST) locations; below: inferior-nasal (IN) and inferior-temporal (IT) locations). Black line indicates the average values for 7 eyes at each directional angle. The standard deviation is represented as shaded areas in gray. The location on the eye is represented by a small icon in the upper left corner.

The MAA parameter was calculated for each polar plot at all scleral locations. The MAAs at the lower eye locations (IN and IT) had a greater inclination with respect to the vertical axis (see Figure 4.14a), with the mean angle being greater at the IN location than at the IT location ($104.2^0 \pm 10.7^0$ vs. $83.0^0 \pm 15.7^0$). Orientation of major axis in superior locations was similar ($93.9^0 \pm 10.8^0$(SN) and $93.0^0 \pm 8.9^0$(ST)). In addition, the MAA shows a subtle tilt from the equatorial circumferential axis (90^0, 270^0). This can be interpreted as an inclination toward the optic nerve head for SN, IN, and IT and toward the corneal limbus for ST (see Figures 4.8 and 4.14b).

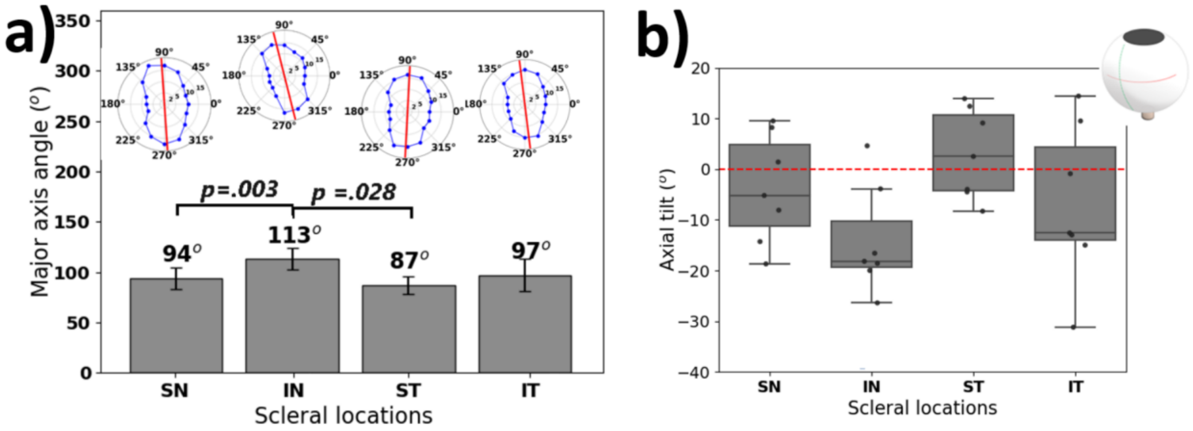

Figure 4.14: Phase speed anisotropy at different scleral locations. a) Thee major-axis angles per each scleral location are shown in bar plot. The polar plot of the mean phase speed is shown at the top of each bar, where the red lines represent the preferred orientation (major-axis) at the corresponding location. MAA was measured from the corneal limbus to the optic nerve head. b) The boxplots show the tilt between the major-axis and the equatorial circumferential axis. Red line indicates zero value. Positive values mean that major-axis is tilted toward the corneal limbus. Negative values indicate that major-axis is tilted toward the optic nerve head. Median values of tilt are: -5.2(SN), -18.2(IN), 2.5 (ST), -12.6(IT). p-values are shown only for significant variations.

4.2.2.5. Shear modulus and Young's modulus correlation

The relationship between shear modulus and Young´s modulus obtained by both OCE and mechanical tests, respectively, was explored. First, shear modulus values were taken on the corresponding meridional axes (data shown in Figure 4.11f) for the scleral nasal locations (SN, IN), and on the vertical axes (at 90^0 and 270^0) of the cornea. These orientations correspond to the symmetry of the strips shown in Figure 4.7b. Subsequently, Young´s modulus at 7% strain was determined from stress-strain curves (see Section 4.2.1.3). The boxplots in Figure 4.15a show that both shear and Young´s moduli in the cornea ($11.6 \pm 4.8\,kPa$ and $1.8 \pm 0.7\,MPa$, respectively) were significantly lower (p=0.04) than scleral shear and Young´s moduli ($22.0 \pm 6.6\,kPa$ and $3.5 \pm 0.9\,MPa$, respectively). Notably, the Young's modulus was two orders of magnitude higher than the shear modulus. By Spearman correlation analysis, shear modulus and Young's modulus showed moderate correlation in cornea without statistical significance (r_s = .68, p = .09), and no correlation in the sclera (r_s = .13, p = .64), see Figure 4.15b.

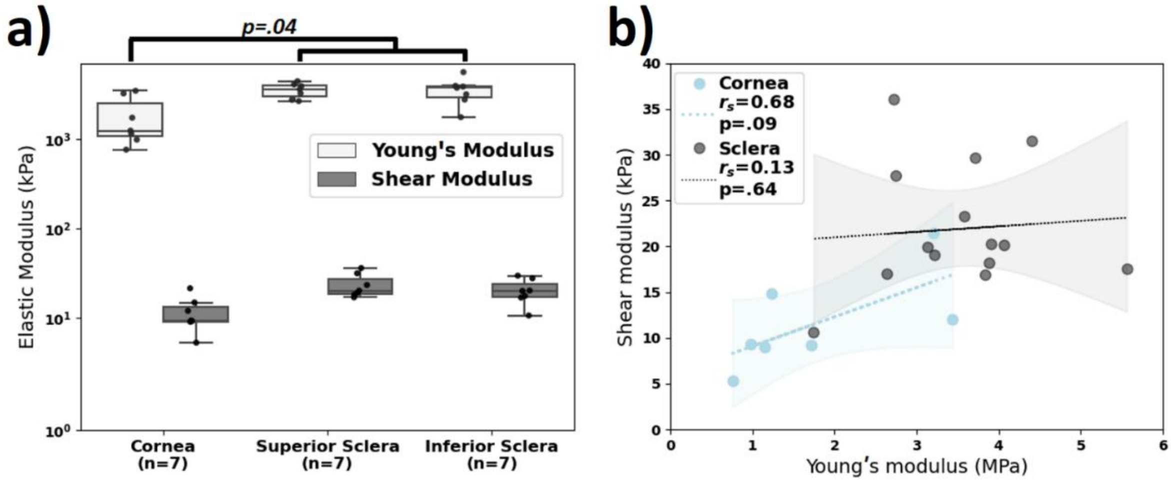

Figure 4.15: Shear modulus and Young's modulus of corneal and sclera tissue. a) Young's modulus (white) at 7% strain and shear modulus (gray) at predefined locations (cornea, superior and inferior sclera) represented as boxplots. The y-axis scale is logarithmic. Black dots indicate data points, and p-values are given for significant differences between respective groups. b) Scatterplot (Young's vs. shear modulus) for the cornea (light blue) and the sclera (gray). Dashed lines represent the corresponding linear regressions, and shaded areas represent 95% of confidence interval, for corneal and scleral data. Spearman correlation coefficient r_s and associated p-values are shown in the upper left corner. This image was published in (Villegas et al., 2024b) , and is used with the permission of the authors.

4.3. Scleral Biomechanics after Scleral Crosslinking

This subchapter presents protocols and results of *ex vivo* experiments on rabbit eye tissue using two photo-crosslinking methods: Rose Bengal with green-light irradiation and riboflavin with UVA-light irradiation. The effectiveness of the method was quantified by subjecting scleral tissue to uniaxial tensile tests and a controlled hydration process.

This chapter is based on the paper "Effects of Different Scleral Photo-Crosslinking Modalities on Scleral Stiffness and Hydration" published in Investigative Ophthalmology & Visual Science Journal (2024). The authors of the paper are Lupe Villegas, James A. Germann, and Susana Marcos. The author of this thesis (1) performed all the experimental measurements in this paper, (2) developed a methodology for measuring and quantifying the Young's modulus and the swelling ratio from experimental data, (3) analyzed the resulting parameters from all the measurements, (4) wrote the draft of the paper.

In addition, the author of this thesis presented the following contributions using the similar methodology: *poster presentation* at Association for Research in Vision and Ophthalmology (ARVO) Annual Meeting on May 3-7, 2020 (Virtual) with the title “Scleral cross-linking using Rose Bengal-Green Light”; *poster presentation* at Association for Research in Vision and Ophthalmology (ARVO) Annual Meeting on May 1-7, 2021 (Virtual) with the title “Biomechanical effects of Scleral crosslinking using Rose Bengal/Green-light and Rivoflavin/UVA”; and *oral presentation* at 2022 Young researchers Biophotonics Summer Meeting of Sociedad Española de Óptica (SEDOPTICA) on June 16, 2022 (Virtual) with the title “Optical imaging techniques for scleral biomechanics”.

A summary of the above contributions is presented in this chapter.

4.3.1. Protocols

4.3.1.1. Preparation of scleral tissues of rabbit eyes

Forty-six eyes were obtained in pairs from rabbits and processed (less than 24h postmortem) as described in Section 3.1.2. The eyes were separated into five groups (see Table 4.8): (1) naïve, (2) RGX, (3) UVX, (4) Hydration-RGX, and (5) Hydration-UVX. Muscle and conjunctival tissue were removed. Treated areas (1 *cm* diameter, handmade holder, Figure 4.16a) were marked on the eyes in the nasal (N) or temporal (T) regions and cross-linked by RGX or UVX. One region (N or T) was treated, and the other was used as a contralateral control (untreated area). Rabbit eyes were cut into strips and the choroid was removed. Posterior scleral samples (1-2 strips per region) were excised from the untreated (Figure 4.16b) and treated (Figure 4.16c) areas, respectively, and subjected to tensile or rehydration-tensile tests according to Table 4.8. The sample strips ($3\,mm \times 20\,mm$) were cut in equatorial direction (see Figure 4.16a) and identified according to their excised region as N or T. The center of the strip was located on the meridional line (green line) approximately 3.5 *mm* (N) and 2.5 *mm* (T) from the nerve head border. After tensile testing, a portion of the scleral strips was stored in formaldehyde solution (4% w/v in PBS, Sigma-Adrich, Switzerland) for subsequent SHG measurements.

Group name	Number of eyes	Method	Resulting parameter
naïve/virgin	6	Tensile tests (Section 4.3.1.3)	Young’s modulus

RGX	12	RGX (Section 4.3.1.2), tensile tests (Section 4.3.1.3), SHG* (Section 4.3.1.5)	Young's modulus, order coefficient
UVX	10	UVX (Section 4.3.1.2) and tensile tests (Section 4.3.1.3), SHG* (Section 4.3.1.5)	Young's modulus, order coefficient
Hydration-RGX	10	RGX (Section 4.3.1.2), rehydration-tensile tests (Section 4.3.1.4)	Young's modulus, swelling ratio, swelling rate
Hydration-UVX	8	UVX (Section 4.3.1.2), rehydration-tensile tests (Section 4.3.1.4)	Young's modulus, swelling ratio, swelling rate

Table 4.8: Overview of the different experiments and data collection. RGX: Rose Bengal with green light, UVX: riboflavin with ultraviolet light. *: Part of these eyes were subjected to Second Harmonic Generation (SHG) methods.

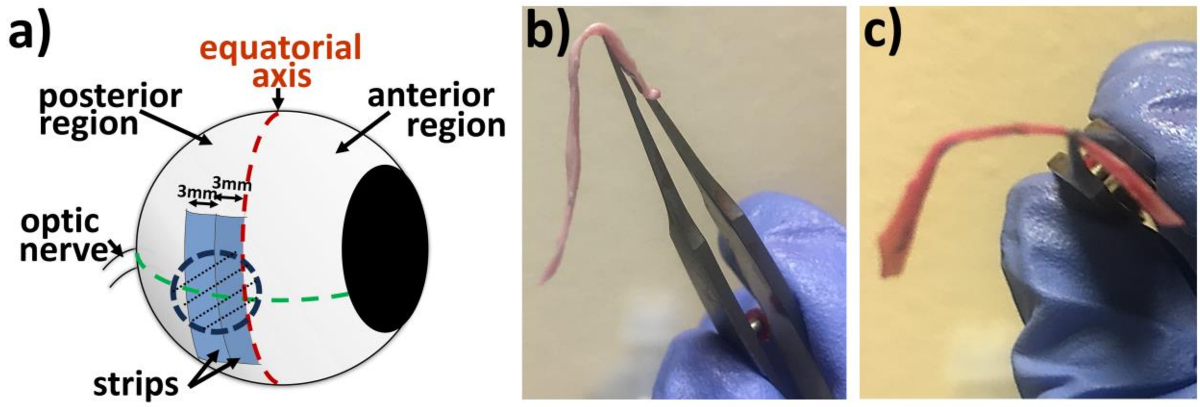

Figure 4.16: Scleral crosslinking tissue. a) Schematic eyeball shows the scleral collagen cross-linking zone. Equatorial line (red) and transversal line (green) were marked in all eyes to identify anterior and posterior scleral regions. Two 3mm-width scleral strips were excised from nasal and temporal sclera. The dashed circle in black represents the treated area of 1cm radius. b) Scleral strip from untreated tissue and c) scleral strip from RGX-treated tissue. Each strip was mounted in a uniaxial stretcher for the tensile test (see section 3.8.1).

4.3.1.2. Photo-crosslinking techniques

In all groups, one side of the globe (nasal or temporal region) was crosslinked and the other left as a contralateral control (untreated area). In RGX groups, the scleral area (black dashed circle in Figure 4.16a) was immersed in RB solution for 150 s and then irradiated by green light for 400 s (see Section 3.11.1 and an example in Figure 4.17a). In UVX groups, the scleral area was instilled with a Riboflavin solution for 60 min and irradiated by UVA light for 30 min (see Section 3.11.2 and Figure 4.17b). The light source was placed 7 cm from the scleral surface.

The difference between treated and untreated tissue can be seen by visual inspection of the strips. Figure 4.16b shows that the untreated sclera was easily deformable, whereas the cross-linked tissue (see Figure 4.16c) had a stiff appearance in the treated area (~1cm).

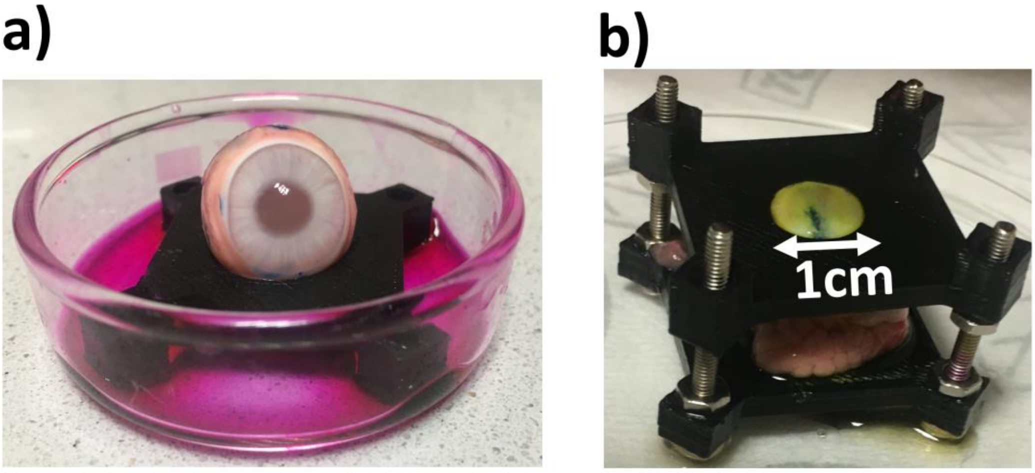

Figure 4.17: Treated zone in ocular globes. The rabbit eyes were placed in a custom holder with a 1 cm diameter hole. The hole allows localization of the treated area. The Rose Bengal (a) and riboflavin (b) photosensitizers were absorbed only for the 1cm-zone and the black plastic absorbed the scattered light.

4.3.1.3. Resulting parameters after tensile test of scleral strips

Eyes from RGX and UVX groups were used for this test. Posterior scleral strips (43 from RGX group, 32 from UVX group) were collected from N and T regions of each eye and tested after excision. Tensile tests were used to test differences due to two effects: strip location (N and T regions), and SXL method (RGX and UVX). The thickness of all strips was measured at the strip center (see Section 3.8.6) with a micrometer, see data in Annexes, Section C (Tables C4 and C5). Strips were mounted on a uniaxial tensile machine (see Section 3.8.1) and subjected to five loading/unloading cycles with a preload force. The results of the tensile test were obtained as strain-stress curves (see methods, Section 3.8.2). Young's modulus $E|_{\varepsilon=8\%}$ was calculated at 8% strain (Section 3.8.3).

4.3.1.4. Resulting parameters after rehydration-tensile test of scleral strips

Rehydration-tensile tests were used to test for swelling and stiffness differences due to three effects: strip location (N and T regions), SXL method (RGX and UVX) and rehydration period (40 min and 100min). Posterior scleral strips (40 from Hydration-RGX and 32 from Hydration-UVX groups, see Table 4.8) were collected from untreated and treated areas of each eye. The samples were dehydrated, rehydrated and mounted on a uniaxial stretcher (see methods, Section 3.8.4). All samples were tested after rehydration period rather than after dissection. The results of the tensile test were obtained as strain-stress curves (see methods, Section 3.8.2). Young's modulus $E|_{\varepsilon=8\%}$ was calculated at 8% strain (Section 3.8.3). Swelling ratio and swelling rate were determined for each strip (see Section 3.8.5).

4.3.1.5. SHG measurements of scleral strips and resulting parameters

21 scleral strips from eyes under groups RGX (6 strips (N) and 6 strips (T)) and UVX (3 strips (N) and 3 strips (T)) (see Table 4.8) were mounted in the second harmonic generation microscope (see Section 3.5.4) to visualize collagen fibers of the tissue. Order coefficient (see Section 3.9) was estimated using SHG images.

4.3.1.6. Statistical analysis

The data were analyzed using IBM SPSS Statistics (Version 29.0, Armonk, NY: IBM Corp). ANOVAs with repeated measures were performed to evaluate differences in Young's modulus and in swelling rate in the corresponding groups. One-way ANOVA was performed to evaluate the difference between treatment (RGX vs UVX) in all conditions. Multiple comparison was adjusted by Bonferroni correction. Spearman and Pearson correlation coefficients were used as an inferential statistic to test the relationship between swelling ratio and elastic properties of the tissue. Means and standard deviations of outcome variables were calculated by region (N y T) and identifying treated/untreated groups. Statistical significance was set at p-value of 0.05. All values in bar plots are indicated as mean± standard deviation and the boxplots display the first quartile, median, and third quartile. Error bars in boxplots are the 95% confidence interval.

4.3.2. Evaluating Biomechanics after scleral crosslinking

4.3.2.1. Same Young's modulus in nasal and temporal naive sclera

The nasal and temporal scleral regions showed similar stiffness. Scleral tissue was cut from rabbit eyes of the naive group (uncrosslinked group) and subjected to mechanical testing (see section 3.8.1). Prior to testing, the posterior scleral regions were identified: temporal and nasal. Stress-strain curves were determined for each region, with the stress in the nasal region ($339.0 \pm 157.5\ kPa$) being similar to that in the temporal region ($335.9 \pm 208.5\ kPa$) at 10% strain (see Figure 4.18a). Correspondingly, regional stiffness was not significantly different ($p = .93$). Young's modulus at 8% strain was $5.8 \pm 2.8\ MPa$ in the nasal region and $6.1 \pm 3.7 MPa$ in the temporal region (see Figure 4.18b). These results suggest that stiffness is not influenced by the region in non-treated eyes. Thus, one side of the eye could be treated and the other left untreated to estimate the regional variation due to treatment (see Section 4.3.1.1).

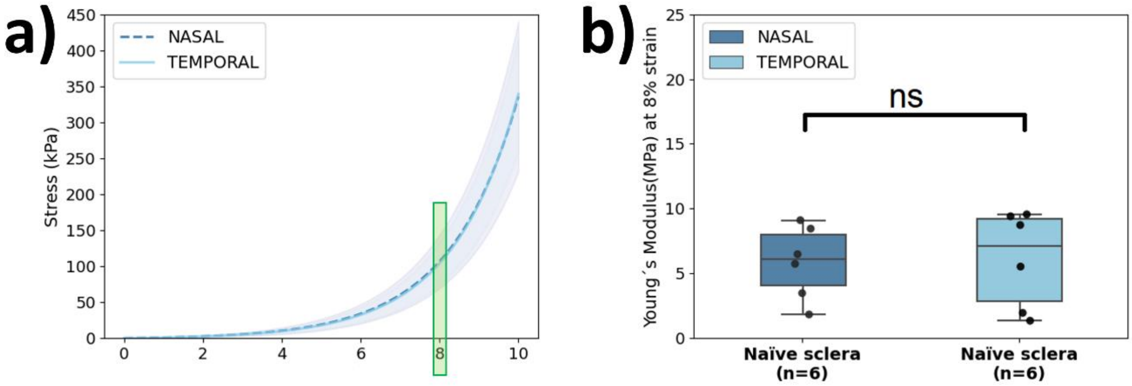

Figure 4.18: No regional variation in stiffness in naïve scleral tissue. a) Uniaxial stress-strain curves of scleral strips from naïve tissues. Scleral strips were obtained from the posterior nasal (dark-blue dashed line) and temporal (light-blue solid line) regions. Young's modulus was calculated from the slope of the stress-strain curves at 8% strain (represented as a green line). b) Here are shown the boxplots of estimated Young's modulus for nasal (dark-blue, n=6 eyes) and temporal (light-blue, n=6 eyes). Each data point represents the mean modulus of two strips in each region per eye. "ns" means not significance.

4.3.2.2. Scleral stiffness after RGX and UVX methods

Sclera stiffness increased after RGX and UVX treatment compared with untreated sclera. Tensile strength at 10% strain (Figures 4.19a and 4.19b) was 174% higher in RGX-treated eyes ($500 \pm 248\ kPa$ vs. $182 \pm 115\ kPa$), and 82% higher in UVX-treated eyes ($824 \pm 231\ kPa$ vs. $452 \pm 198\ kPa$). In a more detailed comparison, the modulus of elasticity was taken at 8% strain (see Section 4.3.1.3). RGX ($9.5 \pm 4.5\ MPa$) and UVX ($15.0 \pm 2.4 MPa$) produced a significantly ($p \leq .013$) increase in the modulus of elasticity compared to untreated sclera ($4.1 \pm 2.2\ MPa$ and $7.9 \pm 2.8M\ Pa$, respectively), see Table 4.9. In the nasal region, the Young's modulus of treated samples increased significantly twice ($p \leq .016$) after both treatments (Figures 4.19c and 4.19d, both on the left side). In the temporal region, Young's modulus was three times higher (RGX samples, $p = .019$) and twice higher (UVX samples, $p = .044$) than contralateral untreated samples (Figures 4.19c and 4.19d, both in right side).

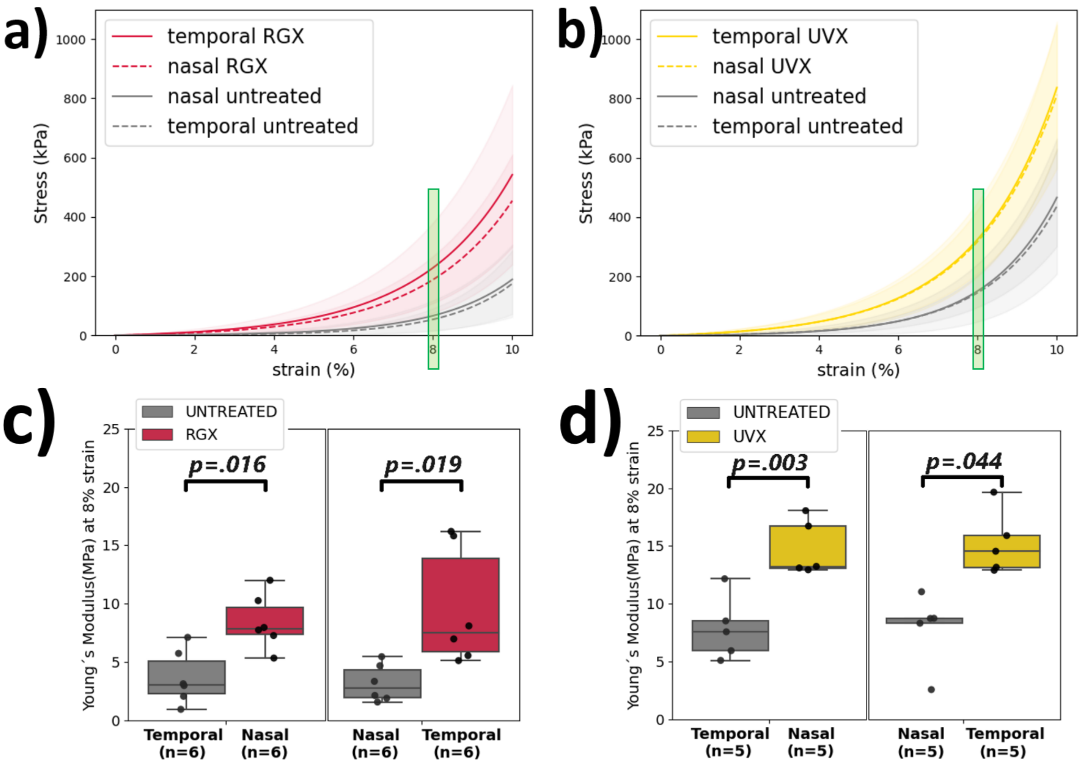

Figure 4.19: Increase in stiffness after RGX and UVX treatment. Above: uniaxial stress-strain results for untreated and crosslinked scleral strips. Scleral strips were obtained from the posterior temporal and nasal regions. (a) Scleral strips from Rose Bengal treated eyes exposed to green light irradiation were referred to as RGX (red curves), and (b) strips from riboflavin treated eyes exposed to ultraviolet light were referred as UVX (yellow curves) and their respective contralateral untreated samples (gray curves). Young's modulus was calculated from the slope of the stress-strain curves at 8% strain (represented as a green line). Below: Estimated Young's modulus for untreated (gray boxes) and treated scleral strips represented as boxplots, RGX-treated eyes (red boxes, n=6 eyes per region) (c) and UVX-treated eyes (yellow boxes, n=5 eyes per region) (d). p-values are shown in the graph for significant differences. The line inside the box is the

median, and data points are shown as black circles. Each data point is the average stiffness of the strips in each region per eye. The images (a) and (b) were adapted from (Villegas et al., 2024a), and are used with the permission of the authors.

	Photo-crosslinking treatment		
	RGX	**UVX**	**Naive**
Zone	Young's Modulus (MPa)	Young's Modulus (MPa)	Young's Modulus (MPa)
Untreaded Sclera	4.1 (2.7-5.4)	7.9(5.5-10.3)	6.0(3.8-8.1)
Crosslinked sclera	9.5(7.3-11.7)	15.0(11.9-18.2)	
Difference	***5.4*** ↑	***7.1*** ↑	

Table 4.9: Mean values (and 95% confidence intervals) of Young's modulus at 8% strain for untreated and treated scleral tissue. Further significant comparisons between regions are shown in Figure 4.19. The completed table is presented in Annexes, Section C.

4.3.2.3. Hydration in scleral tissue treated by RGX and UVX methods

The swelling ratio was determined to explore the influence of PBS absorption (hydration) on treated (RGX or UVX) and untreated scleral tissue (see Section 4.3.1.4). The results of the temporal evolution of rehydration are shown in Figure 4.20. The swelling curves show an approximately linear behavior up to 40-min of rehydration in all cases, and a constant value at 100-min of rehydration in the untreated tissue (217.6 ± 13.6%) and in the treated tissue (205.9 ± 23.5%). There were no clear differences between swelling-time curves in any of the cases, except for the temporal region treated with RGX (see Figure 4.20b), where the swelling ratio decreased by 8% at 100-min of rehydration (see further information in Annexes, section C, Table C2).

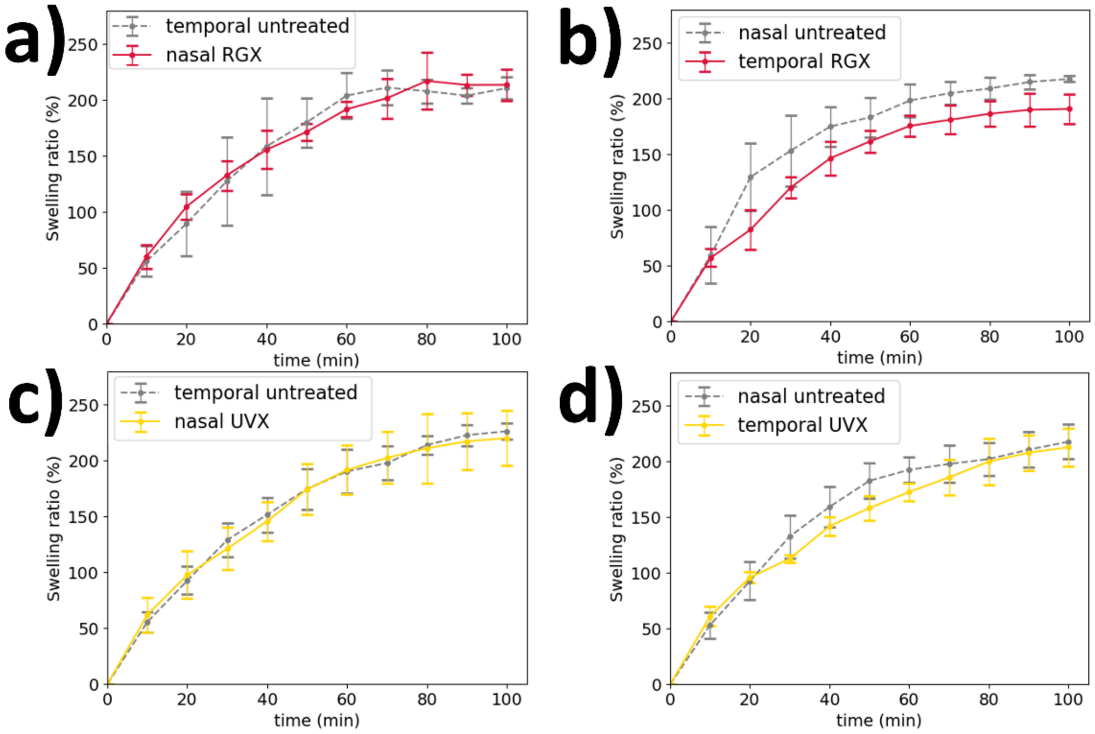

Figure 4.20: Swelling-temporal curves of scleral strips from treated and untreated tissues. a) y b) Swelling ratio in function of time for RGX-treated strips (red curves) compared to contralateral untreated strips (gray curves) in nasal and temporal regions, respectively. c) y d) Swelling-time curves for UVX-treated strips (yellow curves) compared to corresponding contralateral untreated strips (gray curves) in nasal and temporal regions, respectively. This image was published in (Villegas et al., 2024a), and is used with the permission of the authors.

However, it was possible to estimate variations after exploring the initial linear behavior of swelling-time curves using the swelling rate (see Section 3.8.5). Untreated scleral tissue absorbed saline at least 12% faster (p=.003) than treated tissue (see Figure 4.21). Particularly, the swelling rate was significantly higher (p=.029) in untreated nasal sclera ($4.0 \pm 0.6\%/min$, $4.1 \pm 0.4\%/min$) compared with treated temporal ($3.3 \pm 0.4\%/min$, $3.5 \pm 0.4\%/min$) and treated nasal sclera ($3.4 \pm 0.6\%/min$, $3.6 \pm 0.4\%/min$) with either of both treatments (RGX, UVX), respectively, see Table 4.10). These results suggest that the RGX and UVX crosslinking methods modified the swelling properties of the scleral tissue by reducing its swelling rate.

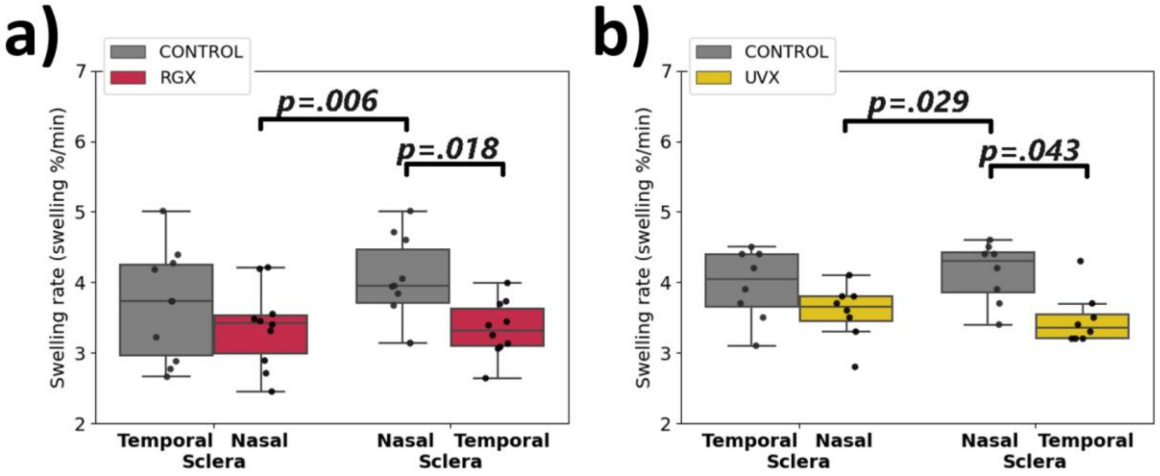

Figure 4.21: Decrease in swelling in RGX and UVX scleral tissue. Swelling rate was calculated from the slope of the swelling-time curves for untreated and crosslinked scleral strips. a) Shown here are boxplots of the swelling rate of treated (red) and untreated (gray) strips of nasal and temporal scleral tissue from eyes under RGX treatment. Data points for each strip (10 (N), 10 (T)) are shown as black circles. b) Boxplots show the swelling rate of treated (yellow) and untreated (gray) strips from eyes under UVX treatment. Data points for each strip (8 (N), 8 (T)) are shown as black circles. p-values are shown in the graph only for significant differences.

	Swelling rate (%/min)	
	RGX	UVX
Untreated sclera	3.8(3.5-4.2)	4.0(3.8-4.3)
Crosslinked sclera	3.4(3.1-3.6)	3.5(3.3-3.7)
Difference	**-0.4↓**	**-0.5↓**

Table 4.10: Swelling rate decreased after crosslinking. Mean values (and 95% confidence intervals) of swelling rate for untreated and crosslinked scleral tissue. Further significant comparisons between regions are shown in Figures 6.21a and 6.21b. The completed table is presented in Annexes, Section C.

4.3.2.4. Hydration and stiffness in scleral tissue treated by RGX and UVX methods

To determine whether scleral stiffness was also affected after rehydration, strips rehydrated in a controlled manner were subjected to tensile tests (see Section 4.3.1.4) after 40 min or 100 min. The resulting stiffness was quantified in both rehydration modes. In the overall comparison, significant ($p = .004$) higher stiffness values (at least 2-fold) after SXL were observed, see Table 4.11.

Surprisingly, cross-linking did not increase scleral stiffness in all cases in the nasal-temporal comparison (see p-values in blue in Figures 4.22b left and 4.22c right). In the samples rehydrated for 40 min, Young's modulus values were higher and showed a high dispersion in the samples treated with RGX (N:$14.0 \pm 6.6\ MPa$ and T:$13.9 \pm 5.3\ MPa$) and UVX (N:$19.7 \pm 4.9\ MPa$ and T: $17.0 \pm 6.9\ MPa$), in contrast, in the samples rehydrated for 100 min, Young's modulus values were lower and showed a lower dispersion in both the RGX ($13.7 \pm 3.1\ MPa$ and $10.8 \pm 2.0\ MPa$) and UVX ($11.4 \pm 3.6\ MPa$ and $11.8 \pm 1.5\ MPa$) treated samples (see Figure 4.22). Thus, tissue stiffness appears to be influenced by hydration levels, and the longer rehydration times result in lower values of Young's modulus in the tissue.

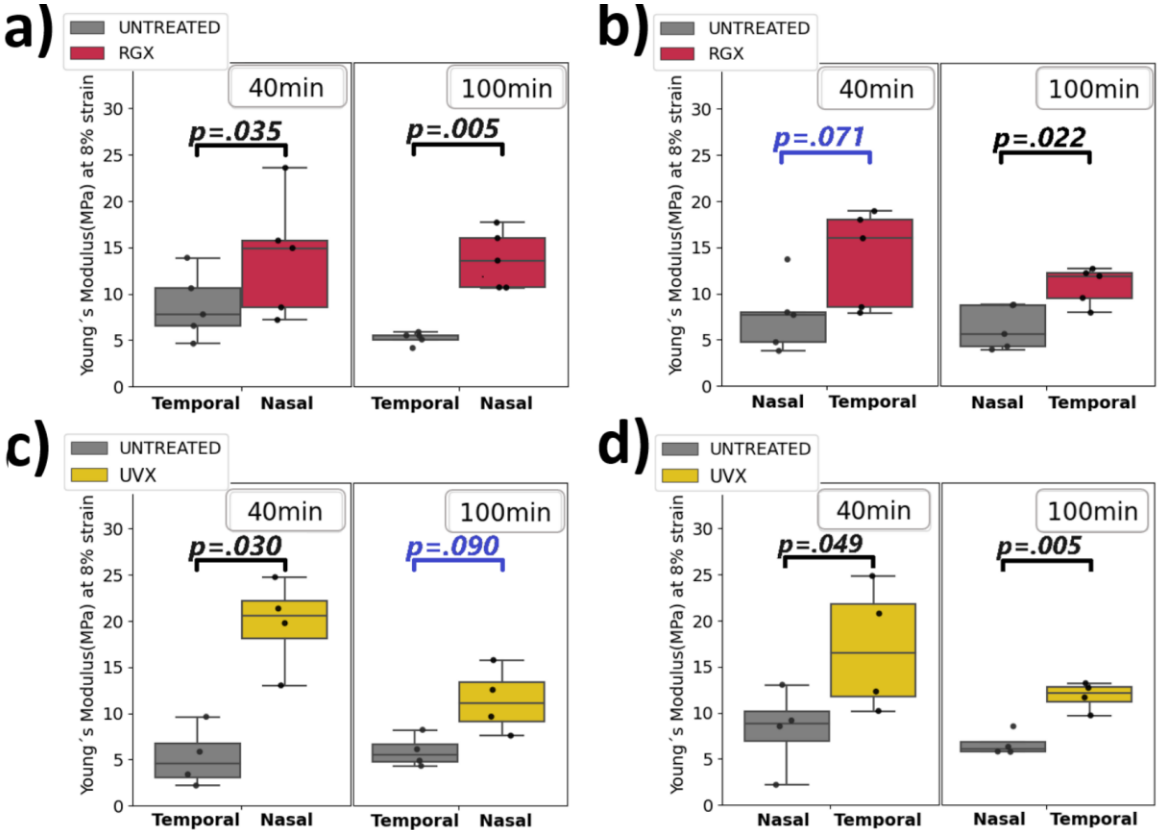

Figure 4.22: Decrease in stiffness after rehydration. Boxplot shows the Young's modulus at 8% strain from the posterior temporal and nasal regions (a and b) for RGX-treated regions (red) and contralateral untreated regions (gray), and (c and d) for UVX (yellow) and their respective contralateral untreated samples (gray). Strips (20 strips (RGX) and 16 strips (UVX)) were rehydrated for 40 min or 100 min. p-values are shown in the graph for significant (in black) and non-significant (in blue) differences between respective groups. Black dots indicate data points, each of which represents a different strip.

	Young's Modulus (MPa)			
	RGX		**UVX**	
	40 min rehydration	**100 min rehydration**	**40 min rehydration**	**100 min rehydration**
Untreated sclera	8.1(5.6-10.7)	5.7(4.5-7.0)	6.7(3.4-10.1)	6.2(5.0-7.5)
Crosslinked sclera	13.9(9.9-17.9)	12.3(10.2-14.4)	18.4(13.6-23.2)	11.6(9.5-13.7)
Difference	***5.8*** ↑	***6.6*** ↑	***11.7*** ↑	***5.4*** ↑

Table 4.11: Mean values (and 95% confidence intervals) of Young's modulus at 8% strain for untreated and crosslinked scleral tissue. Further significant comparisons between regions are shown in Figure 4.22. The completed table is presented in Annexes, Section C.

4.3.2.5. Swelling ratio and Young's modulus correlation

The relationship between swelling and stiffness was tested by measuring swelling before tensile test (see Section 4.3.1.4). Swelling was determined as the percentage of PBS uptake by dry scleral tissue (see Section 3.8.5). Final swelling ratio before stretching and Young's modulus measurements were inversely correlated in RGX ($r = -0.514$, $p = .021$), UVX ($r = -0.514$, $p = .042$), and untreated sclera ($r = -0.541$, $p = .014$, in RGX-treated eyes). Correlation values are shown in the corresponding comparison in Figures 4.23 and 4.24. Specifically, strong inverse correlations were found in temporal scleral tissue ($r = -0.622$, $p = .045$) in RGX-treated eyes (see Figure 4.23 right side in dark red) and in nasal tissue ($r = -0.758$, $p = .037$) in UVX-treated eyes (see Figure 4.24 right side in light yellow), underlying a possible influence not only of the treatment applied but also of the scleral region (nasal and temporal). As expected, the lower the swelling, the higher the stiffness in both treated and untreated scleral samples. Higher correlation coefficients were found in the RGX-treated tissue.

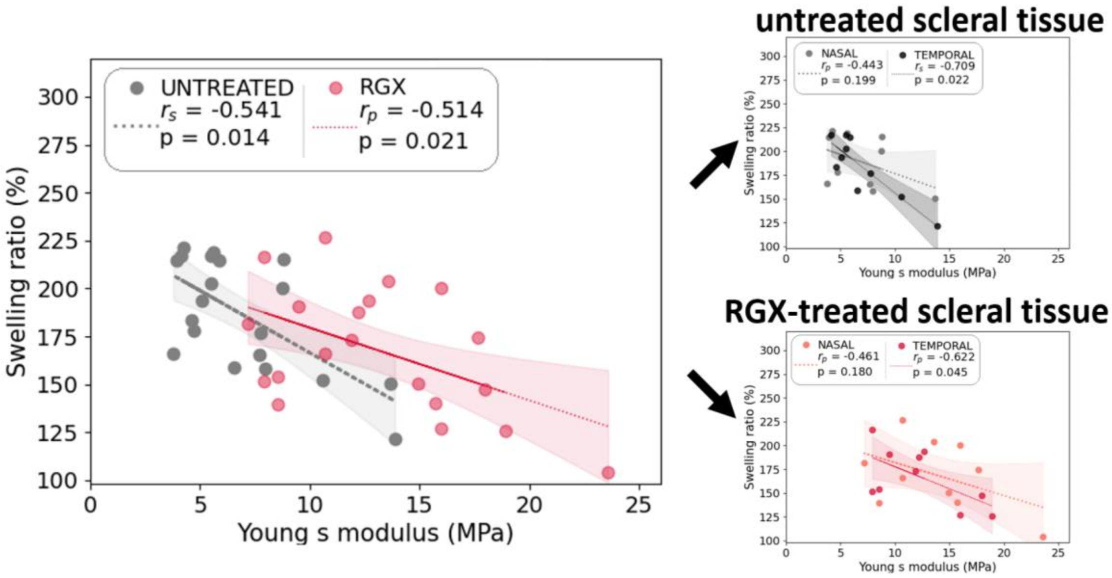

Figure 4.23: Inverse correlation between swelling and stiffness of RGX and untreated sclera. The swelling ratio before stretching and the corresponding Young's modulus at 8% strain of each strip represented as scatterplots for the untreated sclera (gray dots) and for RGX-treated sclera (red dots). Dashed lines represent the corresponding linear regressions, and shaded areas represent 95% of confidence interval for data. Spearman or Pearson correlation coefficients, respectively, and associated p-values are shown in the upper left corner. On the right, scatterplots of the data are divided by nasal (light colors) and temporal region (dark colors).

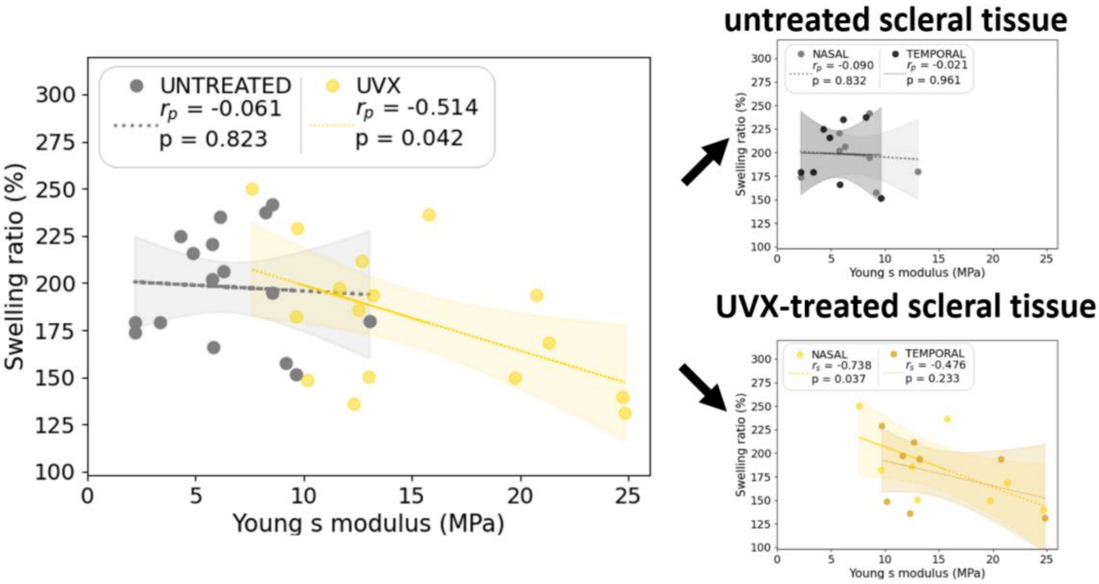

Figure 4.24: Inverse correlation between swelling and stiffness of UVX and untreated sclera. Swelling ratio before stretching and the corresponding Young's modulus at 8% strain of each strip represented as scatterplots for the untreated sclera (grey dots) and for UVX-treated sclera (yellow dots). Dashed lines represent the corresponding linear regressions, and shaded areas represent 95% of confidence interval for data. Spearman or

Pearson correlation coefficients, respectively, and associated p-values are shown in the upper left corner. On the right, scatterplots of the data are divided by nasal (light colors) and temporal region (dark colors).

4.3.2.6. RGX and UVX treatment comparison

Figure 4.25 illustrates the nonlinear stress-strain behavior of all evaluated tissues and scleral regions. A qualitative comparison of the nonlinearity between the curves is made by measuring the similarity using the discrete Fréchet distance (Eiter and Mannila, 1994) between the RGX curve and the naïve curve (~86% similarity) and between the UVX curve and the naïve curve (~67% similarity); see Figure 4.25a. To determine the influence of the treatment on the control tissue, the stress-strain curves of the contralateral tissue after treatment (labelled as: "untreated in UVX" or "untreated in RGX") were compared with the curves of the naïve tissue (see Figure 4.25b). At 8% strain, the stiffness of the non-UVX-treated sclera ($7.9 \pm 2.8\ MPa$, grey curves) is higher than that of the naïve tissue ($6.0 \pm 3.2\ MPa$, blue curves) and the non-RGX-treated sclera ($4.1 \pm 2.2\ MPa$, black curves). There is only a statistical difference in stiffness between control and treated eyes ($p = .026$). There is no difference in stiffness between control and naive tissue ($p > .050$), nor between nasal and temporal areas. The change in Young's modulus after RGX and UVX, even in the untreated area, suggested an overall change in scleral sheath stiffness due to photo-crosslinking treatment.

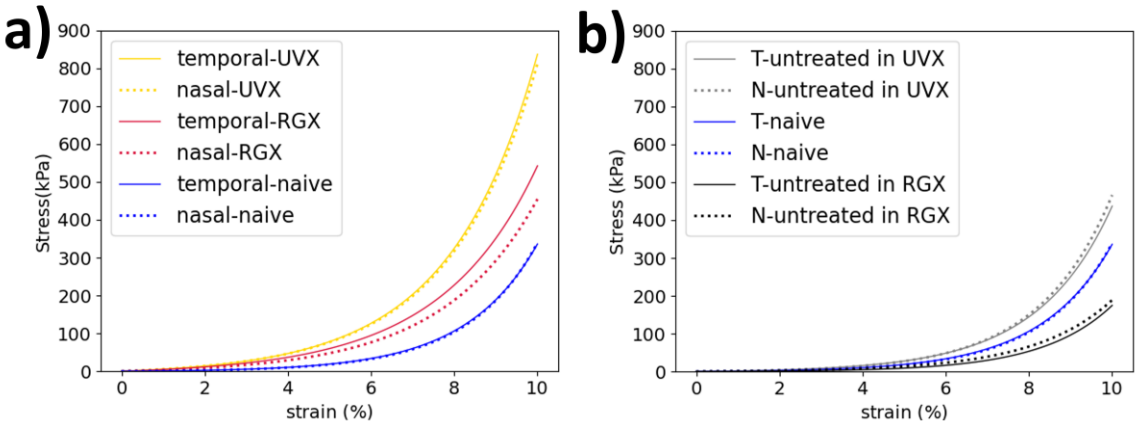

Figure 4.25: Higher stress in treated regions. a) Mean stress-strain curves for UVX-treated (yellow), RGX-treated(red) and naïve (blue) scleral strips. b) Mean stress-strain curves for untreated tissue and naïve tissue in nasal (N) and temporal (T) regions, respectively.

To compare the results of RGX and UVX treatments in the sclera, differences in Young's modulus were calculated between the treated regions and the corresponding contralateral untreated regions (see data in sections 4.3.2.2 and 4.3.2.4). Figure 4.26a shows slightly higher values of Young's modulus after UVX treatment than after RGX treatment (~54% of similarity). In fact, the stiffness increased almost 1.7 MPa more after UVX (7.1 MPa) compared to the increase after RGX treatment (5.4 MPa) at 8% strain (see green shaded area in Figure 4.26a and Table 4.9). However, the effect of treatment on the increase in Young's modulus was not significant (p-values in blue, Figure 4.26b) in scleral tissues stretched immediately after treatment and after 100 min of rehydration. Surprisingly, the increase in tissue stiffness after 40 min of rehydration was statistically dependent on treatment ($p = .045$), with higher values in UVX-treated samples ($11.6 \pm 6.7 MPa$), see Figure 4.26b and Table 4.11. The results suggest that changes in scleral stiffness were influenced by the application of the UVX method only at shorter rehydration times.

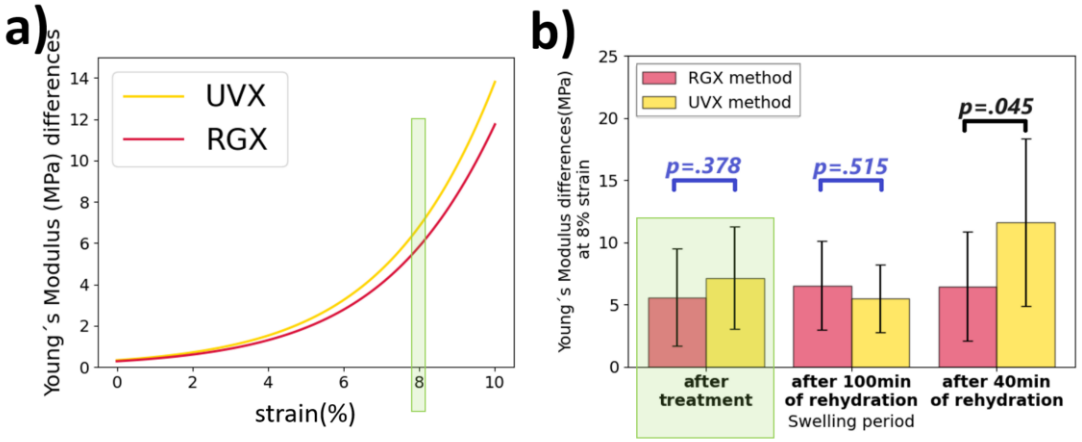

Figure 4.26: Comparison of stiffness differences. a) Average modulus versus strain curves for the RGX and UVX methods. The data shown in the green shaded area are the same as those used to calculate the difference at 8% strain in figure b on the right-hand side. b) The bar plot shows the differences in Young's modulus between treated and untreated tissue for RGX-treated eyes (red) and UVX-treated eyes (yellow). Stiffness was compared for strips stretched immediately after treatment, after 100 min and after 40 min of rehydration. p-values are indicated for non-significant (in blue) and significant (in black) differences between the respective groups. The image (b) was adapted from (Villegas et al., 2024a) , and used with the permission of the authors.

4.3.2.7. Collagen organization after RGX and UVX treatment

The Order coefficient (see Section 3.9) is a measure of the uniformity of fiber direction (1 for oriented in one direction and 0 for uniform distribution). RGX and UVX treatments significantly ($p < 0.01$) increased OC by 5.1% and 3.9%, respectively, in the nasal region, and UVX increased OC by 2.2% ($p < 0.05$) and RGX decreased OC by 1.5% in the temporal region in comparison to untreated sclera (see Figure 4.27). In the nasal scleral region, the OC was 0.400 ± 0.008 in untreated tissue, 0.421 ± 0.007 in RGX-treated tissue, and 0.417 ± 0.012 in UVX-treated tissue. For the temporal scleral region, 0.413 ± 0.007 in untreated tissue, 0.407 ± 0.014 in RGX-treated tissue, and 0.422 ± 0.010 (T) in UVX-treated tissue. UVX produced a higher collagen organization in rabbit sclera than RGX.

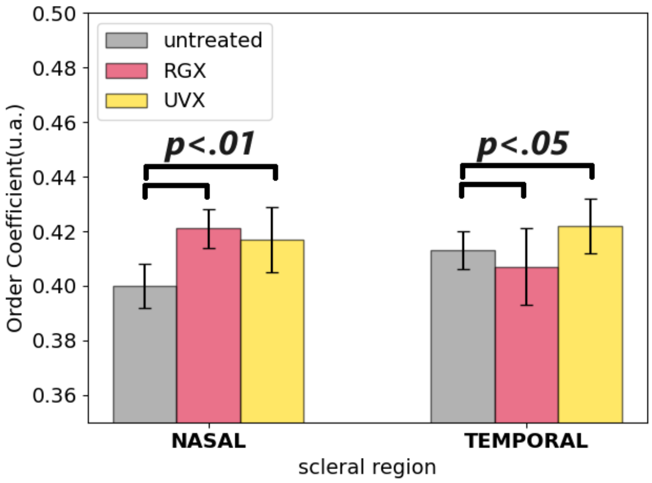

Figure 4.27: Changes in order coefficient in treated and untreated sclera. Average order coefficient for untreated (gray bars), RGX-treated (red bars) and UVX-treated (yellow bars) tissue from nasal and temporal scleral regions. p-values were obtained after T-test and are indicated between the respective groups. Data provided by Dr. James Germann, with partial results published in ARVO abstract 2021;62(8):3276 (Germann et al., 2021).

4.4. Scleral Biomechanics after Myopia Induction

The biomechanics of healthy porcine and rabbit scleral tissues have been studied using Air-puff Deformation Imaging (Chapter 4.1) and Ultrasound Optical Coherence Elastography (Chapter 4.2). The results indicated that the tissue response depends on the scleral region, the thickness, and the internal structure of the tissue (collagen fiber bundles), which varies between animal models. Furthermore, an increase in rabbit scleral stiffness after photo-crosslinking was demonstrated (Chapter 4.3). Conversely, it is known that scleral remodeling occurs during the development of myopia, therefore it is of interest to study the biomechanical parallels of excessive axial elongation in myopia.

This subchapter presents protocols and results of *in vivo,* and *ex vivo* experiments on guinea pig eyes. In the *in vivo* studies, myopia was induced in one of the guinea pig eyes by light deprivation, and the other eye was left as a control. All myopic eyes were treated, and the axial lengths and refractive errors of each eye were measured during myopia induction. In the *ex vivo* studies, changes in scleral biomechanics in the enucleated eyes were quantified by ACUS-OCE and uniaxial tensile tests. Finally, the orientation of the collagen fibers in the scleral tissue was estimated by SHG microscopy.

Part of this subchapter is based on the following contributions: *poster presentation* of Lupe Villegas *et al.* at Association for Research in Vision and Ophthalmology (ARVO) Annual Meeting on April 23-27, 2023 in New Orleans-USA with the title "Myopia control by atropine and latanoprost in a guinea pig model", *paper presentation* of James Germann *et al.* in the same meeting with the title "Effects of pharmacological treatments of myopia on scleral collagen organization in myopic guinea pig models", and the *invited talked* of Susana Marcos at the International Myopia Conference on 25-28 September, 2024 in Sanya-China with the tittle "Scleral biomechanics and collagen organization in myopia and treatment".

4.4.1. Protocols

4.4.1.1. Animals and form-deprived myopia model

Six guinea pigs (2-12 weeks-old, see section 3.2) are presented, divided into four groups: (1) saline (control group, n=2), (2) latanoprost (n=2) and (3) atropine (n=2) (see Table 4.12). All animals in groups 1-3 underwent monocular FDM (see Section 3.10.1) with removable plastic diffuser in one eye for 10 weeks (see Figure 4.28a). The same eye was also treated with one of the three treatments (saline, latanoprost, or atropine). Untreated contralateral eyes served as controls in all groups.

After 10 weeks of myopia induction, all guinea pigs were euthanized by an overdose of anesthesia (Pentobarbital, 50 mg/kg). The animal was first anesthetized by inhalation (isoflurane, 1.5-2% oxygen) for 1 minute, followed by an intraperitoneal injection of pentobarbital (Dolethal, 200 mg/ml, Vetoquinol S.A.). Both eyes were enucleated and fresh tissue (<24h hours postmortem) was used for OCE and tensile measurements. The tissue was then preserved in Formaldehyde solution (4% w/v in PBS, Sigma-Adrich, Switzerland). The animal was anesthetized throughout the treatment and its vital signs were monitored with the assistance of Javier Fernández Martínez (veterinarian) and Luis Revuelta Rueda (animal project supervisor).

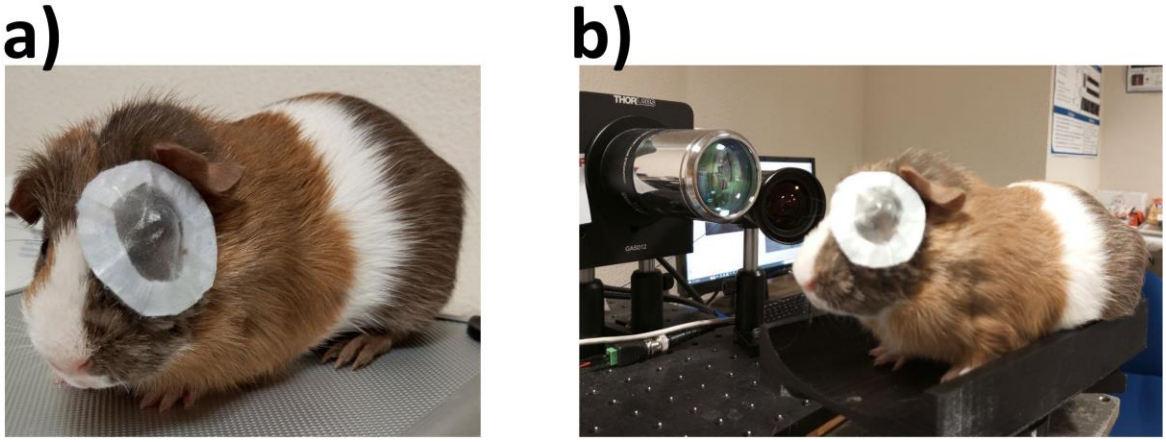

Figure 4.28: Photographs of guinea pigs during myopia induction period. a) Guinea pig wearing a diffuser attached to the left eye. b) Guinea pig undergoing axial length measurement with the 3D Biometer.

For the *in vivo* procedures, customized OCT-based biometric measurements (see Section 3.10.2 and Figure 4.28b) were performed to obtain axial length and retinoscopy (see Section 3.10.3) was performed to obtain the spherical equivalent during the course of myopia induction. During this period, six biometric measurements were performed on awake guinea pigs. For the *ex vivo* procedures, OCE measurements (see Section 3.7.1) were performed to obtain shear modulus and then Young's modulus was obtained from tensile testing (see Section 3.8.1). After tensile testing, scleral strips were stored in formaldehyde solution for subsequent SHG measurements to obtain collagen ordering (see Section 3.9).

Group name	Number of guinea pigs	Method	Resulting parameter
Saline	2	Myopia induction (Section 4.4.1.1), saline treatment (Section 4.4.1.2), biometric measurements (Section	Axial length, spherical equivalent, shear

		4.4.1.3), OCE measurements (Section 4.4.1.4), tensile tests (Section 4.4.1.4), SHG microscopy imaging (Section 4.4.1.4)	modulus, Young's modulus, order coefficient.
Latanoprost	2	Myopia induction (Section 4.4.1.1), latanoprost treatment (Section 4.4.1.2), biometric measurements (Section 4.4.1.3) OCE measurements (Section 4.4.1.4), tensile tests (Section 4.4.1.4), SHG microscopy imaging (Section 4.4.1.4)	Axial length, spherical equivalent, shear modulus, Young's modulus, order coefficient.
Atropine	2	Myopia induction (Section 4.4.1.1), atropine treatment (Section 4.4.1.2), biometric measurements (Section 4.4.1.3), OCE measurements (Section 4.4.1.4), tensile tests (Section 4.4.1.4), SHG microscopy imaging (Section 4.4.1.4)	Axial length, spherical equivalent, shear modulus, Young's modulus, order coefficient.

Table 4.12: Overview of the different experiments and data collection. OCE: Optical Coherence Elastography, RGX: Rose Bengal with green light crosslinking. SHG: second harmonic generation

4.4.1.2. Pharmacological treatment procedures

The myopic eye (see Section 3.10.1) of each animal in its respective group was treated (from postnatal day 21) with a daily drop of one of the following treatments: saline solution (sterile BSS), atropine (1%, see section 3.11.3), or latanoprost (0.005%, see section 3.11.4).

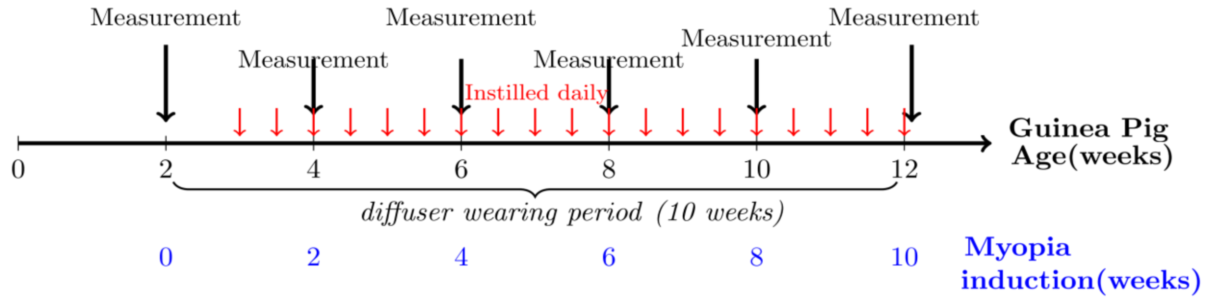

Figure 4.29: Timeline of treatment during the myopia induction period. Guinea pigs (2 weeks old, shown in black numbers) were induced myopia using an attached diffuser in one eye for 10 weeks (shown in blue numbers). During induction, biometric measurements (shown with black arrows) were performed on awake guinea pigs at 0, 2, 4, 6, 8, and 10 weeks. Animals were treated by daily instillation of saline, atropine or latanoprost drops (shown with red arrows). During this period, six biometric measurements were performed on awake guinea pigs.

4.4.1.3. Axial lengths and refractive error measurements

For the *in vivo* procedures, form-deprived animals (see Section 3.10.1) underwent biometric measurements at 6 time points (0, 2, 4, 6, 8, and 10 weeks) during the myopic induction period (see timeline in Figure 4.29). Axial lengths and refractive errors were measured in treated and untreated eyes of awake animals using a SS-OCT 3D Biometer (see Section 3.5.3) and using retinoscopy (see Section 3.4.2), respectively. From the Biometer images, the axial length was manually estimated (see Figure 3.22 in Section 3.10.2). From the refractive error measurements, the spherical equivalent was estimated per eye (see Section 3.10.3).

4.4.1.4. Biomechanics and microscopy measurements of scleral specimens

Treated and untreated eyes were used for biomechanical measurements. After 10 weeks of myopia induction, animals were euthanized by an overdose of anesthesia (see Section 4.4.1.1). For the *ex vivo* procedures, both ocular globes were enucleated, prepared (as in Methods Section 3.1), and were subjected to ACUS-OCE measurements (see Section 3.7.1). The shear moduli were estimated from wave speeds (see Section 3.7.3). Subsequently, one corneal and four scleral strips (one strip per zone, see Figure 4.30) were removed (less than 3 hours post-mortem). Scleral strips ($1.0\,mm \times 3.0\,mm$, 4 strips per eye) were cut transversely and subjected to uniaxial tests (see Section 3.8.1). From stress-strain curve fitting, Young's modulus at 14% strain was calculated (see Section 3.8.2). Finally, scleral strips were stored in formaldehyde solution (4% w/v in PBS) for subsequent SHG microscopy measurements (see Section 3.9). The order coefficient was estimated from the SHG images.

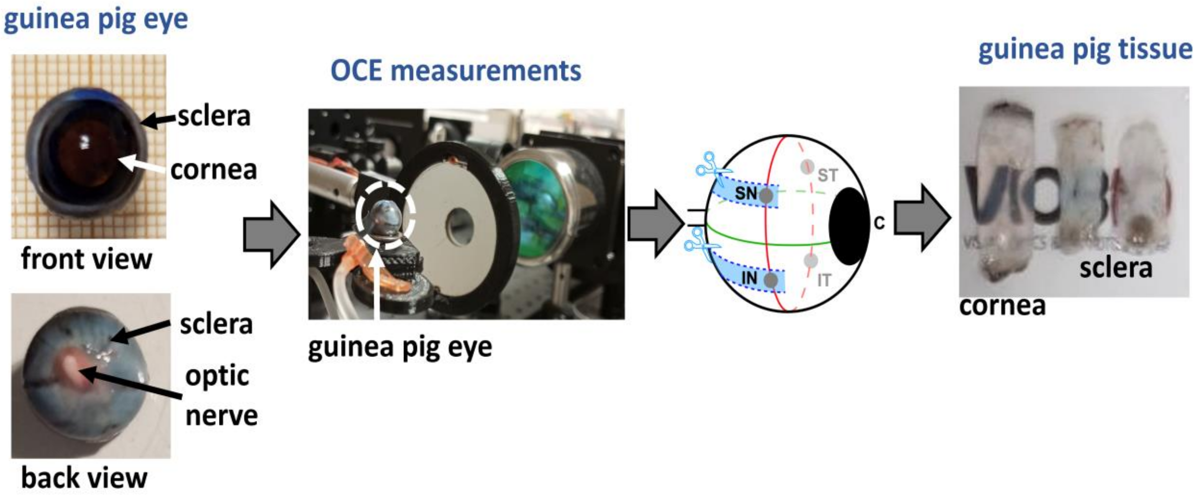

Figure 4.30: Schematic representation of *ex vivo* procedures. Guinea pig eyes were tested by the OCE method, where IOP was monitored by needle cannulation. After OCE measurements, the eyes were dissected, and one corneal and four scleral strips were removed. The scleral strips were taken from SN (superior nasal), IN (inferior nasal), ST (superior temporal) and IT (inferior temporal) zones. The ocular tissues were subjected to tensile test, and then second harmonic generation microscopy images were obtained.

4.4.1.5. Statistical analysis

The data were analyzed using IBM SPSS Statistics (Version 29.0, Armonk, NY: IBM Corp). ANOVAs with repeated measures were performed to evaluate differences in axial lengths, spherical equivalent, wave speed and Young's modulus, order coefficient in the corresponding groups. Multiple comparison was adjusted by Bonferroni correction. Statistical significance was set at p-value of 0.05. All values in bar plots and line plots are indicated as mean± standard deviation.

4.4.2. Evaluating Biometric and Biomechanical Changes Throughout Myopia Induction

4.4.2.1. Change in axial length measurements during myopia induction

The axial length was examined immediately before (week 0) and at weeks 2, 4, 6, 8, and 10 after myopia induction. At baseline, there were no significant differences in AXL between the three groups (see Figure 4.31). However, over time, the AXL between the nonmyopic eye (fellow eye) and the treated eye (form-deprived eye) became progressively longer in the saline (Figure 4.31a), latanoprost (Figure

4.31.b) and atropine (Figure 4.31c) groups. After 10 weeks of FD, the axial lengths of the myopic eyes (form-deprived +treatment) were longer than those of the nonmyopic eyes in all groups: saline ($9.06 \pm 0.15\,mm$ vs. $8.81 \pm 0.08\,mm$, black curves), latanoprost ($9.14 \pm 0.01\,mm$ vs. $8.97 \pm 0.04\,mm$, red curves), and atropine ($8.97 \pm 0.01\,mm$ vs. $8.79 \pm 0.03\,mm$, blue lines), see Figure 4.31 and Table 4.13 for details.

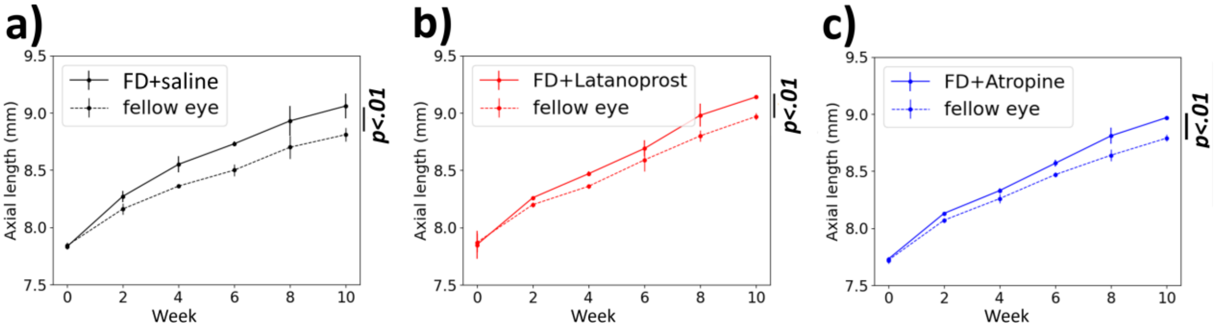

Figure 4.31: Comparison of axial length between groups during the myopic induction period. Line graph showing axial lengths (in millimeters, mm) in myopic (form-deprived and treated) and in nonmyopic (fellow) eyes of guinea pigs in the saline group (a), latanoprost group (b) and atropine group (c). Data from myopic eyes are shown as solid lines and data from nonmyopic eyes are shown as dashed lines. FD stands for form-deprived eye. Error bars represent standard error.

Pharmacological treatment	**Eye**	**Axial length (mm) at 0 week**	**Axial length (mm) at 6 weeks**	**Axial length (mm) at 10 weeks**
Saline	FD (treated)	7.83 ± 0.01	8.73 ± 0.03	9.06 ± 0.15
	Fellow(untreated)	7.84 ± 0.04	8.50 ± 0.07	8.81 ± 0.08
Latanoprost	FD (treated)	7.85 ± 0.18	8.69 ± 0.11	9.14 ± 0.01
	Fellow (untreated)	7.87 ± 0.12	8.59 ± 0.15	8.97 ± 0.04
Atropine	FD (treated)	7.73 ± 0.01	8.57 ± 0.03	8.97 ± 0.01
	Fellow (untreated)	7.72 ± 0.03	8.47 ± 0.02	8.79 ± 0.03

Table 4.13: Axial length values of guinea pig eyes for each group. Mean values ± standard deviations of axial length (in millimeters) after 0, 6, and 10 weeks of myopia induction.

Values measured for form-deprived (FD) and corresponding fellow guinea pig eyes. Comparisons along the entire myopia induction period are shown in Figure 4.31. The completed table is presented in Annexes, Section D, Tables D1 and D2.

4.4.2.2. Changes in refractive error during myopia induction

The refractive error was monitored weekly (at 0, 2, 4, 5, 8, 10 weeks) after myopia induction. At baseline, there were no significant differences in spherical equivalent between the three groups (see Figure 4.32). Over time, the refractive error between the nonmyopic eye (fellow eye) and treated eye (form-deprived eye) became significantly longer in the saline (Figure 4.32a), latanoprost (Figure 4.32b) and atropine (Figure 4.32c) groups. After 10 weeks of induction, the form-deprived eyes exhibited more negative refractive errors than their corresponding fellow eyes in all groups: saline ($-6.1 \pm 0.8\,D$ vs. $1.3 \pm 0.1\ D$, black curves), latanoprost ($-3.0 \pm 1.3\,D$ vs. $1.6 \pm 0.5\,D$, red curves), atropine ($-3.4 \pm 1.4\ D$ vs. $1.0 \pm 0.2\,D$, blue lines), see Figure 4.32 and Table 4.14 for details.

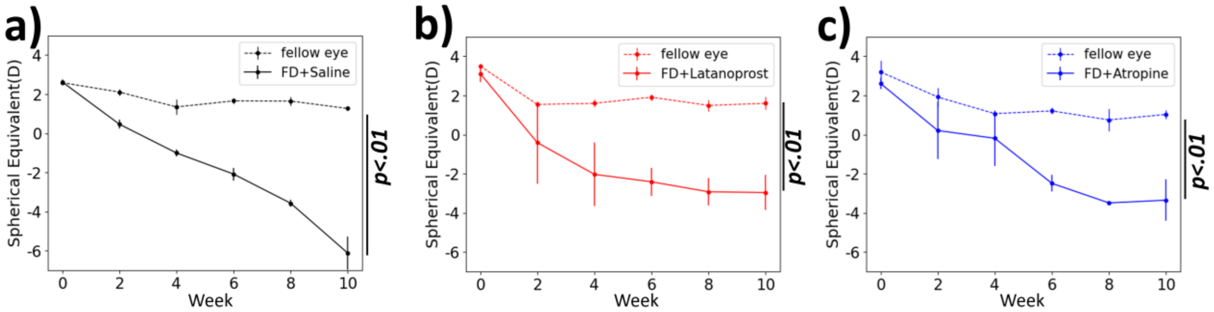

Figure 4.32: Comparison of spherical equivalent between groups during the myopic induction period. Line graph showing spherical equivalent values (in Diopters, D) in nonmyopic (fellow) and myopic (form-deprived (FD) and treated) eyes of guinea pigs in the saline group (a), latanoprost group (b) and atropine group (c). Data from nonmyopic eyes are shown as dashed lines and data from myopic eyes are shown as solid lines. Error bars represent standard error. Spherical equivalent ≤ -0.50D measured in either eye in humans (see Section 3.3) is considered myopia according to WHO (World Health Organization and Brien Holden Vision Institute, 2016).

Pharmacological treatment	**Eye**	**Spherical equivalent (D) at 0 week**	**Spherical equivalent (D) at 6 weeks**	**Spherical equivalent (D) at 10 weeks**

Saline	FD (treated)	2.6 ± 0.1	-2.1 ± 0.3*	-6.1 ± 0.8**
	Fellow (untreated)	2.6 ± 0.1	1.7 ± 0.2	1.3 ± 0.1
Latanoprost	FD (treated)	3.1 ± 0.6	-2.4 ± 1.0*	-3.0 ± 1.3*
	Fellow (untreated)	3.5 ± 0.2	1.9 ± 0.2	1.6 ± 0.5
Atropine	FD (treated)	2.6 ± 0.4	-2.5 ± 0.5*	-3.4 ± 1.4*
	Fellow (untreated)	3.2 ± 0.6	1.2 ± 0.2	1.0 ± 0.2

Table 4.14: Spherical equivalent values of guinea pig eyes for each group. Mean values ± standard deviations of spherical equivalent (in diopters) after 0, 6, and 10 weeks of myopia induction. Values measured for form-deprived (FD) and corresponding fellow guinea pig eyes. Comparisons of the entire myopia induction period are shown in Figure 4.32. *****: Spherical equivalent ≤ -0.50D in either eye in humans is considered *myopia* and ******: spherical equivalent ≤-5.00D is *high myopia* according to WHO (World Health Organization and Brien Holden Vision Institute, 2016). The completed table is presented in Annexes, Section D, Tables D3 and D4.

4.4.2.3. Comparison of saline, latanoprost and atropine biometric measurements

When comparing treatments, the interocular difference in axial length appeared to increase similarly between atropine and latanoprost groups (see Figure 4.33a), and the difference in spherical equivalent showed a reduction effect in latanoprost and atropine groups at 6 weeks (Figure 4.33b). After 6 weeks of myopic induction, the myopic eye was $0.22 \pm 0.02\,mm$ (saline), $0.10 \pm 0.01\,mm$ (latanoprost), $0.09 \pm 0.02\,mm$ (atropine) longer and its refraction was $-3.7 \pm 0.2\,D$ (saline), $-4.3 \pm 1.42\,D$ (latanoprost), $-3.7 \pm 0.7\,D$ (atropine) higher than that of the nonmyopic eye. At the end of the myopia induction period, the myopic eye was $0.24 \pm 0.05\,mm$ (saline), $0.18 \pm 0.03\,mm$ (latanoprost), $0.18 \pm 0.04\,mm$ (atropine) longer and its refraction was $-7.4 \pm 0.93\,D$ (saline), $-4.6 \pm 1.22\,D$ (latanoprost), $-4.4 \pm 1.6\,D$ (atropine) higher than that of the fellow nonmyopic eye. Results suggest that latanoprost and atropine treatments have a similar effect over biometric measurements.

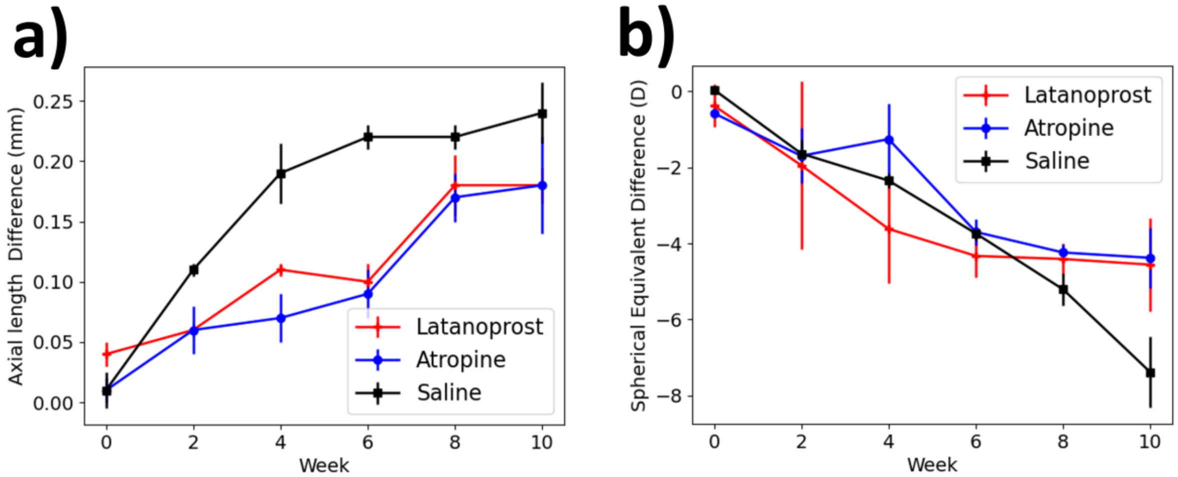

Figure 4.33: Comparison of interocular difference between groups during the myopic induction period. Line graph showing differences in axial length (a) and in spherical equivalent (b) between nonmyopic (fellow) and myopic (treated) eyes of guinea pigs in the saline group (black line), atropine group (blue line) and latanoprost group (red line). Error bars represent standard error.

4.4.2.4. Scleral biomechanics in nonmyopic and myopic eyes

Animals were euthanized and the elastic properties of the sclera were characterized. Ocular tissues were subjected to OCE measurements and tensile tests. From ACUS-OCE measurements, elastic waves on the scleral surface propagated faster in nontreated tissue than treated tissue (from myopic eyes) in saline ($21.1 \pm 4.8\, m/s$ vs. $19.5 \pm 0.8\, m/s$, black bars) and latanoprost ($15.7 \pm 3.4\, m/s$ vs. $14.3 \pm 2.1\, m/s$, red bars) groups, but waves propagated slower in the atropine group ($8.4 \pm 1.1\, m/s$ vs. $14.6 \pm 5.3\, m/s$, blue bars), see Figure 4.34a for details. This resulted in an increase in the shear modulus in saline ($10.4 \pm 1.3\, MPa$ vs. $10.2 \pm 0.1\, MPa$, black bars) and latanoprost ($9.6 \pm 0.9\, MPa$ vs. $9.5 \pm 0.6\, MPa$, red bars) groups and a decrease in the shear modulus in atropine group ($8.6 \pm 0.2\, MPa$ vs. $9.5 \pm 1.5\, MPa$, blue bars) in the myopic eye compared to the nonmyopic eye (see Figure 4.34b). Interestingly, from the analysis of wave propagation speed in different regions of the sclera (SN, ST, IN, IT), we found significant differences ($p<0.05$) in wave speed in the inferior temporal (IT) sclera of eyes treated with latanoprost ($10.8 \pm 1.2\, m/s$ vs. $20.2 \pm 7.0\, m/s$) and atropine ($21.2 \pm 7.1\, m/s$ vs. $4.1 \pm 2.3\, m/s$) compared with the fellow eye, see Figure D1 in Annexes, Section D .

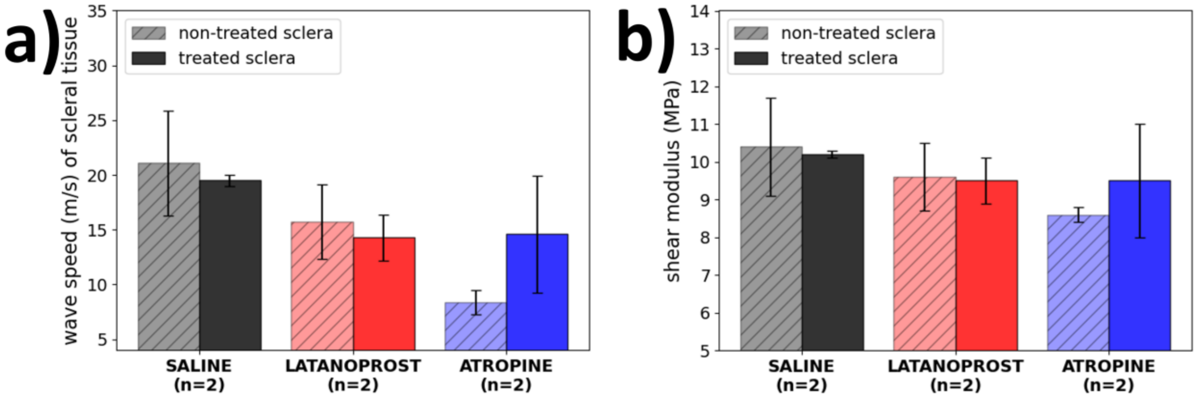

Figure 4.34: Comparison between groups of wave speed and shear modulus of guinea pig sclera. Ocular globes from guinea pigs (n=2 per each group) were subjected to ACUS-OCE measurements. Guinea pig eyes were in the saline (black bars), latanoprost (red bars) or atropine (blue bars) groups. a) Average wave speed values of scleral tissue around different points of the sclera. b) The bar plot shows shear modulus of untreated and treated scleral tissue was estimated from wave speed. Data from untreated tissue (from nonmyopic eyes) are shown as hatched bars and data from treated tissue (from myopic eyes) are shown as solid bars.

From tensile tests, scleral Young's moduli (see Figures 4.35a, 4.35b, 4.35c, left side) of fellow nonmyopic eyes were higher than those of myopic eyes in all groups: saline ($13.0 \pm 0.1\,MPa$ vs. $10.7 \pm 0.7\,MPa$, black bars), latanoprost ($16.3 \pm 1.6\,MPa$ vs. $15.7 \pm 0.6\,MPa$, red bars), and atropine ($7.2 \pm 2.9\,MPa$ vs. $5.7 \pm 2.3\,MPa$, blue bars). Young's moduli of corneas (see Figures 4.35a, 4.35b, 4.35c, right side) of fellow eyes were higher than those of myopic eyes in the saline ($7.0 \pm 1.3\,MPa$ vs. $5.4 \pm 1.2\,MPa$, black boxes) and latanoprost ($4.7 \pm 2.3\,MPa$ vs. $3.6 \pm 1.9\,MPa$, red bars) groups, but not in the atropine group ($2.6 \pm 2.0\,MPa$ vs. $5.8 \pm 1.0\,MPa$, blue bars). The non-significant differences shown between untreated and treated sclera (see Figures 4.35b and 4.35c) may indicate that both myopia-control treatments are able to restore scleral mechanics.

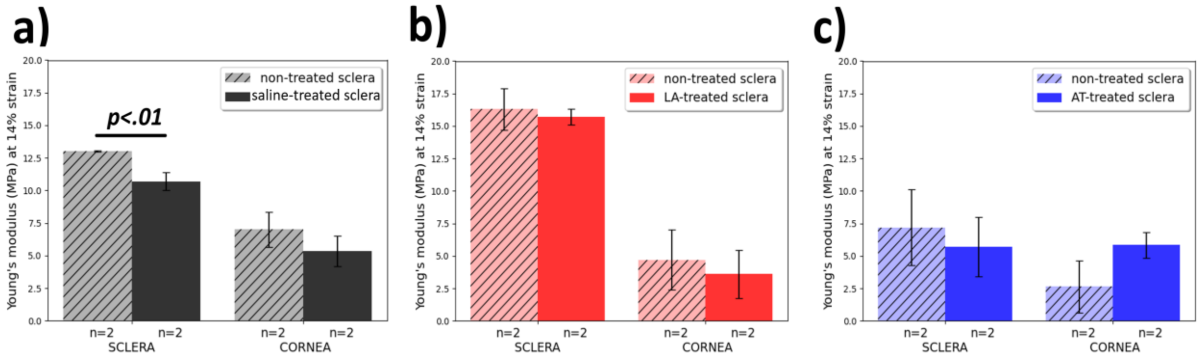

Figure 4.35: Comparison of Young's modulus between groups. Scleral and corneal tissues from guinea pigs (n=2) were subjected to tensile tests. The bar plot shows Young's modulus at 14% strain (four scleral strips per eye) between treated and untreated tissue of guinea pig eyes in the saline group (a), latanoprost group (b), and atropine group (c). Data from non-treated tissue (from nonmyopic eyes) are shown as hatched bars and data from treated tissue (from myopic eyes) are shown as solid bars.

4.4.2.5. Collagen organization in nonmyopic and myopic eyes

SHG imaging of scleral tissues (e.g., see Figure 4.36) allows visualization and quantification of the arrangement of collagen fibers. Three types of collagen fiber variations were identified in the SHG images: areas with marked collagen loss (gradual decrease in collagen fiber intensity), areas with restoration of collagen interweaving (collagen fibers are more intertwined) and areas with loss of collagen interweaving (collagen fibers are straighter). Scleral collagen fibers in myopic eyes appeared to be more aligned (organized in a single direction) in areas of collagen loss (white arrows in Figure 4.36) and interweaving loss (rectangles in Figure 4.36) compared to disorganized interweaving fibers (fibers organized in multiple directions) in the sclera of untreated fellow eyes. In the sclera of latanoprost- and atropine-treated eyes, collagen fibers showed areas of apparent recovery of interweaving (stars in Figure 4.36). The loss of collagen in the sclera of myopic eyes is directly related to the increase in matrix metalloproteinase 2 (MMP-2) in animal models of myopia (H.-H. Liu et al., 2017; Zhao et al., 2018). The production of MMP-2 promotes collagen degradation.

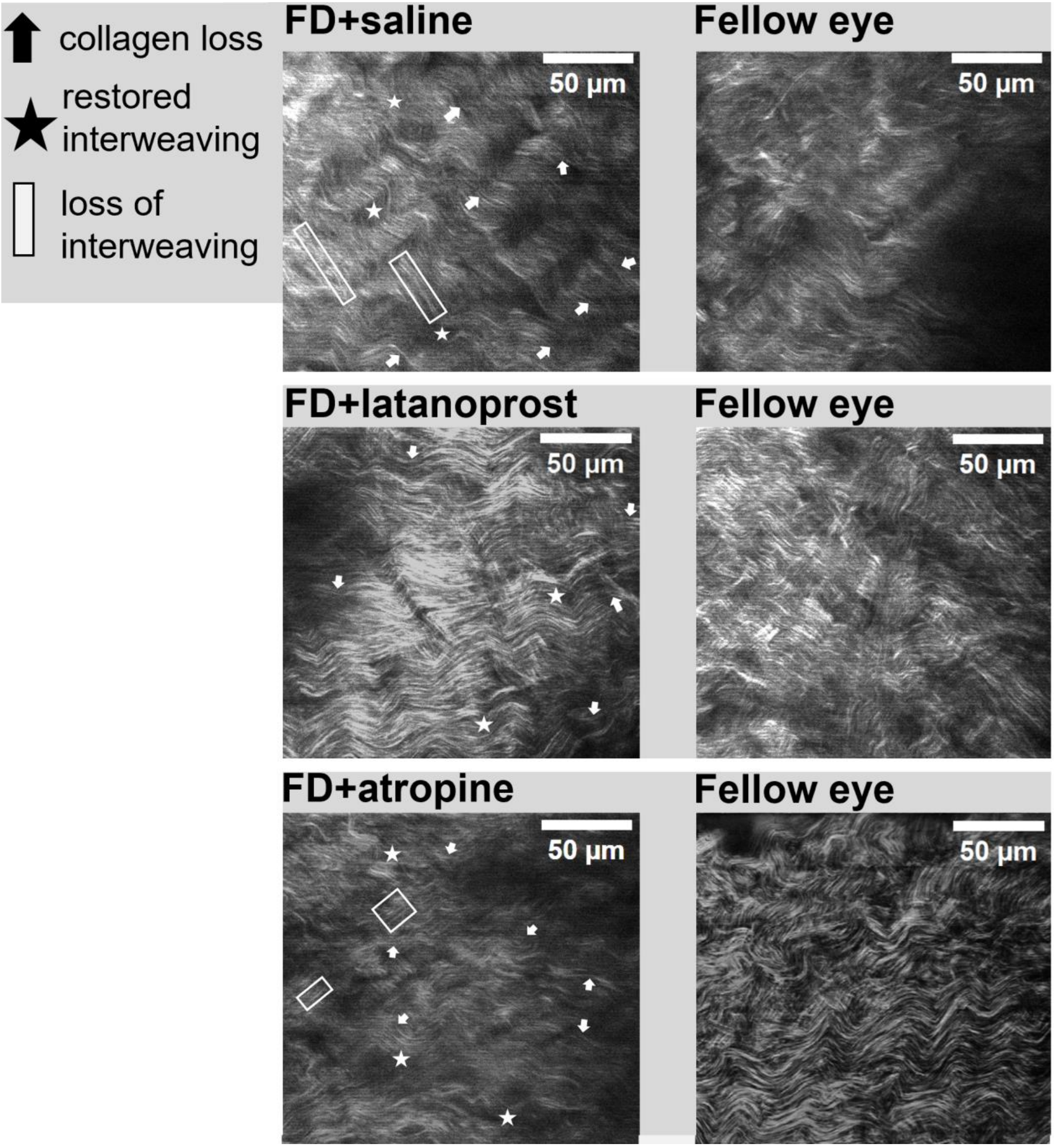

Figure 4.36: Collagen SHG images of guinea pig scleral tissues. SHG images at 40-45 μm below the outer surface of the posterior sclera of myopic treated eyes (left column) and from the corresponding untreated fellow eyes (right column). Myopic eyes were treated with saline (first row), latanoprost (second row) or atropine (third row). Arrows indicate collagen loss in the fibers, stars indicate areas where collagen interweaving was restored, and rectangles indicate areas where collagen interweaving was lost. Data provided by Dr. James Germann, with results published in ARVO Abstract 2023;64(8):2859 (Germann et al., 2023).

From the image processing, we can determine changes in collagen organization along the depth by quantifying the order coefficient (see Section 3.9). The OC is a measure of the uniformity of fiber direction (1 for unidirectional and 0 for random). The order coefficient of fellow nonmyopic eye (non-treated sclera) were lower than that of myopic eyes (treated sclera) in the saline (0.33±0.02 vs. 0.35±0.02, black bars) and atropine (0.34 vs. 0.35, blue bars) groups, but higher in the latanoprost group (0.34±0.02 vs. 0.33±0.01, red bars), see Figure 4.37. The higher OC values in myopic eyes suggests a preferential fiber direction gained by scleral remodeling (see Figure 4.36 left side, with titles: FD+saline and FD+atropine). A significant change in OC (37% increase) only in the scleral tissue of myopic eyes in the saline group suggests that latanoprost and atropine were able to restore substantial changes in collagen fiber organization. Therefore, latanoprost and atropine may prevent microstructural changes during myopia progression.

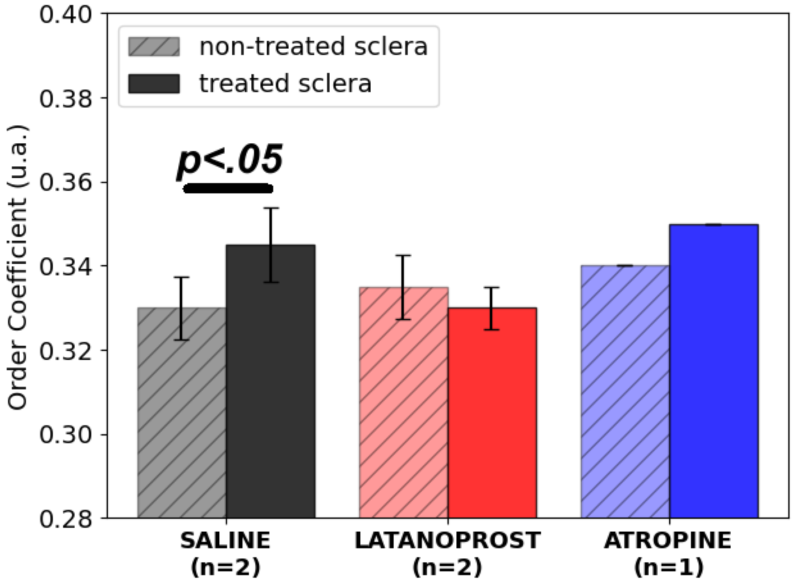

Figure 4.37: Comparison of Order Coefficient between groups. Scleral tissues from guinea pigs (n=2 for saline and latanoprost groups, and n=1 for atropine group) were subjected to SHG microscopy. a) Average order coefficient (organization measurement) of scleral tissue from eyes were treated by saline (black bars), by latanoprost (red bars) or atropine (blue bars) and the fellow untreated eyes (hatched bars). It is shown the number of guinea pigs in each group. Data provided by Dr. James Germann, with partial results published in ARVO abstract 2023;64(8):2859 (Germann et al., 2023).

5. DISCUSSION

This chapter presents the discussion of the results of the thesis. For clarity, the discussion has been divided into four different subchapters. The first subchapter is about scleral biomechanics using Air-puff Deformation Imaging, the second subchapter is about scleral biomechanics using Optical Coherence Elastography, the third subchapter is about scleral biomechanics after scleral crosslinking, and the last subchapter is about scleral biomechanics and biometric measurements after myopia induction.

5.1. Interpretation of Scleral Biomechanics Findings through Air-puff Deformation Imaging

Air-puff deformation imaging was used to study the response of the cornea and sclera at seven locations in porcine and rabbit eyes. Tissue behavior was compared between the two animal models, and the influence of air-puff pressure (AP1 and AP2) was tested only in rabbit eyes. A different deformation response was observed at each location, especially between the cornea and the sclera, for maximum displacement, temporal displacement, and temporal speed. The cornea was one of the most deformed tissues using both animal models with both configurations. In contrast, the maximum deformation in the sclera was found in the superior and inferior locations (porcine) with AP2, in rabbit equatorial sclera with AP1, and in the rabbit equatorial nasal and inferior sclera with AP2. Return speeds to the initial position were at least twice as fast as the deformed speeds during air-puff excitation in both animal models. Comparison between AP1 and AP2 showed that the amplitude of deformations increased (25%) after the high-pressure configuration (AP2) at all locations, except at ET. From FE simulations, the porcine cornea showed a larger nonlinear response and was at least 3 times less stiff than the porcine sclera. Thus, the deformation behavior was not only dependent on the location, but also on the animal model and the air-puff outflow force applied.

Corneal biomechanics have previously been evaluated in *ex vivo* studies using porcine and rabbit eyes. The maximum corneal apex displacement was $1.22 \pm 0.43\ mm$ in porcine eyes at $15\ mmHg$ using a peak pressure of $\sim 14.7\ kPa$ (Kling and Marcos, 2013) or $18.2\ kPa$ (Maczynska et al., 2019a), and $1.31 \pm 0.05\ mm$ in rabbit eyes at 15 $mmHg$ using a commercial system a commercial system (Corvis ST) (Bekesi et al., 2015). Comparable values in this study were $0.98 \pm 0.10\ mm$ in porcine cornea with AP2 ($15.4\ kPa$), but lower in rabbit cornea of $0.86 \pm 0.02\ mm$ with AP1 ($7.8\ kPa$) and $0.90 \pm 0.04\ mm$ with AP2 using eyes at 15 $mmHg$.

The maximum displacement of the apex point showed different values along the sclera, with the superior and inferior locations being five times greater than the equatorial and posterior sclera in porcine eyes. The same was not true for rabbit eyes, where the equatorial (ET with AP1 and EN with AP2) was at most 1.5 times greater than other scleral locations. Although the IOP was set at 15 $mmHg$ in both animal models and the same AP2 configuration was used, these discrepancies in results may be partly due to the geometry of the ocular globe. The porcine eyeball is elliptical in shape, whereas the rabbit eyeball is more spherical (Vézina, 2013). In adult porcine eyes (Bartholomew et al., 1997), the mean axial length ($20.33 - 21.64\ mm$) was measured to be 13% smaller than the equatorial diameter ($24.48 - 25.48\ mm$). In comparison, rabbit eyes (8 weeks old) have similar values of the axial length ($16.24 \pm 0.01\ mm$) and equatorial diameter ($16.24 \pm 0.01\ mm$) (Barathi et al., 2002).

Scleral thickness varies across the sclera in different species, including humans (Norman et al., 2010; Vézina, 2013). In adult animals, the thickness of porcine sclera (from big-sized animal of 27-81 kg) varies significantly from $430.0 \pm 160.0\ \mu m$ to $1120.0 \pm 23.0\ \mu m$ (Olsen et al., 2002) and rabbit sclera (from 18-weeks-old animals weighing 3-4 kg) varies from $275.6 \pm 39.5\ \mu m$ to $382.8 \pm 54.6\ \mu m$ (Barathi et al., 2002). However, the thickness varies not only with the size of the eye but also with the region of the eye. In the case of the porcine eye, the minimum thickness occurred $\sim 6\ mm$ from the limbus; in the rabbit, the minimum thickness occurred $\sim 2\ mm$ from the limbus (Barathi et al., 2002; Olsen et al., 2002). Near the equator (region measured during these experiments in this thesis), the recorded thickness was $860.0 \pm 180.0\ \mu m$ in porcine eyes and $300.9 \pm 40.5\ \mu m$ in rabbits. Porcine sclera was measured to be at least twice as thick as rabbit sclera. Greater thicknesses were reported in the posterior sclera (Olsen et al., 2002), which may explain the small amplitude of deformation observed in porcine eyes, but not the behavior of the rabbit sclera.

Changes in arc length over time are related to the compression/extension behavior of the tissue during air puff deformation. In porcine scleral tissue, there were differences in arc length when comparing the superior and inferior locations, which undergo extension, with the equatorial and posterior locations, which undergo compression. This is not the case in rabbit tissue, where all locations analyzed showed an overall compressive response. A possible explanation for the influence of the air puff on the change in arc length between species may be related to the tissue structure, specifically the arrangement of collagen fibers. The cornea and sclera are composed of collagen fibers (see Section 2.1) that intertwine to form bundles of varying width and thickness (Komai and Ushiki, 1991). The orientation of the collagen bundles is also moderately organized in the cornea and an interwoven structure in the sclera (Komai and Ushiki, 1991; Watson and Young, 2004). Significant differences in the interlamellar distance of collagen from porcine ($6460 \pm 1180\,nm$) and rabbit ($4410 \pm 1330\,nm$) corneas were found by light and transmission electron microscopy (Subasinghe et al., 2021). Although the fibrillar diameters of collagen were similar between porcine ($32.87 \pm 0.87\,nm$) and rabbit ($33.67 \pm 1.97\,nm$) corneal tissue (Subasinghe et al., 2021), this greater distance between lamellae suggests that these variations in the transverse organization of collagen may influence biomechanics and produce different responses depending on the animal model used.

Young’s moduli of porcine cornea and sclera were determined for each location using finite element modeling and experimental air-puff deformation data. The Young’s modulus of the porcine cornea was equivalent to previously reported valued of $0.99\text{–}1.59\,MPa$ (Bekesi et al., 2016a), with a similar value to the estimated value of $1.41\,MPa$ in the rabbit cornea (Bekesi et al., 2017), both using air-puff deformation imaging. Similarities were also found in the Young’s modulus of the posterior sclera, with values approximately of $4.5\,MPa$ estimated in porcine and rabbit tissue by uniaxial tension at 10% strain (Zhang et al., 2014). Although the estimated Young's modulus values do not appear to differ between pigs and rabbits, it has been reported that tissue deformation patterns by air-puffing were sensitive to IOP (Kling and Marcos, 2013) and changes in tissue elastic properties (Kling and Marcos, 2013; Zhang et al., 2014). Indeed, under the same conditions, rabbit sclera was more susceptible to changes in stiffness after its biomechanical properties were altered by collagen cross-linking. Thus, Young's modulus is probably not an effective parameter for determining the influence of the animal model on the air-puff deformation parameters of the tissue.

During the air-puff deformation imaging measurement, the eyes were mounted in the custom holder. Although the holder helps us stabilize the eye during the measurement and the finite element model considers surfaces that represent this fixed support, the support defines unnatural boundaries in the sclera. These constraints on the eye can create artificial limits to scleral deformation, affecting the redistribution of IOP during deformation (Kling and Marcos, 2013; De La Hoz et al., 2024) and leading to overestimation or underestimation of stiffness (Metzler, et al., 2014). Although no deformation was observed outside these limits, the fact that the measurements were analyzed on a bounded surface means that these results should be interpreted with caution. Future studies will need to consider correction factors for accurate biomechanical assessments.

5.2. Interpretation of Scleral Biomechanics Findings through Optical Coherence Elastography

We have presented, for the first time to our knowledge, multi-directional wave-based OCE as a method to map the anisotropic behavior across the sclera in comparison to the cornea in intact (whole globe) rabbit eyes. Both the Young's modulus and the shear modulus were lower in the cornea than in the sclera, and while there was some association (reaching not statistical significance) between the moduli, they appeared to be uncorrelated in the sclera. The sclera was also found to be stiffer, both circumferentially (along the equator) and in the anterior zone, than meridionally (nasal-temporal axis) and in the posterior zone. The highest shear modulus values were found in the circumferential superior sclera. Multi-directional OCE allowed radial mapping of mechanical properties in different locations and orientations in intact eyes. In addition, the shear modulus obtained by OCE may capture highly relevant information related to biochemical composition and collagen organization of ocular tissues.

The discrepancy between Young's modulus and shear modulus is not unexpected. The Young’s modulus describes tensile elasticity, quantifying the relationship between stress and strain under uniaxial force (see Section 3.8.1), compression, or tension. In contrast, the shear modulus describes the tendency of an object to deform in response to a tangential force, causing a change in shape without a change in volume. In this case, although it has seen a nonlinear behavior in Young's modulus (see Section 3.8.2), linear relationships were used to calculate the shear modulus (see Section 3.7.3). These linear elastic relationships apply only to isotropic homogeneous materials, while the cornea and sclera material properties rather respond to a structural composite material with a high degree of heterogeneity and anisotropy (Boote et al., 2020; Dupps and Wilson, 2006), which we found to be even larger in the sclera.

Differences in Young's and shear modulus have been previously reported in the human cornea (Knox Cartwright et al., 2011; Ramier et al., 2020). In addition, the nearly incompressible transverse isotropy (NITI) model (Pitre et al., 2020) has demonstrated a decoupling of tensile and shear response in porcine corneal OCE measurements, showing that corneal biomechanics describe an isotropic behavior at pressures below 30 mmHg. Specifically, arguments have been made that tensile tests may be related to the stiffness of the individual collagen fibrils, whereas the OCE technique may depend primarily on the properties of the interfibrillar and interlamellar matrix. This is of particular interest in the sclera, where regional variations in the composition of the collagen fibril network and GAGs were associated with the scleral mechanical behavior (Hatami-Marbini and Pachenari, 2021a; Pachenari and Hatami-Marbini, 2021). Furthermore, the Young's modulus has a significant effect on the deformation of collagen fibrils, whereas the shear modulus affects the deformation of the scleral shell plane, as shown in a study of the elastic response of the sclera to IOP changes using a constitutive model (Grytz et al., 2014). The assumption that the shear modulus estimated from the OCE can evaluate the mechanical properties of the scleral extracellular hydrogel and the stiffness resulting from the collagen fibril interweaving, may partially explain the lack of significant differences in the tensile behavior of normal and GAG-depleted scleral strips in uniaxial tests (Hatami-Marbini and Pachenari, 2021a).

Corneal and scleral tissues have different mechanical properties that are influenced by their specific collagen fibril composition and organization (Watson and Young, 2004). Human corneal collagen fibrils are small in diameter ($25\,nm$) and moderately organized (parallel lamellae of collagen fibrils) compared with scleral collagen, which has wider fibrils ($25-230\,nm$) and an interwoven structure (nonuniform, intertwined collagen fibril bundles) (Komai and Ushiki, 1991). These differences in tissue organization may explain the differences in phase speed (and consequently, the shear modulus) between corneal ($5.9 \pm 1.4\,m/s$) and scleral ($12.1 \pm 3.2\,m/s$) tissues reported here. Furthermore, the phase speed data presented in this thesis are consistent with recent results from patient studies reporting a 2-fold higher wave speed in the sclera than in the cornea (Ramier et al., 2020).

Scleral and corneal anisotropy were compared using four anisotropic parameters: degree of anisotropy, normalized fractional anisotropy, maximum modified planar anisotropy coefficient and major-axis angle. Significantly higher anisotropy was observed in the sclera than in the cornea, but no significant differences in anisotropy were found between scleral locations. Apparent corneal isotropy, which has been studied extensively (Elsheikh and Alhasso, 2009; Singh et al., 2017; Whitford et al., 2015), was not examined in this thesis because the focus was on the sclera. However, we should emphasized that the NFA values (0.17 ± 0.05) in rabbit corneal tissue were similar to those previously reported in porcine cornea (0.56 ± 0.05) (Singh et al., 2016b), and the polar plots of MPAC values (see Figure 4.13, left panel) also showed identical anisotropic mechanical pattern (MPAC values close to 0) in corneas at 15 mmHg. Moreover, the MAA (which possible reflects the predominant collagen fiber orientation) showed a dorsal tilt (toward the optic nerve head, see Figure 4.14a) for all locations except at the ST location, where it was tilted slightly ventrally (see Figure 4.14b).

The relatively lower anisotropy in the cornea compared to the sclera is consistent with previous studies in cornea using different techniques. For example, angle-dependent measurements of phase speed in corneal tissues have been studied with Brillouin microscopy and constitutive models (Eltony et al., 2022; Webb et al., 2020). Specifically, Eltony *et al.* (Eltony et al., 2022) reported a degree of anisotropy (considering the fiber-aligned composite) of 0.18 ± 0.03 in the porcine cornea and 0.12 ± 0.02 in the human cornea. For better comparison, we calculated an analogous anisotropy parameter (degree of anisotropy, see Section 4.2.2.4) based on phase speed (Thomsen, 1986). This resulted in lower values for the rabbit cornea (0.03 ± 0.11) and higher values for the sclera (0.78 ± 0.22) compared to the degree of anisotropy calculated by Eltony *et al.* (Eltony et al., 2022).

In this study, the phase speed was found to be dependent on the scleral zone and direction. Local measurements in the sclera showed significantly higher mean phase speed in the anterior zone ($10.1 \pm 1.8\ m/s$) than in the posterior zone ($8.0 \pm 1.7\ m/s$) and almost double along circumferential direction ($15.4 \pm 3.7\ m/s$) than in meridional direction ($9.1 \pm 1.5\ m/s$). Similar values of phase speed in porcine (Vinas-Pena et al., 2022; Zvietcovich et al., 2020b) and human sclera (Ramier et al., 2020) have been reported in previous literature using piezoelectric excitation. Specifically, the phase speed was at least 63% faster in circumferential zones than in other zones of the scleral tissue. This result appears consistent with other studies (Grytz et al., 2014; Pijanka et al., 2014, 2012; Schwaner et al., 2020) which found that this direction-dependent mechanical behavior is related to the preferential orientation of collagen fibers. In addition, a comparable shape was also found between the collagen fibril distribution maps reported in previous studies (Coudrillier et al., 2015; Grytz et al., 2014; Pijanka et al., 2014) and the phase speed polar plots at the same scleral location in this thesis (see Figure 5.2).

The anterior and posterior scleral zones showed different elastic behavior. The shear modulus of the anterior scleral zone was 53% higher than that of the posterior zone. These differences are consistent with the results from previous studies using tensile testing which found that the tangent modulus of the anterior sclera was twice that of the posterior sclera (Elsheikh et al., 2010; Park et al., 2021). Previous work has interpreted these differences in mechanical properties as arising from regional variations in scleral thickness for humans (Elsheikh and Wang, 2007; Girard et al., 2011), porcine (Olsen et al., 2002), and rabbit (Barathi et al., 2002) eyes. However, our OCE-based results showed that when the scleral thickness is compensated for, the posterior scleral shear modulus is still lower than that of the anterior sclera, at all locations (see Figures 4.11b and 4.11c). Interestingly, in the superior nasal region, the scleral thickness is higher than in the other locations, however the wave speed remains lower than in the anterior zones. This suggests that the posterior sclera is more susceptible to deformation due to its inherent mechanical properties rather than scleral thickness.

The highest shear modulus of rabbit sclera was measured in the circumferential orientation along the equator. On average, the circumferential shear modulus was 66% higher than that in meridional sclera at all locations. Our results are consistent with those observed in previous studies in which the circumferential direction was reported to be stiffer than the meridional direction after biaxial mechanical testing in the porcine sclera (Cruz Perez et al., 2014; Ndlovu et al., 2022). They also confirm a preferential circumferential orientation and suggest a high density and/or high degree of interweaving of collagen fibrils in the circumferential direction at the equator. However, our results differ from the earlier published preferential meridional orientation for rat scleral fibers (Girard et al., 2011), but they are broadly consistent with earlier experiments (Coudrillier et al., 2015; Pijanka et al., 2014; Schwaner et al., 2020) and constitutive models (Grytz et al., 2014) in mouse, human, and rat scleral tissues.

The findings in this study are subject to at least three limitations. First, scleral tissue thickness, which is thicker than the investigated rabbit tissue ($500 - 800\ \mu m$ in humans vs. $200 - 400\ \mu m$ in rabbits), may be difficult to estimate from OCT images due to higher scattering and opacity of the sclera compared to the cornea. The custom-developed PhS-SS-OCT system uses $1300\ nm$ swept-source and has a high penetration because of the long wavelength band and ideally signal roll-off along the axial depth, making it challenging to improve the imaging capabilities for the sclera. Second, the shear modulus was calculated based on a linear elastic approximation. The modified Rayleigh-Lamb frequency equation model (see Section 3.7.3 and Section E) considers a viscoelastic material with isotropic and homogenous response. Nevertheless, the sclera is a non-linear elastic material (Grytz et al., 2014) with an anisotropic structure (Girard et al., 2011) and subject to prestress tension (Crutison et al., 2022). These are important considerations for modeling wave propagation in the sclera in future research. In this study, our calculated values of the shear modulus in the cornea agree with previous studies in rabbits using atomic force microscopy (Thomasy et al., 2014) and an inflation test with inverse analysis,(Bao et al., 2017) so it is likely that these assumptions only moderately affect our results. In any case, given the expected intrinsic differences between Young's and shear modulus in the sclera, future work may elucidate the physicochemical and microstructural factors underlying the scleral biomechanical properties captured by each technique, and the value that they offer in understanding basic mechanisms of the scleral physiology, its changes with disease and its response to treatment.

Third, an important consideration regarding the elastic properties of the sclera is the influence of the fixed IOP during OCE measurements. IOP induces a pre-stressing effect on ocular tissues that directly affect tissue stiffness (Pierscionek et al., 2007; Whitford et al., 2016). Simulations have shown that the estimated phase speed at frequencies around $2\,kHz$ (the frequency used in this thesis) can be affected by pre-stress (Crutison et al., 2022) in a transversely isotropic material. Specifically, Sun *et al.* (Sun et al., 2022) have described a 2-fold reduction in corneal shear modulus at 15 mmHg in porcine eyes, which may also apply to the sclera. Thus, although OCE has a key advantage over strip extensiometry in its non-invasive nature, this technique requires the eye to be maintained at constant IOP conditions, or it could have a significant effect on the shear modulus estimation. Therefore, future work using our set-up will include the measurement of controlled IOP changes and its effects on the estimation of scleral biomechanical parameters. Favorably, OCE at lower frequencies $(1-3kHz)$ appears to have the advantage of introducing less additional stress (Crutison et al., 2022) than other non-invasive techniques, such as air-puff deformation.

5.3. Interpretation of Scleral Biomechanics Findings after Scleral Crosslinking

We demonstrated that photo-crosslinking techniques effectively induce posterior scleral stiffening in rabbit tissue. Both RGX ($532\ nm$, $80\ J/cm^2$) and UVX ($365\ nm$, $5.4\ J/cm^2$) methods similarly increased Young's modulus as compared with untreated sclera immediately after cross-linking and after longer (up to 100 minutes) hydration times (Tables 6.2 and 6.3). Young's modulus at 8% strain was 132% higher in RGX-treated scleral tissue ($9.5 \pm 4.5\ MPa$ vs. $4.1 \pm 2.2\ MPa$) and 90% higher in UVX-treated scleral tissue ($15.0 \pm 2.4\ MPa$ vs. $7.9 \pm 2.8\ MPa$) than in untreated tissue, respectively. The different baseline Young's modulus in the two groups indicates that variability may occur in untreated scleral tissue, and therefore stiffness is presented in relative terms. In addition, RGX and UVX modified the swelling properties of the sclera by reducing the swelling rate by 11% and 13%, respectively. The stiffness of the treated sclera was also affected by hydration levels, with lower Young's modulus values after longer rehydration times. In particular, there was an inverse correlation between swelling ratio and Young's modulus of the treated scleral tissue. The lower the swelling, the higher the stiffness in RGX ($-3.8\%\ swelling/MPa$) and UVX ($-3.5\%\ swelling/MPa$) treated sclera. Scleral tissue stiffness was influenced by a combination of cross-linking method and tissue hydration levels in specific regions of the sclera.

The 2.3-fold and 1.9-fold increases in Young's modulus after RGX and UVX, respectively, are comparable to those values reported in the literature using tensile tests in rabbit sclera after UVX: 1.4-fold ($5.4\ J/cm^2$) (Zhang et al., 2013), 2.8-fold ($5.4\ J/cm^2$) (Wang et al., 2015), 2.1-fold ($7.2\ J/cm^2$) (Zhang et al., 2014), and 5.6-fold ($7.2\ J/cm^2$) (Wollensak et al., 2005), as well as in other species: 2.5-fold ($5.4\ J/cm^2$) in porcine sclera (Wollensak and Spoerl, 2004) and 2-fold (5.4 J/cm^2) in human sclera (Wang et al., 2012). Interestingly, the only prior report of scleral stiffness after rose bengal (and white light irradiation for 60 min) showed no difference from untreated tissue (Wollensak and Spoerl, 2004). An obvious difference between the previous RGX study and ours is the use of a broad-spectrum source by Wollensak et al. (Wollensak and Spoerl, 2004) as opposed to a narrow bandwidth around the excitation wavelength in our study. Singh et al. (Singh et al., 2016a) also found no increase in estimated Young's modulus after RGX ($150\ J/cm2$) in rabbit cornea using OCE. Remarkably, OCE measures the wave propagation speed along the corneal/scleral surface, a behavior that is roughly dominated by the shear modulus

(Pitre et al., 2020; Ramier et al., 2020), unlike uniaxial tests that provide a direct quantification of Young's modulus. In fact, by separately defining in-plane (approx. Young's modulus) and out-of-plane (approx. shear modulus) elastic moduli, the recent elastic wave propagation model (Pitre et al., 2020) has allowed the decoupling of tensile and shear properties, showing an increase in both moduli after UVX in human donor corneas (Regnault et al., 2023). In addition, the model quantified lower values of in-plane modulus when using a single-layer model than when using a two-layer model (Regnault et al., 2023), therefore single-layer models may underestimate Young's modulus. The layer-dependent elasticity values (penetration depth of a crosslinker into the tissue) combined with the measurement method and the estimation model may explain the reported lack of efficacy of RGX in previous studies.

In this study, we chose to cross-link an area in the nasal or temporal region of the sclera and use the contralateral side as a control. We did not find statistical differences in the untreated nasal and temporal regions, unlike a previous report using OCE in porcine sclera (Vinas-Pena et al., 2022). We did not find significant differences in the effect of cross-linking on either the temporal or nasal sclera, with only a tendency for the RGX-treated temporal sclera to show a slightly greater increase in stiffness (see Annexes, Section C, Table C1). However, regional effects were observed in the variation of swelling properties, where the lowest swelling rate value ($3.3 \pm 0.4\,\%/min$) with a reduction in swelling rate of approximately 4.6% per MPa was measured in the RGX-treated temporal scleral tissue. Previous reports of higher shear modulus change in temporal porcine sclera after SXL (Vinas-Pena et al., 2022) and higher collagen organization in rabbit temporal sclera than in the nasal region after cross-linking (Germann J, et al. IOVS 2021;62(8): ARVO E-Abstract 3276), suggest a relationship between collagen arrangement and out-of-plane modulus, which may be more affected by collagen organization than the in-plane modulus. Furthermore, the regional differences in saline uptake (lower in the temporal than nasal sclera after RGX) may be a result of structural differences (more cross-linked or interwoven collagen) in the temporal sclera after cross-linking.

The hydration process of the scleral tissue was affected by RGX and UVX crosslinking only during the initial swelling phase. In a 40-min rehydration period, the swelling rate decreased significantly by 11% after RGX and by 13% after UVX. In a second, slower swelling phase, the swelling ratio decreased non-significantly by 6% after RGX and by 5% after UVX after 100-min rehydration. This two-phase hydration process has been previously described in porcine corneas, where an initial non-significant decrease of 5% was observed, followed by a final increase in hydration of 10% after UVX treatment (Hayes et al., 2013). This swelling behavior can be explained by the collagen dehydration process in which there appears to be first a change in the interior of the fibrils and then a global change in collagen fibril length (Fratzl and Daxer, 1993; Haverkamp et al., 2022).

Scleral stiffness appears to be influenced by hydration levels, with shorter rehydration times resulting in higher Young's modulus values. Hydration variation in collagen-rich tissues such as the sclera has been linked to GAG content. Indeed, Pachenari *et al.* (Pachenari and Hatami-Marbini, 2021) found that depletion of GAGs decreased hydration (swelling ratio) by at least 5.5% and increased stress by 42% in posterior porcine sclera. However, how collagen cross-links interact with GAGs remains unknown. Previous studies have reported that riboflavin with UVA in bovine and rabbit corneas causes cross-linking of collagen molecules and proteoglycan proteins with each other (Hayes et al., 2013; Zhang et al., 2011), but corneal GAGs isolated from their core proteins do not cross-link and do not form cross-links with collagen (Zhang et al., 2011). Therefore, although glycosaminoglycans are involved in the hydration process, cross-linking may not be directly related to glycosaminoglycan/collagen binding. These complex interactions may have different effects on different measurement techniques and may be dependent on SXL modality.

Several limitations of this study should be noted. One obvious limitation is that the tensile test is a destructive technique with a direct influence on hydration (Hatami-Marbini and Pachenari, 2020; Hatami-Marbini and Rahimi, 2016) and mechanical properties of tissues (Lari et al., 2012; McKee et al., 2011). Specifically, a previous study concluded that uniaxial tensile test estimated lower scleral stiffness than the inflation test (Lari et al., 2012). While the intact eye in inflation tests more closely approximates physiological conditions, the scleral properties reconstructed from inflation tests are necessarily influenced by assumptions regarding the cornea (Elsheikh and Anderson, 2005; Kling et al., 2010) and ocular tissues as well as the preconditioning response during inflation (Bianco et al., 2021). However, the tensile test provides us with a direct quantification of the Young's modulus of tissues that other techniques can only obtain through inverse viscoelastic reconstruction techniques from air-puff deformation measurements (Bekesi et al., 2017, 2016b; Bronte-Ciriza et al., 2021) or optical coherence elastography measurements (Regnault et al., 2023; Singh et al., 2016a). In addition, some studies have identified a preferential orientation of scleral collagen fibers (Coudrillier et al., 2015; Girard et al., 2009). The equatorial orientation (measured here) has been reported to be stiffer than the meridional orientation estimated in scleral tissue by biaxial mechanical testing (Ndlovu et al., 2022) and by OCE (Villegas et al., 2024c, 2022). Certainly, tensile tests should be complemented with new techniques which allow quantification of mechanical properties in several directions simultaneously and avoid destruction of the ocular tissue.

In terms of translation to *in vivo* studies, there is only one pilot study of riboflavin/UVA-induced scleral cross-linking in patients with pathologic myopia blindness (Li et al., 2023), which resulted in comparable biometric measurements to another common surgical procedure (posterior scleral reinforcement). It should be noted that crosslinking techniques still have challenges, such as severe inflammatory response (Iseli et al., 2015; Zhang et al., 2013) and the inability to treat the posterior sclera without surgery. In addition, although scleral crosslinking with genipin (a chemical crosslinker) may slow the progression of myopia in a guinea pig model, crosslinking was found to increase IOP, alter optic nerve head morphology, and induce changes associated with glaucoma, such as a higher cup-to-disc ratio and thinner retinal nerve fiber layer (Guo et al., 2022). Translating crosslinking methods into human trials in a minimally invasive manner, as offered by pharmacological approaches, remains a challenge.

5.4. Interpretation of Biometric and Biomechanical findings after Myopia Induction

We successfully induced myopia in guinea pigs using the form deprivation model and compared two pharmacological treatments (latanoprost and atropine). We found a similar 2% increase in axial length and an equivalent difference (range -4.4 to -4.6) in spherical equivalent by both treatments after 10 weeks of myopia induction. The biomechanical response showed that latanoprost attenuated the decrease in stiffness, but atropine increased the scleral shear modulus. Collagen fibers were more organized in myopic eyes. These results suggest that latanoprost and atropine may restore scleral mechanics and collagen fiber organization.

Our form-deprivation guinea pig model shows similar refractive and axial length changes compared to previous data in the literature. For example, studies have reported changes in lens-induced guinea pigs at 4 weeks ($-3.34\ D/0.24\ mm$) (Wang et al., 2023), and in form-deprived guinea pigs at 4 weeks ($-2.79\,D/0.27\,mm$) and 10 weeks ($-8.2\,D/0.29\,mm$) (El-Nimri and Wildsoet, 2018). In general, our model seems to induce a lower magnitude of myopia/axial length change ($-30\,D/mm$ at 10 weeks) compared to $-45\,D/mm$ (diffuser worn) at 11 days (Howlett and McFadden, 2006) and $-66\,D/mm$ (-4D lens worn) at 10 days (Howlett and McFadden, 2009). These differences are expected given the different strains in the pigmented guinea pig colonies and the type of occluder worn.

The development of form-deprived myopia in the eye is associated with scleral remodeling, where the smaller diameter of collagen fibrils due to myopia induction can provide tissues with lower tensile strength (Doillon et al., 1985; Yu and Zhou, 2022). In our study, induced myopia in guinea pig eyes was associated with a 2% ($0.2MPa$) decrease in scleral shear modulus and a 21% ($2.3\,MPa$) decrease in Young's modulus. Latanoprost treatment appeared to decrease myopic scleral stiffness, whereas atropine increased the shear modulus. In previous studies, guinea pig sclera subjected to tensile testing also showed a decrease in Young's modulus of $2.3\,MPa$ (Wang and Corpuz, 2015), $0.95\,MPa$ (Chu et al., 2016), $14.6\,MPa$ (dehydrated strips) (Guo et al., 2022) in myopic tissue compared with nonmyopic tissue. However, tissue examined by scanning acoustic microscopy showed a nonsignificant difference in scleral bulk modulus (along the transverse axis, similar to our study) between myopic and nonmyopic tissue of guinea pig eyes (Hoang et al., 2019). The relationship between these biomechanical properties of the sclera remains unclear, but there is an apparent disparity between them in our study. We speculate that this may be due to the different techniques used (Young's modulus form tensile test and shear modulus from OCE). Atropine and latanoprost may act directly on the scleral matrix to inhibit ocular growth (Chia et al., 2012; El-Nimri and Wildsoet, 2018), but the primary mechanism of action is unknown, making it difficult to determine whether the scleral biomechanical variations were a direct influence of the treatment or a combination of effects.

Microstructural changes in the myopic sclera, such as tissue loss and thinning, have been reported in the development of myopia. In our study, collagen fibers in myopic eyes shown a preferential fiber direction (more aligned) and a large area of collagen and interweaving loss compared to fellow eyes. Small changes of 2%-3% in scleral collagen fiber organization were observed in the treated sclera, indicating that latanoprost and atropine may restore the scleral collagen microstructure during myopia induction. Previous studies have reported greater fiber orientation in collagen (similar to our study) and smaller diameter collagen fibers (Hoerig et al., 2022; McBrien et al., 2001) in myopic eyes compared to fellow eyes, which showed wider collagen fibers and a higher percentage of smaller fibers (El-Nimri et al., 2019; Hoerig et al., 2022). In addition, El-Nimri *et al.* (El-Nimri et al., 2019)have tested latanoprost in form-deprived eyes and showed that collagen fibers from treated eyes had a comparable percentage of small fibers to fellow eyes, also showing possible collagen restoration. Latanoprost, which has been shown to be effective in lowering IOP, has been raised as a potential treatment to control axial length changes and refractive errors (P. Wang et al., 2021),although the exact mechanism is unclear, it appears to have a more direct effect on scleral properties than atropine.

6. CONCLUSIONS

The work performed in this thesis has led to the following conclusions:

1) Custom anterior segment swept-source optical coherence tomography (wavelength=1300 nm; axial resolution=16 μm, transverse resolution =40 μm) coupled with air-puff stimulation (wide hole=2.4 mm; air-puff pressure = 7.28 kPa / 15.4 kPa) and ultrasound excitation (aperture diameter=15 mm; excited with a 3-cycle 2kHz train) has allowed, along with uniaxial tensile testing, geographic characterization of the mechanical properties of the sclera in porcine, rabbit, and guinea pig eyes. Custom-developed swept-source optical coherence tomography (wavelength=1060 nm; axial resolution=11 μm, transverse resolution $=23-31\mu m$) imaging system was used to image the entire ocular axial structure in guinea pig eyes. Custom-developed Second Harmonic Generation (wavelength=800 nm; 80 fs pulses; 80 MHz), quantified with a Fourier-based, collagen order coefficient, allowed sectional imaging of collagen organization in the sclera by forward/backward scattering in these model eyes, and without clearing in guinea pigs. Because of the scleral important role in the regulation of ocular growth and axial elongation, quantification of the biomechanical properties and collagen organization in the scleral tissue is critical in myopia.
2) Scleral deformation to air-puff stimulus varies as a function of anatomic tissue location, animal model, and tissue structural factors. Using the same air-puff configuration, porcine sclera deformed more at the inferior ($0.92 \pm 0.26\, mm$) and superior ($0.83 \pm 0.19\, mm$) locations and rabbit sclera deformed more at the nasal equatorial ($0.98 \pm 0.02\, mm$) and inferior ($0.86 \pm 0.05\, mm$) locations. Because of species differences in ocular anatomy, scleral composition, and response to stimuli, choosing the right animal model ensures reliable and translatable findings for human myopia management.
3) The air puff deformation profile differs between cornea and sclera. The deformation amplitude is largest in the cornea, only comparable to inferior and superior sclera. Furthermore, the sclera accelerates less and remains at maximum velocity for a longer time, a behavior that reflects differences in the non-linear properties of both tissues. Corneal and scleral tissues

respond differently to mechanical and environmental influences, understanding these distinctions aids in targeted interventions in scleral tissue for myopia management and its possible effects in corneal biomechanics.

4) Elastic properties were obtained from corneal and scleral deformation parameters using inverse modeling techniques. Modeling showed that tissue thickness, scleral material properties, and IOP were the most influential parameters on tissue apex displacement. These results allow us to focus on the influences of parameters such as thickness, material properties and IOP in biomechanical changes during myopia progression and to evaluate treatment interventions.

5) Speed of waves propagating across the sclera as a result of ultrasound excitation in multi-directional optical coherence elastography vary across locations revealing that the mechanical behavior of the scleral surface is regional (anterior and posterior sclera) and directional (circumferential and meridional sclera) dependent. The shear modulus in rabbit scleral tissue was higher in the anterior $(27.3 \pm 1.8\,kPa)$ than in the posterior sclera $(17.8 \pm 1.4\,kPa)$, and in the circumferential direction $(65.4 \pm 31.9\,kPa)$ than in the meridional direction $(22.5 \pm 7.2\,kPa)$, suggesting a regional organization of collagen fibers and a preferential orientation within the sclera in the circumferential direction. In addition, the scleral surface is mechanically anisotropic. The scleral tissue is at least three times more anisotropic than the cornea, with no significant differences between scleral locations. Polar plots of the planar anisotropy coefficient showed a circular pattern for the cornea and a tilted pattern for the sclera, with a preferred axis along the equator. Understanding regional differences in scleral tissue helps to design targeted and optimized treatments for myopia control.

6) A comparison of Young's modulus obtained from uniaxial tensile tests and shear modulus from OCE in the scleral tissue $(3.5 \pm 0.9\,MPa$ and $22.0 \pm 6.6\,kPa$, respectively, averaged across different locations) reveals that the Young's modulus is two orders of magnitude higher than the shear modulus in the same direction and at the same locations, although no correlation was found between the values in the sclera. Shear modulus and Young's modulus obtained together for the same scleral tissue provide a complete picture of mechanical behavior, which is essential for accurate modeling

and understanding of structural changes, especially in conditions such as myopia.

7) Rose Bengal in combination with green light can be used to crosslink the posterior sclera. Instillation of 0.1% (w/v) Rose Bengal solution for 150 seconds followed by 532-nm laser light irradiation (80 J/cm^2, 400 s) increased scleral stiffness by 132% (as measured by strip extensiometry). Compared with a commonly used cross-linking method (riboflavin with UVA light), Young's modulus of the posterior sclera increased 2.3-fold after RGX ($9.5 \pm 4.5\,MPa$ vs. $4.1 \pm 2.2\,MPa$) and 1.9-fold after UVX ($15.0 \pm 2.4\,MPa$ vs. $7.9 \pm 2.8\,MPa$), demonstrating that RGX was sufficiently effective in stiffening the scleral tissue and emerging as a potential method to control myopia progression.

8) RGX and UVX altered scleral swelling properties by reducing the scleral swelling rate (11%-13%) and collagen organization by increasing the scleral order coefficient (3.9%-5.1%). In addition, swelling coefficient and Young's modulus were inversely correlated in both SXL-treated and untreated scleral tissues, with stiffness being greater the lower the scleral swelling. Swelling properties influence tissue hydration, collagen spacing, and biomechanical integrity, so studying the effects of swelling on scleral stiffness may be useful in understanding the biomechanical basis of myopia and in evaluating treatments such as scleral cross-linking.

9) Guinea pigs that were monocularly form-deprived at 2 weeks postnatal, developed interocular differences of $-7.4\,D$ in spherical error and 0.25 mm in axial length at 10 weeks of induction. The form-deprived guinea pig eyes were treated with saline (control), atropine (1% w/v), or latanoprost (0.05% w/v). In our model, atropine was as effective as latanoprost in slowing myopia progression with similar end points. The axial length differences were statistically lower for latanoprost ($0.18 \pm 0.03\,mm$) and atropine significantly ($0.18 \pm 0.04\,mm$) than for the control group ($0.24 \pm 0.05\,mm$, saline). Similarly, eyes treated with latanoprost ($-4.6 \pm 1.22\,D$) and atropine ($-4.4 \pm 1.6\,D$) were statistically less myopic than control eyes ($-7.4 \pm 0.93\,D$, saline) higher than that of the nonmyopic eye, consistent with previous work that latanoprost, a prostaglandin analogue used in glaucoma treatment, may be an alternative treatment for myopia control.

10) From biomechanical measurements, the Young's modulus of scleral tissue in myopic guinea pig eyes was reduced by $2.3\,MPa$ (saline), $1.5\,MPa$ (atropine), and $0.6\,MPa$ (latanoprost), compared with untreated tissue. Accordingly, the shear modulus decreased in the sclera-treated tissue by $0.2\,MPa$ (saline), and by $0.1\,MPa$ (latanoprost), but increased by $0.9\,MPa$ in the atropine group compared with untreated tissue. This apparent discrepancy between Young's modulus and shear modulus in the atropine group may be due to the different techniques used (Young's modulus from tensile test and shear modulus from OCE). It highlights the importance of decoupling Young's modulus and shear modulus to determine exactly which elastic parameter is being determined to quantify the effectiveness of myopia treatment by increasing or decreasing scleral elasticity.

11) Scleral collagen fibers in myopic eyes were more aligned (organized in only one direction) and appeared to have large areas of collagen loss and interweaving loss compared with disorganized interweaving fibers in the sclera of nonmyopic eyes. The scleral order coefficient varied nonsignificant by 2% (latanoprost) and 3% (atropine) in the treated groups, compared with the 4% increase in order coefficient in the control (saline) group. These small nonsignificant changes may indicate that latanoprost and atropine can restore scleral collagen microstructure during myopia induction.

7. THESIS ACHIEVEMENTS

I have accomplished the following during this thesis:

1) Implemented scleral-specific experimental protocols for mechanical measurements in a swept-source optical coherence tomography; air-puff scleral deformation imaging and ultrasound excitation optical coherence elastography. Strip tensile testing was also performed as a control.
2) Implemented protocols for volumetric second harmonic generation imaging and quantification of collagen organization in rabbits and guinea pigs.
3) Obtained first regional-dependent measurements of air-puff deformation in rabbit and porcine eyes and wave propagation speeds in rabbit and guinea pig eyes.
4) Developed finite element models to reconstruct Young's modulus and analytical tools to estimate scleral shear modulus at different locations on intact ocular globes.
5) Evaluated the effect of two cross-linking modalities (Riboflavin/UVA and Rose Bengal/Green light) on scleral stiffness and collagen organization and evaluated the effect of hydration on Young's modulus.
6) Implemented a form-deprivation myopia model in guinea pigs. Established retinoscopy and OCT-based biometric measurements for refractive and axial length characterization of the model.
7) Evaluated the effect of two potential treatments for myopia control (latanoprost and atropine) on refraction and axial length as well as on scleral mechanical properties (Young's modulus from tensile tests, shear modulus from ocular coherence elastography) and collagen organization from second harmonic generation imaging.

8. LIST OF PUBLICATIONS AND CONFERENCE CONTRIBUTIONS

List of publications and conference contributions associated with this thesis.

8.1. Scientific papers

- **Villegas L**, Germann JA, Marcos S. "Effects of Different Scleral Photo-Crosslinking Modalities on Scleral Stiffness and Hydration". Invest Ophthalmol Vis Sci. 2024 Jul 1;65(8):8. doi: 10.1167/iovs.65.8.8. PMID: 38958968; PMCID: PMC11223619.
- **Villegas L,** Zvietcovich F, Marcos S, Birkenfeld JS. "Revealing regional variations in scleral shear modulus in a rabbit eye model using multi-directional ultrasound optical coherence elastography". Sci Rep 14, 21010 (2024). https://doi.org/10.1038/s41598-024-71343-0
- de la Hoz A, **Villegas L**, Marcos S, Birkenfeld JS. "A simple computational model for scleral stiffness assessments via air-puff deformation OCT". Front. Bioeng. Biotechnol. 12 – 2024, doi: 10.3389/fbioe.2024.1426060
- Bronte-Ciriza D, Birkenfeld JS, de la Hoz A, Curatolo A, Germann JA, **Villegas L**, Varea A, Martínez-Enríquez E, Marcos S. "Estimation of scleral mechanical properties from air-puff optical coherence tomography". Biomed Opt Express. 2021 Sep 17;12(10):6341-6359. doi: 10.1364/BOE.437981. PMID: 34745741; PMCID: PMC8548012.

8.2. Conference contributions presented by the author

- **Villegas L**, Zvietcovich F, Marcos S, Birkenfeld JS. "Scleral anisotropy in *ex vivo* rabbit eyes using ultrasonic optical coherence elastography". Proc. SPIE 12844, Optical Elastography and Tissue Biomechanics XI, 1284409 (12 March 2024); https://doi.org/10.1117/12.3005441.
- **Villegas L**, Urizar MP, Zvietcovich F, Olalla P, de Castro A, Curatolo A, Revuelta L, Marcos S. "Myopia control by atropine and latanoprost in a

guinea pig model: impact on refraction, biometry and scleral mechanics". Invest. Ophthalmol. Vis. Sci. 2023;64(8):4958. New Orleans-USA. https://iovs.arvojournals.org/article.aspx?articleid=2788805

- **Villegas L**, Zvietcovich F, Varea A, Curatolo A, Birkenfeld JS, Marcos S. "Poster Session: Experimental assessment of scleral anisotropy using multi-meridian air-coupled ultrasonic optical coherence elastography". J Vis. 2023 Sep 1;23(11):72. doi: 10.1167/jov.23.11.72. PMID: 37733506.
- **Villegas L**, Zvietcovich F, Varea A, Birkenfeld JS, Marcos S. "Spatial characterization of scleral biomechanics in *ex vivo* rabbit eyes using multi-meridian Optical Coherence Elastography". Invest. Ophthalmol. Vis. Sci. 2022;63(7):1454 – F0412. Denver-USA. https://iovs.arvojournals.org/article.aspx?articleid=2779636
- **Villegas L.** "Optical imaging techniques for scleral biomechanics". 2022 Young Researchers Biophotonics, Sociedad Española de Óptica (SEDOPTICA). 16 June 2022. Virtual. Invited Talked.
- **Villegas L**, Birkenfeld JS, Germann J, Marcos S. "Mapping the properties of the sclera through optical imaging techniques". Young Researcher Vision Camp, European Vision Institute EEIG, Tübingen. 25 June 2021. Virtual. Oral presentation.
- **Villegas L**, Germann J, Marcos S. "Biomechanical effects of Scleral crosslinking using Rose Bengal/Green-light and Rivoflavin/UVA". ARVO Annual Meeting 1-7 May 2021. https://arvo2021.arvo.org/meetings/virtual/WvEFM8RkTLCzhkMnQ
- **Villegas L**, Birkenfeld JS, Bronte D, Varea A, Curatolo A, Marcos S. "Investigation on scleral biomechanics in rabbit model using OCT air-puff deformation imaging with two excitation configurations", Optics and Photonics for scientific progress 2021, Student-led conference. University of Surrey Student Chapter. 13-14 April 2021. Virtual. Poster presentation.
- **Villegas L**, Birkenfeld JS, Varea A, Marcos S. "Comparison of scleral biomechanics in rabbit and porcine models using OCT air-puff deformation imaging". IOSA Scientific Seminars, The Optical Society, Institute of Optics (IO-CSIC). 17 December 2020. Virtual. Oral presentation. https://www.youtube.com/watch?v=-emDJemczG

- **Villegas L**, Bronte D, Germann J, Marcos S. "Scleral cross-linking using Rose Bengal-Green Light". Invest. Ophthalmol. Vis. Sci. 2020;61(7):3415.

8.3. Conference contributions presented by collaborators

- Marcos S, **Villegas L,** Tecse A, Germann J, de la Hoz A., Zvietcovich F, Birkenfeld J, Savage D, Baratta R. "Scleral biomechanics and collagen organization: implications in myopia and its treatment". International Myopia Conference. Invited talked 2024 September 27. Sanya-China.
- Germann JA, **Villegas L**, Revuelta L, Marcos S. "Effects of pharmacological treatments of myopia on scleral collagen organization in myopic guinea pig models". Invest. Ophthalmol. Vis. Sci. 2023;64(8):2859. New Orleans-USA. https://iovs.arvojournals.org/article.aspx?articleid=2787487
- Birkenfeld JS, **Villegas L**, de la Hoz A, Bronte-Ciriza A., Varea A., Martinez-Enriquez E., Curatolo A., Germann JA, Marcos S. "Estimation of scleral biomechanical properties from air-puff-coupled optical coherence tomography". Journal of Vision 2023;23(11):38. Rochester -USA. https://doi.org/10.1167/jov.23.11.38. Rochester -USA.
- Birkenfeld JS, Bronte-Ciriza D, de la Hoz A, Curatolo A, Germann JA, **Villegas L,** Varea A, Martínez-Enríquez E, Marcos S. "Method to Estimate Scleral Mechanical Properties From Air-Puff Optical Coherence Tomography: a Proof-of-Concept". Invest. European Conferences on Biomedical Optics. 20-24 June 2021. Oral presentation
- Germann J, **Villegas L**, Martinez-Enriquez E, Revuelta L, Cómitre B, Sanderson D, Llorente V, Desco M, Gómez-Gaviro MV, Marcos S. "Collagen Organization in the Posterior Rabbit Sclera Post Cross-Linking". Invest. Ophthalmol. Vis. Sci. ARVO Annual Meeting 1-7 May 2021. Virtual. Oral presentation.https://arvo2021.arvo.org/meetings/virtual/nXAbJg2zLAiGiba9c

9.FUTURE WORK

9.1. Improved Quantification of Shear Modulus from OCE Measurements

To model wave propagation, the modified Rayleigh-Lamb frequency equation model should be replaced by a new model that takes into account the nonlinear elasticity and anisotropic structure of the scleral tissue. In fact, a recent multilayer model (Regnault2023) can estimate elasticity values that depend on the inner layer of the tissue. This may be useful in future studies, for example, to estimate the change in elasticity as a function of the depth of penetration of a crosslinker into a tissue.

9.2. New Experimental Considerations for Air-Puff and OCE Measurements

The elastic properties of the sclera are influenced by fixed intraocular pressure. IOP induces a pre-stressing effect on ocular tissues that directly affects tissue stiffness. Therefore, we will measure the controlled IOP changes and their effects on the estimation of scleral biomechanical parameters.

In addition, the custom holder can introduce extra forces to the eye that may affect stiffness estimation. Therefore, the influence of the custom holder on the biomechanical response will be estimated.

9.3. *In vivo* Crosslinking Technique with Rose Bengal and Green Light

Rose Bengal with green light irradiation has been successfully tested for scleral crosslinking and showed an increase in scleral rigidity in rabbits. Therefore, we can propose to test RGX technique as a possible treatment for myopia control. The feasibility of this procedure will be tested in vivo in a guinea pig eye. A minimally invasive procedure (a small conjunctival incision) will be used to treat specific areas of the sclera of myopic eyes. For this future study, in vivo and ex vivo measurements will be performed on guinea pig eyes to measure biometric changes in awake animals, as well as elastic moduli and collagen arrangement in the targeted scleral tissue.

REFERENCES

Alm, A., 2014. Latanoprost in the treatment of glaucoma. Clinical ophthalmology 1967–1985.

Asejczyk-Widlicka, M., Schachar, R.A., Pierscionek, B.K., 2008. Optical coherence tomography measurements of the fresh porcine eye and response of the outer coats of the eye to volume increase. J Biomed Opt 13, 024002.

Atta, G., Tempfer, H., Kaser-Eichberger, A., Traweger, A., Heindl, L.M., Schroedl, F., 2022. Is the human sclera a tendon-like tissue? A structural and functional comparison. Annals of Anatomy - Anatomischer Anzeiger 240, 151858.

Avetisov, E.S., Savitskaya, N.F., Vinetskaya, M.I., Iomdina, E.N., 1983. A study of biochemical and biomechanical qualities of normal and myopic eye sclera in humans of different age groups. Metab Pediatr Syst Ophthalmol 7, 183–188.

Backhouse, S., Gentle, A., 2018. Scleral remodelling in myopia and its manipulation: A review of recent advances in scleral strengthening and myopia control. Ann Eye Sci 3, 1–15.

Bao, F., Deng, M., Zheng, X., Li, L., Zhao, Y., Cao, S., Yu, Ay., Wang, Q., Huang, J., Elsheikh, A., 2017. Effects of diabetes mellitus on biomechanical properties of the rabbit cornea. Exp Eye Res 161, 82–88.

Barathi, A., Thu, M.K., Beuerman, R.W., 2002. Dimensional Growth of the Rabbit Eye. Cells Tissues Organs 171, 276–285.

Bartholomew, L.R., Pang, D.X., Sam, D.A., Cavender, J.C., 1997. Ultrasound biomicroscopy of globes from young adult pigs. Am J Vet Res 58, 942–948.

Battaglioli, J.L., Kamm, R.D., 1984. Measurements of the compressive properties of scleral tissue. Invest Ophthalmol Vis Sci 25, 59–65.

Baumann, B., Rauscher, S., Glösmann, M., Götzinger, E., Pircher, M., Fialová, S., Gröger, M., Hitzenberger, C.K., 2014. Peripapillary Rat Sclera Investigated In Vivo With Polarization-Sensitive Optical Coherence Tomography. Invest Ophthalmol Vis Sci 55, 7686–7696.

Beach, K.M., Hung, L.-F., She, Z., Ostrin, L.A., Smith, E.L., 2019. The Effects of Latanoprost on Negative-Lens-Induced Myopia in Rhesus Monkeys. Invest Ophthalmol Vis Sci 60, 5897.

Bekerman, I., Gottlieb, P., Vaiman, M., 2014. Variations in eyeball diameters of the healthy adults. J Ophthalmol 503645, 1–5.

Bekesi, N., Dorronsoro, C., De La Hoz, A., Marcos, S., 2016a. Material properties from air puff corneal deformation by numerical simulations on model corneas. PLoS One. 28;11(10):e0165669.

Bekesi, N., Gallego-Muñoz, P., Ibarés-Frías, L., Perez-Merino, P., Martinez-Garcia, M.C., Kochevar, I.E., Marcos, S., 2017. Biomechanical changes after in vivo collagen cross-linking with rose bengal–green light and riboflavin-UVA. Invest Ophthalmol Vis Sci 58, 1612–1620.

Bekesi, N., Kochevar, I.E., Marcos, S., 2016b. Corneal Biomechanical Response Following Collagen Cross-Linking With Rose Bengal–Green Light and Riboflavin-UVA. Invest Ophthalmol Vis Sci 57, 992–1001.

Bekesi, N., Pérez-Merino, P., Ibares-Frías, L., Martinez-Garcia, C., Kochevar, I.E., Marcos, S., 2015. Corneal deformation imaging of Rose Bengal-green light cross-linked rabbit corneas: in vivo vs ex vivo treatments and measurements. Invest Ophthalmol Vis Sci 56, 1135.

Bianco, G., Levy, A.M., Grytz, R., Fazio, M.A., 2021. Effect of different preconditioning protocols on the viscoelastic inflation response of the posterior sclera. Acta Biomater 128, 332–345.

Birkenfeld, J.S., Villegas, L., de la Hoz, A., Bronte-Ciriza, D., Varea, A., Martínez-Enríquez, E., Curatolo, A., Germann, J.A., Marcos, S., 2023. Poster Session: Estimation of scleral biomechanical properties from air-puff-coupled optical coherence tomography. J Vis 23, 38.

Black, A.C., Jones, S., Yanovitch, T.L., Enyedi, L.B., Stinnett, S.S., Freedman, S.F., 2009. Latanoprost in pediatric glaucoma-pediatric exposure over a decade. Journal of the American Association for Pediatric Ophthalmology and Strabismus (JAAPOS) 13, 558–562.

Blackburn, B.J., Rollins, A.M., Dupps Jr., W.J., 2021. Biomechanics of Ophthalmic Crosslinking. Transl Vis Sci Technol 10, 8.

Boote, C., Sigal, I.A., Grytz, R., Hua, Y., Nguyen, T.D., Girard, M.J.A., 2020. Scleral structure and biomechanics. Prog Retin Eye Res 74, 1–87.

Borcherding, M.S., Blacik, L.J., Sittig, R.A., Bizzell, J.W., Breen, M., Weinstein, H.G., 1975. Proteoglycans and collagen fibre organization in human corneoscleral tissue. Exp Eye Res 21, 59–70.

Bozkir, G., Bozkir, M., Dogan, H., Aycan, K., Güler, B., 1997. Measurements of axial length and radius of corneal curvature in the rabbit eye. Acta Med Okayama 51, 9–11.

Bronte-Ciriza, D., Birkenfeld, J.S., de la Hoz, A., Curatolo, A., Germann, J.A., Villegas, L., Varea, A., Martínez-Enríquez, E., Marcos, S., 2021. Estimation of scleral mechanical properties from air-puff optical coherence tomography. Biomed Opt Express 12, 6341.

Brown, D.M., Yu, J., Kumar, P., Paulus, Q.M., Kowalski, M.A., Patel, J.M., Kane, M.A., Ethier, C.R., Pardue, M.T., 2023. Exogenous All-Trans Retinoic Acid Induces Myopia and Alters Scleral Biomechanics in Mice. Invest Ophthalmol Vis Sci 64, 22.

Cellscale, 2017. UStretch user manual. URL https://www.cellscale.com/

Chagnon, G., Ohayon, J., Martiel, J.-L., Favier, D., 2017. Chapter 1 - Hyperelasticity Modeling for Incompressible Passive Biological Tissues, in: Payan, Y., Ohayon, J. (Eds.), Biomechanics of Living Organs. Academic Press, Oxford, pp. 3–30.

Chakravarti, S., Petroll, W.M., Hassell, J.R., Jester, J. V, Lass, J.H., Paul, J., Birk, D.E., 2000. Corneal Opacity in Lumican-Null Mice: Defects in Collagen Fibril Structure and Packing in the Posterior Stroma. Invest Ophthalmol Vis Sci 41, 3365–3373.

Cheng, S., Clarke, E.C., Bilston, L.E., 2009. The effects of preconditioning strain on measured tissue properties. J Biomech 42, 1360–1362.

Cherfan, D., Verter, E.E., Melki, S., Gisel, T.E., Doyle, F.J., Scarcelli, G., Yun, S.H., Redmond, R.W., Kochevar, I.E., 2013. Collagen cross-linking using rose bengal and green light to increase corneal stiffness. Invest Ophthalmol Vis Sci 54, 3426–3433.

Chia, A., Chua, W.-H., Cheung, Y.-B., Wong, W.-L., Lingham, A., Fong, A., Tan, D., 2012. Atropine for the Treatment of Childhood Myopia: Safety and Efficacy of 0.5%, 0.1%, and 0.01% Doses (Atropine for the Treatment of Myopia 2). Ophthalmology 119, 347–354.

Chia, A., Lu, Q.-S., Tan, D., 2016. Five-Year Clinical Trial on Atropine for the Treatment of Myopia 2: Myopia Control with Atropine 0.01% Eyedrops. Ophthalmology 123, 391–399.

Chu, Y., Cheng, Z., Liu, J., Wang, Y., Guo, H., Han, Q., 2016. The Effects of Scleral Collagen Cross-Linking Using Glyceraldehyde on the Progression of Form-Deprived Myopia in Guinea Pigs. J Ophthalmol. 2016: 3526153.

Clark, T.Y., Clark, R.A., 2015. Atropine 0.01% Eyedrops Significantly Reduce the Progression of Childhood Myopia. Journal of Ocular Pharmacology and Therapeutics 31, 541–545.

Cooper, J., Citek, K., Feldman, J.M., 2011. Comparison of refractive error measurements in adults with Z-View aberrometer, Humphrey autorefractor, and subjective refraction. Optometry - Journal of the American Optometric Association 82, 231–240.

Corboy, J.M., 2003. The retinoscopy book: an introductory manual for eye care professionals. Slack Incorporated.

Couade, M., Pernot, M., Messas, E., Bel, A., Ba, M., Hagege, A., Fink, M., Tanter, M., 2011. In Vivo quantitative mapping of myocardial stiffening and transmural anisotropy during the cardiac cycle. IEEE Trans Med Imaging 30, 295–305.

Coudrillier, B., Pijanka, J., Jefferys, J., Sorensen, T., Quigley, H.A., Boote, C., Nguyen, T.D., 2015. Collagen Structure and Mechanical Properties of the Human Sclera: Analysis for the Effects of Age. J Biomech Eng 137.

Coudrillier, B., Tian, J., Alexander, S., Myers, K.M., Quigley, H.A., Nguyen, T.D., 2012. Biomechanics of the human posterior sclera: Age- and glaucoma-related changes measured using inflation testing. Invest Ophthalmol Vis Sci 53, 1714–1728.

Cristaldi, M., Olivieri, M., Pezzino, S., Spampinato, G., Lupo, G., Anfuso, C.D., Rusciano, D., 2020. Atropine differentially modulates ECM production by ocular fibroblasts, and its ocular surface toxicity is blunted by colostrum. Biomedicines 8, 78.

Crutison, J., Sun, M., Royston, T.J., 2022. The combined importance of finite dimensions, anisotropy, and pre-stress in acoustoelastography. J Acoust Soc Am 151, 2403–2413.

Cruz Perez, B., Tang, J., Morris, H.J., Palko, J.R., Pan, X., Hart, R.T., Liu, J., 2014. Biaxial mechanical testing of posterior sclera using high-resolution ultrasound speckle tracking for strain measurements. J Biomech 47, 1151–1156.

Cui, D., Trier, K., Zeng, J., Wu, K., Yu, M., Hu, J., Chen, X., Ge, J., 2011. Effects of 7-methylxanthine on the sclera in form deprivation myopia in guinea pigs. Acta Ophthalmol 89, 328–334.

Curatolo, A., Birkenfeld, J., Martínez, E., Germann, J.A., Palací, J., Pascual, D., Muralidharan, G., Solarski, J., Karnowski, K., Wojtkowski, M., 2020a. Customized swept-source optical coherence tomography system for air-puff induced corneal deformation imaging on multiple meridians (Conference Presentation), in: Ophthalmic Technologies XXX. SPIE, p. 112180V.

Curatolo, A., Birkenfeld, J.S., Martinez-Enriquez, E., Germann, J.A., Muralidharan, G., Palací, J., Pascual, D., Eliasy, A., Abass, A., Solarski, J., Karnowski, K., Wojtkowski, M., Elsheikh, A., Marcos, S., 2020b. Multi-meridian corneal imaging of air-puff induced deformation for improved detection of biomechanical abnormalities. Biomed Opt Express 11, 6337.

Curtin, B.J., Iwamoto, T., Renaldo, D.P., 1979. Normal and Staphylomatous Sclera of High Myopia: An Electron Microscopic Study. Archives of Ophthalmology 97, 912–915.

Curtin, B.J., Jampol, L.M., 1986. The myopias: basic science and clinical management. Retina 6, 132.

Curtin, B.Y.B.J., 1969. Physiopathologic aspects of scleral stress-strain. Trans Am Ophthalmol Soc 67, 417.

David, T., Smye, S., James, T., Dabbs, T., 1997. Time-dependent stress and displacement of the eye wall tissue of the human eye. Med Eng Phys 19, 131–139.

Daxer, A., Misof, K., Grabner, B., Ettl, A., Fratzl, P., 1998. Collagen fibrils in the human corneal stroma: structure and aging. Invest Ophthalmol Vis Sci 39, 644–648.

de Castro, A., Martinez-Enriquez, E., Perez-Merino, P., Velasco-Ocaña, M., Revuelta, L., McFadden, S., Marcos, S., 2020. Crystalline lens gradient refractive index distribution in the guinea pig. Ophthalmic and Physiological Optics 40, 308–315.

De La Hoz, A., Villegas, L., Marcos, S., Birkenfeld, J.S., 2024. A simple computational model for scleral stiffness assessments via air-puff deformation OCT. Front Bioeng Biotechnol 12.

De Stefano, V.S., Seven, I., Randleman, B.J., Dupps, W.J.Jr., 2018. Custom air puff-derived biomechanical variables in a refractive surgery screening setting: Study from 2 centers. J Cataract Refract Surg 44.

Dhillon, B., Armani, J., Nickla, D.L., 2008. The Ocular Growth Inhibition Effected by Dopamine Agonists and Atropine Is Associated With Transient Increases in Choroidal Thickness in Chicks. Invest Ophthalmol Vis Sci 49, 1732.

Doillon, C.J., Dunn, M.G., Bender, E., Silver, F.H., 1985. Collagen Fiber Formation in Repair Tissue: Development of Strength and Toughness. Coll Relat Res 5, 481–492.

Dolgin, E., 2015. The myopia boom. Nature 519, 276–278.

Dong, F., Zhi, Z., Pan, M., Xie, R., Qin, X., Lu, R., Mao, X., Chen, J.-F., Willcox, M.D.P., Qu, J., 2011. Inhibition of experimental myopia by a dopamine agonist: different effectiveness between form deprivation and hyperopic defocus in guinea pigs. Mol Vis 17, 2824.

Dong, L., Shi, X.H., Kang, Y.K., Wei, W. Bin, Wang, Y.X., Jonas, J.B., 2019. Ocular size and shape in lens-induced Myopization in young Guinea pigs. BMC Ophthalmol 19, 1–8.

Dorronsoro, C., Pascual, D., Pérez-Merino, P., Kling, S., Marcos, S., 2012. Dynamic OCT measurement of corneal deformation by an air puff in normal and cross-linked corneas. Biomed Opt Express 3, 473.

Dotan, A., Kremer, I., Livnat, T., Zigler, A., Weinberger, D., Bourla, D., 2014. Scleral cross-linking using riboflavin and ultraviolet-A radiation for prevention of progressive myopia in a rabbit model. Exp Eye Res 127, 190–195.

Doughty, M.J., 2000. Swelling of the collagen-keratocytematrix of the bovine corneal stroma ex vivo in various solutions and its relationship to tissue thickness. Tissue Cell 32, 478–493.

Downs, J.C., Suh, J.-K.F., Thomas, K.A., Bellezza, A.J., Hart, R.T., Burgoyne, C.F., 2005. Viscoelastic Material Properties of the Peripapillary Sclera in Normal and Early-Glaucoma Monkey Eyes. Invest Ophthalmol Vis Sci 46, 540–546.

Dupps, W.J., Wilson, S.E., 2006. Biomechanics and wound healing in the cornea. Exp Eye Res 83, 709–720.

Ebneter, A., Häner, N.U., Zinkernagel, M.S., 2015. Metrics of the normal anterior sclera: imaging with optical coherence tomography. Graefe's Archive for Clinical and Experimental Ophthalmology 253, 1575–1580.

Eilaghi, A., Flanagan, J.G., Tertinegg, I., Simmons, C.A., Wayne Brodland, G., Ross Ethier, C., 2010. Biaxial mechanical testing of human sclera. J Biomech 43, 1696–1701.

Eiter, T., Mannila, H., 1994. Computing discrete Fréchet distance.

El Hamdaoui, M., Levy, A.M., Gaonkar, M., Gawne, T.J., Girkin, C.A., Samuels, B.C., Grytz, R., 2021. Effect of Scleral Crosslinking Using Multiple Doses of Genipin on Experimental Progressive Myopia in Tree Shrews. Transl Vis Sci Technol. 10(5):1

Eliasy, A., Chen, K.-J., Vinciguerra, R., Maklad, O., Vinciguerra, P., Ambrósio, R., Roberts, C.J., Elsheikh, A., 2018. Ex-vivo experimental validation of biomechanically-corrected intraocular pressure measurements on human eyes using the CorVis ST. Exp Eye Res 175, 98–102.

El-Nimri, N.W., Jiang, L., Dahanayake, D., Sweidan, S., Smith, B.E., Wildsoet, C.F., 2022. Effect of topical latanoprost on choroidal thickness and vessel area in Guinea pigs. Exp Eye Res 225, 109286.

El-Nimri, N.W., Wildsoet, C.F., 2018. Effects of topical latanoprost on intraocular pressure and myopia progression in young guinea pigs. Invest Ophthalmol Vis Sci 59, 2644–2651.

El-Nimri, N.W., Yao, M., Huerta, A., Hoang, M., Wildsoet, C.F., 2019. Effect of chronic topical latanoprost on the sclera and lamina cribrosa of form-deprived myopic Guinea pigs. Exp Eye Res 186, 107740.

Elsheikh, A., 2010. Finite element modeling of corneal biomechanical behavior. Journal of Refractive Surgery 26, 289–300.

Elsheikh, A., Alhasso, D., 2009. Mechanical anisotropy of porcine cornea and correlation with stromal microstructure. Exp Eye Res 88, 1084–1091.

Elsheikh, A., Anderson, K., 2005. Comparative study of corneal strip extensometry and inflation tests. J R Soc Interface 2, 177–185.

Elsheikh, A., Geraghty, B., Alhasso, D., Knappett, J., Campanelli, M., Rama, P., 2010. Regional variation in the biomechanical properties of the human sclera. Exp Eye Res 90, 624–633.

Elsheikh, A., Wang, D., 2007. Numerical modelling of corneal biomechanical behaviour. Comput Methods Biomech Biomed Engin 10, 85–95.

Eltony, A.M., Shao, P., Yun, S.H., 2022. Measuring mechanical anisotropy of the cornea with Brillouin microscopy. Nat Commun 13, 1–19.

Enaholo, E.S., Musa, M.J., Zeppieri, M., 2023. The Spherical Equivalent. Treasure Island (FL): StatPearls Publishing. URL https://www.ncbi.nlm.nih.gov/books/NBK589657/ (accessed 11.28.23).

Feldkaemper, M., Schaeffel, F., 2013. An updated view on the role of dopamine in myopia. Exp Eye Res 114, 106–119.

Flitcroft, D.I., He, M., Jonas, J.B., Jong, M., Naidoo, K., Ohno-Matsui, K., Rahi, J., Resnikoff, S., Vitale, S., Yannuzzi, L., 2019. IMI – Defining and Classifying Myopia: A Proposed Set of Standards for Clinical and Epidemiologic Studies. Invest Ophthalmol Vis Sci 60, M20–M30.

Fratzl, P., Daxer, A., 1993. Structural transformation of collagen fibrils in corneal stroma during drying. An x-ray scattering study. Biophys J 64, 1210–1214.

Freund, I., Deutsch, M., 1986. Second-harmonic microscopy of biological tissue. Opt Lett 11, 94–96.

Fung, Y.-C., 1993. The Meaning of the Constitutive Equation, in: Fung, Y.-C. (Ed.), Biomechanics: Mechanical Properties of Living Tissues. Springer New York, New York, NY, pp. 23–65.

Fung, Y.C., 1967. Elasticity of soft tissues in simple elongation. American Journal of Physiology-Legacy Content 213, 1532–1544.

Gachon, E., Mesquida, P., 2022. Mechanical properties of collagen fibrils determined by buckling analysis. Acta Biomater 149, 60–68.

Gallego-Muñoz, P., Ibares-Frías, L., Lorenzo, E., Marcos, S., Peréz-Merino, P., Bekesi, N., Kochevar, I.E., Martínez-García, M.C., 2017. Corneal Wound Repair After Rose Bengal and Green Light Crosslinking: Clinical and Histologic Study. Invest Ophthalmol Vis Sci 58, 3471–3480.

Gao, Q., Liu, Q., Ma, P., Zhong, X., Wu, J., Ge, J., 2006. Effects of direct intravitreal dopamine injections on the development of lid-suture induced myopia in rabbits. Graefe's Archive for Clinical and Experimental Ophthalmology 244, 1329–1335.

Gerberich, B.G., Hannon, B.G., Hejri, A., Winger, E.J., Schrader Echeverri, E., Nichols, L.M., Gersch, H.G., MacLeod, N.A., Gupta, S., Read, A.T., Ritch, M.D., Sridhar, S., Toothman, M.G., Gershon, G.S., Schwaner, S.A., Sánchez-Rodríguez, G., Goyal, V., Toporek, A.M., Feola, A.J., Grossniklaus, H.E., Pardue, M.T., Ethier, C.R., Prausnitz, M.R., 2021. Transpupillary collagen photocrosslinking for targeted modulation of ocular biomechanics. Biomaterials 271, 120735.

Germann, J., Villegas, L., Martinez-Enriquez, E., Revuelta, L., Cómitre, B., Sanderson, D., Llorente, V., Desco, M., Gómez-Gaviro, M.V., Marcos, S., 2021. Collagen Organization in the Posterior Rabbit Sclera Post Cross-Linking. Invest Ophthalmol Vis Sci 62, 3276.

Germann, J.A., Martinez-Enriquez, E., Marcos, S., 2018. Quantization of collagen organization in the stroma with a new order coefficient. Biomed Opt Express 9, 173.

Germann, J.A., Martínez-Enríquez, E., Martínez-García, M.C., Kochevar, I.E., Marcos, S., 2020. Corneal Collagen Ordering After In Vivo Rose Bengal and Riboflavin Cross-Linking. Invest Ophthalmol Vis Sci 61, 28.

Germann, J.A., Villegas, L., Revuelta, L., Marcos, S., 2023. Effects of pharmacological treatments of myopia on scleral collagen organization in myopic guinea pig models. Invest Ophthalmol Vis Sci 64, 2859.

Girard, M., Suh, J.-K.F., Hart, R.T., Burgoyne, C.F., Downs, J.C., 2007. Effects of Storage Time on the Mechanical Properties of Rabbit Peripapillary Sclera After Enucleation. Curr Eye Res 32, 465–470.

Girard, M.J.A., Dahlmann-Noor, A., Rayapureddi, S., Bechara, J.A., Bertin, B.M.E., Jones, H., Albon, J., Khaw, P.T., Ross Ethier, C., 2011. Quantitative mapping of scleral fiber orientation in normal rat eyes. Invest Ophthalmol Vis Sci 52, 9684–9693.

Girard, M.J.A., Downs, J.C., Burgoyne, C.F., Suh, J.-K.F., 2009. Peripapillary and posterior scleral mechanics–part I: development of an anisotropic hyperelastic constitutive model. J Biomech Eng 131 5, 051011.

Gora, M., Karnowski, K., Szkulmowski, M., Kaluzny, B.J., Huber, R., Kowalczyk, A., Wojtkowski, M., 2009. Ultra high-speed swept source OCT imaging of the anterior segment of human eye at 200 kHz with adjustable imaging range. Opt Express 17, 14880–14894.

Grytz, R., Fazio, M.A., Girard, M.J.A., Libertiaux, V., Bruno, L., Gardiner, S., Girkin, C.A., Crawford Downs, J., 2014. Material properties of the posterior human sclera. J Mech Behav Biomed Mater 29, 602–617.

Guggenheim, J.A., McBrien, N.A., 1996. Form-deprivation myopia induces activation of scleral matrix metalloproteinase-2 in tree shrew. Invest Ophthalmol Vis Sci 37, 1380–1395.

Guo, L., Hua, R., Zhang, X., Yan, T.Y., Tong, Y., Zhao, X., Chen, S.C., Wang, M., Bressler, N.M., Kong, J., 2022. Scleral Cross-Linking in Form-Deprivation Myopic Guinea Pig Eyes Leads to Glaucomatous Changes. Invest Ophthalmol Vis Sci 63, 24.

Han, M., Giese, G., Bille, J.F., 2005. Second harmonic generation imaging of collagen fibrils in cornea and sclera. Opt Express 13, 5791.

Han, Z., Li, J., Singh, M., Wu, C., Liu, C. hao, Raghunathan, R., Aglyamov, S.R., Vantipalli, S., Twa, M.D., Larin, K. V., 2017. Optical coherence elastography assessment of corneal viscoelasticity with a modified Rayleigh-Lamb wave model. J Mech Behav Biomed Mater 66, 87–94.

Harper, A.R., Summers, J.A., 2015. The dynamic sclera: Extracellular matrix remodeling in normal ocular growth and myopia development. Exp Eye Res 133, 100–111.

Hatami-Marbini, H., 2023. On the Mechanical Roles of Glycosaminoglycans in the Tensile Properties of Porcine Corneal Stroma. Invest Ophthalmol Vis Sci 64, 0–5.

Hatami-Marbini, H., Jayaram, S.M., 2018. Effect of UVA/Riboflavin Collagen Crosslinking on Biomechanics of Artificially Swollen Corneas. Invest Ophthalmol Vis Sci 59, 764–770.

Hatami-Marbini, H., Pachenari, M., 2021. Tensile Viscoelastic Properties of the Sclera after Glycosaminoglycan Depletion. Curr Eye Res 46, 1299–1308.

Hatami-Marbini, H., Pachenari, M., 2020. Hydration related changes in tensile response of posterior porcine sclera. J Mech Behav Biomed Mater 104, 103562.

Hatami-Marbini, H., Rahimi, A., 2016. Interrelation of Hydration, Collagen Cross-Linking Treatment, and Biomechanical Properties of the Cornea. Curr Eye Res 41, 616–622.

Hatami-Marbini, H., Rahimi, A., 2014. The relation between hydration and mechanical behavior of bovine cornea in tension. J Mech Behav Biomed Mater 36, 90–97.

Haverkamp, R.G., Sizeland, K.H., Wells, H.C., Kamma-Lorger, C., 2022. Collagen dehydration. Int J Biol Macromol 216, 140–147.

Hayes, S., Kamma-Lorger, C.S., Boote, C., Young, R.D., Quantock, A.J., Rost, A., Khatib, Y., Harris, J., Yagi, N., Terrill, N., Meek, K.M., 2013. The Effect of Riboflavin/UVA Collagen Cross-linking Therapy on the Structure and Hydrodynamic Behaviour of the Ungulate and Rabbit Corneal Stroma. PLoS One. 8(1):e52860.

Hitzenberger, C.K., 1991. Optical measurement of the axial eye length by laser Doppler interferometry. Invest Ophthalmol Vis Sci 32, 616–624.

Hoang, Q. V, Rohrbach, D., McFadden, S.A., Mamou, J., 2019. Regional changes in the elastic properties of myopic Guinea pig sclera. Exp Eye Res 186, 107739.

Hocking, A.M., Shinomura, T., McQuillan, D.J., 1998. Leucine-rich repeat glycoproteins of the extracellular matrix. Matrix Biology 17, 1–19.

Hoerig, C., McFadden, S., Hoang, Q. V, Mamou, J., 2022. Biomechanical changes in myopic sclera correlate with underlying changes in microstructure. Exp Eye Res 224, 109165.

Holden, B.A., Fricke, T.R., Wilson, D.A., Jong, M., Naidoo, K.S., Sankaridurg, P., Wong, T.Y., Naduvilath, T.J., Resnikoff, S., 2016. Global Prevalence of Myopia and High Myopia and Temporal Trends from 2000 through 2050. Ophthalmology 123, 1036–1042.

Howlett, M.C., McFadden, S.A., 2002. A Fast and Effective Mammalian Model to Study the Visual Regulation of Eye Growth. Invest Ophthalmol Vis Sci 43, 2928.

Howlett, M.H.C., McFadden, S.A., 2009. Spectacle lens compensation in the pigmented guinea pig. Vision Res 49, 219–227.

Howlett, M.H.C., McFadden, S.A., 2006. Form-deprivation myopia in the guinea pig (Cavia porcellus). Vision Res 46, 267–283.

Huang, J., Wen, D., Wang, Q., McAlinden, C., Flitcroft, I., Chen, Haisi, Saw, S.M., Chen, Hao, Bao, F., Zhao, Y., Hu, L., Li, X., Gao, R., Lu, W., Du, Y., Jinag, Z., Yu, A., Lian, H., Jiang, Q., Yu, Y., Qu, J., 2016. Efficacy Comparison of 16 Interventions for Myopia Control in Children: A Network Meta-analysis. Ophthalmology 123, 697–708.

Huang, Y., Meek, K.M., 1999. Swelling Studies on the Cornea and Sclera: The Effects of pH and Ionic Strength. Biophys J 77, 1655–1665.

Iseli, H.P., Körber, N., Karl, A., Koch, C., Schuldt, C., Penk, A., Liu, Q., Huster, D., Käs, J., Reichenbach, A., Wiedemann, P., Francke, M., 2015. Damage threshold in adult rabbit eyes after scleral cross-linking by riboflavin/blue light application. Exp Eye Res 139, 37–47.

Iseli, H.P., Spoerl, E., Wiedemann, P., Krueger, R.R., Seiler, T., 2008. Efficacy and safety of blue-light scleral cross-linking. J Refract Surg 24, S752-5.

Iuvone, P.M., Tigges, M., Fernandes, A., Tigges, J., 1989. Dopamine synthesis and metabolism in rhesus monkey retina: Development, aging, and the effects of monocular visual deprivation. Vis Neurosci 2, 465–471.

Jain, V., Liang, P.J.M., Raja, S., Mikhael, M., Cameron, M.A., 2023. Light activation of the dopaminergic system occurs after eye-opening in the mouse retina. Frontiers in Ophthalmology. 9, 3:1184627.

Jiang, L., Long, K., Schaeffel, F., Zhang, S., Zhou, X., Lu, F., Qu, J., 2011. Disruption of emmetropization and high susceptibility to deprivation myopia in albino guinea pigs. Invest Ophthalmol Vis Sci 52, 6124–6132.

Jiang, L., Long, K., Schaeffel, F., Zhou, X., Zheng, Y., Ying, H., Lu, F., Stell, W.K., Qu, J., 2014. Effects of Dopaminergic Agents on Progression of Naturally Occurring Myopia in Albino Guinea Pigs (Cavia porcellus). Invest Ophthalmol Vis Sci 55, 7508–7519.

Jiménez-villar, A., Mączyńska, E., Cichański, A., Wojtkowski, M., Kałużny, B.J., Grulkowski, I., 2019. High-speed OCT-based ocular biometer combined with an air-puff system for determination of induced retraction-free eye dynamics. Biomed Opt Express 10, 3663–3680.

Jin, N., Stjernschantz, J., 2000. Effects of prostaglandins on form deprivation myopia in the chick. Acta Ophthalmol Scand 78, 495–500.

Kaiti, R., Shyangbo, R., Sharma, I.P., 2022. Role of Atropine in the control of Myopia Progression-A Review. Beyoglu Eye J. 7(3), 157–166.

Kirby, M.A., Pelivanov, I., Song, S., Ambrozinski, Ł., Yoon, S.J., Gao, L., Li, D., Shen, T.T., Wang, R.K., O'Donnell, M., 2017. Optical coherence elastography in ophthalmology. J Biomed Opt. 22(12):1-28.

Kirby, M.A., Pitre, J.J., Liou, H.-C., Li, D.S., Wang, R.K., Pelivanov, I., O'Donnell, M., Shen, T.T., 2021. Delineating Corneal Elastic Anisotropy in a Porcine Model Using Noncontact OCT Elastography and Ex Vivo Mechanical Tests. Ophthalmology Science. 1(4):100058

Kling, S., Marcos, S., 2013. Contributing factors to corneal deformation in air puff measurements. Invest Ophthalmol Vis Sci 54, 5078–5085.

Kling, S., Remon, L., Pérez-Escudero, A., Merayo-Lloves, J., Marcos, S., 2010. Corneal biomechanical changes after collagen cross-linking from porcine eye inflation experiments. Invest Ophthalmol Vis Sci 51, 3961–3968.

Knox Cartwright, N.E., Tyrer, J.R., Marshall, J., 2011. Age-Related Differences in the Elasticity of the Human Cornea. Invest Ophthalmol Vis Sci 52, 4324–4329.

Kochevar, I.E., Redmond, R.W., 2000. Photosensitized production of singlet oxygen. Methods in Enzymology. 319:20-28.

Komai, Y., Ushiki, T., 1991. The three-dimensional organization of collagen fibrils in the human cornea and sclera. Invest Ophthalmol Vis Sci 32, 2244–2258.

Koob, T.J., Vogel, K.G., 1987. Site-related variations in glycosaminoglycan content and swelling properties of bovine flexor tendon. Journal of Orthopaedic Research 5, 414–424.

Lagarias, J.C., Reeds, J.A., Wright, M.H., Wright, P.E., 1998. Convergence Properties of the Nelder-Mead Simplex Method in Low Dimensions. SIAM Journal on Optimization. 9, 112–147.

Lai, L., Trier, K., Cui, D.-M., 2023. Role of 7-methylxanthine in myopia prevention and control: A mini-review. Int J Ophthalmol. 16(6):969-976.

Lamb, H., 1881. On the Vibrations of an Elastic Sphere. Proceedings of the London Mathematical Society. s1-13, 189–212.

Landau L, Lifshitz E, 1987. Fluid Mechanics, Second Edition. ed, Teoretičeskaja fizika. Pergamon Press, Oxford, England.

Lankford, W.T., Snyder, S.C., Bauscher, J.A., 1950. New criteria for predicting the performance of deep drawing sheets. Transactions of American Society of Metals 42, 1197–1225.

Lari, D.R., Schultz, D.S., Wang, A.S., Lee, O.-T., Stewart, J.M., 2012. Scleral mechanics: Comparing whole globe inflation and uniaxial testing. Exp Eye Res 94, 128–135.

Larin, K. V., Sampson, D.D., 2017. Optical coherence elastography – OCT at work in tissue biomechanics [Invited]. Biomed Opt Express. (2):1172-1202.

Levy, A.M., Fazio, M.A., Grytz, R., 2018. Experimental myopia increases and scleral crosslinking using genipin inhibits cyclic softening in the tree shrew sclera. Ophthalmic and Physiological Optics 38, 246–256.

Li, W., Lan, W., Yang, S., Liao, Y., Xu, Q., Lin, L., Yang, Z., 2014. The Effect of Spectral Property and Intensity of Light on Natural Refractive Development and Compensation to Negative Lenses in Guinea Pigs. Invest Ophthalmol Vis Sci 55, 6324–6332.

Li, X., Wu, M., Zhang, Luyi, Liu, H., Zhang, Lan, He, J., 2017. Riboflavin and ultraviolet A irradiation for the prevention of progressive myopia in a guinea pig model. Exp Eye Res 165, 1–6.

Li, Y., Qi, Y., Sun, M., Zhai, C., Wei, W., Zhang, F., 2023. Clinical Feasibility and Safety of Scleral Collagen Cross-Linking by Riboflavin and Ultraviolet A in Pathological Myopia Blindness: A Pilot Study. Ophthalmol Ther. 12, 853–866.

Li, Y., Zhang, F., Sun, M., Lai, L., Lv, X., Liu, C., Wang, M., Wang, N., 2021. Safety and Long-term Scleral Biomechanical Stability of Rhesus Eyes after Scleral Cross-linking by Blue Light. Curr Eye Res 46, 1061–1070.

Lindsey, J.D., Kashiwagi, K., Kashiwagi, F., Weinreb, R.N., 1997. Prostaglandins alter extracellular matrix adjacent to human ciliary muscle cells in vitro. Invest Ophthalmol Vis Sci 38, 2214–2223.

Litwiller, D. V, Lee, S.J., Kolipaka, A., Mariappan, Y.K., Glaser, K.J., Pulido, J.S., Ehman, R.L., 2010. MR elastography of the ex vivo bovine globe. Journal of Magnetic Resonance Imaging. 32, 44–51.

Liu, H.-H., Kenning, M.S., Jobling, A.I., McBrien, N.A., Gentle, A., 2017. Reduced Scleral TIMP-2 Expression Is Associated With Myopia Development: TIMP-2

Supplementation Stabilizes Scleral Biomarkers of Myopia and Limits Myopia Development. Invest Ophthalmol Vis Sci 58, 1971–1981.

Liu, S., Li, S., Wang, B., Lin, X., Wu, Y., Liu, H., Qu, X., Dai, J., Zhou, X., Zhou, H., 2016. Scleral cross-linking using riboflavin UVA irradiation for the prevention of myopia progression in a guinea pig model: Blocked axial extension and altered scleral microstructure. PLoS One. 11, 1–16.

Liu, T.X., Wang, Z., 2017. Biomechanics of sclera crosslinked using genipin in rabbit. Int J Ophthalmol. 10, 355–360.

Liu, Y., Wang, Y., Lv, H., Jiang, X., Zhang, M., Li, X., 2017. α-adrenergic agonist brimonidine control of experimentally induced myopia in guinea pigs: A pilot study. Mol Vis 23, 785.

Lorenzo-Martín, E., Gallego-Muñoz, P., Ibares-Frías, L., Marcos, S., Pérez-Merino, P., Fernández, I., Kochevar, I.E., Martínez-García, M.C., 2018. Rose Bengal and Green Light Versus Riboflavin–UVA Cross-Linking: Corneal Wound Repair Response. Invest Ophthalmol Vis Sci 59, 4821–4830.

Lu, F., Zhou, X., Zhao, H., Wang, R., Jia, D., Jiang, L., Xie, R., Qu, J., 2006. Axial myopia induced by a monocularly-deprived facemask in guinea pigs: A non-invasive and effective model. Exp Eye Res 82, 628–636.

Maczynska, E., Karnowski, K., Szulzycki, K., Malinowska, M., Dolezyczek, H., Cichanski, A., Wojtkowski, M., Kaluzny, B., Grulkowski, I., 2019a. Assessment of the influence of viscoelasticity of cornea in animal ex vivo model using air-puff optical coherence tomography and corneal hysteresis. J Biophotonics. 12(2):e201800154.

Maczynska, E., Rzeszewska-Zamiara, J., Jimenez Villar, A., Wojtkowski, M., Kaluzny, B.J., Grulkowski, I., 2019b. Air-Puff-Induced Dynamics of Ocular Components Measured with Optical Biometry. Invest Ophthalmol Vis Sci 60, 1979–1986.

Maeda-Chubachi, T., Chi-Burris, K., Simons, B., Brémond-Gignac, D., Freedman, S., Khaw, P.T., Wirostko, B., Yan, E., Group, the A.S., 2013. Impact of Age, Diagnosis, and History of Glaucoma Surgery on Outcomes in Pediatric Patients Treated With Latanoprost. J Glaucoma. 22(8):614-619

Maeda-Chubachi, T., Chi-Burris, K., Simons, B.D., Freedman, S.F., Khaw, P.T., Wirostko, B., Yan, E., 2011. Comparison of Latanoprost and Timolol in

Pediatric Glaucoma: A Phase 3, 12-Week, Randomized, Double-Masked Multicenter Study. Ophthalmology 118, 2014–2021.

Markov, P.P., Eliasy, A., Pijanka, J.K., Htoon, H.M., Paterson, N.G., Sorensen, T., Elsheikh, A., Girard, M.J.A., Boote, C., 2018. Bulk changes in posterior scleral collagen microstructure in human high myopia. Mol Vis 24, 818–833.

McAuley, R., Nolan, A., Curatolo, A., Alexandrov, S., Zvietcovich, F., Varea Bejar, A., Marcos, S., Leahy, M., Birkenfeld, J.S., 2022. Co-axial acoustic-based optical coherence vibrometry probe for the quantification of resonance frequency modes in ocular tissue. Sci Rep. 12(1):18834.

McBrien, N.A., Cornell, L.M., Gentle, A., 2001. Structural and ultrastructural changes to the sclera in a mammalian model of high myopia. Invest Ophthalmol Vis Sci 42, 2179–2187.

McBrien, N.A., Gentle, A., 2003. Role of the sclera in the development and pathological complications of myopia. Prog Retin Eye Res 22, 307–338.

McBrien, N.A., Jobling, A.I., Gentle, A., 2009. Biomechanics of the sclera in myopia: extracellular and cellular factors. Optometry and Vision Science 86, E23–E30.

McBrien, N.A., Lawlor, P., Gentle, A., 2000. Recovery from Axial Myopia in the Tree Shrew. Invest Ophthalmol Vis Sci 41, 3713–3719.

McFadden, S., Wallman, J., 1995. Guinea pig eye growth compensates for spectacle lenses. Invest Ophthalmol Vis Sci 36, S758.

McFadden, S.A., Howlett, M.H.C., Mertz, J.R., 2004. Retinoic acid signals the direction of ocular elongation in the guinea pig eye. Vision Res 44, 643–653.

McKee, C.T., Last, J.A., Russell, P., Murphy, C.J., 2011. Indentation versus tensile measurements of young's modulus for soft biological tissues. Tissue Eng Part B Rev 17, 155–164.

Meek, K.M., Knupp, C., 2015. Corneal structure and transparency. Prog Retin Eye Res 49, 1–16.

Metzler, K.M., Mahmoud, A.M., Liu, J. and Roberts, C.J., 2014. Deformation response of paired donor corneas to an air puff: intact whole globe versus mounted corneoscleral rim. Journal of Cataract & Refractive Surgery, 40(6), pp.888-896.

Mlyniuk, P., Maczynska-Walkowiak, E., Rzeszewska-Zamiara, J., Grulkowski, I., Kaluzny, B.J., 2021. Probing biomechanical properties of the cornea with air-puff-based techniques - An overview. Advanced Optical Technologies. 10, 375–391.

Mortazavi, A.M., Simon, B.R., Stamer, W.D., Vande Geest, J.P., 2009. Drained secant modulus for human and porcine peripapillary sclera using unconfined compression testing. Exp Eye Res 89, 892–897.

Murienne, B.J., Chen, M.L., Quigley, H.A., Nguyen, T.D., 2016. The contribution of glycosaminoglycans to the mechanical behaviour of the posterior human sclera. J R Soc Interface. 13, 20160367.

Nan-Ji, L., Ahmed, E., J, R.J., Nikki, H., M, A.I., Mark, H., Daniel, E., Christian, F., Carina, K., Le-Le, C., Farhad, H., 2022. Combining Spectral-Domain OCT and Air-Puff Tonometry Analysis to Diagnose Keratoconus. Journal of Refractive Surgery 38, 374–380.

National Center for Biotechnology Information, 2023. PubChem Compound Summary for, Atropine. URL https://pubchem.ncbi.nlm.nih.gov/compound/Atropine (accessed 4.10.24).

Ndlovu, Z., Desai, D., Pandelani, T., Ngwangwa, H., 2022. Biaxial Estimation of Biomechanical Constitutive Parameters of Passive Porcine Sclera Soft Tissue. 2022:4775595.

Nemati, B., Rylander, H.G., Welch, A.J., 1996. Optical properties of conjunctiva, sclera, and the ciliary body and their consequences for transscleral cyclophotocoagulation. Appl Opt 35, 3321–3327.

Nguyen, B.A., Roberts, C.J., Reilly, M.A., 2019. Biomechanical impact of the sclera on corneal deformation response to an air-puff: A finite-element study. Front Bioeng Biotechnol 6, 1–8.

Nickla, D.L., Totonelly, K., Dhillon, B., 2010. Dopaminergic agonists that result in ocular growth inhibition also elicit transient increases in choroidal thickness in chicks. Exp Eye Res 91, 715–720.

Norman, R.E., Flanagan, J.G., Rausch, S.M.K., Sigal, I.A., Tertinegg, I., Eilaghi, A., Portnoy, S., Sled, J.G., Ethier, C.R., 2010. Dimensions of the human sclera: Thickness measurement and regional changes with axial length. Exp Eye Res 90, 277–284.

Norton, T.T., Rada, J.A., 1995. Reduced extracellular matrix in mammalian sclera with induced myopia. Vision Res 35, 1271–1281.

Ocklind, A., 1998. Effect of Latanoprost on the Extracellular Matrix of the Ciliary Muscle. A Study on Cultured Cells and Tissue Sections. Exp Eye Res 67, 179–191.

Olsen, T.W., Sanderson, S., Feng, X., Hubbard, W.C., 2002. Porcine sclera: Thickness and surface area. Invest Ophthalmol Vis Sci 43, 2529–2532.

Ostrin, L.A., Frishman, L.J., Glasser, A., 2004. Effects of Pirenzepine on Pupil Size and Accommodation in Rhesus Monkeys. Invest Ophthalmol Vis Sci 45, 3620–3628.

Ottani, V., Martini, D., Franchi, M., Ruggeri, A., Raspanti, M., 2002. Hierarchical structures in fibrillar collagens. Micron 33, 587–596.

Pachenari, M., Hatami-Marbini, H., 2021. Regional Differences in the Glycosaminoglycan Role in Porcine Scleral Hydration and Mechanical Behavior. Invest Ophthalmol Vis Sci 62, 28.

Pan, M., Guan, Z., Reinach, P.S., Kang, L., Cao, Y., Zhou, D., Srinivasalu, N., Zhao, F., Qu, J., Zhou, X., 2021. PPARγ modulates refractive development and form deprivation myopia in Guinea pigs. Exp Eye Res. 202:108332.

Park, J., Shin, A., Jafari, S., Demer, J.L., 2021. Material properties and effect of preconditioning of human sclera, optic nerve, and optic nerve sheath. Biomech Model Mechanobiol 20, 1353–1363.

Pérez-Merino, P., Velasco-Ocana, M., Martinez-Enriquez, E., Revuelta, L., McFadden, S.A., Marcos, S., 2017. Three-dimensional OCT based guinea pig eye model: relating morphology and optics. Biomed Opt Express 8, 2173–2184.

Phillips, J.R., Khalaj, M., McBrien, N.A., 2000. Induced myopia associated with increased scleral creep in chick and tree shrew eyes. Invest Ophthalmol Vis Sci 41, 2028–2034.

Phillips, J.R., McBrien, N.A., 1995. Form deprivation myopia: elastic properties of sclera. Ophthalmic and Physiological Optics 15, 357–362.

Pierscionek, B.K., Asejczyk-Widlicka, M., Schachar, R.A., 2007. The effect of changing intraocular pressure on the corneal and scleral curvatures in the fresh porcine eye. British Journal of Ophthalmology. 91(6):801-803.

Pijanka, J.K., Coudrillier, B., Ziegler, K., Sorensen, T., Meek, K.M., Nguyen, T.D., Quigley, H.A., Boote, C., 2012. Quantitative mapping of collagen fiber orientation in non-glaucoma and glaucoma posterior human sclerae. Invest Ophthalmol Vis Sci 53, 5258–5270.

Pijanka, J.K., Kimball, E.C., Pease, M.E., Abass, A., Sorensen, T., Nguyen, T.D., Quigley, H.A., Boote, C., 2014. Changes in scleral collagen organization in murine chronic experimental glaucoma. Invest Ophthalmol Vis Sci 55, 6554–6564.

Pineles, S.L., Kraker, R.T., VanderVeen, D.K., Hutchinson, A.K., Galvin, J.A., Wilson, L.B., Lambert, S.R., 2017. Atropine for the Prevention of Myopia Progression in Children: A Report by the American Academy of Ophthalmology. Ophthalmology 124, 1857–1866.

Pitre, J.J., Kirby, M.A., Li, D.S., Shen, T.T., Wang, R.K., O'Donnell, M., Pelivanov, I., 2020. Nearly-incompressible transverse isotropy (NITI) of cornea elasticity: model and experiments with acoustic micro-tapping OCE. Sci Rep 10, 1–14.

Quinn, G.E., Berlin, J.A., Young, T.L., Ziylan, S., Stone, R.A., 1995. Association of Intraocular Pressure and Myopia in Children. Ophthalmology 102, 180–185.

Raber, S., Courtney, R., Maeda-Chubachi, T., Simons, B.D., Freedman, S.F., Wirostko, B., 2011. Latanoprost Systemic Exposure in Pediatric and Adult Patients with Glaucoma: A Phase 1, Open-Label Study. Ophthalmology 118, 2022–2027.

Rada, J.A., Achen, V.R., Penugonda, S., Schmidt, R.W., Mount, B.A., 2000. Proteoglycan Composition in the Human Sclera During Growth and Aging. Invest Ophthalmol Vis Sci 41, 1639–1648.

Raiskup, F., Herber, R., Lenk, J., Ramm, L., Wittig, D., Pillunat, L.E., Spoerl, E., 2023. Corneal Crosslinking With Riboflavin and UVA Light in Progressive Keratoconus: Fifteen-Year Results. Am J Ophthalmol 250, 95–102.

Raiskup, F., Spoerl, E., 2013. Corneal crosslinking with riboflavin and ultraviolet A. I. principles. Ocular Surface 11, 65–74.

Ramier, A., Eltony, A.M., Chen, Y.T., Clouser, F., Birkenfeld, J.S., Watts, A., Yun, S.H., 2020. In vivo measurement of shear modulus of the human cornea using optical coherence elastography. Sci Rep 10, 1–10.

Raspanti, M., Congiu, T., Alessandrini, A., Gobbi, P., Ruggeri, A., 2000. Different patterns of collagen-proteoglycan interaction: a scanning electron microscopy and atomic force microscopy study. European Journal of Histochemistry 44, 335–344.

Redmond, R.W., Kochevar, I.E., 2019. Medical Applications of Rose Bengal- and Riboflavin-Photosensitized Protein Crosslinking. Photochem Photobiol 95, 1097–1115.

Regnault, G., Kirby, M.A., Wang, R.K., Shen, T.T., O'Donnell, M., Pelivanov, I., 2023. Possible depth-resolved reconstruction of shear moduli in the cornea following collagen crosslinking (CXL) with optical coherence tomography and elastography. Biomed Opt Express 14, 5005–5021.

Roberts, C., Mahmoud, A., Bons, J., Hossain, A., Elsheikh, A., Vinciguerra, R., Vinciguerra, P., Ambrósio, R., 2017. Introduction of Two Novel Stiffness Parameters and Interpretation of Air Puff–Induced Biomechanical Deformation Parameters With a Dynamic Scheimpflug Analyzer. Journal of Refractive Surgery 33, 266–273.

Rose, J.L., 1999. Ultrasonic guided waves in solid media. Cambridge university press.

Roth, S., Freund, I., 1979. Second harmonic generation in collagen. J Chem Phys 70, 1637–1643.

Runge, J., Kischkel, S., Keiler, J., Grabow, N., Schmitz, K.-P., Siewert, S., Wree, A., Guthoff, R.F., Stahnke, T., 2024. Experimental glaucoma microstent implantation in two animal models and human donor eyes—an ex vivo micro-computed tomography-based evaluation of applicability. Quant Imaging Med Surg. 14(8):5321-5332

Russo, A., Riva, I., Pizzolante, T., Noto, F., Quaranta, L., 2008. Latanoprost ophthalmic solution in the treatment of open angle glaucoma or raised intraocular pressure: a review. Clinical Ophthalmology 2, 897–905.

Salvetat, M.L., Zeppieri, M., Tosoni, C., Felletti, M., Grasso, L., Brusini, P., 2015. Corneal Deformation Parameters Provided by the Corvis-ST Pachy-Tonometer in Healthy Subjects and Glaucoma Patients. J Glaucoma 24(8):568-574.

Sánchez-Tena, M.Á., Martinez-Perez, C., Villa-Collar, C., González-Pérez, M., González-Abad, A., Afflelou, G. de I.A., Alvarez-Peregrina, C., 2024.

Prevalence and estimation of the evolution of myopia in Spanish children. J Clin Med 13(6):1800.

Scarcelli, G., Polacheck, W.J., Nia, H.T., Patel, K., Grodzinsky, A.J., Kamm, R.D., Yun, S.H., 2015. Noncontact three-dimensional mapping of intracellular hydromechanical properties by Brillouin microscopy. Nat Methods 12, 1132–1134.

Scarcelli, G., Yun, S.H., 2012. In vivo Brillouin optical microscopy of the human eye. Opt Express 20, 9197–9202.

Schaeffel, F., Feldkaemper, M., 2015. Animal models in myopia research. Clin Exp Optom 98, 507–517.

Schaeffel, F., Glasser, A., Howland, H.C., 1988. Accommodation, refractive error and eye growth in chickens. Vision Res 28, 639–657.

Schmid, G.F., Papastergiou, G.I., Nickla, D.L., Riva, C.E., Lin, T., Stone, R.A., Laties, A.M., 1996. Validation of laser Doppler interferometric measurements in vivo of axial eye length and thickness of fundus layers in chicks. Curr Eye Res 15, 691–696.

Schuldt, C., Karl, A., Körber, N., Koch, C., Liu, Q., Fritsch, A.W., Reichenbach, A., Wiedemann, P., Käs, J.A., Francke, M., 2015. Dose-dependent collagen cross-linking of rabbit scleral tissue by blue light and riboflavin treatment probed by dynamic shear rheology. Acta Ophthalmol 93, e328–e336.

Schwahn, H.N., Kaymak, H., Schaeffel, F., 2000. Effects of atropine on refractive development, dopamine release, and slow retinal potentials in the chick. Vis Neurosci 17, 165–176.

Schwaner, S.A., Hannon, B.G., Feola, A.J., Ethier, C.R., 2020. Biomechanical properties of the rat sclera obtained with inverse finite element modeling. Biomech Model Mechanobiol 19, 2195–2212.

Schwiegerling, J., 2004. Field guide to visual and ophthalmic optics. Spie Bellingham, Washington, USA.

Shadwick, R.E., 1990. Elastic energy storage in tendons: Mechanical differences related to function and age. J Appl Physiol 68, 1033–1040.

Shao, P., Besner, S., Zhang, J., Scarcelli, G., Yun, S.-H., 2016. Etalon filters for Brillouin microscopy of highly scattering tissues. Opt Express 24, 22232–22238.

Sherman, S.M., Norton, T.T., Casagrande, V.A., 1977. Myopia in the lid-sutured tree shrew (Tupaia glis). Brain Res 124, 154–157.

Shih, Y.-F., Chen, C.-H., Chou, A.-C., Ho, T.-C., Lin, L.L.-K., Hung, P.-T., 1999. Effects of Different Concentrations of Atropine on Controlling Myopia in Myopic Children. Journal of Ocular Pharmacology and Therapeutics 15, 85–90.

Siatkowski, R.M., Cotter, S., Miller, J.M., Scher, C.A., Crockett, R.S., Novack, G.D., Group, U.S.P.S., 2004. Safety and Efficacy of 2% Pirenzepine Ophthalmic Gel in Children WithMyopia: A 1-Year, Multicenter, Double-Masked, Placebo-Controlled ParallelStudy. Archives of Ophthalmology 122, 1667–1674.

Singh, J.K., Dhawahir, F.E., Hamid, A.F.A., Chell, P.B., 2004. The use of dye in ophthalmology. Journal of Audiovisual Media in Medicine 27, 62–67.

Singh, M., Li, J., Han, Z., Raghunathan, R., Nair, A., Wu, C., Liu, C.-H., Aglyamov, S., Twa, M.D., Larin, K. V, 2017. Assessing the effects of riboflavin/UV-A crosslinking on porcine corneal mechanical anisotropy with optical coherence elastography. Biomed Opt Express 8, 349–366.

Singh, M., Li, J., Han, Z., Vantipalli, S., Liu, C.H., Wu, C., Raghunathan, R., Aglyamov, S.R., Twa, M.D., Larin, K. V., 2016a. Evaluating the effects of riboflavin/UV-a and rose-bengal/green light cross-linking of the rabbit cornea by noncontact optical coherence elastography. Invest Ophthalmol Vis Sci. 57(9):OCT112-20.

Singh, M., Li, J., Han, Z., Wu, C., Aglyamov, S.R., Twa, M.D., Larin, K. V, 2016b. Investigating Elastic Anisotropy of the Porcine Cornea as a Function of Intraocular Pressure With Optical Coherence Elastography. Journal of Refractive Surgery 32, 562–567.

Sloan, S.R., Khalifa, Y.M., Buckley, M.R., 2014. The location- and depth-dependent mechanical response of the human cornea under shear loading. Invest Ophthalmol Vis Sci 55, 7919–7924.

Soeken, T.A., Zhu, H., DeMartelaere, S., Davies, B.W., Kim, M., Wang, H.C., Aden, J., Grimm, R., Alt, C., Kochevar, I.E., Johnson, A.J., 2018. Sealing of corneal lacerations using photoactivated rose bengal dye and amniotic membrane. Cornea 37, 211–217.

Subasinghe, S.K., Ogbuehi, K.C., Mitchell, L., Dias, G.J., 2021. Animal model with structural similarity to human corneal collagen fibrillar arrangement. Anat Sci Int 96, 286–293.

Summers, J.A., Schaeffel, F., Marcos, S., Wu, H., Tkatchenko, A. V., 2021. Functional integration of eye tissues and refractive eye development: Mechanisms and pathways. Exp Eye Res 209, 108693.

Summers Rada, J.A., Shelton, S., Norton, T.T., 2006. The sclera and myopia. Exp Eye Res 82, 185–200.

Sun, M.G., Son, T., Crutison, J., Guaiquil, V., Lin, S., Nammari, L., Klatt, D., Yao, X., Rosenblatt, M.I., Royston, T.J., 2022. Optical coherence elastography for assessing the influence of intraocular pressure on elastic wave dispersion in the cornea. J Mech Behav Biomed Mater 128:105100.

Tan, D.T.H., Lam, D.S., Chua, W.H., Shu-Ping, D.F., Crockett, R.S., 2005. One-year multicenter, double-masked, placebo-controlled, parallel safety and efficacy study of 2% pirenzepine ophthalmic gel in children with myopia. Ophthalmology 112, 84–91.

The MathWorks Inc., 2021. Statistics and Machine Learning Toolbox version: 12.1 (R2021a).

Thomasy, S.M., Raghunathan, V.K., Winkler, M., Reilly, C.M., Sadeli, A.R., Russell, P., Jester, J. V, Murphy, C.J., 2014. Elastic modulus and collagen organization of the rabbit cornea: Epithelium to endothelium. Acta Biomater 10, 785–791.

Thomsen, L., 1986. Weak elastic anisotropy. Geophysics 51, 1954–1966.

Tian, T., Zou, L., Wu, S., Liu, H., Liu, R., 2019. Wavelength Defocus and Temporal Sensitivity Affect Refractive Development in Guinea Pigs. Invest Ophthalmol Vis Sci 60, 2173–2180.

Trier, K., Cui, D., Ribel-Madsen, S., Guggenheim, J., 2023. Oral administration of caffeine metabolite 7-methylxanthine is associated with slowed myopia progression in Danish children. British Journal of Ophthalmology 107, 1538.

Trier, K., Olsen, E.B., Kobayashi, T., Ribel-Madsen, S.M., 1999. Biochemical and ultrastructural changes in rabbit sclera after treatment with 7-methylxanthine, theobromine, acetazolamide, or L-ornithine. British Journal of Ophthalmology 83, 1370.

Troilo, D., Nickla, D.L., Mertz, J.R., Rada, J.A.S., 2006. Change in the synthesis rates of ocular retinoic acid and scleral glycosaminoglycan during experimentally altered eye growth in marmosets. Invest Ophthalmol Vis Sci 47, 1768–1777.

Uddin, M., Zuo, B., Wang, J., Catral, K.P.C., To, C., Tse, D.Y., 2022. Topical latanoprost inhibits the developments of form-deprivation myopia and lens-induced myopia in the chick model. Invest Ophthalmol Vis Sci 63, 1882-A0011-1882 - A0011.

Urizar, M.P., Gambra, E., de Castro, A., de la Peña, Á., Cetinkaya, O., Marcos, S., Curatolo, A., 2023. Optical beam scanner with reconfigurable non-mechanical control of beam position, angle, and focus for low-cost whole-eye OCT imaging. Biomed Opt Express 14, 4468–4484.

Vareilles, P., Conquet, P., Le Douarec, J.C., 1977. A method for the routine intraocular pressure (IOP) measurement in the rabbit: Range of IOP variations in this species. Exp Eye Res 24(4):369-75

Vera-Diaz, F.A., 2010. Myopia, in: Dartt, D.A. (Ed.), Encyclopedia of the Eye. Academic Press, Oxford, pp. 98–105.

Vézina, M., 2013. Comparative Ocular Anatomy in Commonly Used Laboratory Animals, in: Weir, A.B., Collins, M. (Eds.), Assessing Ocular Toxicology in Laboratory Animals. Humana Press, Totowa, NJ, pp. 1–21.

Viktorov, I.A., 1967. Rayleigh and Lamb waves, 1st ed, Rayleigh and Lamb Waves. Springer , New York, NY.

Villegas, L., Germann, J., Marcos, S., 2021. Biomechanical effects of Scleral crosslinking using Rose Bengal/Green-light and Rivoflavin/UVA. Invest Ophthalmol Vis Sci 62, 2281.

Villegas, L., Germann, J.A., Marcos, S., 2024a. Effects of Different Scleral Photo-Crosslinking Modalities on Scleral Stiffness and Hydration. Invest Ophthalmol Vis Sci 65(8):8.

Villegas, L., Urizar, M.P., Zvietcovich, F., Olalla, P., de Castro, A., Curatolo, A., Revuelta, L., Marcos, S., 2023a. Myopia control by atropine and latanoprost in a guinea pig model: impact on refraction, biometry and scleral mechanics. Invest Ophthalmol Vis Sci 64, 4958.

Villegas, L., Zvietcovich, F., Marcos, S., Birkenfeld, J.S., 2024b. Revealing regional variations in scleral shear modulus in a rabbit eye model using multi-directional ultrasound optical coherence elastography. Sci Rep 14(1):21010.

Villegas, L., Zvietcovich, F., Marcos, S., Birkenfeld, J.S., 2024c. Scleral anisotropy in ex vivo rabbit eyes using ultrasonic optical coherence elastography, in: Proc.SPIE. p. 1284409.

Villegas, L., Zvietcovich, F., Varea, A., Birkenfeld, J.S., Marcos, S., 2022. Spatial characterization of scleral biomechanics in ex vivo rabbit eyes using multi-meridian Optical Coherence Elastography. Invest Ophthalmol Vis Sci 63, 1454 -F0412-1454- F0412.

Villegas, L., Zvietcovich, F., Varea, A., Curatolo, A., Birkenfeld, J.S., Marcos, S., 2023b. Poster Session: Experimental assessment of scleral anisotropy using multi-meridian air-coupled ultrasonic optical coherence elastography. J Vis 23, 72.

Villegas Lopez, L.I., Bronte, D., Germann, J., Marcos, S., 2020. Scleral cross-linking using Rose Bengal-Green Light. Invest Ophthalmol Vis Sci 61, 3415.

Vinas-Pena, M., Feng, X., Li, G., Yun, S.-H., 2022. In situ measurement of the stiffness increase in the posterior sclera after UV-riboflavin crosslinking by optical coherence elastography. Biomed. Opt. Express 13, 5434–5446.

Vinciguerra, R., Ambrósio, R., Elsheikh, A., Roberts, C.J., Lopes, B., Morenghi, E., Azzolini, C., Vinciguerra, P., 2016. Detection of Keratoconus With a New Biomechanical Index. Journal of Refractive Surgery 32, 803–810.

Virtanen, P., Gommers, R., Oliphant, T.E., Haberland, M., Reddy, T., Cournapeau, D., Burovski, E., Peterson, P., Weckesser, W., Bright, J., van der Walt, S.J., Brett, M., Wilson, J., Millman, K.J., Mayorov, N., Nelson, A.R.J., Jones, E., Kern, R., Larson, E., Carey, C.J., Polat, İ., Feng, Y., Moore, E.W., VanderPlas, J., Laxalde, D., Perktold, J., Cimrman, R., Henriksen, I., Quintero, E.A., Harris, C.R., Archibald, A.M., Ribeiro, A.H., Pedregosa, F., van Mulbregt, P., Vijaykumar, A., Bardelli, A. Pietro, Rothberg, A., Hilboll, A., Kloeckner, A., Scopatz, A., Lee, A., Rokem, A., Woods, C.N., Fulton, C., Masson, C., Häggström, C., Fitzgerald, C., Nicholson, D.A., Hagen, D.R., Pasechnik, D. V., Olivetti, E., Martin, E., Wieser, E., Silva, F., Lenders, F., Wilhelm, F., Young, G., Price, G.A., Ingold, G.L., Allen, G.E., Lee, G.R., Audren, H., Probst, I., Dietrich, J.P., Silterra, J., Webber, J.T., Slavič, J., Nothman, J., Buchner, J., Kulick, J., Schönberger, J.L., de Miranda Cardoso, J.V., Reimer, J., Harrington, J., Rodríguez, J.L.C., Nunez-Iglesias, J., Kuczynski, J., Tritz, K., Thoma, M., Newville, M., Kümmerer, M., Bolingbroke, M., Tartre, M., Pak, M., Smith, N.J., Nowaczyk, N., Shebanov, N., Pavlyk, O., Brodtkorb, P.A., Lee, P., McGibbon, R.T., Feldbauer, R., Lewis, S., Tygier, S., Sievert, S., Vigna, S., Peterson, S., More, S., Pudlik, T., Oshima, T., Pingel, T.J., Robitaille, T.P., Spura, T., Jones, T.R., Cera, T., Leslie, T., Zito, T., Krauss, T., Upadhyay, U., Halchenko, Y.O., Vázquez-Baeza, Y., 2020. SciPy 1.0: fundamental algorithms for scientific computing in Python. Nat Methods 17, 261–272.

Voorhees, A.P., Jan, N.J., Hua, Y., Yang, B., Sigal, I.A., 2018. Peripapillary sclera architecture revisited: A tangential fiber model and its biomechanical implications. Acta Biomater 79, 113–122.

Wallman, J., Turkel, J., Trachtman, J., 1978. Extreme Myopia Produced by Modest Change in Early Visual Experience. Science (1979) 201, 1249–1251.

Wang, M., Corpuz, C.C.C., 2015. Effects of scleral cross-linking using genipin on the process of form-deprivation myopia in the guinea pig: A randomized controlled experimental study. BMC Ophthalmol 15, 1–7.

Wang, M., Zhang, F., Liu, K., Zhao, X., 2015. Safety evaluation of rabbit eyes on scleral collagen cross-linking by riboflavin and ultraviolet A. Clin Exp Ophthalmol 43, 156–163.

Wang, M., Zhang, F., Qian, X., Zhao, X., 2012. Regional biomechanical properties of human sclera after cross-linking by riboflavin/ultraviolet A. Journal of Refractive Surgery 28, 723–728.

Wang, N., Lindsey, J.D., Angert, M., Weinreb, R.N., 2001. Latanoprost and matrix metalloproteinase-1 in human choroid organ cultures. Curr Eye Res 22, 198–207.

Wang, P., Chen, S., Liu, Y., Lin, F., Song, Y., Li, T., Aung, T., Zhang, X., for the GSHM study group, 2021. Lowering Intraocular Pressure: A Potential Approach for Controlling High Myopia Progression. Invest Ophthalmol Vis Sci 62, 17.

Wang, S., Larin, K. V, 2014. Shear wave imaging optical coherence tomography (SWI-OCT) for ocular tissue biomechanics. Opt. Lett. 39, 41–44.

Wang, T., Zhu, L., Zhu, J., Peng, Y., Shen, N., Yu, Y., Yao, M., 2018. Subacute effects of rose Bengal/Green light cross linking on rabbit thin corneal stability and safety. Lasers Surg Med 50, 324–332.

Wang, W., Chen, C., Chang, J., Chien, L., Shih, Y., Lin, L., Pang, C.P., Wang, I.J., 2021. Pharmacotherapeutic candidates for myopia: A review. Biomedicine & Pharmacotherapy 133, 111092.

Wang, X., Sun, Y., Wang, K., Yang, S., Luan, C., Wu, B., Zhang, W., Hao, R., 2023. Effects of blue light exposure on ocular parameters and choroidal blood perfusion in Guinea pig. Exp Eye Res 235, 109619.

Wang, Y., Cao, H., 2022. Corneal and scleral biomechanics in ophthalmic diseases: An updated review. Med Nov Technol Devices 15, 100140.

Watson, P.G., Young, R.D., 2004. Scleral structure, organisation and disease. A review. Exp Eye Res 78, 609–623.

Webb, J.N., Zhang, H., Roy, A.S., Randleman, J.B., Scarcelli, G., 2020. Detecting mechanical anisotropy of the cornea using brillouin microscopy. Transl Vis Sci Technol 9, 1–11.

Welch Allyn, 2020. Welch Allyn 18200 Streak Retinoscopy Service Manual.

Whitford, C., Joda, A., Jones, S., Bao, F., Rama, P., Elsheikh, A., 2016. Ex vivo testing of intact eye globes under inflation conditions to determine regional variation of mechanical stiffness. Eye and Vision 3, 21.

Whitford, C., Studer, H., Boote, C., Meek, K.M., Elsheikh, A., 2015. Biomechanical model of the human cornea: Considering shear stiffness and regional variation of collagen anisotropy and density. J Mech Behav Biomed Mater 42, 76–87.

Wiesel, T.N., Raviola, E., 1977. Myopia and eye enlargement after neonatal lid fusion in monkeys. Nature 266, 66–68.

Willemse, J., Gräfe, M.G.O., Verbraak, F.D., de Boer, J.F., 2020. In Vivo 3D Determination of Peripapillary Scleral and Retinal Layer Architecture Using Polarization-Sensitive Optical Coherence Tomography. Transl Vis Sci Technol 9, 21.

Wollensak, G., 2006. Crosslinking treatment of progressive keratoconus: new hope. Curr Opin Ophthalmol 17(4):356-360.

Wollensak, G., Iomdina, E., 2009. Long-term biomechanical properties of rabbit sclera after collagen crosslinking using riboflavin and ultraviolet A (UVA). Acta Ophthalmol 87, 193–198.

Wollensak, G., Iomdina, E., 2008. Crosslinking of scleral collagen in the rabbit using glyceraldehyde. J Cataract Refract Surg 34, 651–656.

Wollensak, G., Iomdina, E., Dittert, D.-D., Salamatina, O., Stoltenburg, G., 2005. Cross-linking of scleral collagen in the rabbit using riboflavin and UVA. Acta Ophthalmol Scand 83, 477–482.

Wollensak, G., Spoerl, E., 2004. Collagen crosslinking of human and porcine sclera. J Cataract Refract Surg 30, 689–695.

Wollensak, G., Spoerl, E., Seiler, T., 2003. Riboflavin/ultraviolet-A-induced collagen crosslinking for the treatment of keratoconus. Am J Ophthalmol 135, 620–627.

Woo, S.L.-Y., Kobayashi, A.S., Schlegel, W.A., Lawrence, C., 1972. Nonlinear material properties of intact cornea and sclera. Exp Eye Res 14, 29–39.

World Health Organization, Brien Holden Vision Institute, 2016. The Impact of Myopia and High Myopia. Report of the Joint World Health Organization–Brien Holden Vision Institute Global Scientific Meeting on Myopia.

Wright, J.C., 1965. The Phenomenon of Earing In Deep Drawing. Sheet Metal Industries 42, 814–831.

Wu, H., Chen, W., Zhao, F., Zhou, Q., Reinach, P.S., Deng, L., Ma, L., Luo, S., Srinivasalu, N., Pan, M., Hu, Y., Pei, X., Sun, J., Ren, R., Xiong, Y., Zhou, Z., Zhang, S., Tian, G., Fang, J., Zhang, L., Lang, J., Wu, D., Zeng, C., Qu, J., Zhou, X., 2018. Scleral hypoxia is a target for myopia control. Proceedings of the National Academy of Sciences 115, E7091–E7100.

Wu, J., Liu, Q., Yang, X., Yang, H., Wang, X. mei, Zeng, J. wen, 2007. Time-course of changes to nitric oxide signaling pathways in form-deprivation myopia in guinea pigs. Brain Res 1186, 155–163.

Wu, Y., Feng, Y., Yang, J., Fan, H., Yu, Z., Xie, X., Dai, Y., Huang, X., Li, W., 2023. Effects of exogenous retinoic acid on ocular parameters in Guinea pigs with form deprivation myopia. Front Cell Dev Biol 11:1160897.

Xiao, H., Fan, Z.Y., Tian, X.D., Xu, Y.C., 2014. Comparison of form-deprived myopia and lens-induced myopia in guinea pigs. Int J Ophthalmol 7, 245–250.

Yakar, K., Kan, E., Duran, M., 2023. Comparison between wavefront-derived refraction and auto-refraction. Photodiagnosis Photodyn Ther 44, 103712.

Yam, J.C., Jiang, Y., Tang, S.M., Law, A.K.P., Chan, J.J., Wong, E., Ko, S.T., Young, A.L., Tham, C.C., Chen, L.J., Pang, C.P., 2019. Low-Concentration Atropine for Myopia Progression (LAMP) Study: A Randomized, Double-Blinded, Placebo-Controlled Trial of 0.05%, 0.025%, and 0.01% Atropine Eye Drops in Myopia Control. Ophthalmology 126, 113–124.

Yamamoto, S., Hashizume, H., Hitomi, J., Shigeno, M., Sawaguchi, S., Abe, H., Ushiki, T., 2000. The Subfibrillar Arrangement of Corneal and Scleral Collagen Fibrils as Revealed by Scanning Electron and Atomic Force Microscopy. Arch Histol Cytol 63, 127–135.

Yang, B., O'Connell, G.D., 2018. Swelling of fiber-reinforced soft tissues is affected by fiber orientation, fiber stiffness, and lamella structure. J Mech Behav Biomed Mater 82, 320–328.

Yang, Y., Wu, J., Wu, D., Wei, Q., Zhong, T., Yang, J., Yang, X., Zeng, M., Zhong, X., 2021. Intravitreal brimonidine inhibits form-deprivation myopia in guinea pigs. Eye and Vision 8, 27.

Yousefi, A., Roberts, C.J., Reilly, M.A., 2022. The Shape of Corneal Deformation Alters Air Puff–Induced Loading. Front Bioeng Biotechnol 10:848060.

Yu, Q., Zhou, J.-B., 2022. Scleral remodeling in myopia development. Int J Ophthalmol 15, 510.

Zhang, F., Lai, L., 2021. Advanced Research in Scleral Cross-Linking to Prevent From Progressive Myopia. Asia-Pacific Journal of Ophthalmology 10, 161-166.

Zhang, X.J., Zhang, Y., Kam, K.W., Tang, F., Li, Y., Ng, M.P.H., Young, A.L., Ip, P., Tham, C.C., Chen, L.J., Pang, C.P., Yam, J.C., 2023. Prevalence of Myopia in Children Before, During, and After COVID-19 Restrictions in Hong Kong. JAMA Netw Open 6, e234080–e234080.

Zhang, Y., Conrad, A.H., Conrad, G.W., 2011. Effects of Ultraviolet-A and Riboflavin on the Interaction of Collagen and Proteoglycans during Corneal Cross-linking. Journal of Biological Chemistry 286, 13011–13022.

Zhang, Y., Li, Z., Liu, L., Han, X., Zhao, X., Mu, G., 2014. Comparison of riboflavin/ultraviolet-A cross-linking in porcine, rabbit, and human sclera. Biomed Res Int 194204, 1–5.

Zhang, Y., Zou, C., Liu, L., Cao, L., Xia, X., Li, Z., Hu, M., Yu, H., Mu, G., 2013. Effect of irradiation time on riboflavin-ultraviolet-A collagen crosslinking in rabbit sclera. J Cataract Refract Surg 39, 1184–1189.

Zhao, F., Zhou, Q., Reinach, P.S., Yang, J., Ma, L., Wang, X., Wen, Y., Srinivasalu, N., Qu, J., Zhou, X., 2018. Cause and Effect Relationship between Changes in Scleral Matrix Metallopeptidase-2 Expression and Myopia Development in Mice. Am J Pathol 188, 1754–1767.

Zheng, L., Liao, Z., Zou, J., 2024. Animal modeling for myopia. Advances in Ophthalmology Practice and Research 4, 173–181.

Zhou, X., Pardue, M.T., Iuvone, P.M., Qu, J., 2017. Dopamine signaling and myopia development: What are the key challenges. Prog Retin Eye Res 61, 60–71.

Zhou, Xuan, Zhang, S., Zhang, G., Chen, Y., Lei, Y., Xiang, J., Xu, R., Qu, J., Zhou, Xiangtian, 2020. Increased Choroidal Blood Perfusion Can Inhibit Form Deprivation Myopia in Guinea Pigs. Invest Ophthalmol Vis Sci 61, 25.

Zhu, H., Alt, C., Webb, R.H., Melki, S., Kochevar, I.E., 2016. Corneal crosslinking with rose bengal and green light: Efficacy and safety evaluation. Cornea 35, 1234–1241.

Zhu, Q., Goto, S., Singh, S., Torres, J.A., Wildsoet, C.F., 2022. Daily or Less Frequent Topical 1% Atropine Slows Defocus-Induced Myopia Progression in Contact Lens-Wearing Guinea Pigs. Transl Vis Sci Technol 11, 26.

Zvietcovich, F., Nair, A., Ambekar, Y.S., Singh, M., Aglyamov, S.R., Twa, M.D., Larin, K. V, 2020a. Confocal air-coupled ultrasonic optical coherence elastography probe for quantitative biomechanics. Opt. Lett. 45, 6567–6570.

Zvietcovich, F., Nair, A., Singh, M., Aglyamov, S.R., Twa, M.D., Larin, K. V., 2022. In vivo assessment of corneal biomechanics under a localized cross-linking treatment using confocal air-coupled optical coherence elastography. Biomed Opt Express 13, 2644.

Zvietcovich, F., Nair, A., Singh, M., Aglyamov, S.R., Twa, M.D., Larin, K. V., 2020b. Dynamic optical coherence elastography of the anterior eye: Understanding the biomechanics of the limbus. Invest Ophthalmol Vis Sci 61(13):7.

Zvietcovich, F., Rolland, J.P., Parker, K.J., 2017a. An approach to viscoelastic characterization of dispersive media by inversion of a general wave propagation model. J Innov Opt Health Sci 10, 1–16.

Zvietcovich, F., Rolland, J.P., Yao, J., Meemon, P., Parker, K.J., 2017b. Comparative study of shear wave-based elastography techniques in optical coherence tomography. J Biomed Opt 22, 035010.

ANNEXES

A. Tables of results for Air-puff measurement

		Maximum displacement of the apex (mm)						
		Central Cornea	Sclera					
Animal model	**Airpuff configuration**	**C**	**EN**	**ET**	**PN**	**PT**	**S**	**I**
Porcine	AP2= 15.4 kPa	**0.98±0.10**	0.21±0.06	0.20±0.10	0.14±0.05	0.15±0.04	**0.83±0.19**	**0.92±0.26**
Rabbit	AP1= 7.28 kPa	**0.86±0.02**	**0.82±0.02**	**0.86±0.04**	0.65±0.02	0.58±0.06	0.65±0.04	0.76±0.04
	AP2= 15.4 kPa	**0.90±0.04**	**0.98±0.02**	0.63±0.03	0.78±0.10	0.80±0.17	0.83±0.05	**0.86±0.05**

Table A.1: Maximum displacement of apex in porcine and rabbit eyes. Mean values (± standard deviation). In bold are the three highest values per row. Data measured in porcine and rabbit eyes using two air-puff configurations (AP1 and AP2). The locations in the eye are: C (central cornea), S (superior), I (inferior), EN (equatorial nasal), ET (equatorial temporal), PN (posterior nasal), and PT (posterior temporal) sclera. The intraocular pressure was maintained at 15 mmHg. Porcine results were taken from our published data in (Bronte-Ciriza et al., 2021).

	Location						
	C	**EN**	**ET**	**PN**	**PT**	**S**	**I**
Porcine eyes using AP2							
V_{max} **before** max. deformation (mm/ms)	0.15±0.02	0.03±0.02	0.02±0.01	0.02±0.01	0.02±0.01	0.10±0.02	0.13±0.06
V_{max} **after** max. deformation (mm/ms)	0.48±0.19	0.07±0.05	0.05±0.02	0.04±0.02	0.04±0.02	0.37±0.18	0.30±0.09
Rabbit eyes using AP1							
V_{max} **before** max. deformation (mm/ms)	0.16±0.04	0.17±0.02	0.16±0.01	0.11±0.03	0.10±0.02	0.11±0.02	0.17±0.03
V_{max} **after** max. deformation (mm/ms)	0.28±0.24	0.35±0.09	0.34±0.09	0.21±0.16	0.25±0.17	0.22±0.17	0.22±0.17
Time interval between speed extremes (ms)	10.82±0.50	9.86±0.48	9.69±0.51	8.33±0.92	10.37±0.38	8.16±0.59	8.33±0.92
Rabbit eyes using AP2							
V_{max} **before** max. deformation (mm/ms)	0.18±0.10	0.26±0.02	0.12±0.04	0.12±0.04	0.13±0.02	0.16±0.03	0.16±0.05
V_{max} **after** max. deformation (mm/ms)	0.45±0.06	0.48±0.04	0.48±0.09	0.33±0.08	0.40±0.22	0.50±0.11	0.50±0.13
Time interval between speed extremes (ms)	11.39±0.70	9.18±0.0	7.82±0.48	9.69±1.41	9.80±0.50	8.16±0.59	8.67±1.28

Table A.2 Maximum deformation speed of the apex before and after maximum deformation. Mean values (± standard deviation). Data calculated in porcine and rabbit eyes using two air-puff configurations (AP1 and AP2). locations in the eye are labeled as C (central cornea), S (superior), I (inferior), EN (equatorial nasal), ET (equatorial temporal, PN (posterior nasal), and PT (posterior temporal) sclera. Time interval between speed extremes was estimated at all locations only for rabbit eyes. Porcine results were taken from our published data in (Bronte-Ciriza et al., 2021).

Porcine tissue	**Young's Modulus (MPa)**	C_{10} **(MPa)**	C_{20} **(MPa)**	C_{20}/C_{10} **(MPa/MPa)**
C	0.69±0.14	0.06	2.14	38.9
ET	6.04±2.11	0.99	4.38	4.4
EN	4.40±1.33	0.83	1.39	1.7
PT	4.54±1.20	0.75	0.23	0.3
PN	4.90±1.06	1.26	0.18	0.1
S	2.19±0.43	0.27	3.77	14.0
I	1.84±0.30	0.26	2.07	8.1

Table A.3: Young's modulus and elastic parameters from Finite Element Model inverse optimization. The Young modulus at 10% strain at all locations. The estimated C_{10} (overall stiffness) ranged from 0.055 MPa for the cornea to 1.249 MPa for the posterior nasal position. The C_{20} (related to the non-linear stress-strain response) ranged from 0.185 MPa for the PT location to 4.379 MPa for the ET location. The ratio C_{20}/C_{10} was higher for the cornea (39) than for the scleral positions (0.14-14), indicating a larger non-linear response The locations in the eye are the C (central cornea), and in the sclera: S (superior), I (inferior), EN (equatorial nasal), ET (equatorial temporal, PN (posterior nasal), and PT (posterior temporal). The intraocular pressure was maintained at 15 mmHg. Porcine results were taken our published data (Bronte-Ciriza et al., 2021).

B. Tables of results for OCE measurements

Zone	Location	Phase Speed (m/s)	Thickness (μm)	Shear Modulus (kPa)
Cornea	C	† 5.9 (5.7-7.0)	‡ 511.1(487.9-534.4)	† 11.2 (9.6-12.9)
Anterior Sclera	SN	10.4 (9.1-11.8)	331.8(305.8-357.8)	28.5 (21.9-35.1)
	IN	9.6 (8.3-11.0)	325.3(299.3-351.2)	24.7 (18.1-31.4)
	ST	10.6 (9.3-11.9)	317.7(291.7-343.7)	30.4 (23.8-37.0)
	IT	9.7 (8.3-11.1)	302.9(276.9-328.9)	25.4 (18.7-32.0)
	Total	***†10.1(9.4-10.8)***	***‡ 319.4(307.3-331.5)***	***†27.3 (23.7-30.9)***
Posterior Sclera	SN	8.1 (6.8- 9.5)	364.5(338.5-390.5)	18.7 (12.1-25.3)
	IN	7.5 (6.2- 8.9)	313.9(287.9-339.9)	16.0 (9.4-22.6)
	ST	8.3 (6.9- 9.6)	302.0(276.0-327.9)	18.7 (12.1-25.4)
	IT	8.2 (6.8- 9.5)	276.2(250.2-302.2)	17.9 (11.3-24.6)
	Total	***†8.0 (7.4-8.7)***	***‡ 314.1(295.6-332.7)***	***†17.8 (15.0-20.7)***

Table B.1: Mean values (and 95% confidence intervals) of phase speed, thickness and shear modulus for three zones: cornea (C), anterior sclera (AS) and posterior sclera (PS). Multiple comparisons between zones revealed statistically significant differences shown between labeled values (†: $p<.004$). Only C vs. AS and C vs. PS comparisons in tissue thickness are significant (‡: $p<.001$).

Zone	**Location**	**Phase Speed (m/s)**	**Thickness (µm)**	**Shear Modulus (kPa)**	**Young's Modulus at 7% strain (MPa)**
Cornea	C	† 5.9 (5.7-7.0)	‡511.1(487.9-534.4)	† 11.2 (9.6-12.9)	1.8 (0.8 - 2.8)
Meridional Sclera	SN	9.3 (7.1 -11.5)	348.1 (322.5-373.8)	23.6 (5.5-41.7)	3.5 (2.9-4.1)
	IN	8.6 (6.4 -10.8)	319.6 (293.9-345.2)	20.4 (2.3-38.5)	3.5 (2.4 -4.6)
	ST	9.4 (7.2 -11.6)	309.8 (284.2-335.5)	24.6 (6.5-42.7)	
	IT	8.9 (6.7 -11.1)	289.5 (263.9-315.2)	21.7 (3.6-39.8)	
	Total	*†9.1 (7.9-10.1)*	*‡316.8 (299.5-334.0)*	*†22.5 (19.7-25.3)*	
Circumferential Sclera	SN	16.8 (14.6-19.0)	335.5 (309.9-361.2)	76.6 (58.5-94.7)	
	IN	13.9 (11.7-16.1)	323.8 (298.2-349.5)	55.5 (37.4-73.6)	
	ST	15.8 (13.6-18.0)	308.3 (282.6-333.9)	67.2 (49.1-85.3)	
	IT	15.0 (12.8-17.2)	290.5 (264.8-316.1)	62.1 (44.0-80.3)	
	Total	*†15.4 (14.3-16.5)*	*‡314.5 (297.3-331.8)*	*†65.4 (53.0-77.8)*	

Table B.2: Mean values (and 95% confidence intervals) of phase speed, thickness, shear modulus and Young's modulus for zones: cornea (C), meridional sclera (MS) and circumferential sclera (CS). Multiple comparisons between zones revealed statistically significant differences shown between labeled values (†: p<.001). Only C vs. MS and C vs. CS comparisons in tissue thickness are significant (‡: p<.001).

C. Tables of results for scleral crosslinking measurements

		Photo-crosslinking treatment		
		RGX	**UVX**	**Naive**
Zone	Region	Young's Modulus at 8% of strain (MPa)	Young's Modulus at 8% of strain (MPa)	Young's Modulus at 8% of strain (MPa)
Untreated sclera	Nasal	3.2(1.5-4.9)	7.9(3.9-11.8)	5.8(2.9- 8.8)
	Temporal	4.9(2.2-7.6)	7.9(4.5-11.3)	6.1(2.2-10.0)
	Total	**4.1 (2.7-5.4) †**	**7.9(5.5-10.3)†**	**6.0(3.8-8.1)**
Treated sclera	Nasal	9.3(4.9-13.8)	14.8(11.8-17.8)	
	Temporal	9.6(4.3-14.9)	15.2(11.8-18.6)	
	Total	**9.5(7.3-11.7)†**	**15.0(11.9-18.2)†**	

Table C.1: Young's Modulus values for untreated and treated sclera. Mean values (and 95% confidence intervals) of Young's modulus for untreated and treated scleral tissue in nasal and temporal regions. Multiple comparisons in zones revealed statistically significant differences in columns between labeled values (†: $p \leq .013$). Results were taken from our published data in (Villegas et al., 2024a).

		Photo-crosslinking treatment	
		RGX	UVX
Zone	**Region**	**Swelling rate (%/min)**	**Swelling rate (%/min)**
Untreated sclera	Nasal	4.0(3.6-4.5)	4.1(3.8-4.5)
	Temporal	3.7(3.1-4.2)	3.9(3.5-4.4)
	Total	**3.8(3.5-4.2) †**	**4.0(3.8-4.3)†**
Treated sclera	Nasal	3.4(3.0-3.8)	3.6(3.3-3.9)
	Temporal	3.3(3.1-3.6)	3.5(3.2-3.8)
	Total	**3.4(3.1-3.6)†**	**3.5(3.3-3.7)†**

Table C.2: Swelling rate values for untreated and treated sclera. Mean values (and 95% confidence intervals) of swelling rate for untreated and treated scleral tissue in nasal and temporal regions. Multiple comparisons in zones revealed statistically significant differences in columns between labeled values (†: $p \leq .003$). Results were taken from our published data in (Villegas et al., 2024a).

		Photo-crosslinking treatment			
		RGX		**UVX**	
		after 40 min rehydration	*after 100 min rehydration*	*after 40 min rehydration*	*after 100 min rehydration*
Zone	**Region**	**Young's Modulus at 8% of strain (MPa)**		**Young's Modulus at 8% of strain (MPa)**	
Untreated sclera	Nasal	7.6(2.8-12.4)	6.3(3.3-9.2)	8.2(1.1-15.4)	6.6(4.5-8.7)
	Temporal	8.7(4.2-13.2)	5.2(4.4-6.0)	5.2(0.03-10.5)	5.9(3.1-8.6)
	Total	**8.1(5.6-10.7) †**	**5.7(4.5-7.0)†**	**6.7(3.4-10.1)†**	**6.2(5.0-7.5)†**
Treated sclera	Nasal	14.0(5.8-22.1)	13.7(9.8-17.6)	19.7(11.9-27.5)	11.4(5.7-17.8.6)
	Temporal	13.9(7.3-20.4)	10.8(8.3-13.4)	17.0(6.0-28.0)	11.8(3.1-8.6)
	Total	**13.9(9.9-17.9)†**	**12.3(10.2-14.4)†**	**18.4(13.6-23.2)†**	**11.6(9.5-13.7)†**

Table C.3: Young's modulus values after 40min and 100min rehydration period. Mean values (and 95% confidence intervals) of Young's modulus for untreated and treated scleral tissue in nasal and temporal regions. Multiple comparisons in zones revealed statistically significant differences in columns between labeled values (†: $p \leq .004$). Results were taken from our published data in (Villegas et al., 2024a).

In tensile test, thickness values were not statistically significantly different in RGX-treated (337.4 ± 31.3 μm vs. 341.2 ± 28.5 μm, p=.43) and UVX-treated (300.3 ± 29.5 μm vs. 324.5 ± 37.4 μm, p=.23) sclera compared to untreated sclera. There were no statistically significant differences in thickness between temporal and nasal regions in virgin sclera (324.2 ± 55.0 μm and 306.8 ± 44.0 μm, p=.58), see Table C4.

		Photo-crosslinking treatment		
		RGX	**UVX**	**Naive**
Zone	**Region**	**Thickness (µm)**	**Thickness (µm)**	**Thickness (µm)**
Untreated sclera	**Nasal**	343(317-369)	323(259-387)	324(266-382)
	Temporal	339(303-375)	326(298-354)	307(261-353)
	Total	**341(323-359)**	**324(298-351)**	**315(285-346)**
Treated sclera	**Nasal**	323(288-358)	294(264-324)	
	Temporal	352(327-376)	307(262-351)	
	Total	**337(317-357)**	**300(279-321)**	

Table C.4: Mean values (and 95% confidence intervals) of thickness for untreated and treated scleral tissue in nasal and temporal regions. Comparisons revealed no statistically significant main effect among the thickness (repeated measures ANOVA, *p=.43* (RGX), p=.23(UVX), and one-way ANOVA p=.58 (Naive)). Results were taken from our published data in (Villegas et al., 2024a).

In hydration-tensile test, there was no statistically significant difference in thickness between RGX-treated ($281.0 \pm 19.6\ \mu m$ vs. $290.6 \pm 36.1\ \mu m$, p=.76) and UVX-treated ($280.6 \pm 15.2\ \mu m$ vs. $280.9 \pm 24.1\ \mu m$, p=.27,(UVX-4 0min)) sclera compared to untreated sclera after 40 minutes of rehydration, nor after 100 minutes of rehydration in RGX-treated ($298.1 \pm 12.7\ \mu m$ vs. $294.2 \pm 23.6\ \mu m$, p=.21) and UVX-treated sclera ($307.9 \pm 22.3\ \mu m$ vs. $321.9 \pm 22.0\ \mu m$, p=.29) sclera compared to untreated sclera, see Table C5.

		Thickness (μm)			
		RGX		**UVX**	
Zone	**Region**	**after 40 min rehydration**	**after 100 min rehydration**	**after 40 min rehydration**	**after 100 min rehydration**
Untreated sclera	**Nasal**	289(236-342)	283(256-310)	268(221-316)	333(329-338)
	Temporal	292(251-334)	305(278-332)	293(284-303)	310(266-354)
	Total	**290(265-317)**	**294(277-311)**	**281(261-301)**	**322(303-340)**
Treated sclera	**Nasal**	284(258-310)	297(279-315)	285(264-305)	303(253-354)
	Temporal	278(253-303)	299(285-314)	277(248-305)	313(296-328)
	Total	**281(267-295)**	**298(289-307)**	**281(268-293)**	**308(289-326)**

Table C.5: Means (and 95% confidence intervals) of thickness for untreated and treated scleral tissue in nasal and temporal regions. Comparisons revealed no statistically significant main effect among the thickness (repeated measures ANOVA, p=.76(RGX-40min), p=.21(RGX-100min), p=.27(UVX-40min), p=.29(UVX-100min)). Results were taken from our published data in (Villegas et al., 2024a).

D. Tables of results for scleral biomechanics after myopia induction

Pharmacological treatment	**Eye**	**Axial length (mm) at 0 week**	**Axial length (mm) at 2 weeks**	**Axial length (mm) at 4 weeks**
Saline	FD (treated)	7.83 ± 0.01	8.27 ± 0.05	8.55 ± 0.07
	Fellow (untreated)	7.84 ± 0.04	8.16 ± 0.05	8.36 ± 0.01
Latanoprost	FD (treated)	7.85 ± 0.18	8.26 ± 0.01	8.47 ± 0.02
	Fellow (untreated)	7.87 ± 0.12	8.20 ± 0.02	8.36 ± 0.02
Atropine	FD (treated)	7.73 ± 0.01	8.13 ± 0.01	8.33 ± 0.02
	Fellow (untreated)	7.72 ± 0.17	8.07 ± 0.02	8.26 ± 0.04

Table D.1: Axial length values of guinea pig eyes for each group. Mean values ± standard deviations of axial length (in millimeters) after 0, 2, and 4 weeks of myopia induction. Values measured for form-deprived (FD) and corresponding fellow guinea pig eyes. Comparisons of the entire myopia induction period are shown in Figure 4.31.

Pharmacological treatment	**Eye**	**Axial length (mm) at 6 weeks**	**Axial length (mm) at 8 weeks**	**Axial length (mm) at 10 weeks**
Saline	FD (treated)	8.73 ± 0.03	8.93 ±0.13	9.06 ± 0.15
	Fellow (untreated)	8.50 ± 0.07	8.70 ±0.05	8.81 ± 0.08
Latanoprost	FD (treated)	8.69 ± 0.11	8.98 ±0.10	9.14 ± 0.01
	Fellow (untreated)	8.59 ± 0.15	8.80 ±0.05	8.97 ± 0.04
Atropine	FD (treated)	8.57 ± 0.03	8.81± 0.07	8.97 ± 0.01
	Fellow (untreated)	8.47 ± 0.02	8.64 ±0.05	8.79 ± 0.03

Table D.2: Axial length values of guinea pig eyes for each group. Mean values ± standard deviations of axial length (in millimeters) after 0, 2, and 4 weeks of myopia induction. Values measured for form-deprived (FD) and corresponding fellow guinea pig eyes. Comparisons of the entire myopia induction period are shown in Figure 4.31.

Pharmacological treatment	**Eye**	**Spherical equivalent (D) at 0 week**	**Spherical equivalent (D) at 2 weeks**	**Spherical equivalent (D) at 4 weeks**
Saline	FD (treated)	2.6 ± 0.1	0.5 ± 0.2	-1.0 ± 0.2*
	Fellow (untreated)	2.6 ± 0.1	2.1 ± 0.2	1.3 ± 0.4
Latanoprost	FD (treated)	3.1 ± 0.6	-0.4 ± 2.1	-2.0 ± 1.6*
	Fellow (untreated)	3.5 ± 0.2	1.5 ± 0.1	1.6 ± 0.2
Atropine	FD (treated)	2.6 ± 0.4	0.2 ± 1.9	-0.2 ± 1.8
	Fellow (untreated)	3.2 ± 0.6	1.9 ± 0.5	1.1 ± 0.01

Table D.3: Spherical equivalent values of guinea pig eyes for each group. Mean values ± standard deviations of spherical equivalent (in diopters) after 0, 6, and 10 weeks of myopia induction. Values measured for form-deprived (FD) and corresponding fellow guinea pig eyes. Comparisons of the entire myopia induction period are shown in Figure 4.32. *:Spherical equivalent ≤ -0.50D in either eye is considered myopia according to WHO (World Health Organization and Brien Holden Vision Institute, 2016).

Pharmacological treatment	**Eye**	**Spherical equivalent (D) at 6 weeks**	**Spherical equivalent (D) at 8 weeks**	**Spherical equivalent (D) at 10 weeks**
Saline	FD (treated)	-2.1 ± 0.3*	-3.6 ± 0.2*	-6.1 ± 0.8**
	Fellow (untreated)	1.7 ± 0.2	1.6 ± 0.2	1.3 ± 0.1
Latanoprost	FD (treated)	-2.4 ± 1.0*	-2.9 ± 0.7*	-3.0 ±1.3*
	Fellow (untreated)	1.9 ± 0.2	1.5 ± 0.3	1.6 ± 0.5
Atropine	FD (treated)	-2.5 ± 0.5*	-3.5 ± 0.1*	-3.4 ± 1.4*
	Fellow (untreated)	1.2 ± 0.2	0.7 ± 0.6	1.0 ± 0.2

Table D.4: Spherical equivalent values of guinea pig eyes for each group. Mean values ± standard deviations of spherical equivalent (in diopters) after 6, 8 and 10 weeks of myopia induction. Values measured for form-deprived (FD) and corresponding fellow guinea pig eyes. *****: Spherical equivalent ≤ -0.50D in either eye is considered myopia and ******: spherical equivalent ≤-5.00D is high myopia according to WHO (World Health Organization and Brien Holden Vision Institute, 2016).

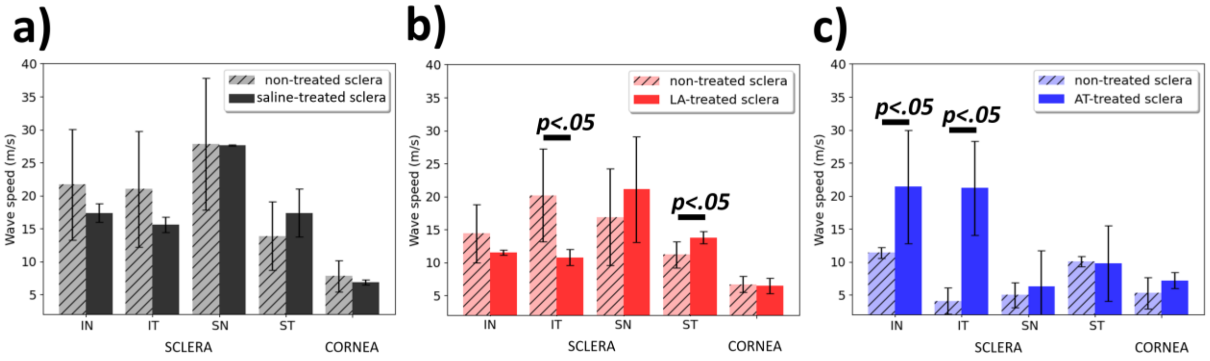

Figure D.1: Comparison between groups of wave speed of sclera and cornea. Ocular globes from guinea pigs (n=2 strips per each region) were subjected to ACUS-OCE measurements. Average wave speed values of scleral tissue around different locations of the sclera (IN, IT, SN, ST) and in the central cornea. Guinea pig eyes were in (a) saline (black bars), (b) latanoprost (red bars) or (c) atropine (blue bars) groups. Data from untreated tissue (from non-myopic eyes) are shown as hatched bars and data from treated tissue (from myopic eyes) are shown as solid bars.

E. Modified Rayleigh-Lamb frequency equation applied to quantify shear modulus

The shear modulus was quantified by solving the mRLFE (Han et al., 2017) at each radial direction and tested location in the eye. The mRLFE (Equation E.4) was applied to a thin membrane (superior layer of cornea and sclera) with no stress on the upper surface and with a fluid-structure interface on the lower surface (internal surface of the cornea and sclera with is in contact with the aqueous humor). Shear modulus values of cornea and sclera were quantified by a Newton-Raphson optimization method (see Section 3.7.3).

The mRLFE was solved to obtain the shear modulus μ corresponding to each measurement of phase speed v_{ph} and tissue thickness from OCE images (see Section 3.7.3). The parameters from the experiment were excitation frequency $f = 2\,kHz$, angular frequency $\omega = 2\pi \cdot f = 2\pi \cdot 2\,kHz$, tissue density $\rho = 988\,kg/m^3$, Poisson's ratio $\nu = 0.498$, shear viscosity $\eta = 0.55\,Pa\,s$, vitreous fluid density $\rho = 1000\,kg/m^3$, and wave speed (speed of sound) in the vitreous fluid $v_F = 1500\,\frac{m}{s}$, and the half of the tissue thickness measurement d corrected by the corresponding refractive indices (see Section 3.7.3). The mRLFE also takes into account the parameters: the Lamé constant $\lambda = \frac{2\mu\nu}{(1-2\nu)}$, the compressional wave (P-wave) speed

$v_1 = \sqrt{\frac{\lambda+2\mu^*}{\rho}}$, the shear wave (S-wave) speed $v_2 = \sqrt{\frac{\mu^*}{\rho}}$, the dynamic shear modulus $\mu^* = \mu + i\omega\eta$, the wave number $k = \frac{\omega}{v_{ph}}$ and the variables in Equations E.1, E.2, E.3.

$$\alpha^2 = k^2 - \frac{\omega^2}{v_1^2} \tag{E.1}$$

$$\beta^2 = k^2 - \frac{\omega^2}{v_2^2} \tag{E.2}$$

$$\alpha_F^2 = k^2 - \frac{\omega^2}{v_F^2} \tag{E.3}$$

$$R = \begin{bmatrix} A\,sinh(\alpha d) & B\,sinh(\beta d) & A \cdot cosh(\alpha d) & B \cdot cosh(\beta d) & 0 \\ C\,cosh(\alpha d) & A\,cosh(\beta d) & C \cdot sinh(\alpha d) & A \cdot\ sinh(\beta d) & 0 \\ -A\,sinh(\alpha d) & -B\,sinh(\beta d) & A \cdot cosh(\alpha d) & B \cdot cosh(\beta d) & \frac{\rho_F \omega^2}{\mu^*} \\ C\,cosh(\alpha d) & A\,cosh(\beta d) & -C \cdot sinh(\alpha d) & -A \cdot sinh(\beta d) & 0 \\ \alpha\,cosh(\alpha d) & k\,cosh(\beta d) & -\alpha\,sinh(\alpha d) & -k\,sinh(\beta d) & -\alpha_F \end{bmatrix} \tag{E.4}$$

Equation E.4 (referred to as the mRLFE model) is solved with the determinant $det\ (R)\ = 0$, where $A = k^2 + \beta^2$, $B = 2k\beta$, and C= $2k\alpha$.